

Lakehead University

**INVESTIGATION AND PERFORMANCE CHARACTERISTICS OF A
HYBRID SOLAR PHOTOVOLTAIC-THERMOELECTRIC POWER
GENERATION RENEWABLE ENERGY SYSTEM**

A Thesis by

Justin Bujold

MASTER OF SCIENCE IN MECHANICAL ENGINEERING

Submitted to the Faculty of Graduate Studies
in Partial Fulfillment of the Requirements for
the Master's Degree in Mechanical Engineering

Supervised by

Dr. BASEL I. ISMAIL, P.Eng.

July 2015

Copyright Exceptions

It is understood that the copyright for the material in this thesis is reserved to the supervisor and author. No parts of this publication may be reproduced, stored in a retrievable system, or transmitted in any form by any means, electronic, mechanical, photocopy, recording, scanning, or otherwise, except as permitted by the main supervisor of this thesis. The non-exclusive right granted to Lakehead University, and moreover, Chancellor Paterson Library to archive the completed work in a publically available manner does not change the copyright status.

Acknowledgments

Firstly, I would like to thank my research supervisor, Dr. Basel I. Ismail, Associate Professor of Mechanical Engineering for his wisdom and encouragement. Dr. Ismail has instilled in me the qualities of a professional engineer and a valued researcher. His expertise in renewable energy technologies and continued support has allowed me to progress in my academic career, more specifically in this research work. I would like to thank my thesis committee, Dr. Murari Roy and Dr. Pedram Fatehi for taking the time to review my thesis and provide valuable feedback to improve my research. I would also like to thank Dr. Ismail's research team, and my fellow colleagues, N. Alabdrabalnabi, J. Gulom Hazrat, E. Aragao de Arruda, J. Fernandes, and R. Alan for their assistance during the preliminary experimental phase of this thesis. Special thanks to the Lakehead University technicians, S. Stangier, J. Ripku, K. Bhatia, and J. Servais, for providing the required resources to complete the experimental simulations.

I would like to acknowledge the love and support I have received from my parents Louis and Shari Bujold, siblings, grandparents, and family. Their encouragement has given me the strength and determination to overcome challenges. I would like to thank Lynnea Maki, for her love, patience and support. I would also like to thank Cathy Maki, for her words of wisdom. Finally, my heartfelt thanks to Larry Stahn, my grandfather, as he inspired my interest in renewable energy.

Abstract

Increasing fossil fuel prices, electricity demand, and global concern for greenhouse gas emissions have increased interest and research of novel renewable energy technologies. Renewable solar-photovoltaic (PV) systems are known for their ability to directly convert solar energy into electrical energy, however, their performance degrades when operating at elevated temperatures. Thus, decreasing the temperature of PV modules using efficient cooling methods tend to improve their overall efficiency and increase power production. Thermoelectric power generation (TEG) technology has the innovative capability to convert a portion of the waste-heat energy dissipated from PV systems directly into electricity, and simultaneously reduce the PV systems operating temperature. Hybrid photovoltaic-thermoelectric power generation (HPV-TEG) systems integrate TEG modules with a PV module to form a more efficient power generation system. There has been a lack of research that has explored this hybrid concept and characterized in detail the performance of HPV-TEG systems. Therefore, the main objective of this research work is to investigate the viability and performance characteristics of a HPV-TEG system through detailed numerical and experimental studies. Numerical simulations showed that the HPV-TEG system was able to generate more electricity than a conventional PV system while operating at high solar radiation intensities and ambient temperatures. Two HPV-TEG test setups (indoor & outdoor) were designed, constructed and fully instrumented in order to achieve the main objective of this research. Detailed indoor and outdoor experimental tests and case studies were consistently performed. Optimization of the HPV-TEG system showed that the addition of an aluminum layer increased the PV and TEG power output by approximately 6.9% and 350%, respectively. The infrared thermal imaging results showed that the HPV-TEG systems' cooling system efficiently reduced the systems' operating temperature. In the outdoor tests, the HPV-TEG systems' minimum and maximum overall daily efficiency were 3.68% and 9.45%, respectively. For all the tests, it was found that the daily electrical energy output from the HPV-TEG system was always higher than the conventional PV system (in one case about 6.4% higher). Finally, a predictive sizing correlation was developed to estimate the power density generated by an HPV-TEG system as a function of solar radiation, ambient air temperature, and TEG's coolant inlet temperature. A conceptual scheme was also proposed in this study for large-scale application using the promising green HPV-TEG technology.

Table of Contents

Table of Figures	v
List of Tables	xii
Nomenclature	xiii
Chapter 1: Introduction	1
1.1 Environmental Issues and Renewable Energy Technologies.....	1
1.2 Fundamentals of Solar Photovoltaic Systems.....	5
1.2.1 Photovoltaic Cells	5
1.2.2 Power Generation Characteristics of Photovoltaic Systems	9
1.2.3 Improving PV Systems Performance	14
1.3 Thermoelectric Technology for Power Generation.....	18
1.4 The Thermoelectric Effects	18
1.4.1 The Seebeck Effect.....	18
1.4.2 The Peltier Effect.....	20
1.4.3 The Thomson Effect	20
1.5 Thermoelectric Devices.....	22
1.5.1 Major Components of a Thermoelectric Module	22
1.5.2 Thermoelectric Materials	26
1.6 Thermoelectric Power Generator Performance Characteristics.....	28
1.6.1 Energy Conversion Efficiency	28
1.6.2 Thermoelectric Figure-of-Merit	30
1.7 Hybrid Photovoltaic-Thermoelectric Power Generation	33
1.8 Thesis Outline	35
Chapter 2: Literature Review.....	37
2.1 Previous Experimental Studies of Solar PV Systems for Optimal Power Generation.....	37
2.2 Previous Experimental Power Generation Characteristic Studies of TEGs	41
2.3 Previous Studies on Characterization of Hybrid TEG Systems	42
2.3.1 Solar Thermal-Concentrator Thermoelectric Generators	42
2.3.2 Recent Research Investigations of HPV-TEG Systems	43
2.4 Thesis Research Objectives.....	46
Chapter 3: Modeling and Numerical Characterization of a HPV-TEG System.....	48

3.1 Numerical Model and Analysis of Conventional and Hybrid Photovoltaic Module	48
3.1.1 Thermal Circuit Analogy	48
3.1.2 Determination Conventional PV Module Temperature Profile.....	49
3.1.3 Determination of the HPV-TEG Module Temperature Profile	53
3.1.4 Modeling the Thermoelectric Power Generator.....	56
3.1.5 Modeling and Simulation of Thomson Effect	59
3.1.6 Equivalent Circuit Model of a Photovoltaic Module	60
3.1.7 Developed Computational Algorithm for Solving the Complex Systems of Equations.....	65
3.1.8 Exergy Analysis of a PV and HPV-TEG System	67
3.2 Numerical Model Results and Discussion	70
3.2.1 Thomson Effect Analysis	70
3.2.2 Performance Analysis of PV and HPV-TEG	75
3.2.3 Energy and Exergy Analyses of HPV-TEG System	79
Chapter 4: Experimental Work.....	86
4.1 Fabrication and Instrumentation of Hybrid Photovoltaic Modules	86
4.2 Indoor Solar Simulation Tests.....	88
4.2.1 Indoor Experimental Solar Simulator Test Setup and Methodology.....	88
4.2.2 Results and Discussion: Indoor Experimental Tests.....	91
4.3 Outdoor Case Studies.....	106
4.3.1 Outdoor Experimental Site Location.....	106
4.3.2 Outdoor Experimental Test Setup and Experimental Procedure.....	108
4.3.3 Results and Discussion: Outdoor Case Studies.....	113
4.4 Proposed Scheme for Large-scale Application of HPV-TEG System.....	147
4.5 Uncertainty Analysis of Experimental Results.....	150
Chapter 5: Conclusion and Future Recommendations.....	152
5.1 Conclusion	152
5.2 Future Works and Recommendations	154
References	156

Table of Figures

Figure 1.1: Global CO ₂ emissions per year due to fossil fuel combustion from 1750-2010 [3].	2
Figure 1.2: Radiative forcing change from 1750 to 2011 [4].....	2
Figure 1.3: Annual global-mean temperature from 1880 to 2013 [6].	4
Figure 1.4: World electricity generation (TWh) from 1970 to 2011 for various energy sources [7].	4
Figure 1.5: Schematic of the major components of a photovoltaic cell.....	6
Figure 1.6: Schematic of a photovoltaic cell, photovoltaic module, and photovoltaic array. ...	8
Figure 1.7: Typical current and power vs. voltage (I-V & P-V) curve of standard photovoltaic module based on experimental data.....	10
Figure 1.8: Typical I-V and P-V curve of photovoltaic cell at various irradiance intensities and constant photovoltaic cell temperature.	12
Figure 1.9: Typical I-V and P-V curve of photovoltaic cell at various temperatures at a constant irradiance intensity.	12
Figure 1.10: Conversion efficiencies of research PV cells from 1976- 2015 [29].....	13
Figure 1.11: Typical photovoltaic-thermal system designs.....	17
Figure 1.12: Principle of (a) the Seebeck effect using a thermocouple, and (b) the thermodynamic heat engine cycle.....	19
Figure 1.13: Principle of (a) the Peltier effect using a thermocouple, and (b) the thermodynamic heat pump cycle.	21
Figure 1.14: Schematic of major components of a typical thermoelectric module.....	23
Figure 1.15: Thermoelectric module acting as a (a) thermoelectric generator (b) thermoelectric cooler.	23
Figure 1.16: (a) single-stage thermoelectric module (b) multi-stage thermoelectric cooler [58] (c) Flexible micro thermoelectric generator [64] (d) ring-structured thermoelectric module [65].....	25
Figure 1.17: Typical current and power vs. voltage (I-V & P-V) curve of standard thermoelectric generator based on experimental data.....	29
Figure 1.18: Figure-of-merit vs. temperature of various thermoelectric materials [50].....	32

Figure 1.19: Experimentally determined dimensionless figure-of-merit vs. mean temperature at various temperature gradients (diamond shape symbols – small temperature difference, circle shape symbols – large temperature difference) [87].	32
Figure 1.20: The concept of a hybrid photovoltaic-thermoelectric generator.	34
Figure 2.1: Flow chart of major components of research thesis.	47
Figure 3.1: Schematic of a simplified model conventional PV module and thermal circuit used in this study.	50
Figure 3.2: Schematic of the simplified HPV-TEG module and thermal circuit used in this work.	54
Figure 3.3: Equivalent circuit model of a photovoltaic module with a single diode.	62
Figure 3.4: Algorithm used to solve complex system of nonlinear equations to determine temperature and performance of PV and HPV-TEG system.	66
Figure 3.5: Thermoelectric power generated temperature difference between accounting and neglecting the Thomson effect vs. irradiance intensity, $T_{amb}=25\text{ }^{\circ}\text{C}$, $h_{conv,top}=20\text{ W/m}^2\cdot\text{K}$.	71
Figure 3.6: Mean thermoelectric generator temperature difference between accounting and neglecting the Thomson effect vs. irradiance intensity, $T_{amb}=25\text{ }^{\circ}\text{C}$, $h_{conv,top}=20\text{ W/m}^2\cdot\text{K}$.	73
Figure 3.7: HPV-TEG photovoltaic cell temperature difference between account and neglecting the Thomson effect vs. irradiance intensity, $T_{amb}=25\text{ }^{\circ}\text{C}$, $h_{conv,top}=20\text{ W/m}^2\cdot\text{K}$.	73
Figure 3.8: HPV-TEG photovoltaic module power output difference between account and neglecting the Thomson effect vs. irradiance intensity, $T_{amb}=25\text{ }^{\circ}\text{C}$, $h_{conv,top}=20\text{ W/m}^2\cdot\text{K}$.	74
Figure 3.9: Photovoltaic cell temperature of PV and HPV-TEG photovoltaic module vs. irradiance intensity, $T_{amb}=25\text{ }^{\circ}\text{C}$, $h_{conv,top}=20\text{ W/m}^2\cdot\text{K}$.	76
Figure 3.10: Power generated by PV and HPV-TEG photovoltaic module vs. irradiance intensity, $T_{amb}=25\text{ }^{\circ}\text{C}$, $h_{conv,top}=20\text{ W/m}^2\cdot\text{K}$.	76
Figure 3.11: Power generated by PV and HPV-TEG photovoltaic module vs. ambient air temperature, $G_T=1000\text{ W/m}^2$, $h_{conv,top}=20\text{ W/m}^2\cdot\text{K}$.	77
Figure 3.12: HPV-TEG photovoltaic cell temperature vs. irradiance intensity vs. ambient air temperature, $h_{conv,top}=20\text{ W/m}^2\cdot\text{K}$.	77
Figure 3.13: Power generated by thermoelectric generator vs. irradiance intensity vs. ambient air temperature, $h_{conv,top}=20\text{ W/m}^2\cdot\text{K}$.	78

Figure 3.14: (a) Energy conversion efficiency and (b) exergy efficiency of PV and HPV-TEG system vs. irradiance intensity, $T_{amb}=25\text{ }^{\circ}\text{C}$, $h_{conv,top} = 20\text{ W/m}^2\cdot\text{K}$	80
Figure 3.15: (a) Energy conversion efficiency and (b) exergy efficiency of PV and HPV-TEG system vs. ambient air temperature, $G_T=1000\text{ W/m}^2$, $h_{conv,top} = 10\text{ W/m}^2\cdot\text{K}$	80
Figure 3.16: Energy conversion efficiency of thermoelectric generator vs. ambient air temperature vs. irradiance intensity, $h_{conv,top} = 20\text{ W/m}^2\cdot\text{K}$	81
Figure 3.17: (a) Energy conversion efficiency and (b) exergy efficiency of PV and HPV-TEG system vs. ambient air temperature, $G_T=1000\text{ W/m}^2$, $T_{amb}=25\text{ }^{\circ}\text{C}$	81
Figure 3.18: (a) Energy conversion efficiency and (b) exergy efficiency of PV and HPV-TEG system vs. irradiance intensity, $T_{amb}=5\text{ }^{\circ}\text{C}$, $h_{conv,top} = 20\text{ W/m}^2\cdot\text{K}$	83
Figure 3.19: Rate of exergy destruction by HPV-TEG system vs. irradiance intensity vs. ambient air temperature, $h_{conv,top}=20\text{ W/m}^2\cdot\text{K}$	83
Figure 3.20: Rate of exergy destruction by HPV-TEG system due to various components vs. irradiance intensity, $T_{amb}=25\text{ }^{\circ}\text{C}$, $h_{conv,top}=20\text{ W/m}^2\cdot\text{K}$	85
Figure 3.21: Rate of exergy destruction by thermoelectric generator vs. irradiance intensity, $T_{amb}=25\text{ }^{\circ}\text{C}$, $h_{conv,top}=20\text{ W/m}^2\cdot\text{K}$	85
Figure 4.1: Back surface of hybrid photovoltaic module with aluminum sheet, thermoelectric generator, and aluminum cooling block.	89
Figure 4.2: Photographs showing fabrication of 10W-HPV-2TEG module.	89
Figure 4.3: The indoor experimental test setup for (a) hybrid photovoltaic system (b) conventional photovoltaic system used in this investigation.....	90
Figure 4.4: A photograph showing the indoor experimental simulation of 40W-HPV-10TEG module using solar simulator used in this investigation.....	90
Figure 4.5: Back photovoltaic module temperature vs. time for 10W-HPV-2TEG system with and without aluminum layer, $G_T=825\text{ W/m}^2$, $T_{w,in}=14\text{ }^{\circ}\text{C}$. $\dot{V}=1\text{ L/min}$	92
Figure 4.6: Thermal profiles of 10W-HPV-2TEG module (a) without aluminum (b) with aluminum, $G_T=825\text{ W/m}^2$, $T_{w,in}=14\text{ }^{\circ}\text{C}$. $\dot{V}=1\text{ L/min}$	92
Figure 4.7: 10W-HPV(-2TEG) module power vs. voltage with and without aluminum layer, $G_T=825\text{ W/m}^2$, $T_{w,in}=13.75\text{ }^{\circ}\text{C}$, $\dot{V}=1\text{ L/min}$	93
Figure 4.8: 2TEG power vs. voltage with and without aluminum layer, $G_T=825\text{ W/m}^2$, $T_{w,in}=13.75\text{ }^{\circ}\text{C}$, $\dot{V}=1\text{ L/min}$	93

Figure 4.9: Thermal profiles of (a) 10W-PV (b) 10W-HPV-2TEG and (c) 10W-HPV-4TEG system, $G_T=825 \text{ W/m}^2$, $T_{w,in}=11 \text{ }^\circ\text{C}$, $\dot{V}=1 \text{ L/min}$	94
Figure 4.10: Power vs. voltage curves of hybrid photovoltaic module for 10W-HPV-2TEG and 10W-HPV-4TEG system, $G_T=825 \text{ W/m}^2$, $T_{w,in}=11 \text{ }^\circ\text{C}$, $\dot{V}=1 \text{ L/min}$	96
Figure 4.11: TEG power vs. voltage curves for 10W-HPV-2TEG and 10W-HPV-4TEG system, $G_T=825 \text{ W/m}^2$, $T_{w,in}=11 \text{ }^\circ\text{C}$, $\dot{V}=1 \text{ L/min}$	96
Figure 4.12: 10W-PV, 10W-HPV(-2TEG), and 2TEG maximum power output vs. irradiance intensity, $T_{w,in}=11 \text{ }^\circ\text{C}$, $\dot{V}=1 \text{ L/min}$	97
Figure 4.13: 40W-PV, 40W-HPV(-10TEG), and 10TEG maximum power point vs. irradiance intensity, $T_{w,in}=2 \text{ }^\circ\text{C}$, $\dot{V}=1 \text{ L/min}$	97
Figure 4.14: Thermal profiles of the (a) 40W-PV and (b) 40W-HPV-10TEG system, $G_T=750 \text{ W/m}^2$, $T_{w,in}=2 \text{ }^\circ\text{C}$, $\dot{V}=1 \text{ L/min}$	98
Figure 4.15: 10TEG thermoelectric generator maximum power output and temperature difference across TEG vs. irradiance intensity, $T_{w,in}=2 \text{ }^\circ\text{C}$, $\dot{V}=1 \text{ L/min}$	100
Figure 4.16: 40W-HPV-(10TEG) module and thermoelectric generator (10TEG) power output vs. water inlet temperature, $G_T=750 \text{ W/m}^2$, $\dot{V}=1 \text{ L/min}$	100
Figure 4.17: Thermal profile of the 40W-HPV-10TEG operating with a water inlet temperature of (a) $2 \text{ }^\circ\text{C}$ and (b) $20 \text{ }^\circ\text{C}$, $G_T=750 \text{ W/m}^2$, $\dot{V}=1 \text{ L/min}$	101
Figure 4.18: Photograph of the concentrated hybrid photovoltaic-thermoelectric power generation module (40W-CHPV-10TEG).....	101
Figure 4.19: The 40W-PV, 10W-HPV-(10TEG), and 40W-CHPV(-10TEG) module power and vs. voltage curves, $G_T=750 \text{ W/m}^2$, $T_{w,in}=2 \text{ }^\circ\text{C}$, $\dot{V}=1 \text{ L/min}$	103
Figure 4.20: Thermal profiles of the (a) 40W-PV-10TEG (b) 40W-HPV-10TEG, and (c) CHPV-TEG module, $G_T=750 \text{ W/m}^2$, $T_{w,in}=2 \text{ }^\circ\text{C}$, $\dot{V}=1 \text{ L/min}$	104
Figure 4.21: The HPV-TEG and CHPV-TEG thermoelectric generator current vs. voltage curves, $G_T=750 \text{ W/m}^2$, $T_{w,in}=2 \text{ }^\circ\text{C}$, $\dot{V}=1 \text{ L/min}$	105
Figure 4.22: The HPV-TEG and CHPV-TEG thermoelectric generator power vs. voltage curves, $G_T=750 \text{ W/m}^2$, $T_{w,in}=2 \text{ }^\circ\text{C}$, $\dot{V}=1 \text{ L/min}$	105
Figure 4.23: Location of Thunder Bay ($48.38 \text{ }^\circ\text{N}$, $89.25 \text{ }^\circ\text{W}$), Ontario, Canada [146].	107

Figure 4.24: Photographs showing the outdoor experimental test setup of (a) 10W-PV/ 10W-HPV-2TEG and 10W-PV/ 10W-HPV-4TEG system (b) 40W-PV/ 40W-HPV-10TEG system.....	110
Figure 4.25: Schematic of the outdoor experimental test setup used in this research work.	111
Figure 4.26: Water inlet temperature vs. time for outdoor test #1 to test #7.	114
Figure 4.27: Water inlet temperature vs. time for outdoor test #8 to test #12.	114
Figure 4.28: Corresponding incident irradiance intensity G_T , ambient air temperature T_{amb} , and wind speed V_{wind} vs. time (test #1).....	115
Figure 4.29: Power output of standard 10W-PV and hybrid 10W-HPV(-2TEG) photovoltaic module vs. time (test #1).....	115
Figure 4.30: Thermoelectric generator (2TEG) power output vs. time (test #1).....	116
Figure 4.31: Back PV temperature vs. time (test #1).....	116
Figure 4.32: Corresponding incident irradiance intensity G_T , ambient air temperature T_{amb} , and wind speed V_{wind} vs. time (test #2).....	118
Figure 4.33: Power output of standard (10W-PV) and hybrid 10W-HPV(-2TEG) photovoltaic module vs. time (test #2).	118
Figure 4.34: Thermoelectric generator (2TEG) power output vs. time (test #2).....	118
Figure 4.35: Corresponding incident irradiance intensity G_T , ambient air temperature T_{amb} , and wind speed V_{wind} vs. time (test #3).....	119
Figure 4.36: Power output of standard (10W-PV) and hybrid 10W-HPV(-2TEG) photovoltaic module vs. time (test #3).	119
Figure 4.37: Thermoelectric generator (2TEG) power output vs. time (test #3).....	119
Figure 4.38: Corresponding incident irradiance intensity G_T , ambient air temperature T_{amb} , and wind speed V_{wind} vs. time (test #4).....	121
Figure 4.39: Power output of standard (10W-PV) and hybrid 10W-HPV(-2TEG) photovoltaic module vs. time (test #4).	121
Figure 4.40: Thermoelectric generator (2TEG) power output vs. time (test #4).....	121
Figure 4.41: Corresponding incident irradiance intensity G_T , ambient air temperature T_{amb} , and wind speed V_{wind} vs. time (test #5).....	122

Figure 4.42: Power output of standard 10W-PV and hybrid 10W-HPV(-4TEG) photovoltaic module vs. time (test #5).....	122
Figure 4.43: Thermoelectric generator (4TEG) power output vs. time (test #5).....	122
Figure 4.44: Thermal profile of 10W-PV and 10W-HPV-4TEG (a) 10:30 AM and (b) 2:00PM (test #5).....	124
Figure 4.45: Corresponding incident irradiance intensity G_T , ambient air temperature T_{amb} , and wind speed V_{wind} vs. time (test #6).....	126
Figure 4.46: Power output of standard 10W-PV and hybrid 10W-HPV(-4TEG) photovoltaic module vs. time (test #6).....	126
Figure 4.47: Thermoelectric generator (4TEG) power output vs. time (test #6).....	126
Figure 4.48: Corresponding incident irradiance intensity G_T , ambient air temperature T_{amb} , and wind speed V_{wind} vs. time (test #7).....	127
Figure 4.49: Power output of standard 10W-PV and hybrid 10W-HPV(-4TEG) photovoltaic module vs. time (test #7).....	127
Figure 4.50: Thermoelectric generator (4TEG) power output vs. time (test #7).....	127
Figure 4.51: Corresponding incident irradiance intensity G_T , ambient air temperature T_{amb} , and wind speed V_{wind} vs. time (test #8).....	129
Figure 4.52: Power output of standard 10W-PV and hybrid 10W-HPV(-4TEG) photovoltaic module vs. time (test #8).....	129
Figure 4.53: Thermoelectric generator (4TEG) power output vs. time (test #8).....	129
Figure 4.54: Incident irradiance intensity G_T , irradiance intensity on horizontal plane G , ambient air temperature T_{amb} , and wind speed V_{wind} vs. time (test #9).	130
Figure 4.55: Power output of standard 10W-PV and hybrid 10W-HPV(-10TEG) photovoltaic module vs. time (test #9).....	130
Figure 4.56: Thermoelectric generator (10TEG) power output vs. time (test #9).	130
Figure 4.57: Thermoelectric generator power vs. TEG temperature difference for (a) 4TEG (test #5) and (b) 10TEG (test #9).	132
Figure 4.58: Thermal profile of 10W-PV (left side) and 10W-HPV-4TEG (right side) at 12:00 PM (test #9).	133
Figure 4.59: Incident irradiance intensity G_T , irradiance intensity on horizontal plane G , ambient air temperature T_{amb} , and wind speed V_{wind} vs. time (test #10).....	135

Figure 4.60: Power output of standard 10W-PV and hybrid 10W-HPV(-10TEG) photovoltaic module vs. time (test #10).	135
Figure 4.61: Thermoelectric generator (10TEG) power output vs. time (test #10).....	135
Figure 4.62: Thermal profile of (a) 10W-PV and (b) 10W-HPV-4TEG at 1:45 PM (test #10).	136
Figure 4.63: Incident irradiance intensity G_T , irradiance intensity on horizontal plane G , ambient air temperature T_{amb} , and wind speed V_{wind} vs. time (test #11).....	137
Figure 4.64: Power output of standard 10W-PV and hybrid 10W-HPV(-10TEG) photovoltaic module vs. time (test #11).	137
Figure 4.65: Thermoelectric generator (10TEG) power output vs. time (test #11).....	137
Figure 4.66: Incident irradiance intensity G_T , irradiance intensity on horizontal plane G , ambient air temperature T_{amb} , and wind speed V_{wind} vs. time (test #12).....	139
Figure 4.67: Power output of standard 10W-PV and hybrid 10W-HPV(-10TEG) photovoltaic module vs. time (test #12).	139
Figure 4.68: Thermoelectric generator (10TEG) power output vs. time (test #12).....	139
Figure 4.69: Daily overall system efficiency of conventional PV and HPV-TEG systems for each outdoor experimental test.	143
Figure 4.70: Thermoelectric generator power density (P_{TEG}/A_{PV}) vs. ($G_T T_{amb}/T_{w,in}$).....	144
Figure 4.71: Thermoelectric generator power density P_{TEG}/A_{PV} vs. temperature gradient across TEG.	146
Figure 4.72: Proposed HPV-TEG system for large-scale application using thermal regulation tank.....	148

List of Tables

Table 1.1: World renewable electricity production (GW) and future projection [8].	4
Table 3.1: Specifications and thermophysical and optical properties of PV and HPV-TEG Module used in simulations of this study.	51
Table 3.2: Thermophysical properties of water based on mean temperature (K) used in the numerical study [117].	54
Table 3.3: Specifications of the thermoelectric generator used in this research.	57
Table 3.4: Electrical specifications of PV and HPV module used in this research study.	62
Table 4.1: Specifications of experimental test setup PV/HPV-TEG modules.	87
Table 4.2: Specifications of experimental test setup photovoltaic modules.	87
Table 4.3: Selected PV tilt angle for each test and the corresponding case study.	109
Table 4.4: Summary of weather conditions for each outdoor experimental test.	140
Table 4.5: Summary of performance characteristics of standard photovoltaic module (PV), hybrid system's photovoltaic module (HPV), and thermoelectric generator (TEG) for each outdoor test.	141
Table 4.6: Uncertainty of experimentally measured and calculated parameters of indoor and outdoor simulations.	151

Nomenclature

Greek

α_A	Absorptance
α_s	Seebeck coefficient (V/K)
β_{cell}	Packing factor
ρ_e	Electrical resistivity ($\Omega \cdot m$)
σ_B	Stephan-Boltzmann constant ($5.67 \times 10^{-8} W/m^2 \cdot K^4$)
λ	Wavelength (m)
μ	Temperature coefficient ($1/^\circ C$)
μ_w	Dynamic viscosity (Pa·s)
η	Efficiency (%)
τ	Transmittance
τ_{TEG}	Thompson coefficient (V/K)
γ_e	Electrical conductivity (S/m)
π	Peltier coefficient (V)
Ω	Ohms

Latin

a	Thermal voltage (V)
A	Area (m^2)
c	Speed of light ($3 \times 10^8 m/s$)
C	Concentration ratio
C_p	Specific heat (J/kg·K)
E	Total energy (Wh) or (mWh)
\dot{E}	Energy rate (W)
\dot{E}_x	Exergy rate (W)
En	Energy conversion
FF	Fill factor
G	Irradiance intensity or solar radiation intensity on horizontal plane (W/m^2)
G_T	Incident irradiance or solar radiation intensity (W/m^2)
h	Specific enthalpy (J/kg)
h_p	Plank's constant ($6.25 \times 10^{-34} J \cdot s$)
h_{conv}	Convective heat transfer coefficient ($W/m^2 \cdot K$)
H_T	Total daily irradiance intensity received by photovoltaic system
I	Current (amps)
k	Thermal conductivity ($W/m \cdot K$)
K	Thermal conductance (W/K) or ($W/^\circ C$)
k_B	Boltzmann constant ($1.381 \times 10^{-23} J/K$)
L	Length (m)
\dot{m}	Mass flow rate (kg/s)
Nu_D	Nusselt number
N_s	Number in series
Re_D	Reynold's number
P	Power (W)

P_w	Wetted perimeter (m)
\dot{Q}	Heat transfer rate (W)
R	Resistance
s	Specific entropy (J/kg·K)
S	Solar radiation absorbed (W)
\dot{S}_{gen}	Rate of entropy generation (W/K)
T	Temperature (°C) or (K)
\bar{T}	Mean temperature (°C) or (K)
TEG	Thermoelectric generator
U	Overall heat loss coefficient (W/m ² ·K)
ν	Frequency (1/s)
V	Voltage (volts)
\dot{V}	Volumetric flow rate (L/min)
V_m	Mean fluid velocity (m/s)
V_{wind}	Wind velocity (m/s)
\dot{W}	Rate of Work (W)
Z	Figure-of-merit (1/K)
$Z\bar{T}$	Dimensionless figure-of-merit

Subscripts

A	Absorptance
amb	Ambient air
bot	Bottom
c	Cold
$carnot$	Carnot engine
$cell$	Photovoltaic cell or module
cer	Ceramic
$conv$	Convection
$chan$	Channel
D	Destruction
ele	electrical
gla	glass
h	hot
hot	Hot
HPV	Hybrid photovoltaic module
$HPV-TEG$	Hybrid photovoltaic-thermoelectric generator
in	Input
j	Joule heat
L	Light or load
n	N-type semiconductor thermoelement
o	Diode reverse saturation
oc	Open-circuit voltage (volts)
opt	Optical
out	Outlet
p	P-type semiconductor thermoelement

<i>p-n</i>	Single p-n type thermocouple
<i>PELTIER</i>	Peltier effect
<i>PV</i>	Photovoltaic
<i>max</i>	Maximum
<i>mp</i>	Maximum power point
<i>rad</i>	Radiation
<i>ref</i>	Reference
<i>s</i>	Series
<i>S</i>	Seebeck
<i>sh</i>	Shunt
<i>sc</i>	Short-circuit current (amps)
<i>sil</i>	Silicon
<i>Sun</i>	Sun
<i>T</i>	Tilted PV system
<i>ted</i>	Tedlar
<i>TEG</i>	Thermoelectric generator
<i>THOM</i>	Thomson effect
<i>top</i>	Top
<i>w</i>	Water
<i>0</i>	Dead state

Chapter 1: Introduction

1.1 Environmental Issues and Renewable Energy Technologies

In today's society, there has been an increasing awareness of climate change and environmental issues pertaining to air pollution and global warming. According to the United Nations Framework Convention on Climate Change (UNFCCC), climate change can be defined as an alteration of the composition of the global atmosphere that is attributed directly or indirectly to human activity, in addition to natural climate variability observed over comparable time periods [1]. Although climate change can be the result of natural forces, such as changes in solar radiation and volcanic eruptions, recent scientific and socio-economic studies have shown that the use of fossil fuels by humans has directly contributed to climate change by releasing greenhouse gases (GHGs) into the atmosphere. Ever since the Industrial Era, many technologies have relied on fossil fuels to operate and these technologies have emitted large amounts of carbon dioxide (CO₂), methane (CH₄), nitrous oxide (N₂O) and other greenhouse gases [2]. Research conducted by the Carbon Dioxide Information Analysis Center has examined that the amount of carbon dioxide released due to the use of fossil fuels has been increasing exponentially from 1750 to 2010, as seen in **Figure 1.1** [3].

Greenhouse gases, especially carbon dioxide, trap thermal energy inside the Earth's atmosphere, leading to an overall increase in the Earth's temperature. One method of measuring this phenomenon is to analyze the radiative forcing (RF) of a greenhouse gas. Radiative forcing is the net change in the energy balance of the Earth system in response to an external effect or force. A positive radiative forcing means that the external effect is increasing the rate at which the Earth is absorbing energy by the Sun's radiation, and a negative radiative forcing decreases this rate. Data provided by the Intergovernmental Panel on Climate Change, shown in **Figure 1.2**, displays the change in radiative forcing of multiple agents from 1750 to 2011. The total radiative forcing for carbon dioxide and other well-mixed greenhouse gases (WMGHS) is approximately 2.8 W/m². The total change in radiative forcing due to human activity is estimated to be 2.25 W/m², while the change in radiative forcing due to natural causes is considered to be minimal [4]. This scientific study

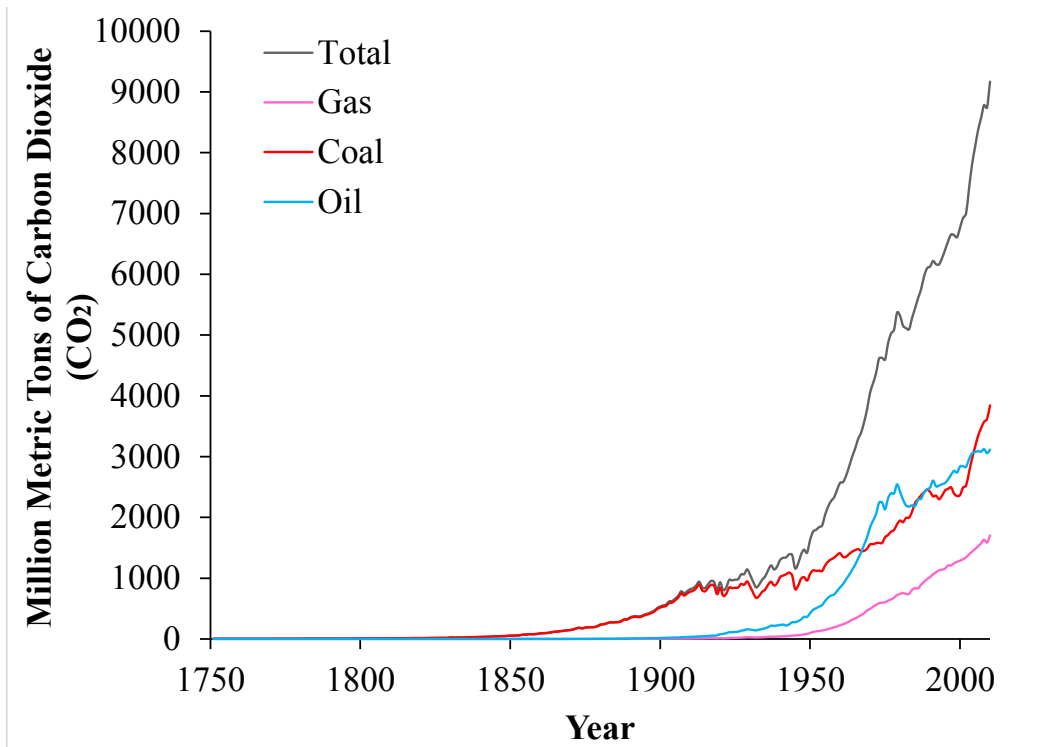


Figure 1.1: Global CO₂ emissions per year due to fossil fuel combustion from 1750-2010 [3].

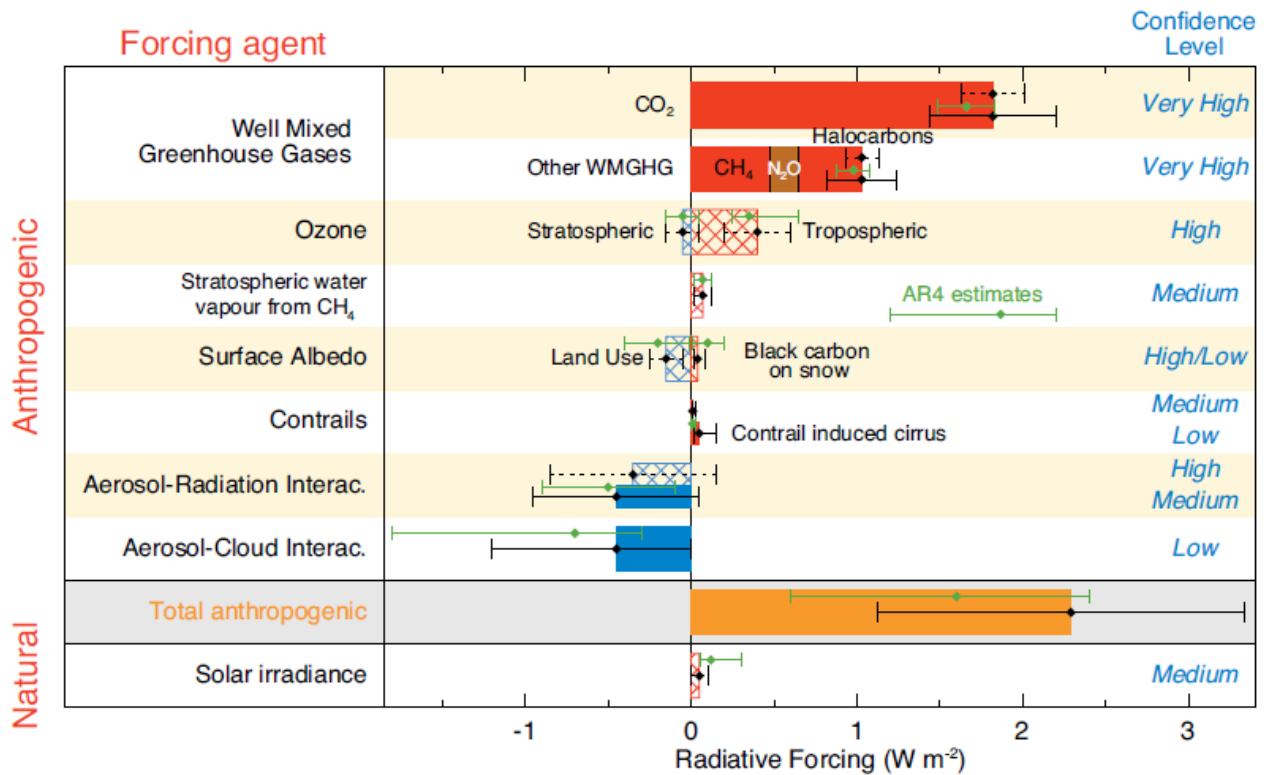


Figure 1.2: Radiative forcing change from 1750 to 2011 [4].

emphasizes that human activities have significantly modified the Earth's natural energy balance. Global warming, the negative consequence of increasing the energy absorbed by the Earth, is evident when analyzing the recent increase in sea level, ocean temperatures, atmospheric carbon dioxide concentration, and the recent decline in Arctic sea-ice level [2]. Further evidence of global warming is demonstrated by the Earth's steadily increasing surface temperature as shown in **Figure 1.3**. The use of fossil fuels must be decreased substantially in order to regulate the amount of greenhouse gases emitted.

Global investment in renewable and clean energy technologies is thought to be a solution to reducing greenhouse gas emissions, while also meeting the growing demand for electrical energy. **Figure 1.4** shows that the global electricity generation and demand has been gradually increasing from 1970 to 2011. Furthermore, the majority of electrical energy production is dependent on the use of fossil fuels. Renewable energy systems such as solar, wind, geothermal, and others rely on natural resources to generate electrical energy while releasing minimal quantities of greenhouse gases and pollutants. In comparison, renewable energy systems generate far less electricity than fossil fuel and nuclear energy systems. For example, estimates of global electricity production at the end of 2013 have suggested that renewable systems only account for 22.1% of the market, while fossil fuels and nuclear energy systems account for 77.9% [5]. Nevertheless, the electricity generated from renewable and alternative energy systems has been increasing and is projected to increase in the near future, as seen in **Table 1.1**. Extensive research studies on the optimization of alternative energy systems have been ongoing in order to increase the overall efficiency, performance, and reliability of these systems. As a result, the feasibility and practicality of implementing solar, wind, and geothermal, and other systems in industrial, commercial and residential sectors have increased. Further improvement in the performance of renewable energy systems, in particular solar energy, is required for these systems to become a competitive alternative to fossil fuel technologies.

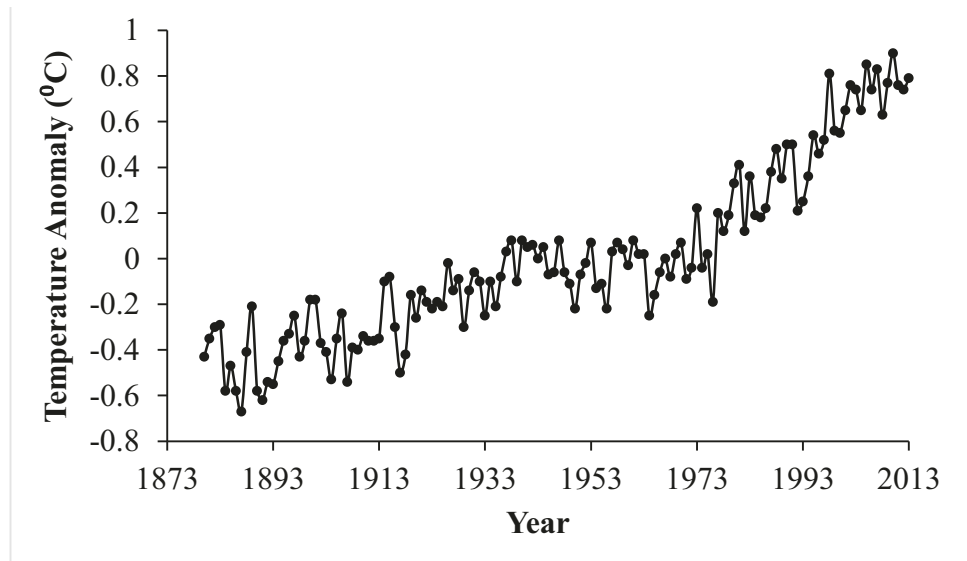


Figure 1.3: Annual global-mean temperature from 1880 to 2013 [6].

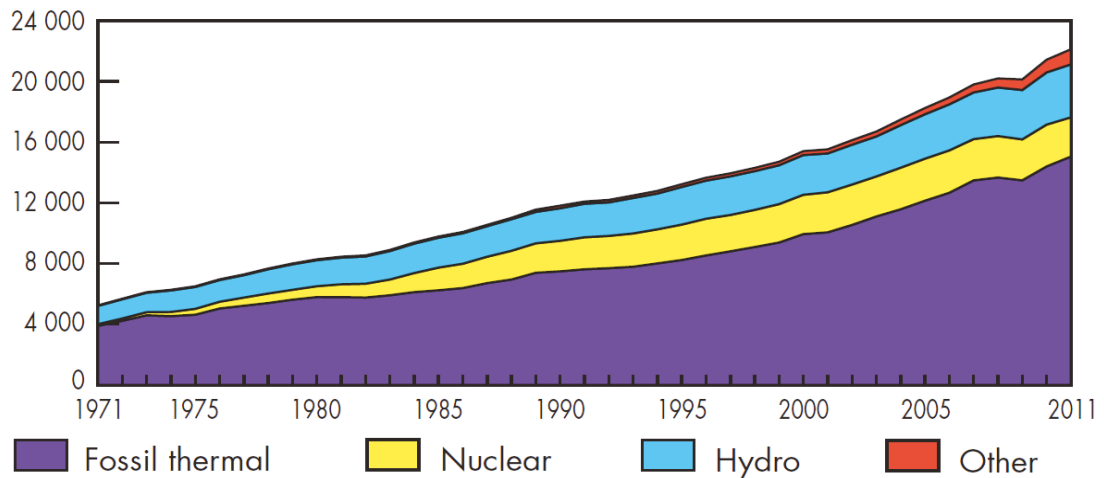


Figure 1.4: World electricity generation (TWh) from 1970 to 2011 for various energy sources [7].

Table 1.1: World renewable electricity production (GW) and future projection [8].

Year	2011	2012	2013	2014	2015	2016	2017	2018
Hydropower	1071	1102	1138	1173	1209	1249	1291	1330
Wind	236	282	321	268	413	459	508	559
Solar PV	69	98	128	161	194	230	268	308
Geothermal	11	11	12	12	13	14	14	15
Ocean	1	1	1	1	1	1	1	1

1.2 Fundamentals of Solar Photovoltaic Systems

1.2.1 Photovoltaic Cells

The process in which a single-junction photovoltaic (PV) cell converts sunlight into electrical energy is dependent on the incident energy of a photon, and the material properties of the PV cell. The solar radiation projected onto a photovoltaic cell may be characterized into smaller energy units known as photons. The energy of a photon is given by [9]:

$$En_{photon} = h_P v \quad (1.1)$$

where, h_P is the Plank's constant (6.25×10^{-34} J·s), and v is the frequency (1/s) of the photon determined by the following equation [9]:

$$v = \frac{\lambda}{c} \quad (1.2)$$

where, c is the speed of light (3×10^8 m/s), and λ is the wavelength (m) of the photon. As seen in **Figure 1.5**, a photovoltaic cell consists of an n-type semiconductor, p-type semiconductor, p-n junction, and an electrical load. The n-type semiconductor may be created by doping crystal-silicon with small impurities of phosphorus, and the p-type semiconductor being doped crystal-silicon with small quantities of boron. By doing so, the n-type semiconductor has an excess amount of electrons (negatively charged), and the p-type semiconductor has an excess amount of holes, the void spaces in the crystal structure that electrons may occupy (positively charged) [9]. When the n-type and p-type semiconductors are directly connected, they form a layer called the p-n junction. Diffusion will occur at the p-n junction, meaning the holes from the p-type semiconductor will move into the n-type semiconductor, and the electrons from the n-type semiconductor will move into the p-type semiconductor. However, not all holes and electrons will diffuse, resulting in a high concentration of holes at the bottom of the n-type semiconductor, and a high concentration of electrons at the top of the p-type semiconductor. As a result of this diffusion, an electric field is created at the p-n junction that stabilizes the diffusion flow and establishes an equilibrium state [10].

When an incident photon is absorbed by the valence electron in the atom of the n-type semiconductor material, the energy of the electron increases by the energy of the photon. If the energy of the incident photon is equal to the band gap of the semiconductor, the electron

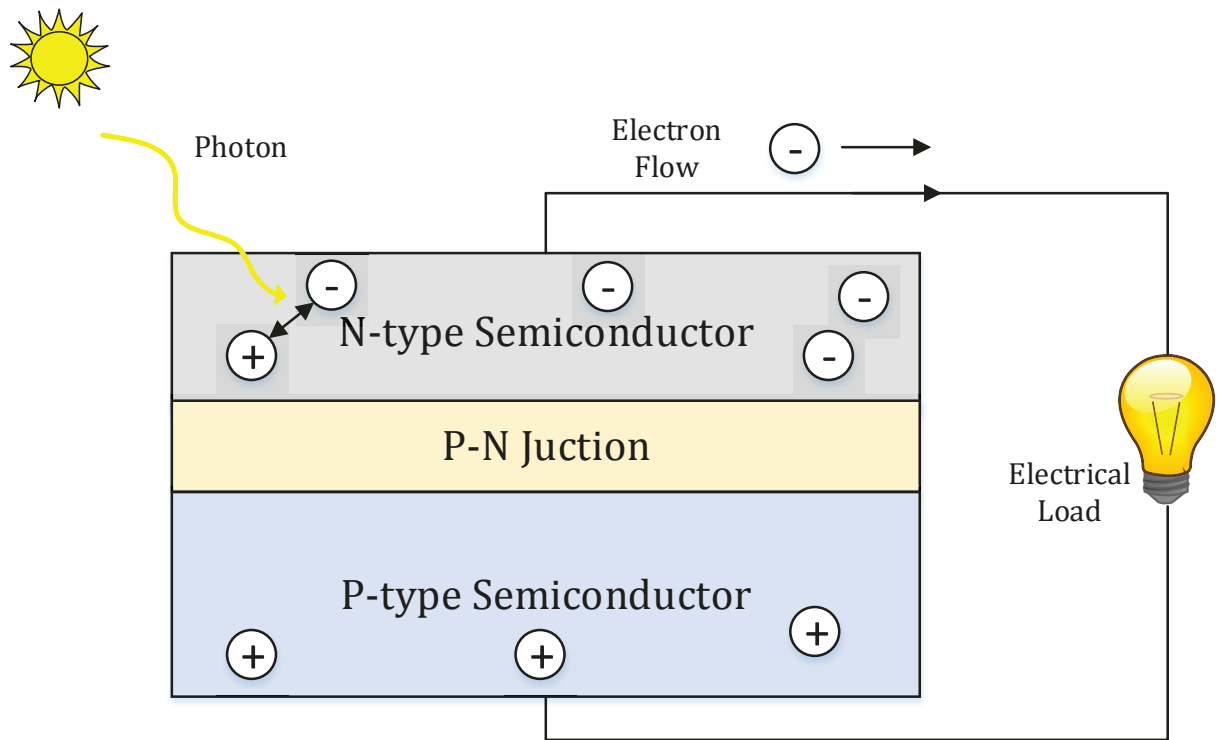


Figure 1.5: Schematic of the major components of a photovoltaic cell.

is freed from the atom, creating an electron-hole pair. If the absorbed photon's energy is greater or less than the band gap, the kinetic energy of the electron is increased, resulting in an increase in temperature of the photovoltaic cell [11]. When the n-type and p-type semiconductor are connected using an electrical circuit, the freed electrons may flow through the circuit to the p-type semiconductors. This flow of electrons through the circuit creates electrical current that can be used to power an electrical load.

Photovoltaic cells are the fundamental component of a photovoltaic system [12]. Photovoltaic modules are comprised of several photovoltaic cells connected electrically in series or in parallel, depending on the demanded power specifications. Photovoltaic modules can be connected in series or parallel to form a photovoltaic array. An illustration of a photovoltaic cell, module and array is depicted in **Figure 1.6**.

Solar photovoltaic (PV) systems are a renewable energy technology that has several advantageous characteristics. The major advantage of a photovoltaic system is its ability to directly convert the Sun's solar energy into electrical energy. In addition, PV systems emit zero pollution when operating, are reliable, have a long operating life, have no mechanical moving parts, and require little to no maintenance once properly installed. They are also an extremely adjustable power source, generating microwatts to megawatts, depending on the size of the PV system and the required application [11]. Photovoltaic cells are made from a variety of semiconductor materials including silicon (Si), cadmium telluride (CdTe), cadmium sulfide (CdS), and gallium arsenide (GaAs) [9, 12]. The atomic structure of silicon photovoltaic cells may be crystalline, multicrystalline or amorphous [13]. Crystalline silicon has an ordered crystal structure in which the atoms are in the ideal position. Therefore, the manufacturing process is very accurate and expensive. Multicrystalline, also known as polycrystalline silicon, is a less expensive material due to its lower manufacturing cost. However, multicrystalline silicon has grain boundaries that reduce the performance of the photovoltaic cell by providing effective recombination sites and creating recombination losses. Amorphous silicon may be produced at a cost lower than polycrystalline, but the structural arrangement of the material establishes areas where disconnected bonds occur. These disconnected bonds decrease the flow of electrons within the semiconductor material and make the doping process more difficult [14].

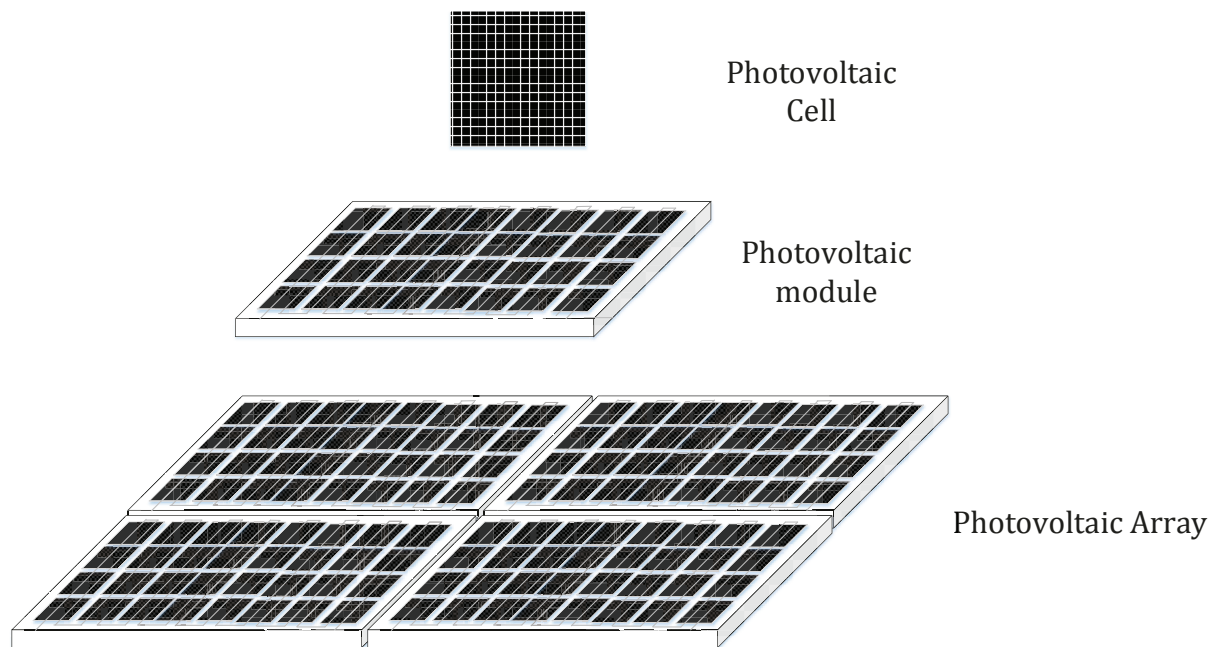


Figure 1.6: Schematic of a photovoltaic cell, photovoltaic module, and photovoltaic array.

Photovoltaic cells may be categorized by type, such as single-junction, multijunction, and thin-film. Single-junction photovoltaic cells consist of a single n-type and p-type semiconductor layer and are limited in efficiency due their inability to convert a large range of photon wavelengths into electrical energy. Multijunction photovoltaic cells consist of subcells with different band gaps connected in series or in parallel, allowing a larger range of photons to be absorbed from the solar spectrum and establishing a relatively high energy conversion efficiency [15]. Thin-film photovoltaic technologies made from such materials as amorphous silicon, silicon germanium alloys, and microcrystalline silicon vary in thickness from hundreds of nanometers to a few micromobeters [16, 17]. Thin-film silicon photovoltaics have seen tremendous growth in recent years due to the low quantity of silicon material required, low production costs, relatively high energy conversion efficiency, and ease of design and installation in photovoltaic modules [17].

1.2.2 Power Generation Characteristics of Photovoltaic Systems

The performance of a photovoltaic cell or module may be characterized using the current vs. voltage (I-V) profile, as shown in **Figure 1.7**. The I-V curve is typically generated under the standard operating condition at an incident irradiance intensity G_T equal to 1000 W/m² at an Air Mass (AM) 1.5 spectrum with an operating photovoltaic cell temperature T_{cell} of 25 °C [18]. The AM spectrum is a standardized irradiance spectrum profile, where AM zero is the solar spectrum outside the Earth's atmosphere, and AM 1.5 is the sea-level solar radiation spectrum [19]. The point at which the photovoltaic module operates on the I-V curve is dependent on the electrical load resistance. The short-circuit current I_{sc} is the current value when the voltage is zero (V=0), and the open-circuit voltage V_{oc} is the point on the I-V curve where the current is zero (I=0). The power output at any point on the I-V curve may be determined using Ohm's law:

$$P_{PV} = I_{PV} V_{PV} \quad (1.3)$$

The maximum power point, as shown in **Figure 1.7**, is the point on the P-V curve where the maximum photovoltaic module or cell power output occurs [20]:

$$P_{PV,mp} = I_{PV,mp} V_{PV,mp} \quad (1.4)$$

The change in power output with respect to current and voltage is zero at the maximum power point [21, 22]:

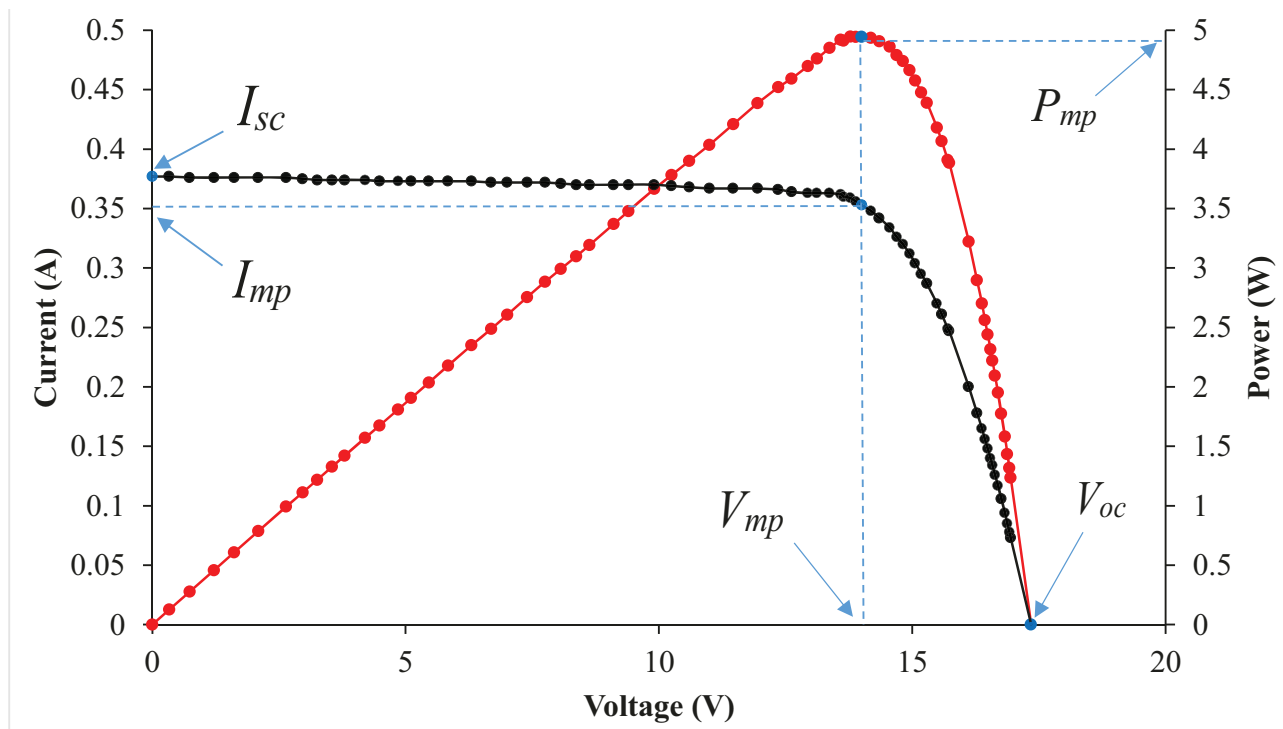


Figure 1.7: Typical current and power vs. voltage (I-V & P-V) curve of standard photovoltaic module based on experimental data.

$$\frac{dP_{PV,mp}}{dI} = 0 \quad (1.5)$$

$$\frac{dP_{PV,mp}}{dV} = 0 \quad (1.6)$$

There are several factors that significantly influence the performance of a photovoltaic cell. These factors include the incident irradiance intensity and the photovoltaic cell temperature. The I-V and P-V curves of a typical PV cell operating at various irradiance intensities and at a constant cell temperature are shown in **Figure 1.8**. The open-circuit current and the maximum power point increases as the irradiance intensity increases. **Figure 1.9** depicts the I-V and P-V curves of a typical photovoltaic cell operating at various temperatures with a constant irradiance intensity. This figure emphasizes that decreasing the photovoltaic cell temperature increases power output. Therefore, maintaining a low cell temperature is beneficial in order to maximize the overall performance of a photovoltaic system.

Besides temperature and irradiance intensity, the efficiency of a photovoltaic cell is dependent on the semiconductor material, and the quality of the manufacturing process of the photovoltaic cell. In recent years, research and development has produced more efficient photovoltaic cells to maximize power output. **Figure 1.10** illustrates the history of the highest confirmed energy conversion efficiencies of research photovoltaic cells. The energy conversion efficiency of a photovoltaic system may be expressed as the ratio of the actual power generated and the total solar irradiance projected onto a photovoltaic system [23, 24]. The energy conversion efficiency of a photovoltaic system may defined as [24, 25, 26]:

$$\eta_{PV} = \frac{P_{PV}}{G_T A_{PV}} \quad (1.7)$$

The maximum power point efficiency of a photovoltaic system may be expressed as [9, 27]:

$$\eta_{PV,mp} = \frac{P_{PV,mp}}{G_T A_{PV}} = \frac{I_{mp} V_{mp}}{G_T A_{PV}} \quad (1.8)$$

The maximum power point efficiency and temperature of a photovoltaic cell or module may be expressed as a linear relationship [28]:

$$\eta_{PV} = \eta_{T_{cell,ref}} [1 - \mu_{mp,ref} (T_{cell} - T_{cell,ref})] \quad (1.9)$$

where, $\eta_{T_{cell,ref}}$ is the efficiency of the cell or module at the reference temperature, and $\mu_{mp,ref}$ is the maximum point efficiency temperature coefficient. The maximum point

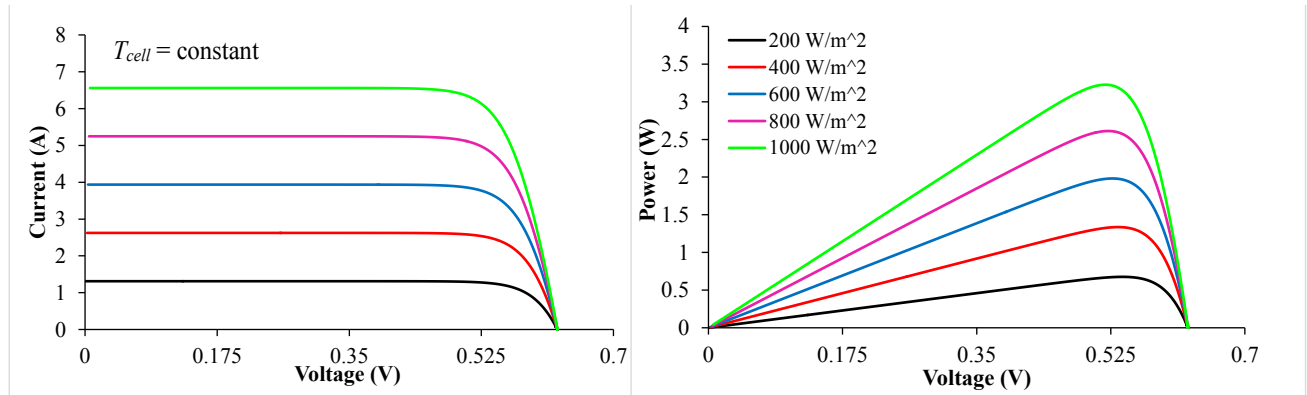


Figure 1.8: Typical I-V and P-V curve of photovoltaic cell at various irradiance intensities and constant photovoltaic cell temperature.

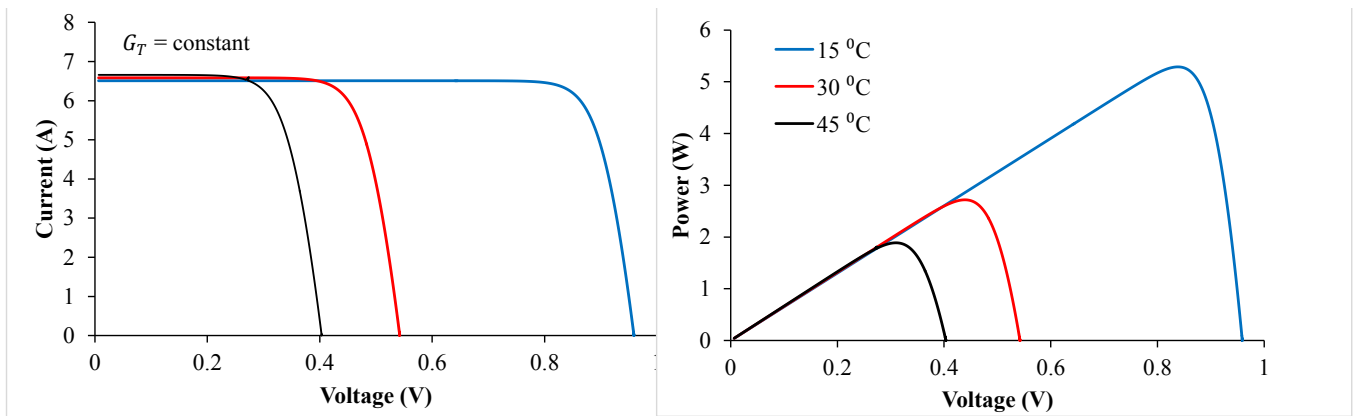


Figure 1.9: Typical I-V and P-V curve of photovoltaic cell at various temperatures at a constant irradiance intensity.

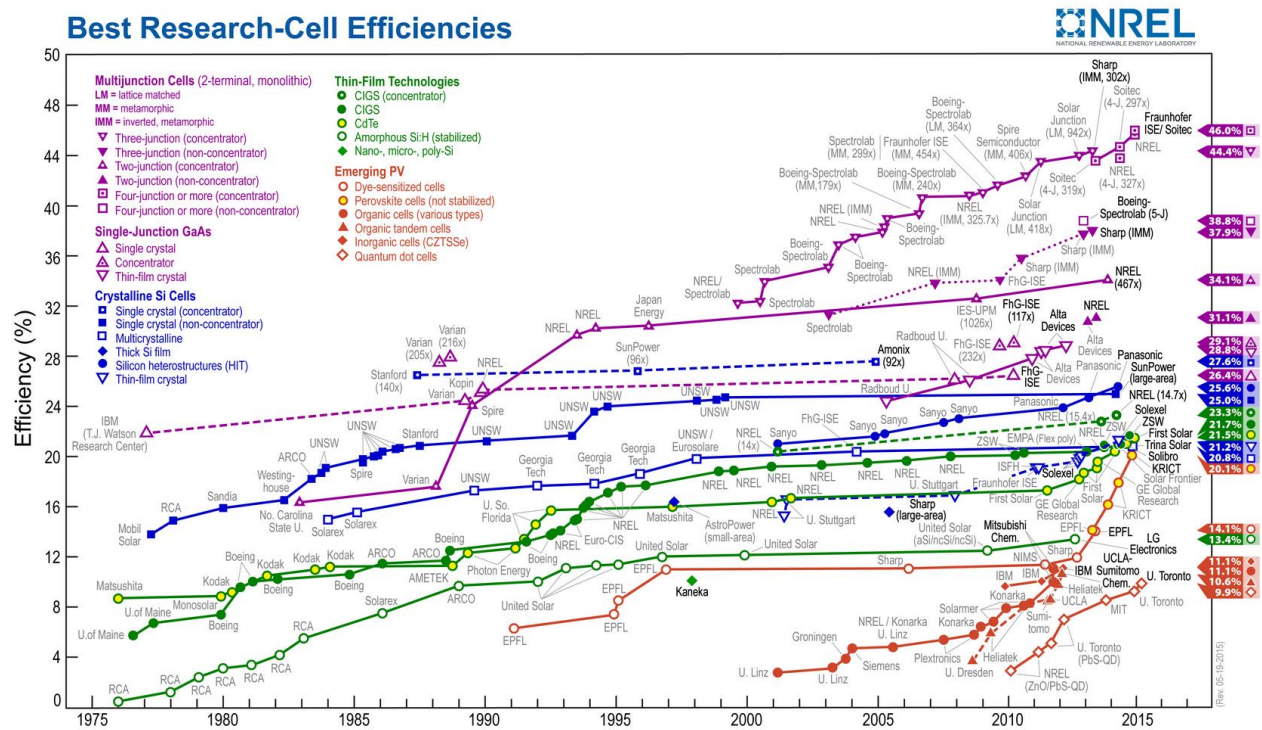


Figure 1.10: Conversion efficiencies of research PV cells from 1976- 2015 [29].

efficiency temperature coefficient typically ranges from 0.2-0.45 %/K depending on the photovoltaic cell or module's material and design [30].

The Fill Factor of a photovoltaic system may be defined as the ratio of the maximum power output and the product of the open-circuit voltage and short-circuit current as given by [31, 32, 33, 34]:

$$FF = \frac{I_{PV,mp} V_{PV,mp}}{V_{PV,oc} I_{PV,sc}} \quad (1.10)$$

The Fill Factor is a dimensionless parameter that represents how closely the performance characteristics of a PV system resemble an ideal PV system [35]. The Fill Factor decreases significantly with cell temperature, highlighting that an increase in the cell temperature negatively affects the energy conversion efficiency of a PV system [30]. The maximum power point efficiency of a photovoltaic system may also be defined in terms of the Fill Factor [31, 32, 33]:

$$\eta_{PV,mp} = \frac{FF V_{PV,oc} I_{PV,sc}}{G_T A_{PV}} \quad (1.11)$$

1.2.3 Improving PV Systems Performance

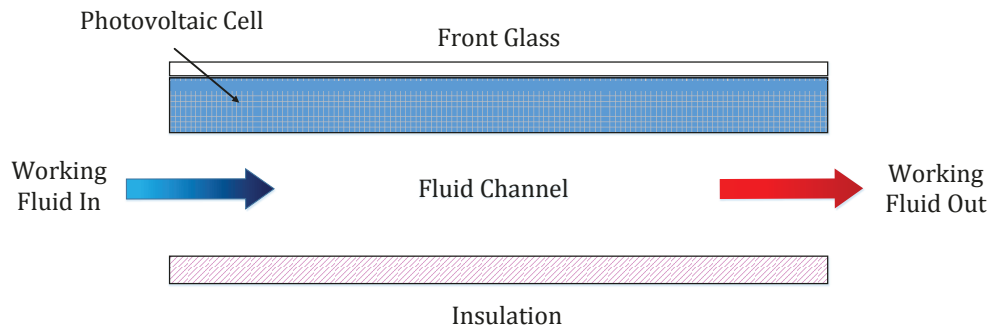
One of the principle limitations in the power output of a photovoltaic system arises when the system is installed in a geographical location with low solar radiation potential. Sun tracking systems typically increase the performance of a photovoltaic system by increasing the annual incident irradiance projected onto the PV array(s). These tracking systems position the PV array in the optimal position to increase the amount of solar energy collected. Solar tracking systems may be categorized as one-axis, or two-axis trackers. One-axis trackers include azimuth, inclined, and horizontal axis trackers, while two-axis trackers can be divided into polar and azimuth/elevation trackers [36]. Tracking systems generally increase the annual output of photovoltaic systems between 30 to 60% depending on the geographical location [36, 37]. The practicality of installing a sun tracker is significantly influenced by the capital and maintenance cost of the tracking system, tracking accuracy, and the amount of power consumed by the tracking system. The application of Sun trackers is more feasible at geographical locations where the Sun remains high on the horizon, generally at latitudes between $+30^\circ$ and -30° [38].

Concentrated photovoltaic (CPV) systems use lenses or mirrors to effectively concentrate incident solar radiation onto relatively small photovoltaic cells. The required photovoltaic module area is reduced due to the concentration of the irradiance intensity, reducing the total cost of the photovoltaic system. The Fresnel lens is commonly used in concentration photovoltaic systems as it is light-weight, robust, and possesses a relatively high optical efficiency [39]. The concentration irradiance uniformity, operating temperature of the photovoltaic cells, and the accuracy of the tracking system are some of the operating factors that significantly impact the performance of concentrating photovoltaic systems. Photovoltaic cells require a uniform irradiance flux distribution to obtain optimal performance. Therefore, it is desired to have lenses or mirrors that have high optical properties that can provide a uniform flux distribution [39]. As previously mentioned, the efficiency of photovoltaic cells is reduced when operating at elevated temperatures. Furthermore, high temperatures can cause optical and material degradation, resulting in a decrease in performance and permanent structural damage [27, 40]. During operation, the temperature of CPV cells is typically well above the ambient air temperature. Passive or active cooling is recommended for medium-to-high concentration ratio CPV systems in order to decrease the temperature of the photovoltaic cells, increase overall efficiency of the energy system, and decrease the probability of permanent material damage occurring. Medium- and high-concentration systems also require accurate tracking systems (i.e. two-axis) to maintain the focus of the solar radiation onto the photovoltaic cells [41].

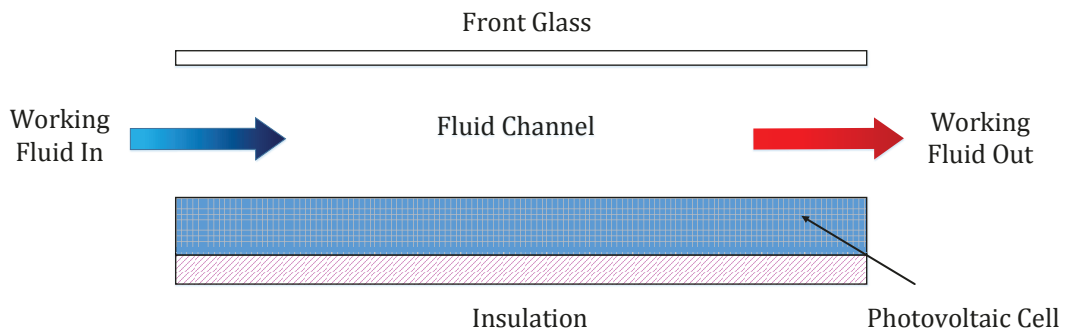
As previously stated, the efficiency of a photovoltaic module is limited by the band gap energy of the photovoltaic cell's semiconductor material and the incident irradiance wavelength spectrum. Longer wavelengths (infrared) do not generate electron-hole pairs, and thus are converted into thermal energy [27]. Commercially available photovoltaic modules vary in efficiency, ranging from 5% to 25%. Therefore, a large portion of the incident solar radiation is converted into thermal energy [42]. A hybrid photovoltaic thermal (PVT) collector integrates a photovoltaic module and cooling components to simultaneously convert solar radiation into electrical and thermal energy. PVT systems use a working fluid, such as air or water, and a heat exchanger system to efficiently remove waste-heat and decrease the temperature of the PV module. Common designs of PVT collectors are illustrated in **Figure 1.11**. By removing this waste-heat, the temperature of the PV module

decreases, which increases the PV module's efficiency and power output. The electrical efficiency of the photovoltaic module can be maximized by using the lowest possible inlet working fluid temperature. The outlet working fluid may be used to provide thermal energy to other systems. For instance, the outlet air from a PVT collector may be used to heat a building, while the outlet water from a PVT collector can be used to heat swimming pools [43]. Since the main benefit of PVT systems is their ability to remove thermal energy from the PV module, they are more suitable in geological locations where PV systems achieve high operating temperatures.

The working fluid and structure of a PVT collector significantly influences the performance of the system. The working fluid is normally dependent on the design and application of the PVT collector. PVT collectors can be categorized as either air-type (PVT-a) or water-type (PVT-w). PVT air collectors that use natural air circulation are a low-cost method to remove the waste-heat from photovoltaic modules. Forced air circulation is a more effective method to remove the thermal energy from the photovoltaic module, however electrical energy must be supplied to a pump or fan which reduces the net electrical energy generated [43]. PVT water collectors are more efficient than air-type collectors due to water's high heat capacity. Extensive and costly modifications must be made to PVT water-type collectors in order to create a water-tight and corrosion-free system [44]. PVT collectors can be further categorized as either glazed or unglazed. Glazed PVT collectors have a well-insulated glass-covered box on top of the photovoltaic module, while unglazed PVT collectors have no additional glass layer. The addition of the glass cover decreases the rate of thermal energy dissipated from the top surface of the PVT collector. Consequently, the temperature of the PV module increases, leading to a decrease in the electrical efficiency [45]. Thus, research has concluded that glazed PVT collectors are more suitable when the production of electrical energy is not critical, due to the fact that the addition of the glass cover increases the thermal energy transferred to the working fluid and the PVT collector temperature, while decreasing the electrical energy generated.



(a) Channel below PV cell



(b) Channel above PV cell

Figure 1.11: Typical photovoltaic-thermal system designs.

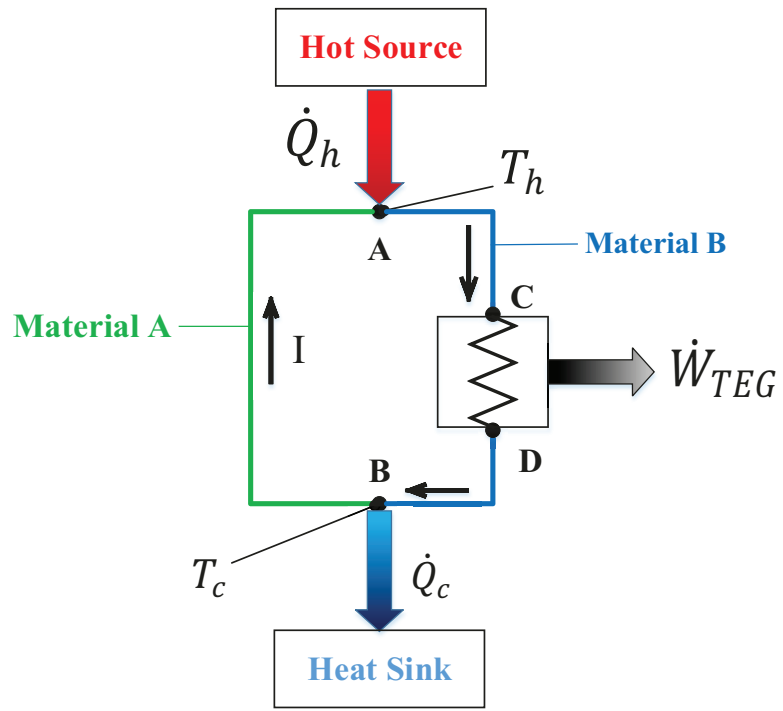
1.3 Thermoelectric Technology for Power Generation

Thermoelectric technologies have the ability to directly convert thermal energy, such as the waste-heat from a photovoltaic module, directly into electrical energy. Thermoelectric devices are a solid-state, reliable technology with no moving parts, and thus are silent in operation. They are also position independent, environmentally friendly, and very safe to use [46]. The practicality of using thermoelectric technologies may be improved upon through two different methodologies. The first method focuses on the improvement of existing thermoelectric materials in order to increase the efficiency and performance of thermoelectric devices. The alternative method can be used to develop innovative applications and hybrid systems that exploit the advantageous characteristics of thermoelectric devices. This work focuses on the latter, conducting research and analyzing the potential of creating a hybrid thermoelectric system. It is important to first have a comprehensive understanding of the thermoelectric effects, thermoelectric devices, and the governing performance parameters before discussing the new concepts of hybrid thermoelectric systems.

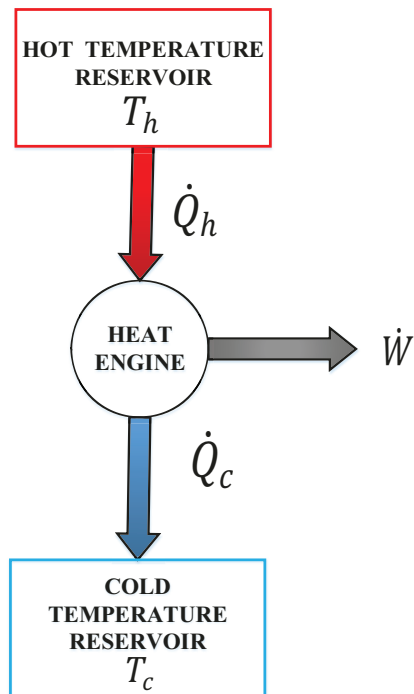
1.4 The Thermoelectric Effects

1.4.1 The Seebeck Effect

Thermoelectric devices are able to generate electrical energy when a temperature differential is established. This physical phenomenon is known as the Seebeck effect, the generation of voltage by placing a material in a temperature gradient [47]. The Seebeck effect was discovered in 1821 by Thomas Seebeck, who observed that a compass needle deviated when a temperature differential was applied at two junctions using two different metals [48, 49]. The principle of the Seebeck effect may be discussed with reference to the schematic of a thermocouple shown in **Figure 1.12**. Connecting two dissimilar materials in series, whether it be metals or semiconductors, and creating a temperature difference at nodes A and B, generates a voltage between the C and D junction once connected to an electrical load. This voltage is known as the Seebeck voltage, and is directly proportional to the Seebeck coefficient [48]. The Seebeck coefficient for the thermocouple may be expressed as the ratio of the voltage generated and the temperature differential given by [50]:



(a) Seebeck Effect



(b) Heat engine cycle

Figure 1.12: Principle of (a) the Seebeck effect using a thermocouple, and (b) the thermodynamic heat engine cycle.

$$\alpha_s = \frac{V}{\Delta T} \quad (1.12)$$

where, the temperature differential ΔT is the difference between the hot T_h and cold T_c junction temperature. The resulting Seebeck coefficient of the thermocouple may be determined based on the Seebeck coefficients of each individual material [50]:

$$\alpha_s = \alpha_A - \alpha_B \quad (1.13)$$

The Seebeck coefficient is positive if the electromotive force causes the current to flow clockwise, and negative if the electromotive force causes the current to flow counter-clockwise [50]. It is also noteworthy to mention that the Seebeck effect resembles the thermodynamic power cycle of a conventional heat engine, with the electrons serving as the working fluid [46].

1.4.2 The Peltier Effect

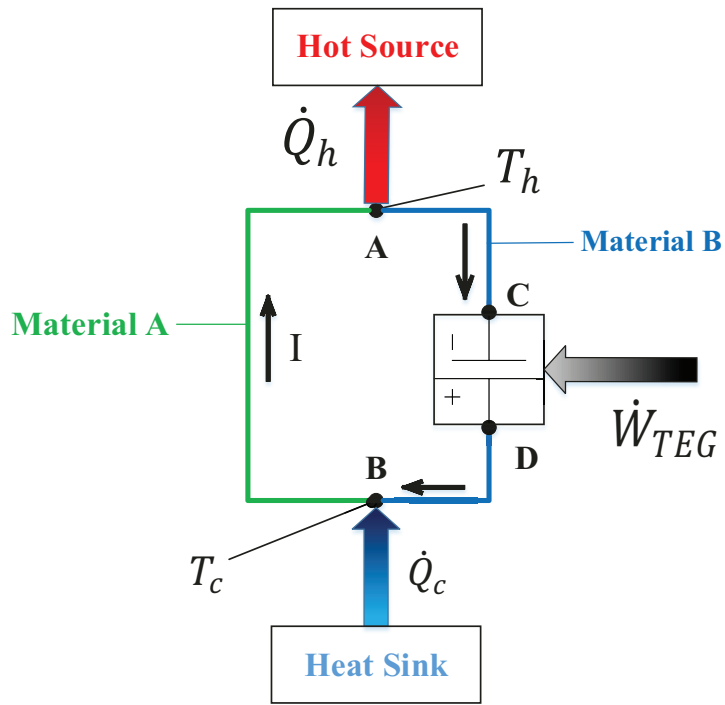
In addition to generating electrical energy, thermoelectric devices also have the ability to transfer thermal energy from one medium to another using electrical energy based on the Peltier effect. The Peltier effect was discovered by Jean C. A. Peltier in 1834 when he discovered that electrical energy may be used to create a temperature differential at two different junctions, as seen in **Figure 1.13** [49]. When an electrical potential (voltage) is created across the C and D junctions, current will flow through the two dissimilar materials and establish a temperature difference between nodes A and B. As a result of the temperature differential, a rate of heating \dot{Q}_H occurs at one junction, and a rate of cooling \dot{Q}_C occurs at the other. The Peltier effect resembles the thermodynamic heat pump cycle. The Peltier coefficient (V) is defined as the ratio of the rate of heating and input current [51]:

$$\pi = \frac{\dot{Q}_h}{I} \quad (1.14)$$

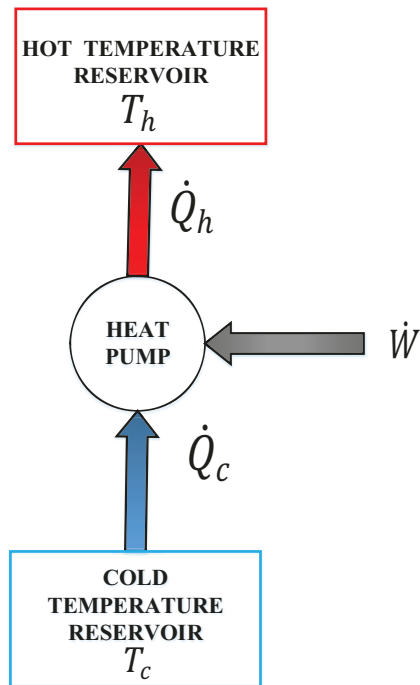
The Peltier effect is considered to be positive if the hot side temperature T_h occurs at node A and the cold temperature T_c occurs at node B [50].

1.4.3 The Thomson Effect

The final thermoelectric effect is known as the Thomson effect. The Thomson effect concludes that a rate of reversible heat is generated when current flows through a semiconductor material that has a uniform temperature profile [50]. Consider a



(a) Peltier effect



(b) Heat pump cycle

Figure 1.13: Principle of (a) the Peltier effect using a thermocouple, and (b) the thermodynamic heat pump cycle.

thermoelectric device that has a temperature-dependent Seebeck coefficient and constant current, due to the temperature-dependent Seebeck coefficient, power in the form of heat is generated due to the charge carriers responding to the changing voltage field along the length of the material. The Thomson coefficient is defined as the rate of heating per unit length that results from the passage of current along a conductor that has a temperature gradient. The Thomson coefficient may be expressed as [52]:

$$\tau_{TEG} = T \frac{d\alpha(T)}{dT} \quad (1.15)$$

Standard numerical models and analysis neglect the Thomson coefficient under the assumption that thermoelectric material is subjected to a small temperature gradient and that the material's Seebeck coefficient is relatively constant with temperature [50, 52].

1.5 Thermoelectric Devices

1.5.1 Major Components of a Thermoelectric Module

The major components of a single-stage thermoelectric device, also known as a thermoelectric module, are shown in **Figure 1.14**. The thermoelectric device is composed of multiple semiconductor thermoelements connected using electrically conductive materials sandwiched between two ceramic substrates. These thermoelements are comprised of several n-type and p-type semiconductor materials connected electrically in series and thermally in parallel. The n-type semiconductor elements are heavily doped to create excess electrons, while the p-type is doped to create a material with an excess number of holes [53]. A thermoelectric module can act as a thermoelectric generator (TEG) by utilizing the Seebeck effect, or as a thermoelectric cooler by utilizing the Peltier effect. **Figure 1.15** illustrates these two different operating conditions of a single thermocouple thermoelectric module. When waste-heat (thermal energy) \dot{Q}_h is transferred at the hot side temperature junction T_h to a thermoelectric generator, a portion of the input thermal energy is converted into electrical energy P_{TEG} . The remaining energy is dissipated as thermal energy \dot{Q}_c at the cold temperature junction T_c . Thus, a thermoelectric generator converts thermal energy into electrical energy from a temperature difference across the thermoelements. Experiments conducted by Rowe and Min [54] have shown that the power output of thermoelectric generators is proportional to the temperature differential and is significantly dependent on

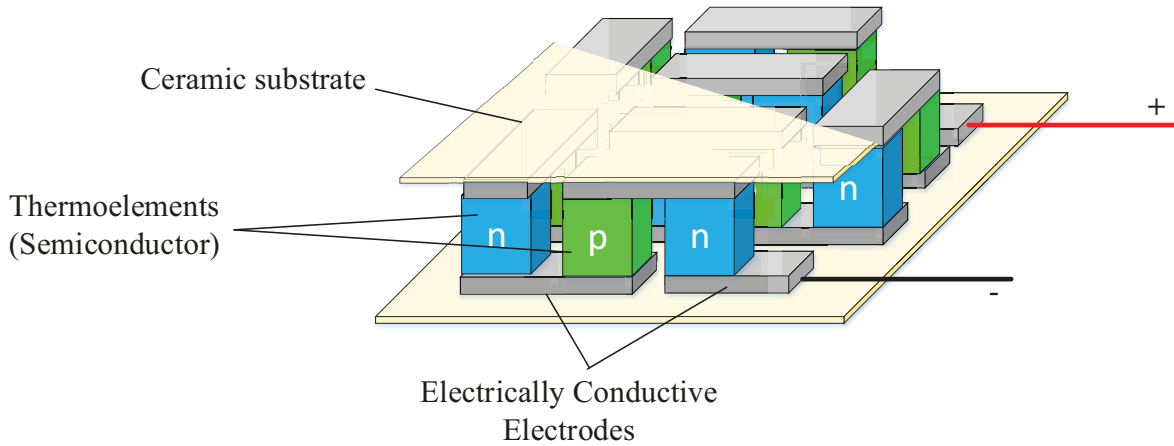
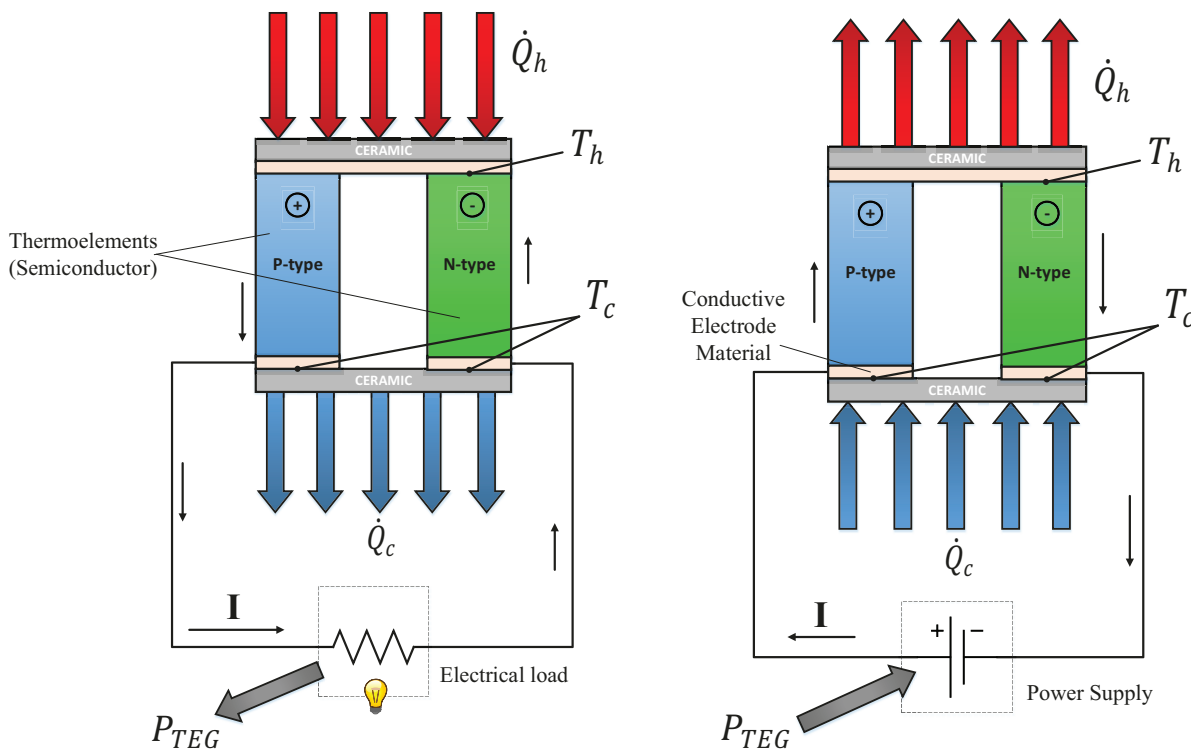


Figure 1.14: Schematic of major components of a typical thermoelectric module.



(a) Thermoelectric generator (TEG)

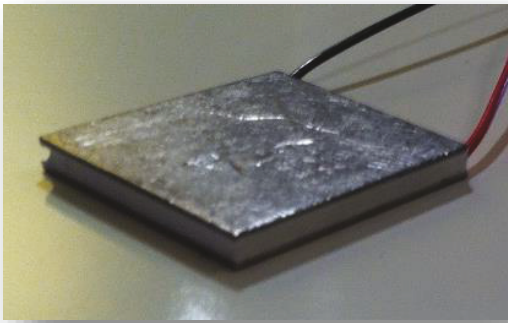
(b) Thermoelectric cooler

Figure 1.15: Thermoelectric module acting as a (a) thermoelectric generator (b) thermoelectric cooler.

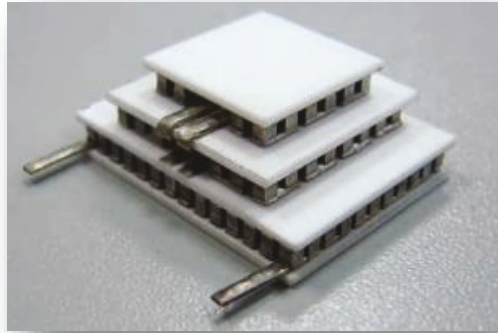
the geometry of the thermoelectric generator. Replacing the electrical load component with an electrical DC source allows the thermoelectric module to act as a heat pump or cooler, dissipating thermal energy \dot{Q}_h from the hot side temperature T_h , and absorbing heat \dot{Q}_c from the cold side temperature junction T_c [48]. Thermal energy may be transferred to and from the thermoelectric module through the use of heat sinks or direct contact with a heat and cooling source.

Thermoelectric modules come in a variety of shapes and sizes depending on the desired application of the device. **Figure 1.16** shows photographs of existing types of thermoelectric generators. Conventional single-stage thermoelectric modules range in height between one and five millimeters, and may have a cross-sectional area ranging between 1 mm² and 3200 mm². The number of thermoelements in commercially available single-stage modules varies between 6 and 400 [55, 56, 57, 58]. Normally, the coefficient of performance (COP) of thermoelectric coolers decreases as the temperature difference across the modules increases [59]. Multistage thermoelectric modules establish a lower temperature difference when operating and thus, are typically used to transfer thermal energy when large temperature gradients occur [59]. Lindler's experimental simulations demonstrated that using a multistage thermoelectric cooler under high temperature gradients establishes a significantly higher coefficient of performance compared to a single-stage thermoelectric cooler [60]. Current manufactured multistage thermoelectric coolers have two to four stages with heights ranging from 10 millimeters to less than 1 millimeter [61, 62]. Standard thermoelectric generators' cross-sectional areas are 30 x 30, 35 x 35, 40 x 40, and 56 x 56 mm and have a graphite cover to decrease heat transfer losses due to inefficient thermal contact [56, 63]. Single-stage and multistage thermoelectric modules can only be mounted to flat surfaces because of their flat-plate structure and rigid shape. This means that when these modules are mounted to flat surfaces, heat is limited to flowing only perpendicular to the ceramic substrates [53].

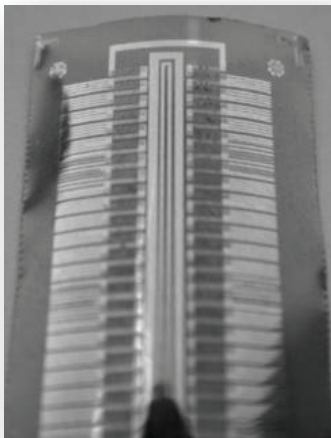
The design and development of efficient, flexible and cylindrical-shaped thermoelectric modules is crucial in increasing the viability of thermoelectric technology for residential or industrial applications. Micro thermoelectric generators are also an emerging technology that generates nanowatts of electrical energy from the waste-heat of electrical



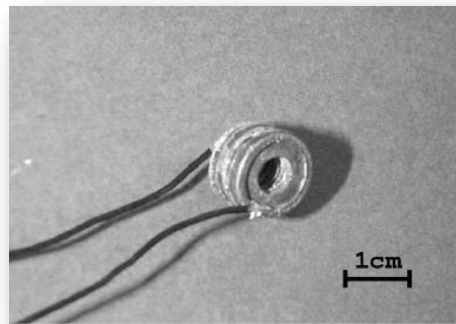
(a)



(b)



(c)



(d)

Figure 1.16: (a) single-stage thermoelectric module (b) multi-stage thermoelectric cooler [58] (c) Flexible micro thermoelectric generator [64] (d) ring-structured thermoelectric module [65].

components or human bodies to power small electronic devices. For example, a wearable micro thermoelectric generator was designed and fabricated by Fracioso et al. [64] to power low-consumption electronics for assisted living applications. The wearable micro thermoelectric generator was able to generate 32 nanowatts at the matched load condition and with a temperature difference of 40 °C [64]. Yadav et al. [66] investigated the proof-of-concept of a flexible thermoelectric power generator made from evaporating thin films of thermoelectric fiber onto a flexible substrate. Experimental results showed that the 7-thermocouple, fiber-based, flexible thermoelectric generator was able to generate approximately 7 nanowatts of electrical power when a temperature gradient of 6.6 °C is applied [66]. A small-scale thermoelectric generator for human body applications, engineered by Wang et al. [67] was able to establish a stable output voltage of 150 milliwatts when being worn on a human body. Min and Rowe [65] experimentally characterized a novel tube-shaped thermoelectric module manufactured from four ring-shaped (two n-type and two p-type) thermoelements by measuring the electrical power output as a function of the temperature differential across the module. This thermoelectric tube has the potential to generate electrical energy using the heat transferred in a radial direction, while simultaneously transporting high temperature fluids to a desired location. Experimental results established a maximum electrical power output of approximately 33 milliwatts at a temperature difference of 70 °C [65]. Due to its unique geometry, advancement in the quality of the manufacturing process of the ring-structure thermoelectric module is required to increase proper contact between the n-type and p-type thermoelements and increase its performance.

1.5.2 Thermoelectric Materials

In general, the material composition of a thermoelectric module significantly affects the performance and efficiency of the device. The type of n-type and p-type thermoelectric semiconductor material can be divided into three distinct categories: low temperature, intermediate temperature, and high temperature applications. Low temperature thermoelectric materials operate under temperatures less than 450 °C and are typically composed of bismuth (Bi), coupled with antimony (An), tellurium (Te) or selenium (Se) [68]. Low temperature materials are suitable for cooling and low-scale power generation

purposes [69]. Intermediate temperature applications, ranging in operating temperatures from 400 to 850 K, are commonly implemented for power generation and are made from lead-based materials (Pb), such as lead telluride (PbTe) [68, 69]. Lead telluride thermoelectric modules have a maximum operating temperature of 900 K. High temperature materials made from silver antimony, lead telluride, cobalt triantimonide-based (CoSb₃) skutterudites, and silicon germanium-based (SiGe) alloys can operate efficiently up to temperatures ranging from 800 to 1300 K [69, 70, 71]. Bismuth telluride (Bi₂Te₃) and lead telluride (PbTe) are two of the most commonly used thermoelectric materials [48, 53, 72], and have a maximum operating temperature of 550 and 900 K, respectively [73]. The major disadvantage of bismuth telluride compounds are that they are toxic and are chemically unstable at high temperatures [74].

The ceramic substrates of a thermoelectric module electrically insulate and protect the thermoelements from being damaged. Ceramic substrates are normally made from white 96% alumina (Al₂O₃) ceramic due to the material's low cost [75]. Alumina-based ceramics have a very low thermal conductivity, which as a result decreases the performance of the thermoelectric module by restricting the rate of heat absorbed and dissipated [76]. Aluminum nitride- (AlN) or beryllium oxide- (BeO) based ceramic substrates have a significantly higher thermal conductivity and cost [77,78]. However, beryllia-based ceramics are very toxic in nature and pose serious health risks. These high thermally conductive ceramic materials may be used to reduce the thermal resistance of the ceramic layer when the performance of the thermoelectric device must be maximized [75].

The electrode strips connecting the n-type and p-type thermoelements are typically composed of a highly electrically conductive material, such as copper [79]. Yamashita et al. [80] found that the electrode material significantly affects the power generated by a p-type and n-type bismuth telluride compound. Their [80] experimental simulation indicated that gold-copper (Au-Cu) and silver-copper (Ag-Cu) electrode pair configurations are able to generate a larger amount of power than the copper-copper (Cu-Cu) electrode pair configuration. The results of the experimental analysis suggested that a thermoelectric module with gold-copper or silver-copper electrodes, although more costly to manufacture, could increase the performance and overall efficiency of a thermoelectric module, compared to the common copper-copper electrode configuration.

1.6 Thermoelectric Power Generator Performance Characteristics

1.6.1 Energy Conversion Efficiency

The energy conversion efficiency of a thermoelectric generator may be determined by the ratio of the electrical energy output P_{TEG} , and the rate of heat supplied to the thermoelectric generator \dot{Q}_h [81, 82, 83]:

$$\eta_{TEG} = \frac{P_{TEG}}{\dot{Q}_h} \quad (1.16)$$

The absolute maximum energy conversion efficiency of an irreversible thermoelectric power generator can be approximated as [50, 74]:

$$\eta_{TEG,max} = \eta_{Carnot} \left[\frac{\sqrt{1 + Z\bar{T}} - 1}{\sqrt{1 + Z\bar{T}} + \frac{T_c}{T_h}} \right] \quad (1.17)$$

where, Z is the figure-of-merit, and the Carnot efficiency for a heat engine is defined as [84]:

$$\eta_{Carnot} = 1 - \frac{T_c}{T_h} \quad (1.18)$$

As previously mentioned, the efficiency of a thermoelectric generator (TEG) is dependent on several factors, such as the thermoelement cross-sectional area, thermoelement length, electrical load resistance, temperature gradient, and material properties of the thermoelectric generator. An experimental evaluation conducted by Rowe and Min [54] indicated that the thermoelement cross-sectional area and length significantly influences the power output of a thermoelectric module. The power curves of a commercially available thermoelectric module at a constant temperature gradient are shown in **Figure 1.17**. The point at which the thermoelectric module operates on the power curve is dependent on the electrical load resistance. The amount of electrical power produced by the TEG is proportional to its temperature gradient. Research [54, 81, 82, 85] has shown that TEG power output increases exponentially as the temperature gradient increases. Thus, it is important to know both the temperature difference and its relationship to electrical power output when analyzing the performance of a thermoelectric generator. Currently, one major shortcoming of commercially available thermoelectric generators is their low energy conversion efficiencies, establishing a maximum efficiency of less than 5 % [46, 86].

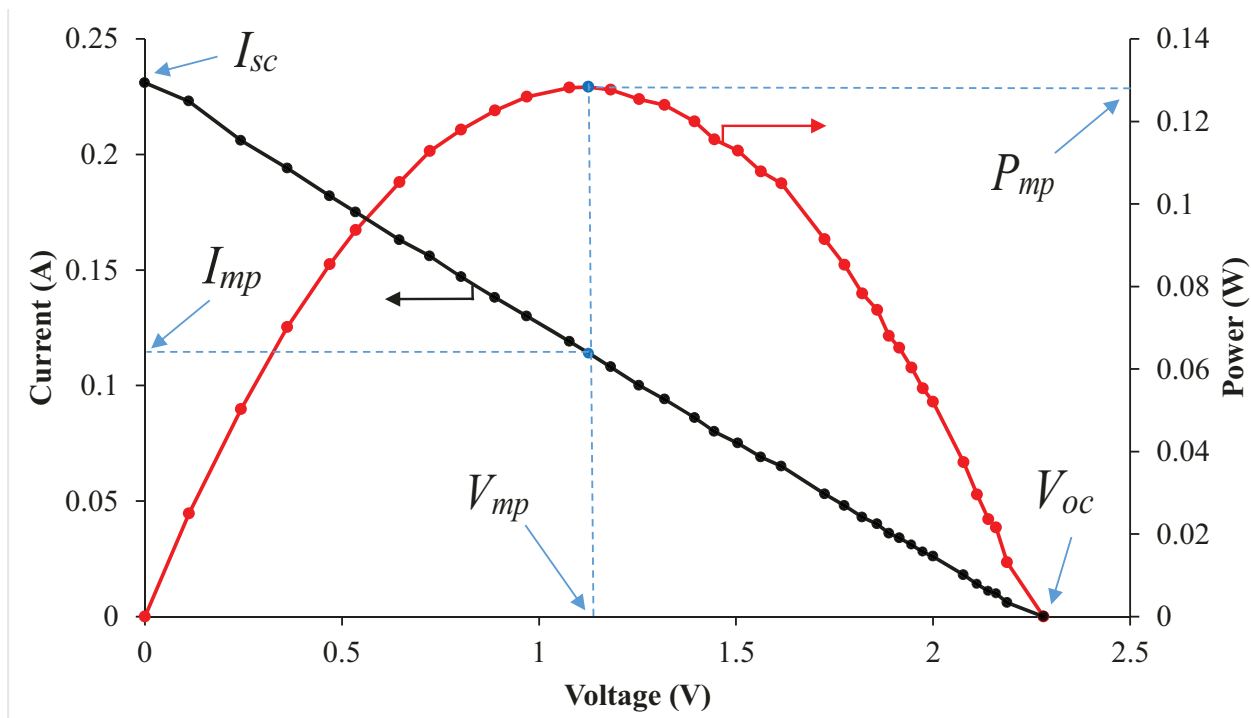


Figure 1.17: Typical current and power vs. voltage (I-V & P-V) curve of standard thermoelectric generator based on experimental data.

1.6.2 Thermoelectric Figure-of-Merit

The figure-of-merit is a temperature-dependent parameter used to define a thermoelectric material's ability to convert thermal energy into electrical energy. The figure-of-merit may be expressed as [50, 87, 88]:

$$Z = \frac{\alpha_s^2 \gamma}{k} = \frac{\alpha_s^2}{k \rho_e} \quad (1.19)$$

where, α_s is the Seebeck coefficient, γ_e is the electrical conductivity, ρ_e is electrical resistivity, and k is the thermal conductivity of the thermoelectric generator. A large figure-of-merit suggests that the thermoelectric device can efficiently generate electrical energy. Based on the figure-of-merit equation (1.19), an ideal thermoelectric generator material will have a high Seebeck coefficient, high electrical conductance (low electrical resistivity), and low thermal conductivity [87]. As discussed previously, the electrical energy produced by a thermoelectric generator increases as the temperature difference increases. Therefore, a low thermal conductivity is desired to maintain a large temperature differential across the thermoelements. Metals and metallic alloys are not used in thermoelectric power generation applications because they have very low Seebeck coefficients and high thermal conductivity, and thus have a low figure-of-merit and do not generate a significant amount of power [49]. Insulators have high Seebeck coefficients and low thermal conductivity; however the electrical conductivity of insulators is essentially zero, which restricts the flow of electrons through the thermoelements [50]. On the other hand, semiconductors have higher Seebeck coefficients, and lower electrical and thermal conductivity than metals [50]. The material properties of semiconductors obtain the highest figure-of-merit values and are the most suitable material for thermoelectric power generation. It is also important to note that the material properties of thermoelectric materials are temperature-dependent. For example, increasing the temperature of bismuth telluride-based alloys has shown to increase the electrical resistivity and decrease the material's thermal conductivity [89, 90, 91]. The figure-of-merit values of established thermoelectric materials are shown in **Figure 1.18**.

The dimensionless figure-of-merit is also used to analyze the performance of a thermoelectric generator. The dimensionless figure-of-merit may be determined by [49, 52, 53]:

$$Z\bar{T} = \frac{\alpha_S^2 \sigma}{k} \bar{T} = \frac{\alpha_S^2}{k\rho_e} \bar{T} \quad (1.20)$$

where, \bar{T} is the mean absolute temperature of the thermoelectric generator (K). The mean absolute temperature of the thermoelectric generator may be estimated by [53]:

$$\bar{T} = \frac{T_h + T_c}{2} \quad (1.21)$$

Min et al. [87] conducted an experimental analysis of the dimensionless figure-of-merit of a commercially available Bi_2Te_3 thermoelectric module under various temperature gradients. The results shown in **Figure 1.19** emphasize that the temperature difference across the thermoelectric generators significantly influences the dimensionless figure-of-merit.

Recently, optimization of a thermoelectric generator's energy conversion efficiency has primarily focused on the research and development of thermoelectric materials with high dimensionless figure-of-merit values. Thermoelectric power generation can become a more promising technology with the development of high-efficiency materials. Thermoelectric materials used in practical applications today have a dimensionless figure-of-merit value approximately equal to one [46, 92]. Difficulties arise in creating thermoelectric materials with $Z\bar{T} > 1$ due to the inability to decrease the thermal conductivity of thermoelectric materials. Recent literature has shown that nanostructuring thermoelectric materials can reduce thermal conductivity and establish dimensionless figure-of-merit values greater than one [93]. Wang et al. [71] report a peak dimensionless figure-of-merit value of 1.3 at 1173 K in an n-type nanostructured silicon germanium alloy. Venkatasubramanian et al. [94] examined the dimensionless figure-of-merit of thin-film thermoelectric materials. Their [94] experimental results show a dimensionless figure-of-merit of 2.4 at 300 K for a high quality p-type $\text{Bi}_2\text{Te}_3/\text{Sb}_3\text{Te}_3$ superlattice. Cobalt triantimonide-based skutterudites have also been identified as potential candidates to establish high-efficiency thermoelectric generators. This is mainly due to the discovery that cobalt triantimonide has lattice voids that may be filled with filler atoms to form filled skutterudites with low thermal conductivities. Recently, Pei et al. [95] introduced sodium (Na) into the voids of a cobalt triantimonide-based skutterudite structure and obtained a dimensionless figure-of-merit of 1.36 at 800 K for an n-type $\text{Ba}_x\text{Yb}_y\text{Co}_4\text{Sb}_{12}$ compound.

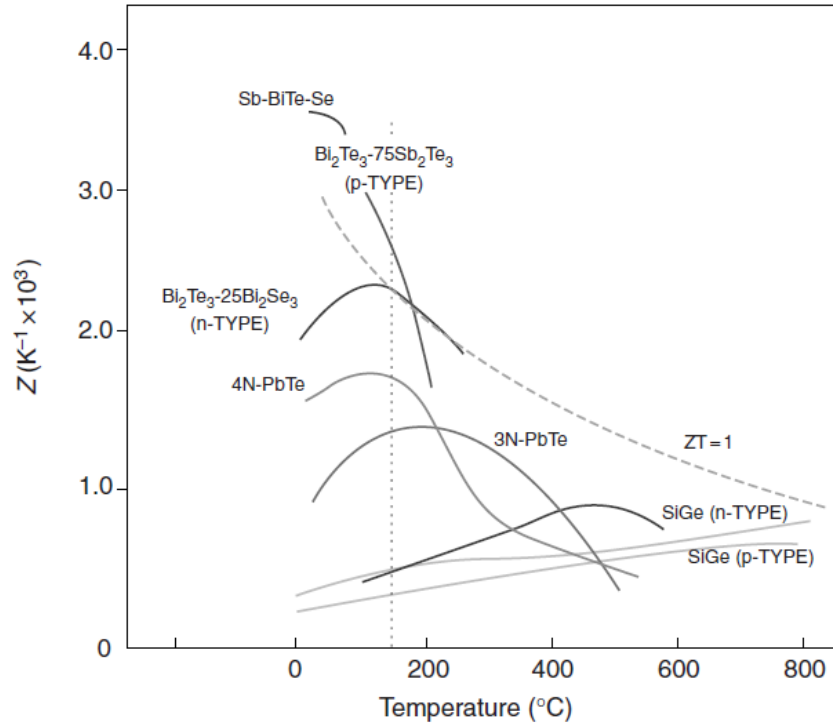


Figure 1.18: Figure-of-merit vs. temperature of various thermoelectric materials [50].

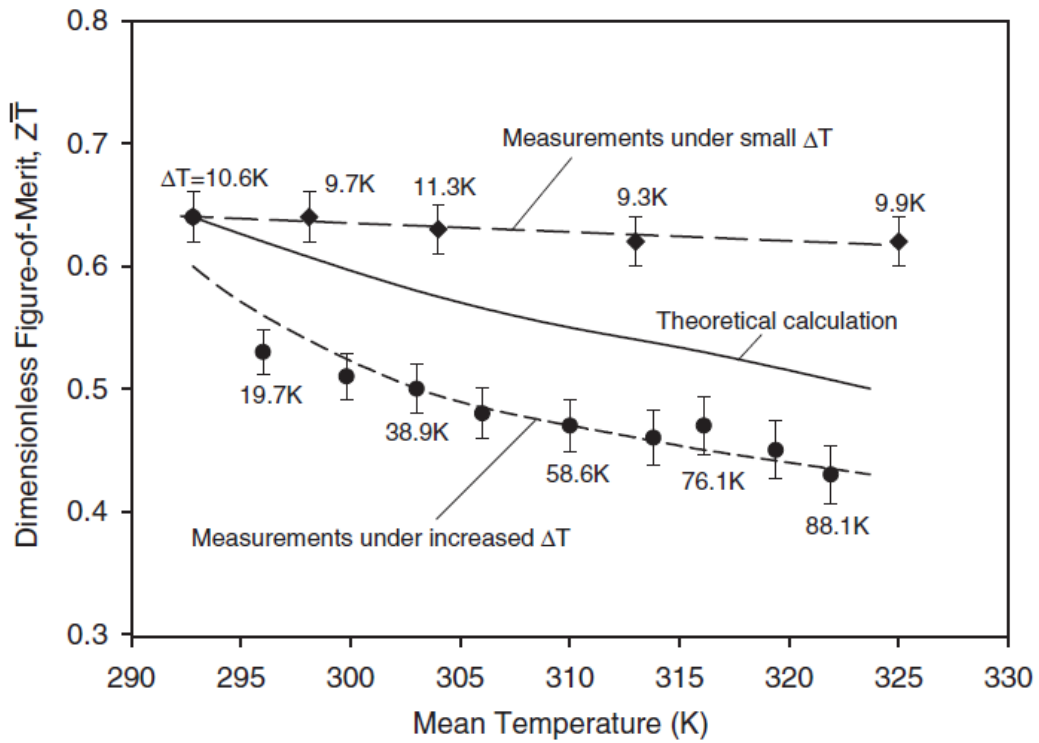


Figure 1.19: Experimentally determined dimensionless figure-of-merit vs. mean temperature at various temperature gradients (diamond shape symbols – small temperature difference, circle shape symbols – large temperature difference) [87].

Heremans et al. [96] obtained a dimensionless figure-of-merit equal to 1.5 at 773 K using p-type lead telluride samples with thallium impurities. Yamashita and Sigihara [90] were able to develop as-grown p-type and annealed n-type bismuth telluride semiconductor materials with relatively steady dimensionless figure-of-merit values from 200 to 360 K. The peak dimensionless figure-of-merit values of the p-type and n-type bismuth telluride compounds were 1.19 and 1.13 at approximately 320 K [90]. Thermoelectric materials with dimensionless figure-of-merit values greater than three must be developed in order for thermoelectric technology to be competitive with modern power systems [97]. Progress in semiconductor material research is key for thermoelectric power generation to become a viable technology.

1.7 Hybrid Photovoltaic-Thermoelectric Power Generation

The new concept of a hybrid photovoltaic-thermoelectric power generation (HPV-TEG) system integrates photovoltaic and thermoelectric technology together to form a more efficient energy system. Thermoelectric power generation has been applied to a variety of applications and research areas including aerospace, medical, thermal waste energy, military, and remote power generation. This particular research focuses on developing a thermoelectric power generator integrated with photovoltaic solar energy in order to form an innovative renewable energy system. In this study an HPV-TEG module, shown in **Figure 1.20** directly attaches a thermoelectric generator to the bottom of a photovoltaic module. When solar energy from the Sun, also known as irradiance, is projected onto the photovoltaic module, a small portion of the energy is converted into electrical energy and transferred to the electrical load R_{PV} . The majority of the incident solar energy is converted into thermal energy that is dissipated at a heat transfer rate from the top $\dot{Q}_{PV,top}$ and from the bottom $\dot{Q}_{PV,bot}$ of the photovoltaic module. The majority of the waste heat can be transferred through and dissipated at a rate of \dot{Q}_c from the thermoelectric generator to a cooling fluid by connecting a heat sink to the bottom of the thermoelectric generator. The photovoltaic operating cell temperature is decreased as a result of removing the thermal energy from the module. As previously discussed, decreasing the operating photovoltaic cell temperature increases the overall performance of the photovoltaic module. Therefore, the electrical

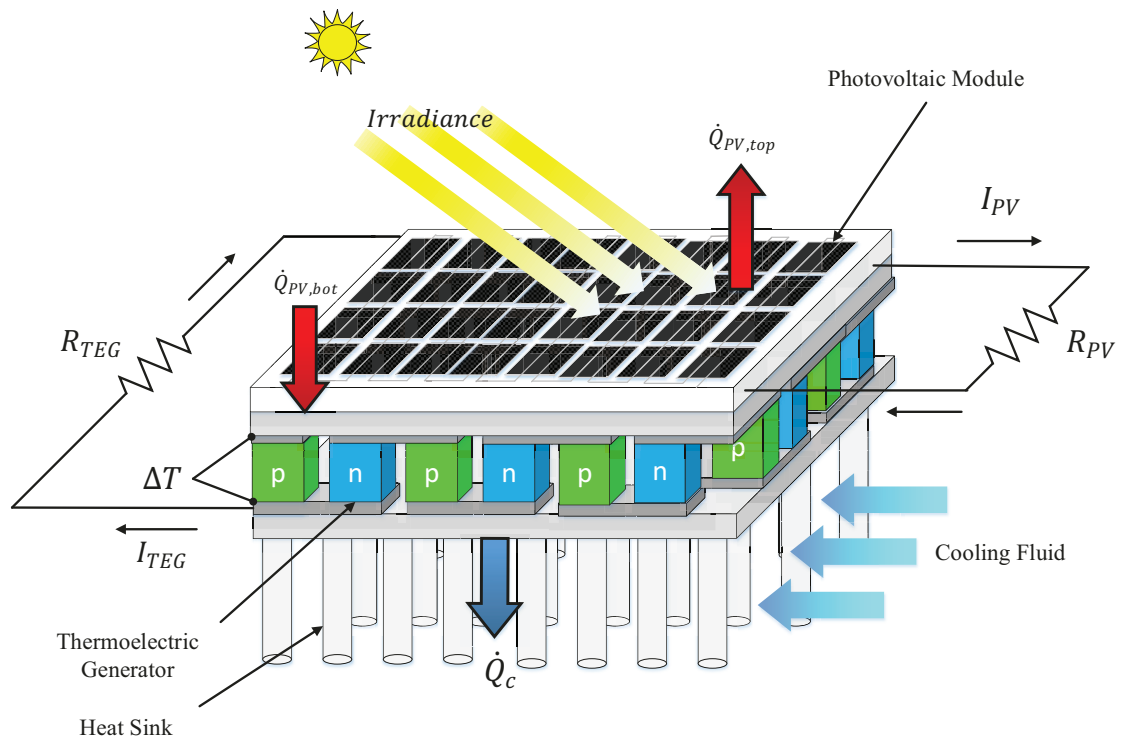


Figure 1.20: The concept of a hybrid photovoltaic-thermoelectric generator.

power delivered to the photovoltaic module's electrical load increases due to the cooling of the photovoltaic module. The photovoltaic module acts as a heat source, creating a temperature gradient ΔT across the thermoelectric generator. The thermoelectric generator utilizes the temperature gradient to convert the waste-heat from the photovoltaic module directly into electrical energy. The additional electrical energy generated from the thermoelectric generator may be supplied to an electrical load R_{TEG} . A hybrid photovoltaic-generator system simultaneously decreases the operating temperature of the photovoltaic module and increases the rate of electrical power produced. The HPV-TEG system has the potential to become a viable hybrid energy system in locations where the PV modules operate at high temperatures. However, further research is necessary to determine the system's viability and optimal design under different operating conditions.

1.8 Thesis Outline

The hybrid concept of integrating solar photovoltaic with thermoelectric power generation for cooling PV system and increasing power generation has not been comprehensively examined. Therefore, research is necessary to determine the feasibility and design constraints limiting the power output of hybrid photovoltaic-thermoelectric power generation systems. This research thesis will effectively review, numerically model, and experimentally investigate the performance of a HPV-TEG system. The thesis is divided into five chapters. Chapter one provides an introduction to the fundamental aspects of photovoltaic and thermoelectric power generation. Chapter two reviews some key previous research studies relating to the topic. Chapter three includes a comprehensive numerical model and presents numerical analysis in order to parametrically investigate the performance of an HPV-TEG system under a variety of operating conditions. Chapter three will also identify the detrimental performance parameters of a HPV-TEG system for better understanding and optimizing the system's performance. Chapter four presents the experimental work, including methodology, analysis, and discussion of the HPV-TEG system test setups used in this research. Chapter four is divided into two parts. In the first part, various designs of HPV-TEG systems are fully characterized using an indoor solar simulator. The second part of the chapter deals with the characterization using an outdoor test setup operating under the dynamic weather conditions of the city of Thunder Bay, Ontario, Canada.

Chapter five concludes the presented research work and provides some useful recommendations for future research related to HPV-TEG technology.

Chapter 2: Literature Review

This chapter reviews some existing literature related to recent innovation and development in the photovoltaic and thermoelectric power generation research field. Also in this chapter, the research objectives and outlines used in this research work are introduced and discussed.

2.1 Previous Experimental Studies of Solar PV Systems for Optimal Power Generation

The primary goal of solar photovoltaic research is to develop a reliable and efficient photovoltaic system that maximizes the rate at which electrical power is produced, while remaining competitive with the cost of modern power technologies. The cost of a photovoltaic module in terms of price per watt-hour (\$/Wh) is normally more expensive compared to other renewable energy technologies, such as wind and hydroelectricity, due to the high cost of semiconductor materials and the low energy conversion efficiency of photovoltaic modules [98]. For example, according to the United States Energy Information Administration (EIA), the average total levelized cost of electricity for wind, hydro, and solar photovoltaic plants entering service in 2019 is approximately 80.3 \$/MWh, 84.3 \$/MWh, and 130 \$/MWh respectively [99]. In the past few years, significant progress has been made to increase the rate of electricity production by creating advanced photovoltaic systems that incorporate additional components.

A significant amount of research on solar photovoltaic module optimization has analyzed the process of efficiently cooling PV modules by further developing photovoltaic-thermal collectors. Outdoor experimental studies have an important role in characterizing the actual performance of different hybrid photovoltaic-thermal system designs. For example, outdoor experiments completed by Tripanagnostopoulos et al. [43] directly compared the performance of PVT collectors, air-type (PVT-a) and water-type (PVT-w), with different designs in an outdoor environment. The PVT collectors were fabricated using commercially available polycrystalline silicon photovoltaic modules. In their study [43], steady-state analysis showed that additional glazing of PVT-a and PVT-w collectors

decreased the electrical efficiency by $\sim 2\%$. Real-time comparisons of a PVT-a, a PVT-w, a standard photovoltaic module, and an insulated photovoltaic module were accomplished under the weather conditions of Patras, Greece from 9:30 AM to 3:30 PM. Tripanagnostopoulos et al. [43] reported that the PVT-a and PVT-w collectors were able to maintain a lower photovoltaic operating temperature than the standard photovoltaic module, while the insulated PV module operated at a higher temperature than all the other systems because of its inability to dissipate thermal energy from its back surface. Also, the PVT-a and PVT-w collectors constantly established a higher electrical efficiency than the standard PV module during the duration of the outdoor experiment. PV water cooling was shown to be more effective in terms of establishing a higher electrical efficiency and a lower PV module temperature than air cooling when there are high irradiance intensities and ambient air temperatures. Although the dimensions of the PVT collectors and the weather conditions of the experimental simulation are provided in [43], accurate comparison of air-type and water-type PVT collectors requires the inlet working fluid characteristics to be published. Volumetric flow rate and temperature of the inlet working fluid are important experimental variables that significantly influence the performance and rate of thermal energy extracted from the system. Unfortunately, uncertainty in the experimental simulation arises due to the build quality of the water-type PVT collector. It was found that the build quality of the PVT-w collector was inadequate due to the described unsatisfactory thermal contact between the photovoltaic module and heat exchanger. Furthermore, the procedure for determining the maximum power output of the PV module was not described in detail by Tripanagnostopoulos et al. [43].

In 2012, Kim and Kim [45] experimentally examined two different absorber designs for an unglazed water-type PVT collector under outdoor conditions, a sheet-and-tube type and a fully wetted type. Each PVT collector was manufactured using a 240-watt monocrystalline silicon photovoltaic module. The study [45] determined that the average electrical efficiency of the fully wetted and sheet-and-tube absorber PVT collector was approximately 12.6% and 14%, respectively. The fully wetted PVT temperature was approximately $17\text{ }^{\circ}\text{C}$ cooler compared to the standard photovoltaic module temperature. Furthermore, the electrical efficiency of the fully wetted PVT was nearly 2% higher than the standard photovoltaic module in [45]. The experimentally determined electrical efficiency

and temperature of the photovoltaic systems were presented as a function of the ratio of the ambient air temperature and irradiance intensity. Neglecting to present these experimental parameters as a function of the actual operating conditions of the system, in this case [45] the outdoor weather conditions and the working fluid temperature, decreases the level of characterization of the PVT collectors. Background information regarding the procedure and instrumentation used to calculate the maximum power output of the photovoltaic systems was not described in [45]. Using the experimental results, the authors [45] concluded that an unglazed PVT collector provides better electrical performance than a standard PV module under the simulated outdoor climate. In their study [45], the location, time and weather conditions of the simulation used in their experimental work were not given, and as a result their experimental results are not consistently understood.

Some researchers have recently opted to use indoor solar simulators to test the performance of photovoltaic-thermal collectors. Indoor solar simulators allow researchers to complete parametric analysis and to study the steady state performance of a photovoltaic system in a controlled environment. Simulation, observation, and optimization of a photovoltaic system can be easily conducted using this type of experimental setup. Once the photovoltaic system has been optimized using an indoor solar simulator, outdoor experimental simulations may be conducted in order to determine the actual performance of the system, since the solar simulators do not accurately simulate the irradiance intensity of the Sun or climate conditions of a specified geographical location.

Agrawal et al. [100] designed and experimentally characterized the performance of two air-type photovoltaic-thermal collectors connected thermally in series using a low cost indoor solar simulator. The outlet of the first PVT collector was connected to the second PVT collector. The solar simulator consists of 28 500-watt tungsten halogen lights, and a screw jack mechanism that adjusts the height of the solar simulator platform and incident irradiance intensity projected onto the photovoltaic system [100]. The PVT system was made from two 2.2-watt monocrystalline silicon solar cells and a rectangular wooden channel with dimensions of 12 cm x 12 cm x 5 mm. A 0.6 watt DC fan was used to circulate air through the wooden air duct at a fixed mass flow rate of 1.08×10^{-4} kg/s and inlet air temperature equal to 38 °C. Irradiance intensities of 600, 700, and 800 W/m² were investigated for this specific experimental study. All solar simulations reached steady state operating condition in

approximately 1.75 hours. Agrawal et al. [100] reported that the maximum outlet air temperatures of the first and second PVT collectors were approximately 89 and 90 °C respectively, at an irradiance intensity equal to 800 W/m². They [100] observed that the waste-heat removed from the first and second PVT collectors was not equal due to the high inlet air temperature from the first PVT collector. The electrical efficiency of the first PVT collector was consistently higher than the second PVT collector due to its lower inlet air temperature and cell temperature. The researchers in another study [100] failed to compare the PVT system with a conventional photovoltaic system in order to show the benefit of using two PVT air-type collectors connected thermally in series. The electrical efficiency of the system was determined by subtracting the power consumed by the small electrical fan from the maximum power point of the photovoltaic module. Assuming the Fill Factor remains constant, the maximum power point of the photovoltaic module was estimated using the Fill Factor, open-circuit voltage, and short-circuit current measurement. This mathematical approach used by the researchers was subject to some inaccuracies because the fill factor increases substantially with temperature [20]. Variations in the inlet air temperature could have been studied to further characterize the PVT system.

Solanki et al. [101] also completed a thermal and electrical characterization of an air-type PVT system using an indoor solar simulator. In their work [101], the PVT system consisted of three 75-watt monocrystalline photovoltaic modules connected thermally in series, and a rectangular duct connected to the bottom of the PV modules. Air was circulated within the duct using a DC fan. The solar simulator had 16 500-watt tungsten halogen lamps orientated in a manner that created a uniform irradiance intensity of 400, 600, 700, 800, and 900 W/m². The PVT system reached steady state operating condition after approximately four hours. The operating temperatures of the first, second, and third PV modules are approximately 75, 81, 84 °C, respectively, at an irradiance intensity equal to 600 W/m², mass flow rate equal to 0.01 kg/s, and an inlet air temperature of 38 °C. Solanki et al. [101] observed that this increase of the PV module temperature was due to the series configuration of the PVT system. At the same operating condition, direct comparison of the PVT collector with a standard PV module shows that the electrical efficiency increases by 4%, and the operating temperature of the PV module decreases by 9 °C. Similar to Agrawal et al. [100], the efficiency of the photovoltaic module was determined mathematically by assuming the

Fill Factor remains constant (FF=0.8) and by measuring the open-circuit voltage and short-circuit current. The thermal model developed by Solanki et al. [101] showed reasonable agreement with the experimental results.

2.2 Previous Experimental Power Generation Characteristic Studies of TEGs

As discussed in the previous section, the removal of waste thermal energy from PV modules is one of the major optimization techniques used to maximize the performance of a PV module. Thermoelectric generators (TEGs) have the potential to utilize this waste thermal energy extracted from a PV module and directly convert a portion of it into electrical energy. A large amount of experimental research in recent years has concentrated on the accurate determination of a thermoelectric generator's performance parameters under different operating conditions. These performance parameters include the overall electrical power output, efficiency, Seebeck coefficient, and electrical conductivity of a thermoelectric generator. For example, as recently as 2014, Wang et al. [86] surveyed major test methods and multiple systems used at research institutes to evaluate the efficiency of thermoelectric generators. Their research suggested that the maximum power point of a thermoelectric generator occurs when the voltage of the load was equal to half of the open-circuit module voltage. Using one of these test methods, experimental analysis of an eight-thermocouple bismuth telluride thermoelectric generator revealed that the efficiency increases from 5% to 6.1% when decreasing the cold side temperature of the generator by 30 °C and maintaining the hot side temperature at 250 °C [86].

Karabetoglu et al. [102] estimated the Seebeck coefficient and electrical conductivity of a bismuth telluride thermoelectric generator under a low temperature range from 100-375 K. The Seebeck coefficient in this particular study was calculated by measuring the open-circuit voltage and the temperature gradient across the thermoelectric generator. Research presented by Hsu et al. [103] proposed the concept of an "effective Seebeck coefficient" to link the discrepancy between the theoretical and experimental Seebeck coefficient. The authors' [103] analysis emphasizes that thermal contact dominates the performance of the TEG module, generating a superior Seebeck coefficient as the clamping force was increased from 0.423 kg/cm² to 0.634 kg/cm².

Technological advances in the thermoelectric field have renewed interest in using

thermoelectric power generation in order to convert the large quantity of unused thermal energy that is transferred to the atmosphere into electricity. For instance, a numerical study completed by Yodovard et al. [104] took data from 27,000 factories from different sectors and analyzed the potential of using thermoelectric power generation to produce electricity. The net potential power generation using thermoelectrics was estimated to be approximately 92 MW. In order to determine the true potential of thermoelectric power generation for particular applications, further design optimization and an understanding of the external parameters that influence power output is necessary. Date et al. [105] provided an in depth review of the recent progress of thermoelectric power generation systems and the factors impeding its development and application in small to medium scale power production. Lesage and Pagé-Potvin [85] investigated the optimal electrical resistance for a liquid-to-liquid thermoelectric generator. The liquid-to-liquid thermoelectric generator apparatus was comprised of 40 commercially available Bi_2Te_3 thermoelectric modules, three aluminum channels, and an electrical circuit that can vary the electrical load resistance. In their study [85], the maximum power output of the generator appeared to increase exponentially as the temperature gradient across the modules increases. Minimal fluctuation in the optimal load resistance occurred when varying the temperature and flow rates of the hot and cold fluid. The experimental simulation suggests that a maximum power point tracker may not be necessary for this particular device, due to the fact that the optimal load resistance remains within 15% of 15.8 ohms for all of the thermal input conditions. In another experimental study, Dai et al. [106] introduced a test setup that exploited the advantageous thermophysical properties of liquid metal by using it as a carrier of waste-heat to a thermoelectric generator. Measurements of the thermoelectric modules' voltage and the temperature distribution of the test setup in [106] were determined to show the concept's feasibility.

2.3 Previous Studies on Characterization of Hybrid TEG Systems

2.3.1 Solar Thermal-Concentrator Thermoelectric Generators

Methods of using thermoelectric generators to produce electrical energy from renewable energy sources, such as solar energy, have become a more popular area of research because of the demand for clean energy technologies. In 2014, Nia et al. [107]

conducted an experimental investigation in Babol, Iran that used a Fresnel lens in order to concentrate solar energy onto an oil reservoir that was attached to a thermoelectric generator. The thermoelectric generator was placed between an oil and water reservoir in order to create a temperature gradient. Assuming the internal resistance of the TEG remains constant, the outdoor results showed a matched load output power of 1.08 watts under an irradiance intensity of 705.9 W/m². In the same year, Chen et al. [108] developed a finite element model and simulation of a thermal-concentrated solar thermoelectric generator. They concluded that increasing the substrate area or reducing the cross-sectional area of the thermoelements improves performance. The finite element model demonstrated that increasing the convective heat transfer coefficient of forced air convection has no significant effect on the system's performance and therefore, water cooling was recommended to maximize the temperature gradient and power output of the thermoelectric generator.

Kramer et al. [109] developed a high-performance solar thermoelectric generator using a spectrally-selective absorber and a single n- and p-type thermoelement pair. The thermoelement's material was based on a nanostructured Bi₂Te₃ alloy, with each thermoelement having dimensions approximately 1.35 mm x 1.35 mm x 1.65 mm. Simulated irradiance intensities of 1 and 1.5 kW/m² at a AM1.5G spectrum established peak efficiencies of approximately 4.6% and 5.2% when maintaining the cold side at 20 °C. Chávez-Urbiola et al. [110] examined the possibility of using thermoelectric generators in four solar hybrid system designs based on the experimental evaluation of a Bi₂Te₃ thermoelectric generator. The researchers suggested that a hybrid system with non-concentrated light was not feasible given the performance characteristics of commercially available thermoelectric generators. The concept of integrating thermoelectric generators with photovoltaic modules operating at a high temperature was introduced as a means of providing thermal stability. Furthermore, numerical analysis suggested that the photovoltaic modules' efficiency increases only if advanced thermoelectric materials with a high figure-of-merit value are incorporated into the system.

2.3.2 Recent Research Investigations of HPV-TEG Systems

The growing demand for more novel and efficient renewable energy systems has prompted greater interest in the integration of photovoltaic and thermoelectric technology

to fabricate an innovative hybrid system. However, despite there being several methods of integrating these two technologies, there seems to be few published works that have experimentally or numerically determined in detail the thermal characteristics and electrical output of a hybrid photovoltaic-thermoelectric (HPV-TEG) system. For example, Daud et al. [111] developed a hybrid photovoltaic-thermoelectric module and investigated its performance in an outdoor setting. In their work [111], the HPV-TEG module was comprised of a photovoltaic module, four Bi_2Te_3 thermoelectric modules connected electrically in series, and a glycol liquid cooling system. The thermoelectric modules were connected to a constant electrical load of 4.3 ohms. The efficiency of the HPV-TEG and standard photovoltaic module was calculated in terms of the power output measured in W/m^2 and the incident irradiance intensity. Compared to the standard photovoltaic module, the HPV-TEG module increased the energy conversion efficiency by 1.84% at an irradiance intensity of $601.12 \text{ W}/\text{m}^2$. The researchers in [111] also reported that the HPV-TEG system has a higher efficiency than the standard photovoltaic system as the irradiance intensity increases.

The main focus of the recent research involving hybrid photovoltaic-thermal systems has primarily been numerical modeling. Some researchers, such as Najafi and Woodbury [112] have analyzed the potential of cooling a photovoltaic system by inputting power to multiple thermoelectric modules using numerical modeling. The Matlab simulation in their [112] research showed that as the ambient air temperature and irradiance intensity increased, the power required by the thermoelectric modules to maintain the temperature of the photovoltaic module increases exponentially. The results of their [112] numerical study concluded that it was not feasible to operate the thermoelectric modules at the optimal performance because the amount of power generated by cooling the photovoltaic modules was far less than the power consumed by the thermoelectric modules. The alternative method of operating the thermoelectric modules at the optimal current suggested extra power can be produced from the proposed hybrid system if the thermoelectric modules have a high figure-of-merit value ($Z > 0.005 \text{ K}^{-1}$).

Using thermoelectric generators for direct conversion of the waste-heat from a photovoltaic module into electrical energy has been proposed as a more valid principle than cooling photovoltaic modules using thermoelectric modules. This type of system is known as a hybrid photovoltaic-thermoelectric power generation (HPV-TEG) system. Another

numerical study developed by Najafi and Woodbury [113] simulated the performance of an HPV-TEG system by developing a thermal circuit model and implementing energy balance analysis. The model has thermoelectric modules installed on the backside of a photovoltaic module, and removes the thermal energy from the TEGs using an air-cooling system. The theoretical results suggested that the power output of the photovoltaic module and TEG increases asymptotically and exponentially as the irradiance intensity increases. Further analysis of the performance of the HPV-TEG system for a typical summer day in Tuscaloosa, Alabama was conducted. The HPV-TEG system was composed of a 75-watt photovoltaic module, 3 x concentrator, single-axis tracker and 36 thermoelectric modules with constant material properties. Total power generated by the TEG and photovoltaic module was estimated to be approximately 28.398 Wh and 1.54 kWh [113].

Similar to the investigation completed by Najafi and Woodbury [113], Liao et al. [114] recently developed a theoretical model of a hybrid photovoltaic-thermoelectric power generation system. This HPV-TEG system was made from a 75-watt photovoltaic module and 11 thermoelectric generators operating with a constant cold side temperature equal to 300 K. The material properties of the thermoelectric generator are considered to be temperature-dependent in the numerical model. Several factors, such as the thermal conductance between the photovoltaic module and thermoelectric generator, concentration ratio, and figure-of-merit are analyzed with respect to the power output of the photovoltaic module and thermoelectric generator. The theoretical model suggested that the optimal electrical load for the photovoltaic module decreases asymptotically, while the optimal load resistance for the thermoelectric generator increases as the irradiance intensity increases. The work of Liao et al. [114] has provided meaningful insights into the design criteria required to optimize the performance of an actual HPV-TEG system.

The feasibility of a HPV-TEG system operating in Malaga, Spain was examined by van Sark [115]. In his study, van Sark [115] developed a model under ideal conditions to determine the performance of an HPV-TEG system operating from August 19th to August 28th in Malaga, Spain. Results from the simulation showed that the thermoelectric generator can establish approximately 24.7% of the total power of the HPV-TEG system, assuming a constant figure-of-merit equal to 0.004 K⁻¹. This numerical model overestimated the performance of the HPV-TEG by neglecting heat loss due to radiation and convection, reflection, and by assuming

that the solar radiation not converted into electricity by the PV module is directly transferred to the thermoelectric module.

2.4 Thesis Research Objectives

The concept of a hybrid photovoltaic-thermoelectric generator has not been thoroughly examined previously by researchers and engineers. Few detailed experimental simulations have been conducted in order to characterize the performance of an HPV-TEG system. Additionally, there is a limited literature that has developed an in-depth model to numerically simulate the performance of an HPV-TEG system. **Figure 2.1** illustrates the major components and objectives of the thesis research work. Due to the lack of detailed studies exploring the viability of an HPV-TEG system, the main objective of this research is to first design, construct, and fully instrument two test setups (indoor and outdoor). Once the experimental test setups are completed, detailed experimental simulations will be performed in order to characterize in detail the HPV-TEG system's performance under a variety of operating conditions. The controlled indoor solar simulator test setup is fabricated in order to analyze the HPV-TEG system under steady state operating conditions, while the real-time outdoor test setup is used to investigate the performance of the HPV-TEG system under the actual dynamic climate conditions of Thunder Bay, Ontario, Canada. A comprehensive numerical model and simulations of an HPV-TEG system will also be developed to provide insight into and further understanding of the performance, with respect to the applied operating conditions.

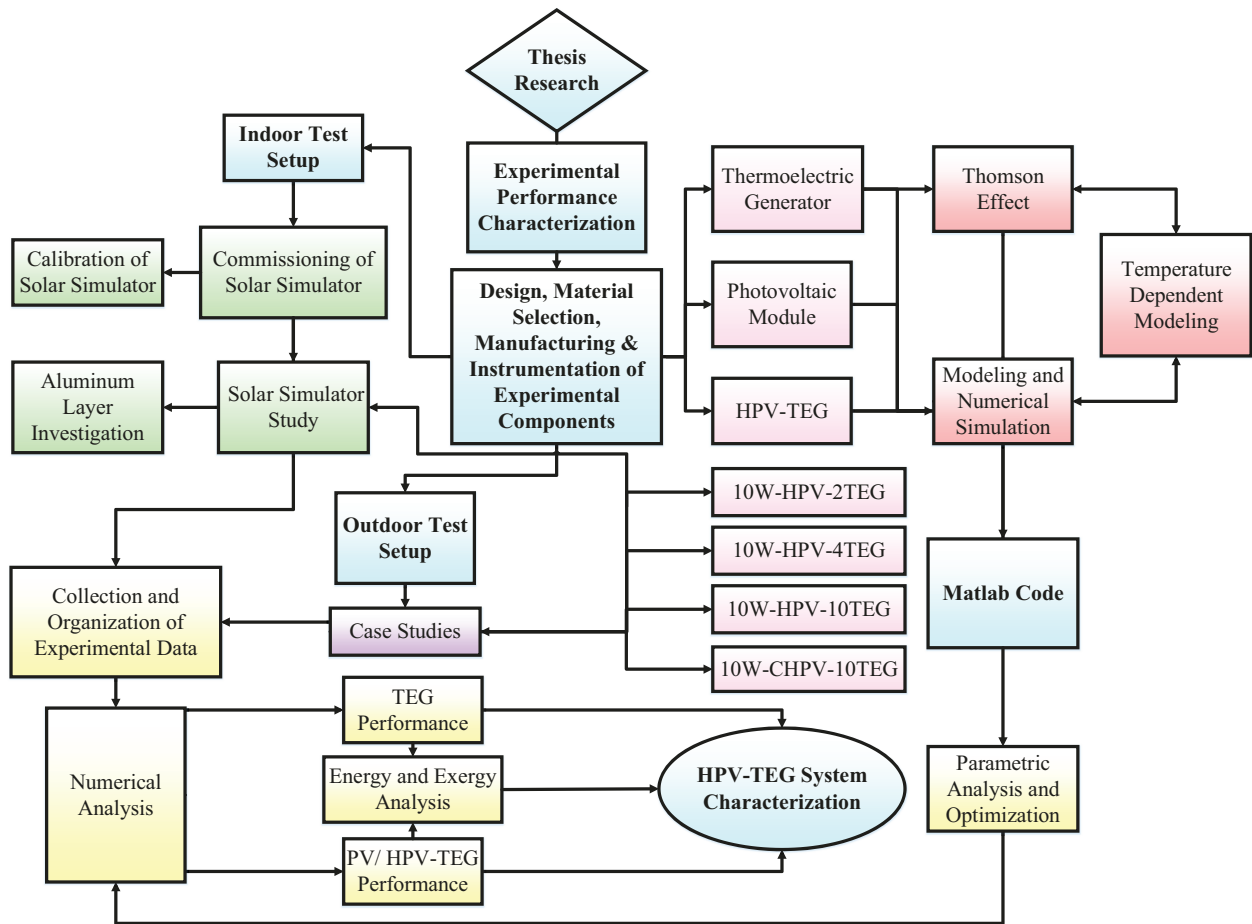


Figure 2.1: Flow chart of major components of this research work.

Chapter 3: Modeling and Numerical Characterization of a HPV-TEG System

This chapter numerically models, simulates and analyzes the performance of a PV and HPV-TEG system by completing parametric analysis. The obtained simulations results will assist in understanding the performance of a HPV-TEG for optimization purposes. Various relationships between the performance, energy conversion efficiency, irradiance intensity, and ambient air temperature of a PV and HPV-TEG system are examined. In addition, the concept of exergy analysis is introduced and used to identify and quantify the main irreversibilities and destruction of exergy rates in a HPV-TEG system for optimization and better understanding of the system's performance.

3.1 Numerical Model and Analysis of Conventional and Hybrid Photovoltaic Module

3.1.1 Thermal Circuit Analogy

Each solar photovoltaic system's temperature distribution is determined by developing and solving a complex set of nonlinear equations. These equations are formulated by using the one-dimensional (1-D) heat transfer thermal circuit analogy, and by applying the first law of thermodynamics to control surfaces within the energy system. The thermal circuit analogy determines the heat transfer rate through a specific boundary based on the thermal resistance and temperature differential across the boundary. This 1-D heat transfer model is similar to electrical current flowing through an electrical resistor. In this case, the heat transfer rate is analogous to the electrical current, the thermal resistance is analogous to the electrical resistance, and the temperature differential is analogous to the voltage difference across the boundary [116]. The thermal circuit analogy is a useful model that is utilized to simplify steady-state one-dimensional heat transfer when no internal heat generation occurs. The photovoltaic module may be modeled using the thermal circuit analogy, assuming that the majority of thermal energy is assumed to transfer one-dimensionally across the thickness of the module. The assumption of 1-D heat transfer flow in this model is reasonable since the thickness of the module is much smaller than its other

dimensions, therefore the majority of the heat transfer will occur across the least resisted path.

3.1.2 Determination Conventional PV Module Temperature Profile

A schematic of the numerically modeled conventional PV module and its thermal circuit is shown in **Figure 3.1**. The PV module experiences uniform convection on the top and bottom surfaces, as well as radiation heat transfer to the sky. The PV module is comprised of a glass layer, silicon layer, and a tedlar layer. The specifications and thermophysical properties of the PV module used in this study are shown in **Table 3.1**. The thermal resistance of the glass, silicon, and tedlar may be determined by the following equations [117]:

$$R_{gla} = \frac{L_{gla}}{k_{gla}A_{PV}} \quad (3.1)$$

$$R_{sil} = \frac{L_{sil}}{k_{sil}A_{PV}} \quad (3.2)$$

$$R_{ted} = \frac{L_{ted}}{k_{ted}A_{PV}} \quad (3.3)$$

where, L is the thickness of the layer, and k is the thermal conductivity of the material. The thermal resistance due to convection at the top and bottom surfaces of the PV module may be expressed as [117]:

$$R_{conv,top} = \frac{1}{h_{conv,top} A_{PV}} \quad (3.4)$$

$$R_{conv,bot} = \frac{1}{h_{conv,bot} A_{PV}} \quad (3.5)$$

The thermal resistance due to radiation heat transfer is given by [117]:

$$R_{rad} = \frac{1}{\varepsilon_{PV}\sigma(T_{cell} + T_{sky})(T_{cell}^2 + T_{sky}^2)A_{PV}} \quad (3.6)$$

where, ε_{PV} is the emissivity of the PV module, σ_B is the Stephan-Boltzmann constant ($5.67 \times 10^{-8} \text{ W/m}^2 \cdot \text{K}$), and T_{sky} is the absolute sky temperature. The sky temperature may be approximated as [113]:

$$T_{sky} = 0.0552 * T_{amb}^{1.5} \quad (3.7)$$

The bottom and top overall heat transfer coefficients may be expressed as [117]:

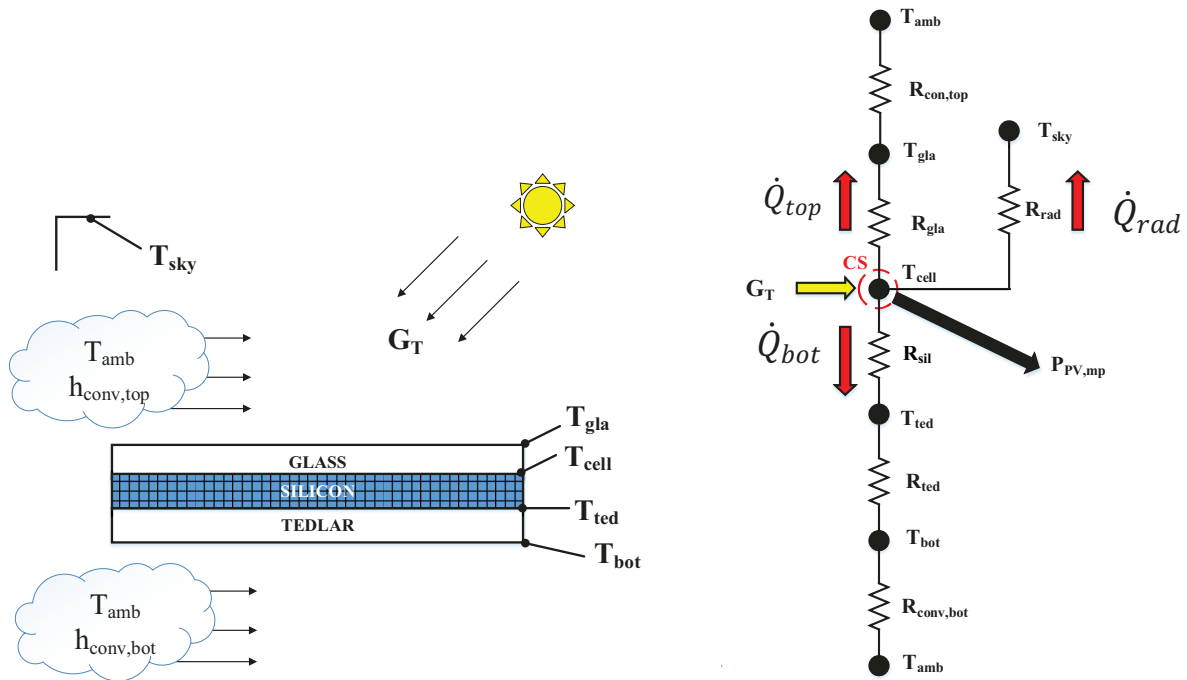


Figure 3.1: Schematic of a simplified model conventional PV module and thermal circuit used in this study.

Table 3.1: Specifications and thermophysical and optical properties of PV and HPV-TEG Module used in simulations of this study.

Parameter	Value
A_{PV} (m ²)	0.098172 [118]
L_{gla} (m)	0.003 [119]
L_{ted} (m)	0.001 [119]
L_{sil} (m)	250×10^{-6} [119]
L_{cer} (m)	0.0025
$\alpha_{A,ted}$	0.5 [113]
$\alpha_{A,sil}$	0.9
β_{cell}	0.88
k_{gla} (W/m·K)	0.78 [116]
k_{ted} (W/m·K)	0.2 [119]
k_{sil} (W/m·K)	148 [119]
k_{cer} (W/m·K)	32 [120]
ϵ_{PV}	0.88 [113]
τ_{gla}	0.86 [116]
$T_{w,in}$ (°C)	10
$h_{conv,bot}$ (W/m ² ·K)	5

$$U_{bot} = \left[\frac{L_{sil}}{k_{sil}} + \frac{L_{ted}}{k_{ted}} \right]^{-1} \quad (3.8)$$

$$U_{top} = \left[\frac{L_{gla}}{k_{gla}} + \frac{1}{h_{conv,t}} \right]^{-1} \quad (3.9)$$

The radiation heat transfer rate, and the heat transfer rates of the top and bottom portions of the PV module to the ambient air may be determined by the following formulae [117]:

$$\dot{Q}_{rad} = \varepsilon_{PV} \sigma A_{PV} (T_{cell}^4 - T_{sky}^4) \quad (3.10)$$

$$\dot{Q}_{top} = U_{top} A_{PV} (T_{cell} - T_{amb}) \quad (3.11)$$

$$\dot{Q}_{bot} = U_{bot} A_{PV} (T_{cell} - T_{bot}) \quad (3.12)$$

The maximum conversion efficiency of the PV module when accounting for the losses due to the glass cover is given by:

$$\eta_{PV,ele} = \frac{P_{PV,mp}}{G_T A_{PV} \tau_{gla} \beta_{cell}} \quad (3.13)$$

where, $P_{PV,mp}$ is the maximum power generated by the PV module, τ_{gla} is the transmittance of the PV glass, and β_{cell} is the packing factor. The packing factor refers to the ratio of a photovoltaic module's area that is covered with photovoltaic cells.

The overall performance of the PV module may be determined by obtaining an energy balance equation around the T_{cell} surface. The amount of solar radiation absorbed by the PV module is determined by the amount of solar radiation absorbed by the silicon and surrounding tedlar layer. The solar radiation that is not converted into electrical energy is dissipated as waste thermal energy. Applying the first law of thermodynamics to the T_{cell} surface yields:

$$\sum_{in} \dot{E}_{in} = \sum_{out} \dot{E}_{out} \quad (3.14)$$

$$\begin{aligned} & \tau_{gla} A_{PV} G_T [\beta_{cell} \alpha_{a,sil} + \alpha_{a,ted} (1 - \beta_{cell})] \\ & = U_{top} A_{PV} (T_{cell} - T_{amb}) + \varepsilon_{PV} \sigma A_{PV} (T_{cell}^4 - T_{sky}^4) \\ & + U_{top} A_{PV} (T_{cell} - T_{amb}) + G_T A_{PV} \tau_{gla} \beta_{cell} \eta_{ele} \end{aligned} \quad (3.15)$$

where, α_A is the absorptance of the material, and T_{amb} is the ambient air temperature.

The heat transfer from the top portion of the PV module may be expressed as:

$$\dot{Q}_{top} = \frac{T_{cell} - T_{gla}}{R_{gla}} = \frac{T_{gla} - T_{amb}}{R_{conv,t}} \quad (3.16)$$

Similarly, the heat transfer from the bottom portion of the PV module may be expressed as:

$$\dot{Q}_{bot} = \frac{T_{cell} - T_{ted}}{R_{sil}} = \frac{T_{ted} - T_{bot}}{R_{ted}} = \frac{T_{bot} - T_{amb}}{R_{conv,b}} \quad (3.17)$$

The temperature profile of the conventional PV module may be determined by simultaneously solving equations 3.15-3.17. Once the temperature profile is known, the electrical power output may be determined using the equivalent circuit model presented later in section 3.0.6.

3.1.3 Determination of the HPV-TEG Module Temperature Profile

Similar to the previous section 3.0.2, the temperature distribution of a hybrid photovoltaic-thermoelectric power generator module may be determined by solving a complex system of nonlinear equations. The modeled HPV-TEG system and its thermal circuit is shown in **Figure 3.2**. The HPV-TEG system has all the same dimensions and specifications of the conventional PV module shown in **Table 3.1**. A thermoelectric generator comprised of several thermoelements sandwiched between two ceramic layers is directly coupled to the back surface of the PV module. A perfectly insulated water cooling channel is attached to the bottom of the thermoelectric generator to ensure that the majority of the waste thermal energy is transferred through the TEG. As shown in **Table 3.2**, the thermophysical properties of water are based on the mean temperature. The thermal resistance of the ceramic layer and the thermal resistance due to the convection heat transfer to the water in the channel may be expressed as [117]:

$$R_{cer} = \frac{L_{cer}}{k_{cer}A_{PV}} \quad (3.18)$$

$$R_{conv,w} = \frac{1}{h_w A_{PV}} \quad (3.19)$$

Based on the thermal circuit, the heat transfer rate to the thermoelectric generator's hot side, and from the thermoelectric generator's cold side are given by [117]:

$$\dot{Q}_{h,TEG} = \frac{T_{cell} - T_{bot}}{R_{sil} + R_{ted}} = \frac{T_{bot} - T_h}{R_{cer}} \quad (3.20)$$

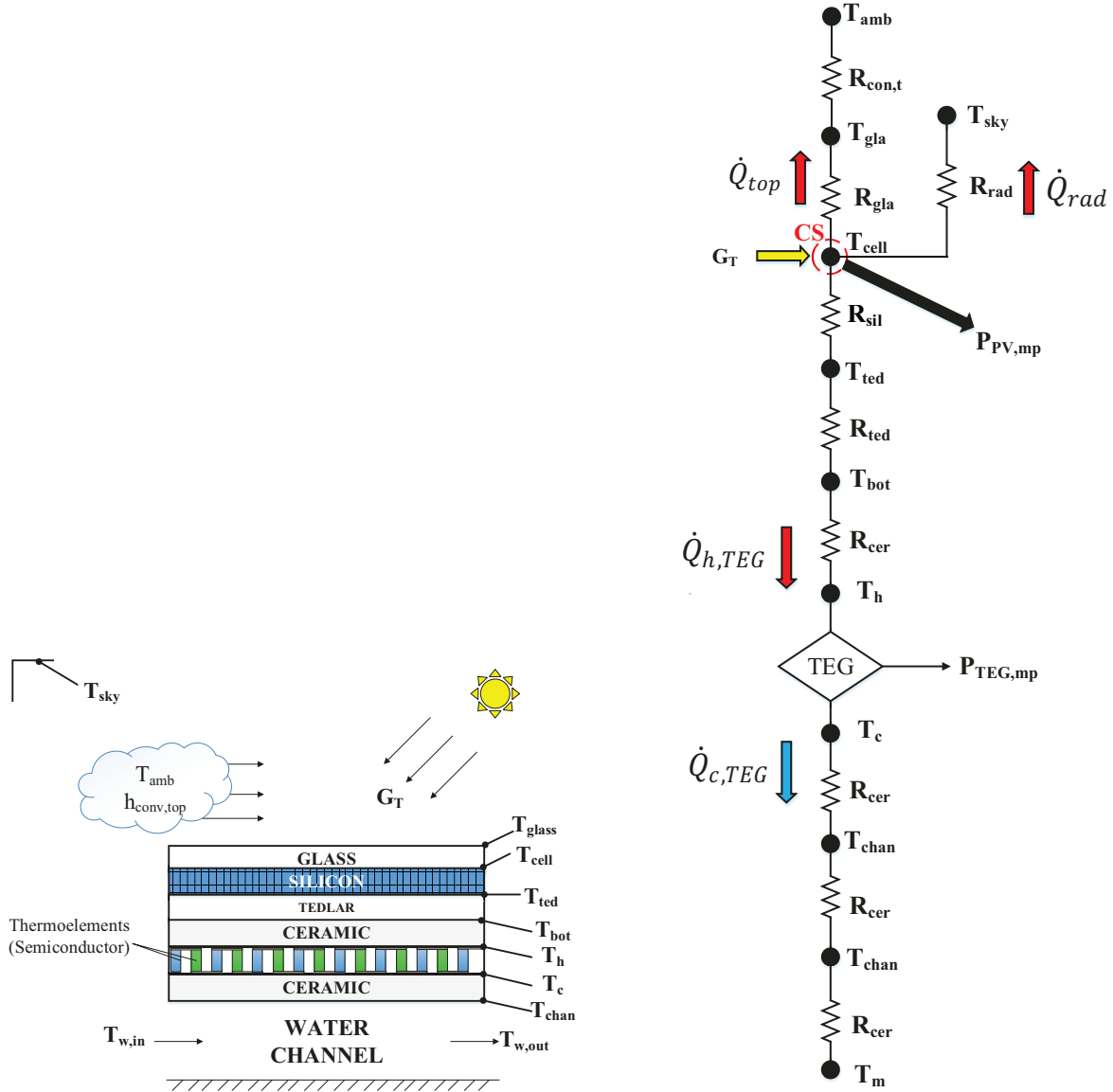


Figure 3.2: Schematic of the simplified HPV-TEG module and thermal circuit used in this work.

Table 3.2: Thermophysical properties of water based on mean temperature (K) used in the numerical study [117].

Parameter	Equation
Specific Heat (J/kg·K)	$C_{p,w} = 0.0599T_m^2 - 35684T_m + 9495.9$
Dynamic viscosity (Pa·s)	$\mu_w = 6.91E - 7T_m^2 - 0.000429T_m + 0.0673$
Thermal conductivity (W/m·K)	$k_w = -7.87E - 6T_m^2 + 000612T_m - 0.515$

$$\dot{Q}_{c,TEG} = \frac{T_c - T_m}{R_{cer} + R_{conv,w}} \quad (3.21)$$

where, T_m is the mean water temperature approximated as:

$$T_m = \frac{T_{w,in} + T_{w,out}}{2} \quad (3.22)$$

Applying energy balance to the control surface around the top channel surface and assuming negligible pressure loss in the channel yields:

$$\frac{T_c - T_{chan}}{R_{cer}} = \dot{m}_w C_{p,w} (T_{w,in} - T_{w,out}) \quad (3.23)$$

where, \dot{m}_w is the mass flow rate of water liquid, and $C_{p,w}$ is the specific heat of the water estimated using the mean temperature of the water [117].

The Reynold's number may be expressed as [116]:

$$Re_D = \frac{\rho_w D_h V_m}{\mu_w} \quad (3.24)$$

where, ρ_w is the density of water (kg/m^3), D_h is the hydraulic diameter, V_m is the mean velocity of the water flow through the channel, and μ_w is the dynamic viscosity of the water.

The hydraulic diameter is given by [116]:

$$D_h = \frac{4A_{chan}}{P_w} \quad (3.25)$$

where, A_{chan} is the cross-sectional area of the channel, and P_w is the wetted perimeter. The model simulates an assumed fully hydrodynamically and thermally developed laminar flow with a uniform heat transfer from the top surface of channel. The flow in the channel is considered to be laminar flow if $Re_D < 2300$, turbulent flow if $Re_D > 10000$, and transitional flow if $2300 \leq Re_D \leq 10000$ [116]. The channel's resulting cross-sectional area ratio of width to length is modeled to be approximately eight. The numerical model presented in this research work establishes a $Re_D \ll 2300$. Based on these conditions, the Nusselt number may be approximated as [117]:

$$Nu_D = 6.49 \quad (3.26)$$

Based on the above equation, the convective heat transfer coefficient of the water flow may be approximated as [117]:

$$h_w = \frac{6.49k_w}{D_h} \quad (3.27)$$

where, k_w is the thermal conductivity of the water, given by the equation shown in **Table 3.2**.

3.1.4 Modeling the Thermoelectric Power Generator

As discussed previously, the thermoelectric generator consists of multiple n-type and p-type thermoelements connected electrically in series, and thermally in parallel. Electrical energy may be generated by establishing a temperature differential across the thermoelements according to the Seebeck effect. The specifications of the thermoelectric generator used in this research are shown in **Table 3.3**. The standard analytical thermoelectric generator model used in this research neglects the thermal conductivity and electrical resistance of the electrode connections between the p- type and n-type thermoelements. The TEG model also assumes no heat loss to the thermoelements' surroundings except at the junction contacts. Based on the standard thermoelectric power generator model, the Seebeck coefficient, electrical resistance, and thermal conductance of a single thermocouple may be determined by the following equations [82, 103, 121, 122]:

$$\alpha_{s,p-n} = \alpha_p - \alpha_n \quad (3.28)$$

$$R_{p-n} = \frac{\rho_p L_p}{A_p} + \frac{\rho_n L_n}{A_n} = \frac{L_{TEG}}{A_{TEG}} (\rho_p + \rho_n) \quad (3.29)$$

$$K_{p-n} = \frac{k_p A_p}{L_p} + \frac{k_n A_n}{L_n} = \frac{L_{TEG}}{A_{TEG}} (k_p + k_n) \quad (3.30)$$

The Seebeck coefficient, electrical resistance, and thermal conductance are temperature-dependent material properties. The numerically modeled thermoelectric generator consists of n-type and p-type bismuth-telluride compounds. The material properties of a single thermocouple are determined through linear regression analysis of the experimental data provided by Yamashita and Sugihara's [90] experimental work. Based on linear regression analysis of Yamashita and Sugihara's [90] research, the Seebeck coefficient, electrical resistance, and thermal conductance as a function of mean TEG temperature (K) are estimated as:

$$\alpha_{s,p-n} = 1.34E - 10T_{TEG}^2 + 1.70E - 6T_{TEG} + 1.22E - 4 \quad (3.31)$$

Table 3.3: Specifications of the thermoelectric generator used in this research.

Parameter	Value
A_p (m ²)	0.000025
A_n (m ²)	0.000025
L_p (m)	0.003
L_n (m)	0.003
N_{TEG}	1350

$$R_{p-n} = 1.02E - 8T_{TEG}^2 + 4.11E - 6T_{TEG} - 7.32E - 5 \quad (3.32)$$

$$K_{p-n} = 3.07E - 7T_{TEG}^2 - 2.16E - 4T_{TEG} + 6.40E - 2 \quad (3.33)$$

The mean TEG temperature is based on the temperature of the hot and cold junctions, and is given by:

$$T_{TEG} = \frac{T_c + T_h}{2} \quad (3.34)$$

The Seebeck coefficient, electrical resistance, and thermal conductance of the entire thermoelectric generator may be determined by the following equations [81, 114]:

$$\alpha_{s,TEG} = N_{TEG}\alpha_{p-n} \quad (3.35)$$

$$R_{TEG} = N_{TEG}\rho_{p-n} \quad (3.36)$$

$$K_{TEG} = N_{TEG}k_{p-n} \quad (3.37)$$

where, N_{TEG} is the total number of thermocouples in the thermoelectric generator.

The Seebeck effect, heat transfer by conduction, and the internal Joule heating effect must be considered in order to derive the heat transfer rate absorbed and dissipated from the thermoelectric generator. The heat transfer rate absorbed from the high temperature side, and released from the low temperature side, due to the Seebeck effect, may be expressed by the following equations [82]:

$$\dot{Q}_{h,PELTIER} = \alpha_{s,TEG}I_{TEG}T_h \quad (3.38)$$

$$\dot{Q}_{h,PELTIER} = \alpha_{s,TEG}I_{TEG}T_c \quad (3.39)$$

Applying Fourier's law of heat conduction, the heat transfer rate due to conduction throughout the thermoelectric generator may be determined by [82, 117]:

$$\dot{Q}_k = K_{TEG}(T_h - T_c) \quad (3.40)$$

The Joule heat generated due to electrical current flowing through the thermoelectric generator may be defined as [82]:

$$\dot{Q}_j = I_{TEG}^2 R_{TEG} \quad (3.41)$$

where, I_{TEG} is the electrical current produced by the thermoelectric generator. The model assumes that the internal Joule heat generated is equally divided between the hot and cold temperature junctions.

Based on the previous analysis discussed above, the total rate of heat absorbed and dissipated by an ideal thermoelectric generator is given by [82, 83, 85, 103, 112, 123, 124]:

$$\dot{Q}_{h,TEG} = \alpha_{s,TEG} I_{TEG} T_h + K_{TEG} (T_h - T_c) - \frac{I_{TEG}^2 R_{TEG}}{2} \quad (3.42)$$

$$\dot{Q}_{c,TEG} = \alpha_{s,TEG} I_{TEG} T_c + K_{TEG} (T_{hot} - T_{cold}) + \frac{I_{TEG}^2 R_{TEG}}{2} \quad (3.43)$$

The electrical current generated by the TEG is given by [113, 122, 125]:

$$I_{TEG} = \frac{\alpha_{s,TEG} (T_h - T_c)}{R_{TEG} + R_{L,TEG}} \quad (3.44)$$

where, $R_{L,TEG}$ is the electrical resistance of the load connected to the TEG. The maximum power output of a thermoelectric generator may be obtained when the electrical load resistance is equal to the internal resistance of the thermoelectric generator. Therefore, the TEG's electric load resistance at the maximum power point is given by [82, 85]:

$$R_{L,TEG} = R_{TEG} \quad (3.45)$$

The thermoelectric generator's maximum electrical power output is determined by [83, 85, 122, 125]:

$$P_{TEG,mp} = \dot{Q}_{h,TEG} - \dot{Q}_{c,TEG} = \alpha_{s,TEG} I_{TEG} (T_h - T_c) - I_{TEG}^2 R_{TEG} \quad (3.46)$$

Based on the derived heat equations shown in Eq. (3.20) and (3.21), the thermoelectric generator's maximum power output is also expressed as a function of temperature distribution and thermal resistances, given by:

$$P_{TEG,mp} = \dot{Q}_{h,TEG} - \dot{Q}_{c,TEG} = \frac{T_{cell} - T_{bot}}{R_{sil} + R_{ted}} - \frac{T_c - T_m}{R_{cer} + R_{conv,w}} \quad (3.47)$$

The conversion efficiency of the thermoelectric generator may be defined as [122]:

$$\eta_{TEG} = \frac{P_{TEG,mp}}{\dot{Q}_{H,TEG}} \quad (3.48)$$

3.1.5 Modeling and Simulation of Thomson Effect

The Thomson effect states that there is a relationship between the rate of heat generation due to the temperature gradient and current passing through a semiconductor material. In this investigation, Thomson effect will be considered and numerically simulated in order to determine its significance on the modeling of the HPV-TEG system. While operating at a constant current, heat is generated and dissipated from a thermoelement due to charge carriers responding to the changing voltage field [52]. The heat absorbed and

dissipated by an ideal thermoelectric generator, when accounting for the Thomson effect, may be expressed as [87, 126]:

$$\begin{aligned} \dot{Q}_{h,TEG} = & \alpha_{s,TEG} I_{TEG,Thom} T_{h,Thom} + K_{TEG} (T_{h,Thom} - T_{c,Thom}) \\ & - \frac{I_{TEG,Thom}^2 R_{TEG}}{2} - \frac{1}{2} \tau_{TEG} (T_{h,Thom} - T_{c,Thom}) I_{TEG,Thom} \end{aligned} \quad (3.49)$$

$$\begin{aligned} \dot{Q}_{c,TEG,Thom} = & \alpha_{s,TEG} I_{TEG,Thom} T_{c,Thom} + K_{TEG} (T_{h,Thom} - T_{c,Thom}) \\ & + \frac{I_{TEG,Thom}^2 R_{TEG}}{2} + \frac{1}{2} \tau_{TEG} (T_h - T_c) I_{TEG} \end{aligned} \quad (3.50)$$

The equations above assume that the Thomson heat given by:

$$\dot{Q}_{THOM} = \tau_{TEG} (T_h - T_c) I_{TEG,Thom} \quad (3.51)$$

is equally released from the hot and cold thermoelement junctions. The power generated by the TEG when accounting for the Thomson effect becomes:

$$\begin{aligned} P_{TEG,mp,Thom} = & \dot{Q}_{h,TEG,Thom} - \dot{Q}_{c,TEG,Thom} \\ = & \alpha_{s,TEG} I_{TEG,Thom} (T_h - T_c) - I_{TEG,Thom}^2 R_{TEG} \\ & - \tau_{TEG} (T_h - T_c) I_{TEG,Thom} \end{aligned} \quad (3.52)$$

Assuming the Thomson coefficient is constant, the Thomson coefficient may be approximated using Eq. (1.15) [52]:

$$\alpha_{s,TEG}(T) = \tau_{TEG} \ln(T) + C \quad (3.53)$$

where, C is the constant of integration. The logarithmic curve fit of the Seebeck coefficient based on Eq. (3.31) estimates the TEG to have a Thomson coefficient approximately equal to 0.000504 V/K. Some numerical TEG simulations [82, 103, 112, 113, 122, 123, 124, 127] have neglected the Thomson effect and assumed the Seebeck coefficient to be constant. The Thomson effect is neglected based on the effect being small under low temperature differences [128]. In other research works [114, 121], the temperature dependency of the Seebeck coefficient, electrical resistivity, and thermal conductivity have been considered. The assumption that the Thomson effect can be neglected will be evaluated prior to completing the PV and HPV-TEG numerical study.

3.1.6 Equivalent Circuit Model of a Photovoltaic Module

The equivalent circuit model may be used to accurately determine the electrical performance of a photovoltaic cell, module, or array. The model presented in this research

will simulate the performance of a photovoltaic module. A schematic of the standard equivalent circuit model with a single diode is shown in **Figure 3.3** [9]. The electrical parameters of the PV and HPV-TEG module are shown in **Table 3.4**. The electrical current supplied to the electrical load at a fixed irradiance intensity and photovoltaic temperature is given by [9, 129]:

$$I_{PV} = I_L - I_D - I_{sh} = I_L - I_o \left[\exp\left(\frac{V_{PV} + I_{PV}R_s}{a}\right) - 1 \right] - \frac{V_{PV} + I_{PV}R_s}{R_{sh}} \quad (3.54)$$

where, I_L is the light current, I_o is the diode reverse saturation current, R_s is the series resistance of the photovoltaic module, R_{sh} is the shunt resistance of the photovoltaic module, and a is the thermal voltage. The reference thermal voltage may be determined by the model equation [9]:

$$a_{ref} = \frac{n k_B T_{cell,ref} N_s}{q} \quad (3.55)$$

where, n is the diode quality coefficient, k_B is the Boltzmann constant ($1.381 \cdot 10^{-23}$ J/K), $T_{cell,ref}$ is the photovoltaic cell temperature at the reference condition (K), N_s is the number of cells in series, and q is the absolute value of an electron's charge ($1.602 \cdot 10^{-19}$ coulomb). Assuming the internal resistance of the PV module is negligible ($R_{sh} \gg R_s$), the diode quality coefficient may be determined by [130]:

$$n = \frac{q(V_{PV,mp,ref} - V_{PV,oc,ref})}{N_s k_B T_{cell,ref}} * \frac{1}{\ln\left(1 - \frac{I_{PV,mp,ref}}{I_{PV,sc,ref}}\right)} \quad (3.56)$$

The series resistance of the PV module may be assumed to be independent of temperature [9]:

$$R_s(T_{cell,ref}) = R_s(T_{cell}) \quad (3.57)$$

The shunt resistance does not significantly vary as the temperature of the PV module changes, however, it is dependent on the incident solar radiation. Previously conducted experimental research by De Soto et al. [131] demonstrated that the shunt resistance may be approximated as:

$$\frac{R_{sh}}{R_{sh,ref}} = \frac{S_{ref}}{S} \quad (3.58)$$

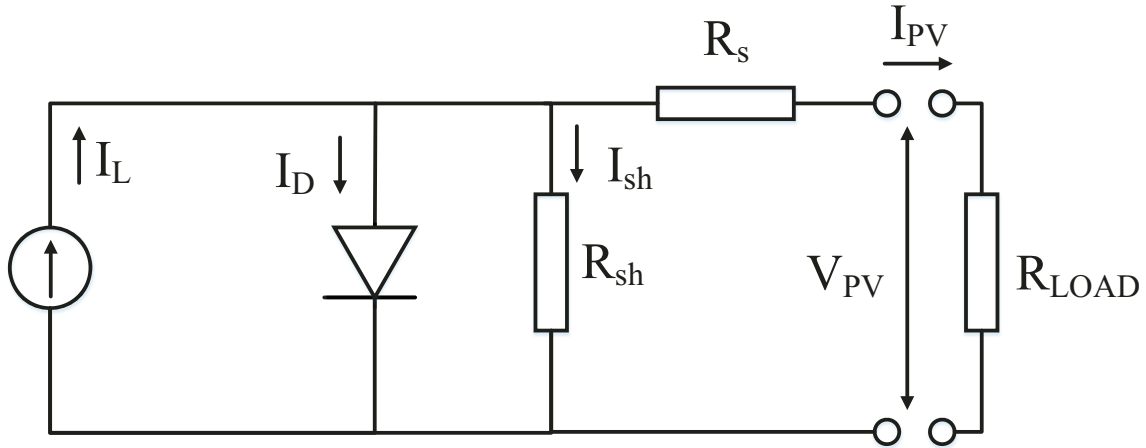


Figure 3.3: Equivalent circuit model of a photovoltaic module with a single diode.

Table 3.4: Electrical specifications of PV and HPV module used in this research study.

Parameter	Value
$R_{s,ref}$ (Ω)	3.23 [118]
$R_{sh,ref}$ (Ω)	654.39 [118]
$V_{PV,oc,ref}$ (V)	20.081 [118]
$I_{PV,sc,ref}$ (A)	0.723 [118]
$V_{PV,mp,ref}$ (V)	16.52 [118]
$I_{PV,mp,ref}$ (A)	0.62 [118]
$T_{cell,ref}$ ($^{\circ}\text{C}$)	25
N_s	36 [118]
\dot{V} (L/min)	5
μ_{Voc} ($1/^{\circ}\text{C}$)	-0.06 [132]
μ_{Isc} ($1/^{\circ}\text{C}$)	0.33 [132]
G_{ref} (W/m^2)	1000

where, S is the solar radiation absorbed by the PV module. Assuming that the absorptivity, reflectivity, and transmissivity of the photovoltaic module remains constant, Eq. (3.58) may be simplified as:

$$\frac{R_{sh}}{R_{sh,ref}} = \frac{G_{T,ref}}{G_T} \quad (3.59)$$

Assuming the diode quality coefficient n is independent of temperature, the parameter a may be defined as a function of the cell temperature by the following equation [9]:

$$\frac{a}{a_{ref}} = \frac{T_{cell}}{T_{cell,ref}} \quad (3.60)$$

The reference light current may be expressed as a function of the reference open-circuit voltage by substituting $I_{PV}=0$ and $V_{PV}=V_{PV,oc}$, into equation (3.54). The fundamental equivalent circuit equation (3.54) becomes:

$$I_{L,ref} = I_{o,ref} \left[\exp\left(\frac{V_{PV,oc,ref}}{a_{ref}}\right) - 1 \right] + \frac{V_{PV,oc,ref}}{R_{sh,ref}} \quad (3.61)$$

The light current, also known as the photocurrent, at a known irradiance intensity G_T and cell temperature T_{cell} , may be approximated based on the reference irradiance intensity G_{ref} and photovoltaic cell temperature $T_{cell,ref}$ [9, 32, 130, 131]:

$$I_L = \frac{G_T}{G_{ref}} [I_{L,ref} + \mu_{Isc}(T_{cell} - T_{cell,ref})] \quad (3.62)$$

where, μ_{Isc} is the short-circuit current temperature coefficient. Experimental simulations completed by Virtuani et al. [132] estimated the short-circuit current and open-circuit voltage temperature coefficients of various types of photovoltaic modules. The experimental results suggest that crystalline silicon-based photovoltaic modules have a short-circuit current and open-circuit voltage temperature coefficient of approximately 0.06 (1/°C) and -0.33 (1/°C) [132].

The diode reverse saturation current I_o is given by [133]:

$$\frac{I_o}{I_{o,ref}} = \left(\frac{T_{cell}}{T_{cell,ref}}\right)^3 \exp\left(\frac{E_g}{k_B T_{cell}} - \frac{E_{g,ref}}{k_B T_{cell,ref}}\right) \quad (3.63)$$

where, E_g is the material band gap energy. The material band gap energy as a function of photovoltaic cell temperature can be found using the model equation [133]:

$$\frac{E_g}{E_{g,ref}} = 1 - C(T_{cell} - T_{cell,ref}) \quad (3.64)$$

where, $E_{g,ref}$ is equal to 1.12 eV (1.794×10^{-19} J), and C is equal to 0.0002677 for crystalline silicon-based photovoltaic cells [9].

The short-circuit current $I_{PV,sc}$ and open-circuit voltage $V_{PV,oc}$ at the operating cell temperature may be determined by solving equation (3.54) at the short-circuit current and open-circuit voltage condition, given by the following two equations:

$$I_{PV,sc} = I_L - I_o \left[\exp\left(\frac{I_{PV,sc}R_s}{a}\right) - 1 \right] - \frac{I_{PV,sc}R_s}{R_{sh}} \quad (3.65)$$

$$I_L = I_{o,ref} \left[\exp\left(\frac{V_{PV,oc}}{a}\right) - 1 \right] + \frac{V_{PV,oc}}{R_{sh,ref}} \quad (3.66)$$

The maximum power point of a photovoltaic module occurs when the derivative of the power curve with respect to voltage and current is set to zero. Therefore, the ratio of the maximum power point current and voltage may be determined by the following equations [9, 21, 22]:

$$\frac{dP_{PV,mp}}{dV} = \frac{dP_{PV,mp}}{dI} = 0 \quad (3.67)$$

$$\frac{dP_{PV,mp}}{dV} = V_{PV,mp} \left(\frac{I_o}{a} \exp\left(\frac{V_{PV,mp} + I_{PV,mp}R_s}{a}\right) + \frac{1}{R_{sh}} \right) \quad (3.68)$$

$$\frac{dP_{PV,mp}}{dI} = I_{PV,mp} \left(\frac{I_o R_s}{a} \exp\left(\frac{V_{PV,mp} + I_{PV,mp}R_s}{a}\right) + \frac{R_s}{R_{sh}} + 1 \right) \quad (3.69)$$

$$\frac{I_{PV,mp}}{V_{PV,mp}} = \frac{\frac{I_o}{a} \exp\left(\frac{V_{PV,mp} + I_{PV,mp}R_s}{a}\right) + \frac{1}{R_{sh}}}{\frac{I_o R_s}{a} \exp\left(\frac{V_{PV,mp} + I_{PV,mp}R_s}{a}\right) + \frac{R_s}{R_{sh}} + 1} \quad (3.70)$$

The maximum current and voltage may also be substituted into equation (3.54). The resulting equation is given by:

$$I_{PV,mp} = I_L - I_o \left[\exp\left(\frac{V_{PV,mp} + I_{PV,mp}R_s}{a}\right) - 1 \right] - \frac{V_{PV,mp} + I_{PV,mp}R_s}{R_{sh}} \quad (3.71)$$

The numerical model will assume that the photovoltaic module operates at the maximum power point, and will determine the maximum power point current and voltage by solving equations (3.70) and (3.71). The maximum power generated by the PV module is then given by [20]:

$$P_{PV,mp} = I_{PV,mp} V_{PV,mp} \quad (3.72)$$

Note that the equivalent circuit model of the hybrid photovoltaic module (HPV) may be determined based on the equations discussed in this section. In the case of the HPV module, all PV subscripts are substituted with HPV subscripts. For example, the power output of the HPV module is given by [20]:

$$P_{HPV,mp} = I_{HPV,mp} V_{HPV,mp} \quad (3.73)$$

The total power generated by the HPV-TEG system is determined using the following equation:

$$P_{HPV-TEG,mp} = P_{HPV,mp} + P_{TEG,mp} \quad (3.74)$$

The overall energy conversion efficiency of the PV and HPV-TEG system is defined as:

$$\eta_{En,PV} = \frac{P_{PV,mp}}{G_T A_{PV}} \quad (3.75)$$

$$\eta_{En,HPV-TEG} = \frac{P_{HPV-TEG,mp}}{G_T A_{PV}} \quad (3.76)$$

3.1.7 Developed Computational Algorithm for Solving the Complex Systems of Equations

The computational algorithm used to solve all of the unknown parameters of the previously described model equations is shown in **Figure 3.4**. The developed Matlab script uses three different algorithms to solve the system of nonlinear equations. The trust-region-dogleg algorithm is first implemented, which is specifically designed to solve a system of nonlinear equations [134]. The Matlab script then implements the trust-region-reflective and Levenberg-Marquardt algorithm that both use various functions and multiple iterations to efficiently converge the solution and determine the unknown parameters [135]. The initial photovoltaic cell temperature and efficiency is assumed to be 25 °C and 9.83%, respectively, and the initial water outlet temperature is assumed to be 14 °C. New values of the water inlet temperature, photovoltaic cell temperature, and photovoltaic module efficiency are determined based on the numerically modeled equations. The new values are substituted back into the solver until the difference between the calculated parameter x_i and the calculated parameter from the previous iteration x_{i-1} have a difference of 0.00001% [113] for

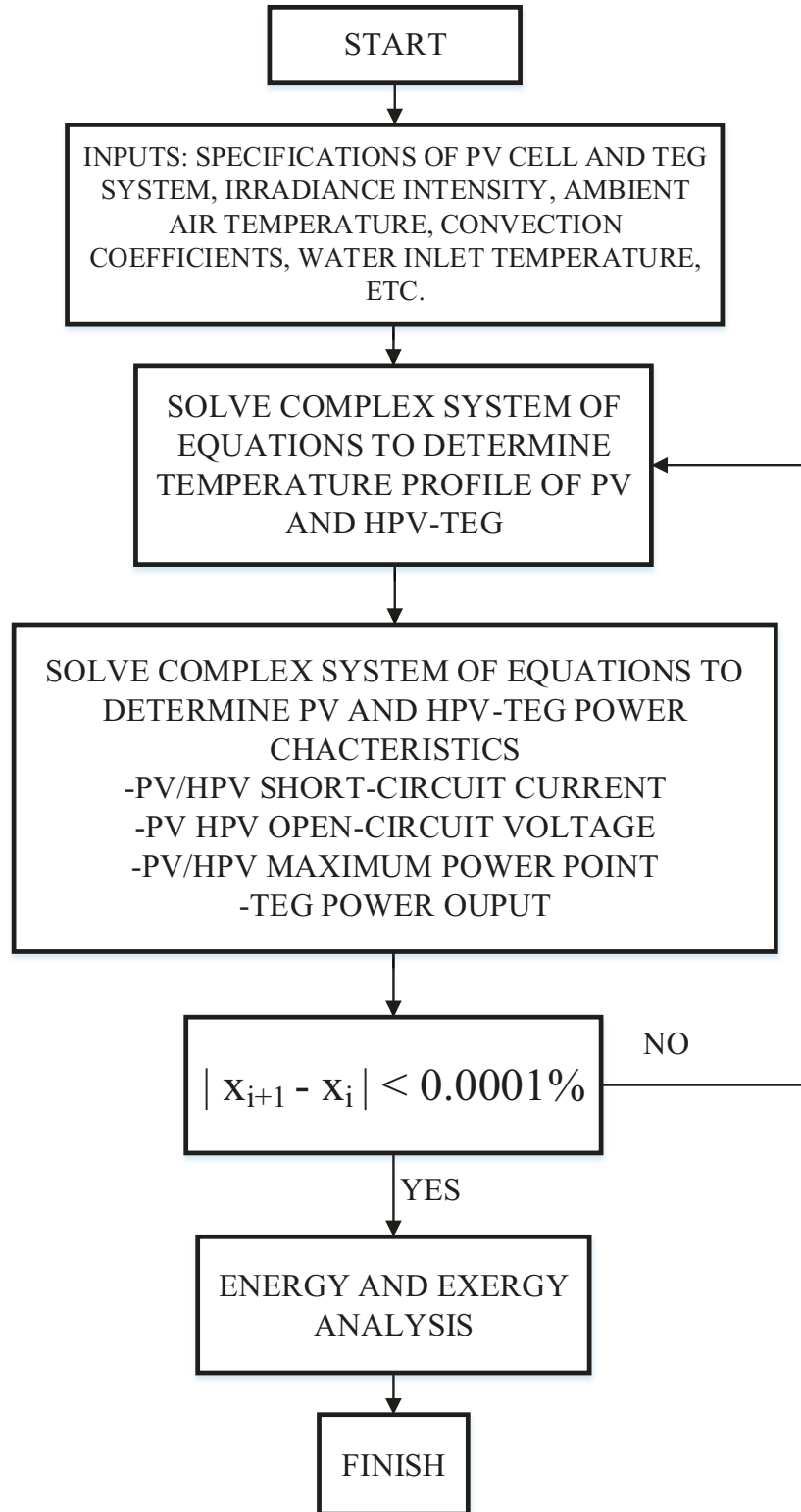


Figure 3.4: Algorithm used to solve complex system of nonlinear equations to determine temperature and performance of PV and HPV-TEG system.

each unknown variable. Once the performance and temperature characteristics of the PV and HPV-TEG are determined, exergy analysis of both systems is completed.

3.1.8 Exergy Analysis of a PV and HPV-TEG System

Energy analysis of an energy system is evaluated based on the first law of thermodynamics, also known as the conservation of energy principle, and is subject to some shortcomings. Energy analysis is a quantitative analysis that does not define the quality of the energy and may not be implemented to study the lost work of an energy system. Exergy analysis combines the first and second laws of thermodynamics to initiate qualitative analysis of the energy [33]. Exergy may be defined as the maximum amount of work a system operating at a specific state generates as it reaches equilibrium with a reference environment [33, 136]. This reference environment is known as the dead state, and is typically considered to have the same properties as the system's surrounding medium. The system is considered to be at the dead state and have zero exergy when it has the same temperature and pressure of the reference environment, and has no kinetic energy, potential energy, or chemical energy potential, with respect to the reference environment [136]. Accounting for only the thermo-mechanical potential of a working fluid, the exergy rate of a mass flow at state i may be expressed as [136]:

$$\dot{E}x_{mass,i} = \dot{m}_i \cdot ex_i \quad (3.77)$$

where, \dot{m}_i is the mass flow rate, and ex_i is the specific exergy of the working fluid at state i given by [136]:

$$ex_i = (h_i - h_0) - T_0(s_i - s_0) + \frac{V_i^2}{2} + gz_i \quad (3.78)$$

where h is specific enthalpy (J/kg), T is temperature (K), s is specific entropy (J/kg·K), V is velocity of the working fluid, g is the gravity constant, z is the elevation height of the system in reference to a specific level, and subscript 0 refers to the condition of the dead state. The rate of exergy by heat transfer is given by [136]:

$$\dot{E}x_{heat,j} = \left(1 - \frac{T_0}{T_j}\right) \dot{Q}_j \quad (3.79)$$

where, T_j is the temperature of the boundary at which heat transfer occurs. As previously

stated, exergy is defined as the useful work potential of a system. Thus, neglecting the case where the system completes boundary work to the surrounding environment, the rate of exergy transferred by work (i.e. electrical, mechanical, etc.) may be expressed as [136]:

$$\dot{E}x_{work} = \dot{W} \quad (3.80)$$

The rate exergy equation for a closed and open system is given by the following equations [136]:

$$\frac{d\dot{E}x}{dt} = \sum \left(1 - \frac{T_0}{T_j}\right) \dot{Q}_j - \left(\dot{W} - P_0 \frac{d\mathcal{V}}{dt}\right) - \dot{E}x_D \quad (3.81)$$

$$\frac{d\dot{E}x}{dt} = \sum \left(1 - \frac{T_0}{T_j}\right) \dot{Q}_j - \left(\dot{W} - P_0 \frac{d\mathcal{V}}{dt}\right) + \sum \dot{E}x_{in} - \sum \dot{E}x_{out} - \dot{E}x_D \quad (3.82)$$

where, t is time, \mathcal{V} is the volume of the system, and $\dot{E}x_D$ is the rate of exergy destruction. Under steady state operating conditions, and neglecting the change in kinetic and potential energy of the working fluid entering and exiting the system, the closed and open system exergy equations become:

$$\dot{E}x_D = \sum \left(1 - \frac{T_0}{T_j}\right) \dot{Q}_j - \dot{W} \quad (3.83)$$

$$\dot{E}x_D = \sum \left(1 - \frac{T_0}{T_j}\right) \dot{Q}_j - \dot{W} + \sum \dot{E}x_{mass,in} - \sum \dot{E}x_{mass,out} \quad (3.84)$$

Unlike energy, exergy may be destroyed. Friction, heat transfer, optical losses, mixing, and other irreversibilities caused by transport processes generate entropy. The rate of exergy destroyed is directly proportional to the rate of entropy generation \dot{S}_{gen} , and is given by [136]:

$$\dot{E}x_D = T_0 \dot{S}_{gen} \quad (3.85)$$

The rate of exergy destruction is zero for a reversible process. Since the rate of exergy destruction represents the lost work potential [136], optimization methods have been developed by analyzing the rate of exergy destruction of various components of a system. Exergy analysis allows engineers to investigate the performance of a device and determine the main components of the system where the majority of the useful work is lost. The useful

work lost from these components may be decreased by changing the material, mass flow rate, pressure, temperature distribution or by completely redesigning the component. Other optimization methodologies, such as the entropy-generation minimization (EGM) method, are used to optimize the performance of real devices that have thermodynamic imperfections [137]. The EGM method is completed by designing, modeling and varying each single physical characteristic of the system at a time to establish the minimum entropy generation rate [137]. In this research, exergy analysis will be completed based on the temperature distribution, heat transfer rates, and power output of the PV and HPV-TEG system to determine design parameters that may be changed to increase performance.

The rate of exergy from the solar radiation may be determined using the following expression [32, 33, 137, 138]:

$$\dot{E}x_{sol} = G_T A_{PV} \left(1 - \frac{T_{amb}}{T_{sun}}\right) \quad (3.86)$$

where, T_{sun} is the temperature of the Sun ($T_{sun}=5760$ K). Based on the previous discussion, the rate of exergy destruction from the PV system may be approximated as:

$$\begin{aligned} \dot{E}x_{D,PV} = & - \left(1 - \frac{T_0}{T_{gla}}\right) \dot{Q}_{top} - \left(1 - \frac{T_0}{T_{bot}}\right) \dot{Q}_{bot} - \left(1 - \frac{T_0}{T_{cell}}\right) \dot{Q}_{rad} \\ & + G_T A_{PV} \left(1 - \frac{T_{amb}}{T_{Sun}}\right) - P_{PV,mp} \end{aligned} \quad (3.87)$$

The rate of exergy destruction from the HPV-TEG system may be determined by the following equations:

$$\dot{E}x_{D,PV} = - \left(1 - \frac{T_0}{T_{gla}}\right) \dot{Q}_{top} - \left(1 - \frac{T_0}{T_{cell}}\right) \dot{Q}_{rad} + G_T A_{PV} \left(1 - \frac{T_{amb}}{T_{Sun}}\right) \quad (3.88)$$

$$+ \dot{E}x_w - P_{HPV-TEG}$$

$$\dot{E}x_w = \dot{m}_w \left((h_{w,in} - h_{w,out}) - T_0 (s_{w,in} - s_{w,out}) \right) \quad (3.89)$$

where, $\dot{E}x_w$ is the rate of exergy transferred from the HPV-TEG system to the water cooling fluid, h_w is the specific enthalpy of the water (J/kg), and s_w is the specific entropy of the water (J/kg·K). Assuming that the water remains completely saturated, the water's enthalpy and entropy as a function of the water temperature T_w (K) is estimated by following correlations [136]:

$$h_w = 4194.25T_w - 114512.99 \quad (3.90)$$

$$s_w = 14.6T_w - 4008.04 \quad (3.91)$$

The rate of electrical exergy destroyed by the PV and HPV module is determined by [33]:

$$\dot{E}x_{D,PV} = I_{PV,sc}V_{PV,oc} - P_{PV,mp} \quad (3.92)$$

$$\dot{E}x_{D,HPV} = I_{HPV,sc}V_{HPV,oc} - P_{HPV,mp} \quad (3.93)$$

The rate of exergy due to optical losses from the top surface of the PV module may be estimated by:

$$\dot{E}x_{D,opt} = G_T A_{PV} \left(1 - \frac{T_{amb}}{T_{Sun}}\right) (1 - \tau_{gla}[\beta_{cell}\alpha_{sil} + (1 - \beta_{cell})\alpha_{ted}]) \quad (3.94)$$

The rate of exergy destroyed by the TEG may be expressed as [139]:

$$\dot{E}x_{D,TEG} = \left(1 - \frac{T_{hot}}{T_0}\right) \dot{Q}_{H,TEG} - \left(1 - \frac{T_{cold}}{T_0}\right) \dot{Q}_{H,TEG} - P_{TEG,mp} \quad (3.95)$$

The exergy efficiency of the PV and HPV-TEG system is defined as the ratio of the rate of useful exergy recovered to the rate of exergy supplied [140]:

$$\eta_{\dot{E}x,PV} = \frac{P_{PV,mp}}{\dot{E}x_{sol}} \quad (3.96)$$

$$\eta_{\dot{E}x,HPV-TEG} = \frac{P_{HPV-TEG}}{\dot{E}x_{sol}} \quad (3.97)$$

3.2 Numerical Model Results and Discussion

3.2.1 Thomson Effect Analysis

The difference between the power generated by the thermoelectric generator when accounting and neglecting the Thomson effect versus irradiance intensity is shown in **Figure 3.5**. The power generated by the TEG when accounting for the Thomson effect is higher than the power generated by the TEG when neglecting the Thomson effect. This difference in TEG power generated when accounting and neglecting the Thomson effect increases nonlinearly as the irradiance intensity increases. As the amount of solar radiation increases, the TEG absorbs and discharges less thermal energy due the Thomson heat being released at the hot and cold junctions of the TEG based on equations (3.49) and (3.50). The Thomson effect has a greater influence on the performance of the TEG as the solar radiation increases, since high solar radiation intensities lead to an increase in the temperature gradient across the TEG,

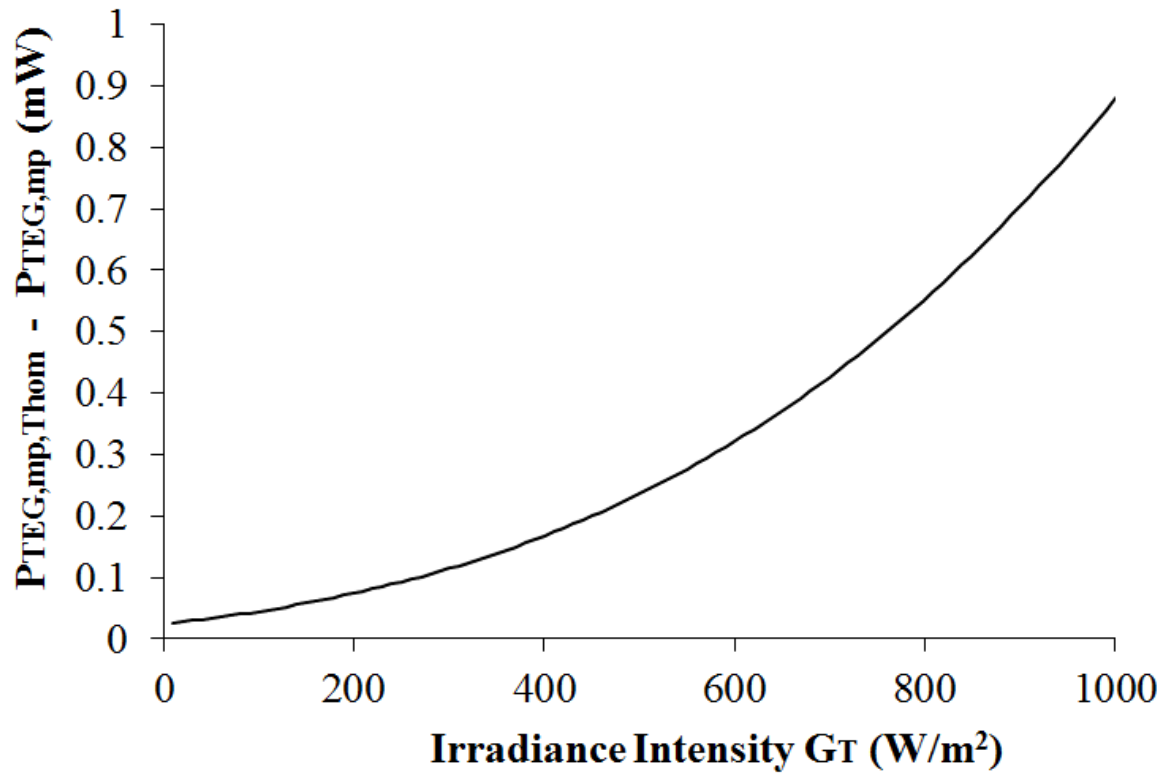


Figure 3.5: Thermoelectric power generated temperature difference between accounting and neglecting the Thomson effect vs. irradiance intensity, $T_{amb}=25$ °C, $h_{conv,top}=20$ $W/m^2\cdot K$.

which is directly proportional to the Thomson heat as indicated in equation (3.51). The additional thermal energy transferred at hot and cold junctions due to the Thomson effect increases the mean temperature of the thermoelectric generator, as shown in **Figure 3.6**. As a result, the temperature-dependent thermoelectric properties (Seebeck coefficient, thermal conductivity, electrical resistivity) of the thermoelectric generator change. As demonstrated by Yamashita and Sugihara [90], the dimensionless figure-of-merit of the n-type and p-type thermoelements used in this numerical model increase with TEG temperature, meaning the TEG's performance improves with temperature. The Thomson effect decreases the thermal energy absorbed and dissipated from the TEG, however for this particular numerical model, this performance deficiency of the Thomson effect is diminished. The increase in the mean TEG temperature improves the thermoelectric properties of the TEG, which in turn establishes a larger TEG power output than the simulation neglecting the Thomson effect.

The Thomson effect also affects the performance of the hybrid photovoltaic module. The hybrid photovoltaic cell's difference between accounting and neglecting the Thomson effect increases nonlinearly, as seen in **Figure 3.7**. The Thomson effect increases the hybrid photovoltaic cell by $0.003\text{ }^{\circ}\text{C}$ at an irradiance intensity of 1000 W/m^2 . As expected, this increase in the photovoltaic cell temperature with irradiance intensity due to the Thomson effect decreases the power output of the module nonlinearly as irradiance intensity increases, as shown in **Figure 3.8**. The power generated by the hybrid photovoltaic module decreases by 0.45 mW when accounting for the Thomson effect at an irradiance intensity of 1000 W/m^2 . This numerical study has demonstrated that the Thomson effect should be considered to improve the accuracy of the numerical model, especially if the HPV-TEG system has a high capacity and if the TEG operates under large temperature gradients. Based on the results in this section, the Thomson effect will be neglected for all of the numerical simulations. The TEG in the numerical model operates under very small temperature gradients, and thus, the Thomson effect does not significantly affect the performance and temperature distribution of the numerically modeled HPV-TEG system.

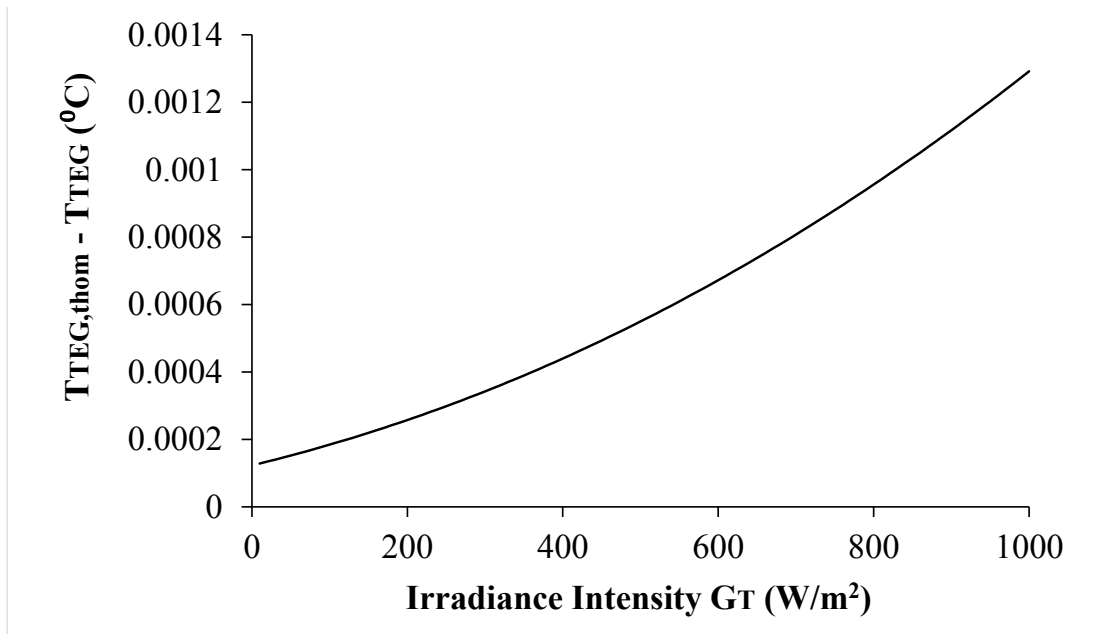


Figure 3.6: Mean thermoelectric generator temperature difference between accounting and neglecting the Thomson effect vs. irradiance intensity, $T_{amb}=25$ °C, $h_{conv,top}=20$ W/m²·K.

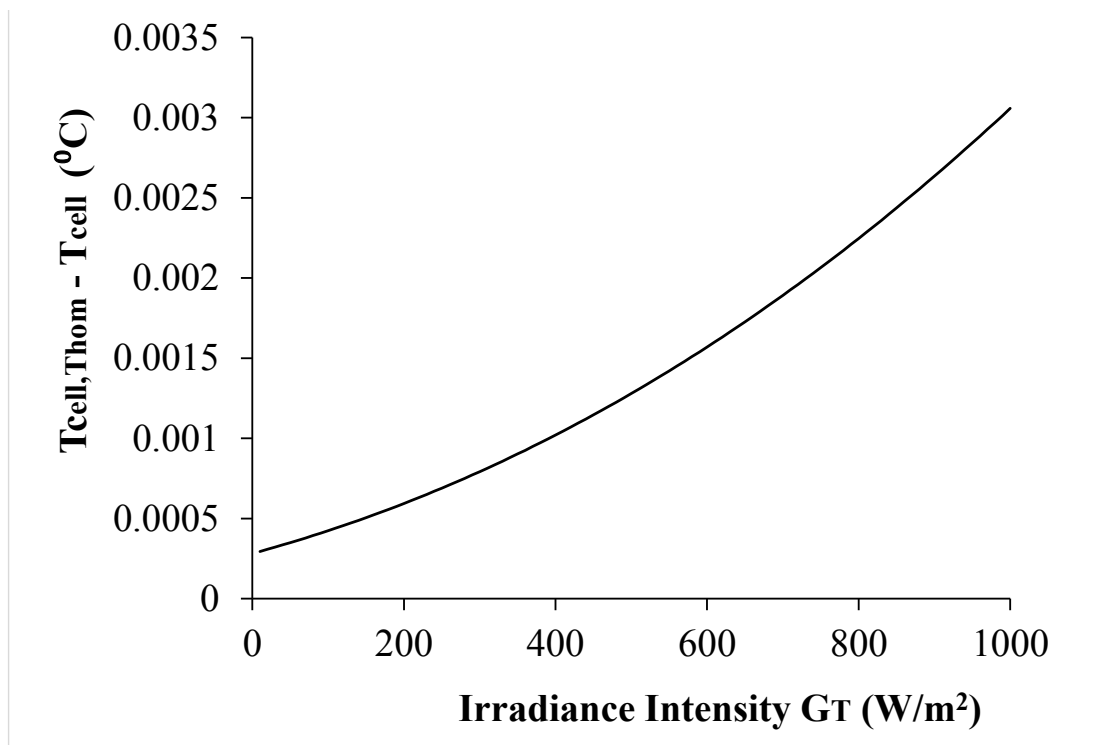


Figure 3.7: HPV-TEG photovoltaic cell temperature difference between account and neglecting the Thomson effect vs. irradiance intensity, $T_{amb}=25$ °C, $h_{conv,top}=20$ W/m²·K.

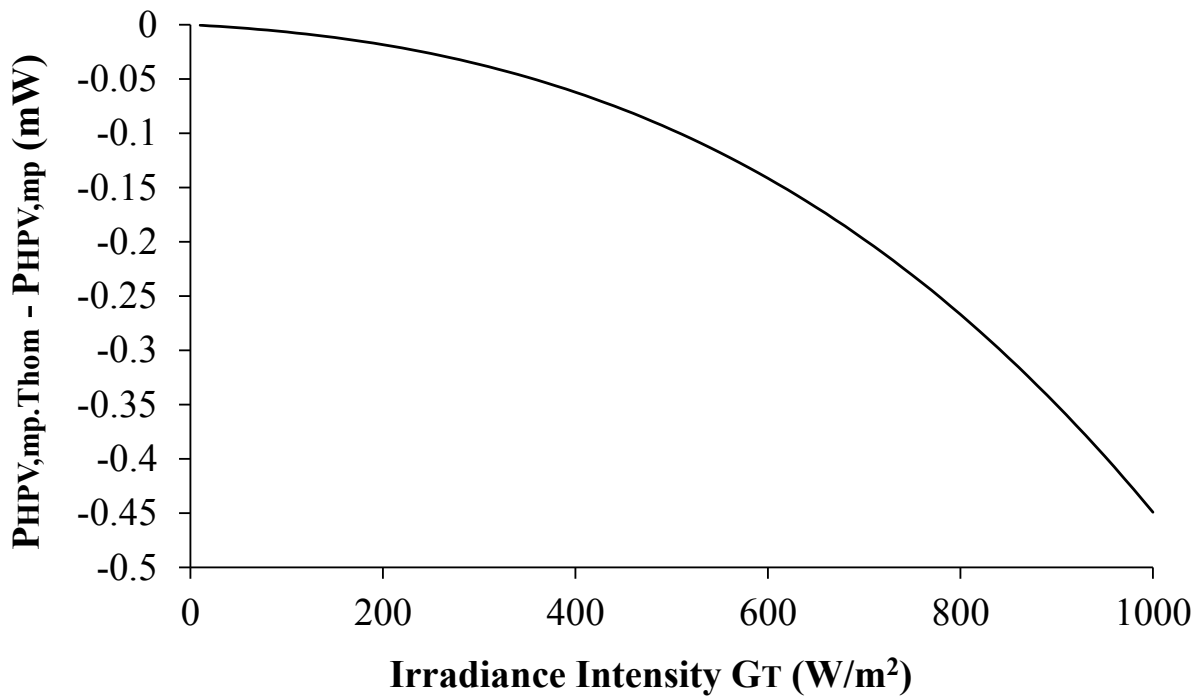


Figure 3.8: HPV-TEG photovoltaic module power output difference between account and neglecting the Thomson effect vs. irradiance intensity, $T_{amb}=25\text{ }^{\circ}\text{C}$, $h_{conv,top}=20\text{ W/m}^2\cdot\text{K}$.

3.2.2 Performance Analysis of PV and HPV-TEG

The HPV module maintains a lower temperature than the standard PV module due to the additional cooling system provided by the TEG system, as shown in **Figure 3.9**. The temperature of both photovoltaic modules increases linearly with respect to irradiance intensity. The hybrid module obtains a photovoltaic temperature 13 to 20 °C less than the standard PV module depending on the irradiance intensity. The simulated maximum power point of the conventional and hybrid photovoltaic module as a function of irradiance intensity is shown in **Figure 3.10**. The difference in power generated between the conventional and hybrid PV module increases as the incident solar radiation intensity onto both photovoltaic modules increases. This difference in power generated between the two PV modules emphasizes that maintaining a low photovoltaic cell temperature increases the power output of the PV module. The difference in photovoltaic module power generated by the two systems at an irradiance intensity of 400 W/m² and 800 W/m² is approximately 0.75 and 1.96 W, respectively. Furthermore, according to **Figure 3.10**, the HPV module produces about 31.8%, 36.8%, and 45% more electrical energy than the conventional PV module under irradiance intensity of 600, 800, and 1000 W/m², respectively. The relationship between the power generated by the PV modules and the ambient air temperature is shown in **Figure 3.11**. The power generated by each PV module decreases somewhat linearly as the ambient air temperature increases. The power generated by the PV and HPV module decreases by approximately 19.7% and 6.3% when increasing the ambient air temperature from 15 to 25 °C.

A three-dimensional representation of the HPV-TEG system's photovoltaic module temperature and thermoelectric power generated as a function of irradiance intensity (50-1000 W/m²) and ambient air temperature (10-40 °C) is shown in **Figure 3.12** and **Figure 3.13**. The temperature profile presented in **Figure 3.12** emphasizes that ambient air temperature and irradiance intensity both significantly affect the temperature of the HPV photovoltaic cell. **Figure 3.13** demonstrates that in order for the thermoelectric generator to maximize power output, the HPV-TEG system must be operated under a high irradiance intensity and ambient air temperature. The power generated from the thermoelectric generator is small, producing approximately 1.66% of the total HPV-TEG electrical power output at an ambient air temperature of 25 °C, irradiance intensity of 900 W/m², and top

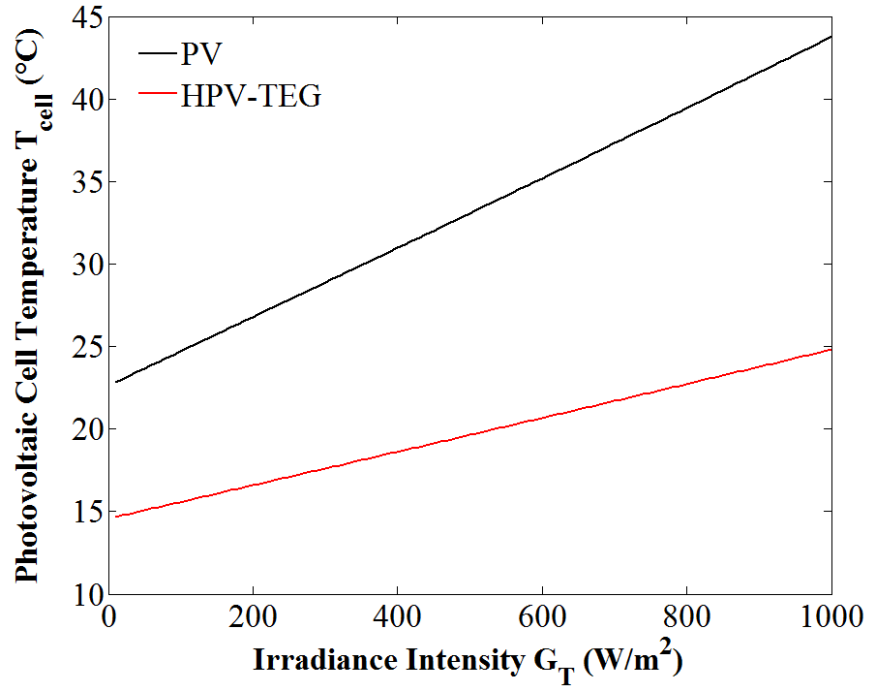


Figure 3.9: Photovoltaic cell temperature of PV and HPV-TEG photovoltaic module vs. irradiance intensity, $T_{amb}=25\text{ }^{\circ}\text{C}$, $h_{conv,top}=20\text{ W/m}^2\cdot\text{K}$.

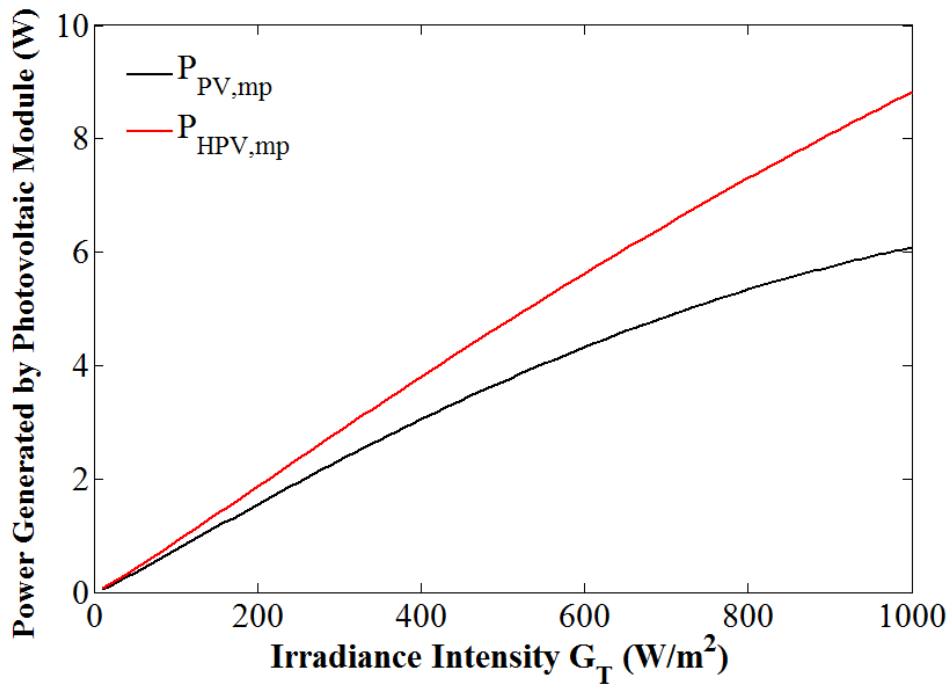


Figure 3.10: Power generated by PV and HPV-TEG photovoltaic module vs. irradiance intensity, $T_{amb}=25\text{ }^{\circ}\text{C}$, $h_{conv,top}=20\text{ W/m}^2\cdot\text{K}$.

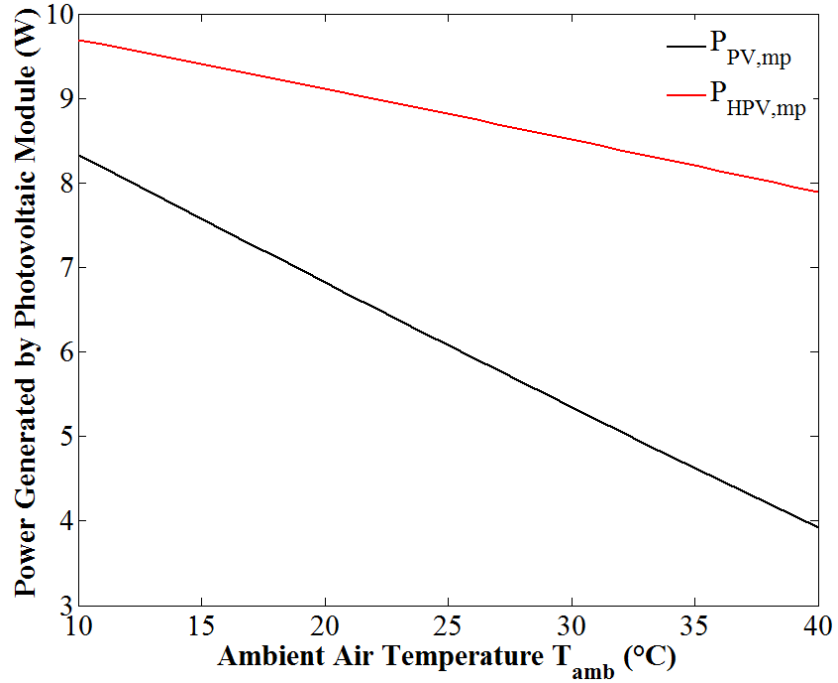


Figure 3.11: Power generated by PV and HPV-TEG photovoltaic module vs. ambient air temperature, $G_T=1000 \text{ W/m}^2$, $h_{conv,top}=20 \text{ W/m}^2\cdot\text{K}$.

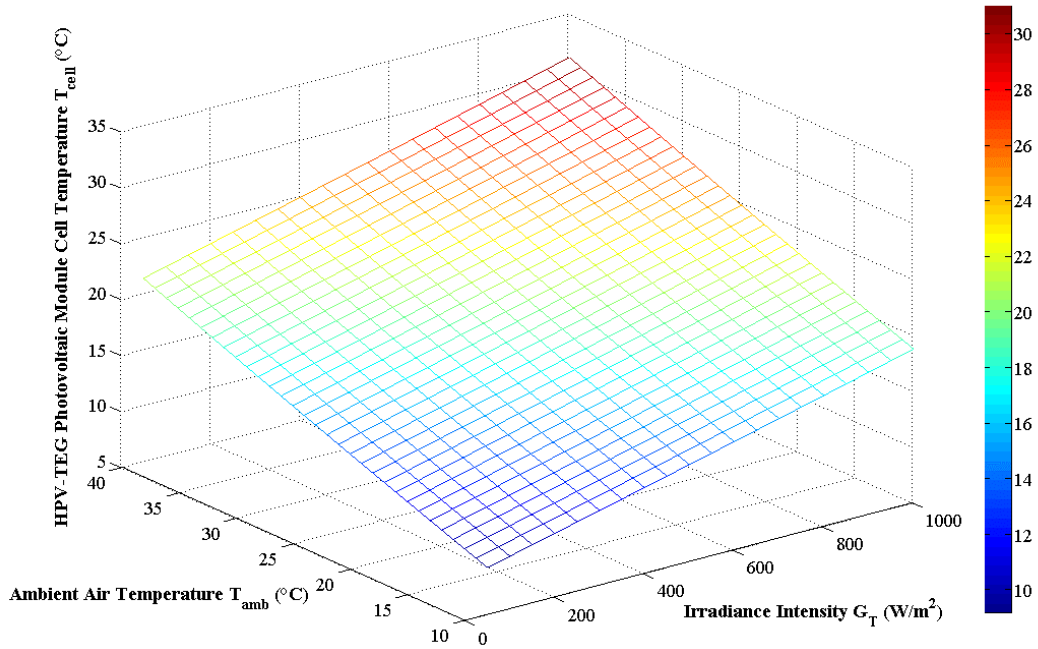


Figure 3.12: HPV-TEG photovoltaic cell temperature vs. irradiance intensity vs. ambient air temperature, $h_{conv,top}=20 \text{ W/m}^2\cdot\text{K}$.

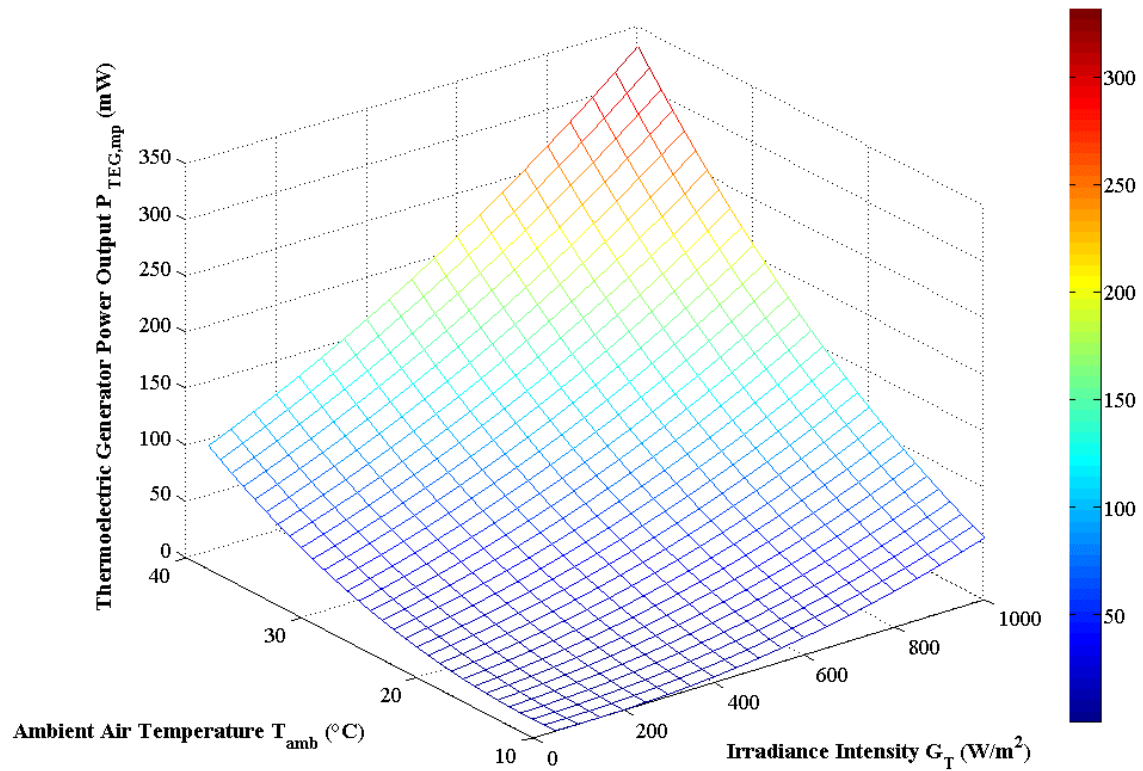


Figure 3.13: Power generated by thermoelectric generator vs. irradiance intensity vs. ambient air temperature, $h_{conv,top}=20 W/m^2 \cdot K$.

convective coefficient of $20 \text{ W/m}^2\cdot\text{K}$. The results of the performance study has shown that the advantageous characteristics of the HPV-TEG system may be exploited while operating under high irradiance intensities and ambient air temperatures.

3.2.3 Energy and Exergy Analyses of HPV-TEG System

Figure 3.14 shows the parametric study of the energy and exergy efficiency of the PV and HPV-TEG system versus irradiance intensity. Similar energy and exergy profiles as a function of irradiance intensity have been developed in literature [24, 31, 32, 141], suggesting that the developed mathematical model in this study was accurately simulated. It may be observed from this figure that an optimal irradiance intensity exists that establishes the maximum energy conversion and exergy efficiency for the PV and HPV-TEG. For the PV system, the maximum energy and exergy efficiency of 7.9% and 8.3% occurs at an irradiance intensity of 250 W/m^2 . The maximum energy and exergy efficiencies of the HPV-TEG system are approximately 9.7% and 10.3% and occurs at an irradiance intensity of 400 W/m^2 . Increasing the optimal irradiance intensity to 900 W/m^2 decreases the energy and exergy conversion efficiencies of the PV system by approximately 1.4% and 1.5%, while the HPV-TEG system's energy and exergy efficiencies decreases by about 0.53%. Further analysis of the energy and exergy efficiencies of the PV and HPV-TEG versus the ambient air temperature is presented in **Figure 3.15**. The energy and exergy efficiencies of both systems decreases linearly with ambient air temperature. Increasing the ambient air temperature from $10 \text{ }^\circ\text{C}$ to $20 \text{ }^\circ\text{C}$ decreases the energy and exergy efficiencies of the PV system by about 1.5% and 1.6%, and HPV-TEG system's energy and exergy efficiencies decreases by about 0.6% and 0.54%. The overall efficiency of the PV and HPV-TEG may be improved upon by minimizing the ambient air temperature at a constant irradiance intensity of 1000 W/m^2 . However, a closer look at the thermoelectric generator's efficiency, as shown in **Figure 3.16**, suggests that a high ambient air temperature is beneficial for the performance of the TEG. As suggested by various researchers [81, 108, 110, 113, 115], the thermoelectric generator's efficiency increases as the temperature differential increases, whether it is by increasing the ambient air temperature or irradiance intensity.

The simulated energy and exergy efficiency of the PV and HPV-TEG system versus the top convection coefficient is shown in **Figure 3.17**. The exergy and energy conversion

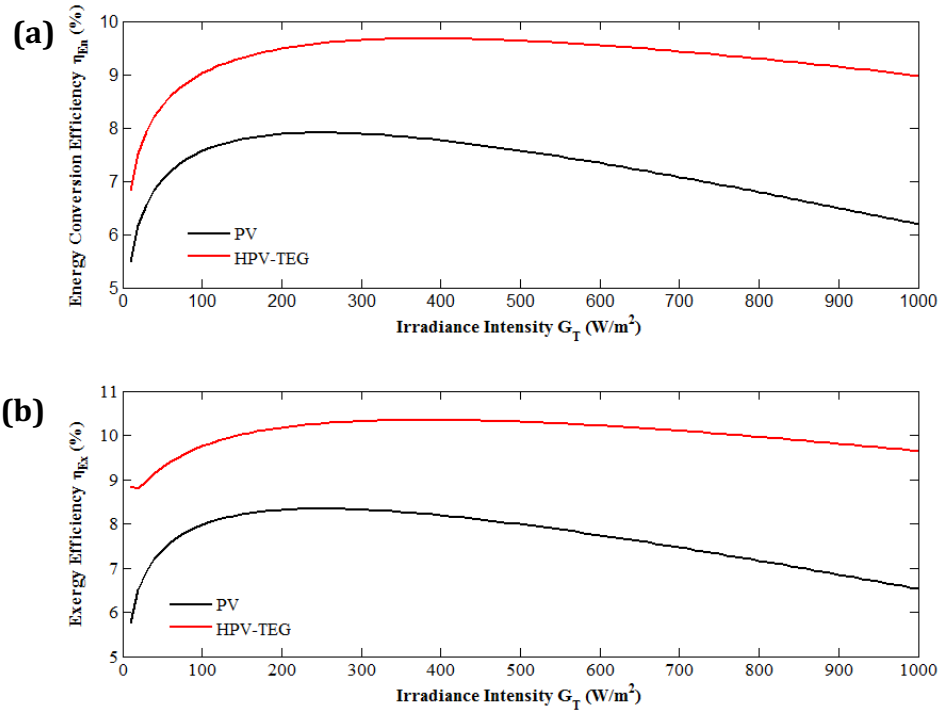


Figure 3.14: (a) Energy conversion efficiency and (b) exergy efficiency of PV and HPV-TEG system vs. irradiance intensity, $T_{amb}=25\text{ }^{\circ}\text{C}$, $h_{conv,top} = 20\text{ W/m}^2\cdot\text{K}$.

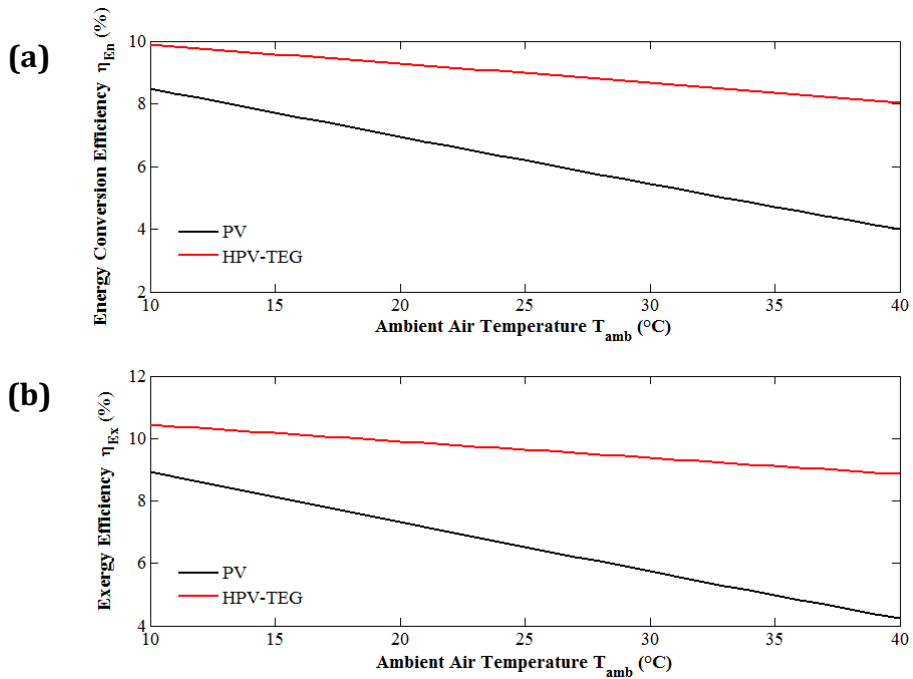


Figure 3.15: (a) Energy conversion efficiency and (b) exergy efficiency of PV and HPV-TEG system vs. ambient air temperature, $G_T=1000\text{ W/m}^2$, $h_{conv,top} = 10\text{ W/m}^2\cdot\text{K}$.

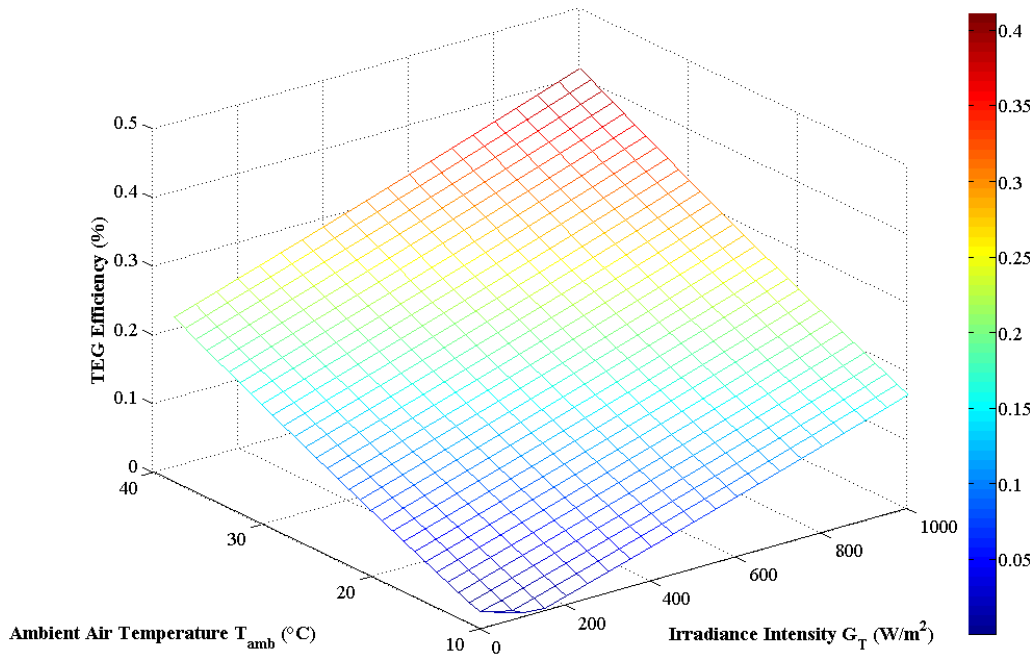


Figure 3.16: Energy conversion efficiency of thermoelectric generator vs. ambient air temperature vs. irradiance intensity, $h_{conv,top} = 20 \text{ W/m}^2\cdot\text{K}$.

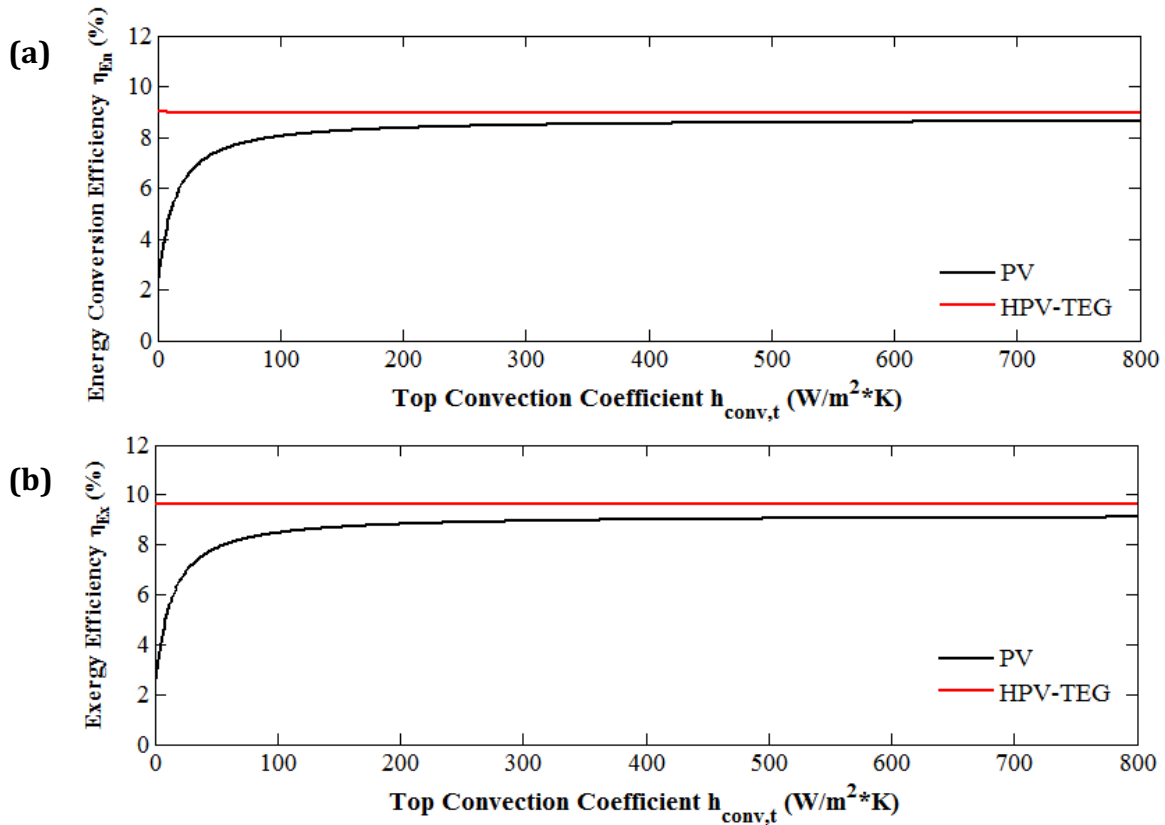


Figure 3.17: (a) Energy conversion efficiency and (b) exergy efficiency of PV and HPV-TEG system vs. ambient air temperature, $G_T = 1000 \text{ W/m}^2$, $T_{amb} = 25 \text{ }^\circ\text{C}$.

efficiency of the PV system increases asymptotically as the top convection coefficient increases. As the top convection coefficient increases, the rate of thermal energy extracted from the top surface of the standard PV module increases, reducing the photovoltaic cell temperature and improving the system's performance. The energy and exergy efficiency of the HPV-TEG system remains constant at approximately 9% and 9.6%. The majority of the thermal energy from the HPV-TEG system is transferred efficiently through the thermoelectric generator to the cooling fluid. As a result, increasing the top convection coefficient does not significantly increase the rate of thermal energy dissipated and the performance of the HPV-TEG system.

HPV-TEG systems establish a greater energy conversion and exergy efficiency than the conventional PV module within the studied range of ambient air temperatures and irradiance intensities. Therefore, the mathematical model has provided strong evidence that the HPV-TEG is able to convert a greater portion of the input energy and exergy into useful work (electricity). However, it is important to mention that the HPV-TEG would not have a superior energy and exergy efficiency if the cooling system was not efficiently removing thermal energy from the system. Such a case may occur if the irradiance intensity is low, ambient air temperature is low, or if the water inlet temperature is high. As shown in **Figure 3.18**, numerically simulating a constant ambient air temperature of 5 °C allows the PV system to obtain a higher energy and exergy efficiency than the HPV-TEG system while operating at an irradiance intensities less than 450 W/m². The combination of a low irradiance intensity, and the water inlet temperature being higher than the ambient air temperature causes the HPV-TEG system to have a higher photovoltaic cell temperature and a lower power output than the conventional PV module. Thus, the operating conditions, such as the available water inlet temperature, and the annual irradiance intensity and ambient air temperature distribution play an important role in determining the feasibility of a HPV-TEG system.

The effect of the irradiance intensity and ambient air temperature on the rate of exergy destruction of the HPV-TEG system is shown in **Figure 3.19**. The figure demonstrates that the rate of exergy destruction of the HPV-TEG system is strongly dependent on the irradiance intensity, and changes minimally when the ambient air temperature increases. Further analysis of the rate of exergy destruction due to the optimal and electrical

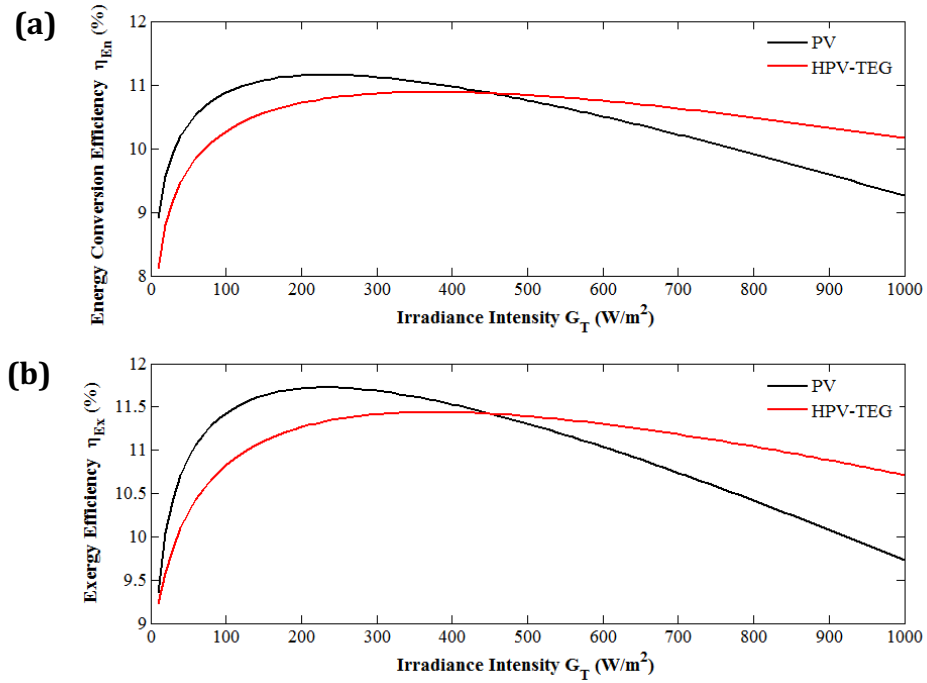


Figure 3.18: (a) Energy conversion efficiency and (b) exergy efficiency of PV and HPV-TEG system vs. irradiance intensity, $T_{amb}=5\text{ }^{\circ}\text{C}$, $h_{conv,top} = 20\text{ W/m}^2\cdot\text{K}$.

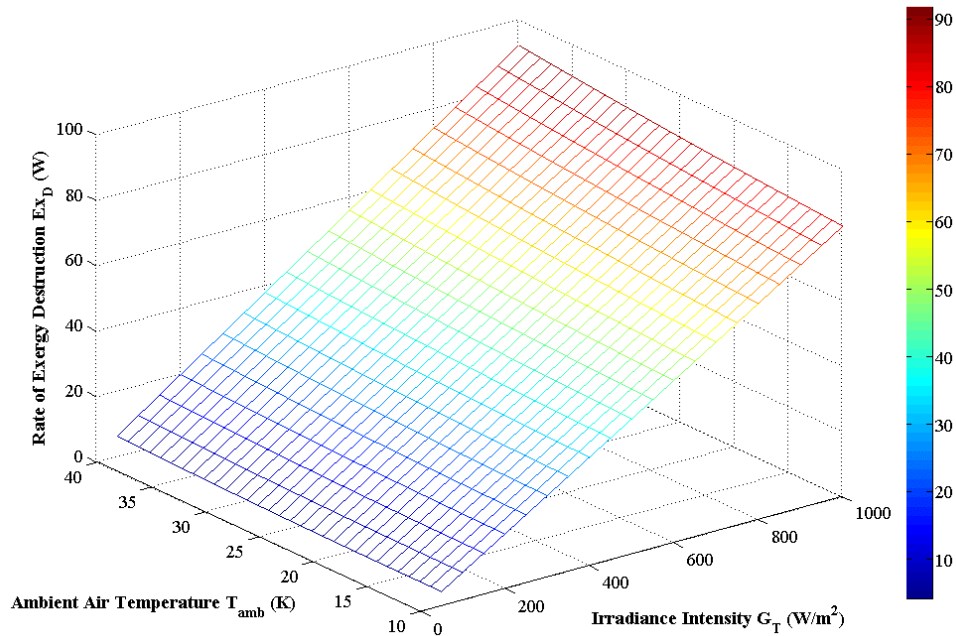


Figure 3.19: Rate of exergy destruction by HPV-TEG system vs. irradiance intensity vs. ambient air temperature, $h_{conv,top}=20\text{ W/m}^2\cdot\text{K}$.

characteristics of the hybrid photovoltaic module versus irradiance intensity is shown in **Figure 3.20**. Furthermore, the rate of exergy destruction by the thermoelectric generator versus irradiance intensity is shown in **Figure 3.21**. Based on **Figure 3.20** and **Figure 3.21**, the rate of exergy destroyed due to optical losses from the top surface of the HPV-TEG module, electrical characteristics of the HPV module, and the thermoelectric generator, accounts for approximately 72.7%, 6.6%, and 0.2% of the total rate of exergy destroyed at an irradiance intensity of 1000 W/m^2 . Exergy analysis has provided strong evidence that optimization efforts should concentrate primarily on improving the optical properties of the top surface of the hybrid photovoltaic module. Increasing the transmittance of the glass layer and the absorptance of the silicon and tedlar material would dramatically reduce the rate of exergy destruction and improve the overall performance of the HPV-TEG system. The numerical model has investigated several variables that influence the performance of a HPV-TEG system. The chapter four will utilize the knowledge gained by the numerical simulation results to manufacture, test, and study the performance of various HPV-TEG systems.

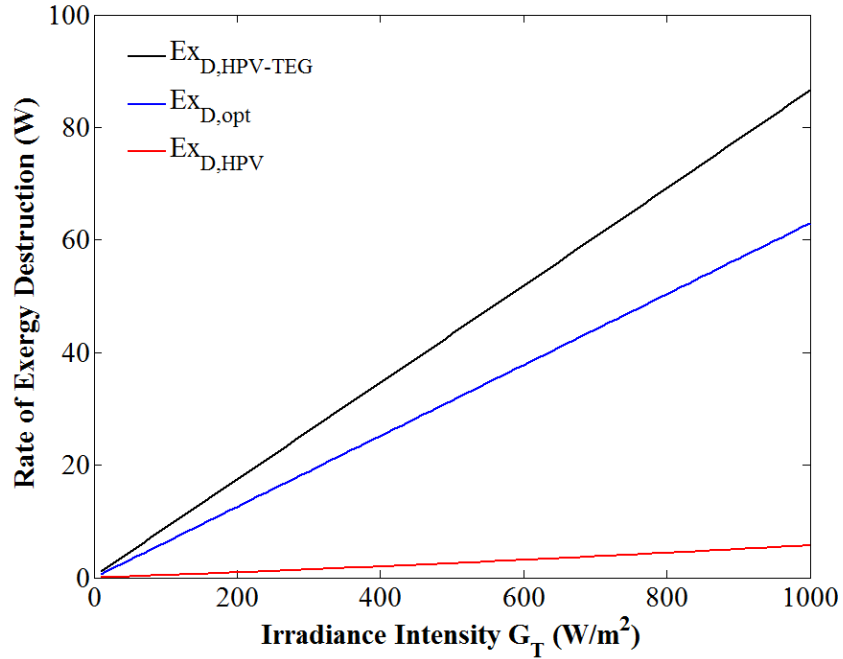


Figure 3.20: Rate of exergy destruction by HPV-TEG system due to various components vs. irradiance intensity, $T_{amb}=25\text{ }^{\circ}\text{C}$, $h_{conv,top}=20\text{ W}/m^2\cdot\text{K}$.

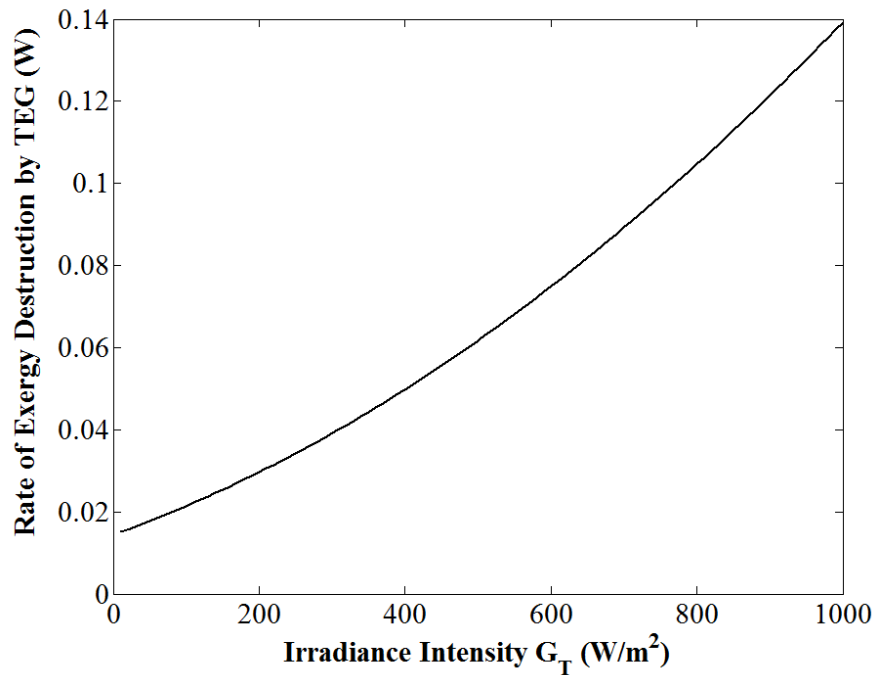


Figure 3.21: Rate of exergy destruction by thermoelectric generator vs. irradiance intensity, $T_{amb}=25\text{ }^{\circ}\text{C}$, $h_{conv,top}=20\text{ W}/m^2\cdot\text{K}$.

Chapter 4: Experimental Work

Previous analysis and discussion in chapters two and three have provided a greater understanding of the factors that impede and improve the performance of a hybrid photovoltaic-thermoelectric power generation system. This major chapter focuses on the indoor and outdoor experimental characterization of various HPV-TEG modules and directly compares their performance with conventional photovoltaic modules. HPV-TEG modules, the indoor solar simulator, and the outdoor experimental test setups were designed using Autodesk Inventor Professional 3D CAD software prior to completing experimental simulations. The HPV-TEG modules use water as a cooling fluid to efficiently remove thermal energy from the hybrid system's photovoltaic module. In the first section of this chapter, the effect of the number of thermoelectric modules, the irradiance intensity, and the water inlet temperature on the temperature distribution and performance of the HPV-TEG modules will be investigated using an indoor solar simulator. In the second section, a series of 12 outdoor tests is implemented to determine the feasibility of various HPV-TEG systems under a variety of weather and operating conditions.

4.1 Fabrication and Instrumentation of Hybrid Photovoltaic Modules

In this research, three fully-instrumented hybrid photovoltaic-thermoelectric power generation (HPV-TEG) modules were designed and manufactured. Additionally, each HPV-TEG module's performance will be compared with its corresponding unaltered conventional photovoltaic module's performance. The composition of the three HPV-TEG case studies are presented in **Table 4.1**. Further information regarding the specifications of the two PV models used in the construction of the HPV-TEG modules are shown in **Table 4.2**. For each hybrid photovoltaic module, a specific number of thermoelectric modules are coupled to a 0.635 mm thick aluminum layer that is placed on the back surface of the hybrid photovoltaic module. As will be analyzed and discussed in detail in section 4.2, the aluminum layer may be removed to study its effect on the performance of the HPV-TEG module. The thermoelectric modules are comprised of bismuth telluride compounds, and have a cross-sectional area of 56 mm x 56 mm. A T-type thermocouple is directly mounted to the hot side temperature of a thermoelectric module. An aluminum water cooling block is attached to

Table 4.1: Specifications of experimental test setup PV/HPV-TEG modules.

Case Study	Photovoltaic Module Type	Number of Thermoelectric Modules
10W-PV	HESPV 10 Watt	0
10W-HPV-2TEG	HESPV 10 Watt	2
10W-HPV-4TEG	HESPV 10 Watt	4
40W-PV	Coleman 40 Watt	0
40W-HPV-10TEG	Coleman 40 Watt	10
40W-CHPV-10TEG	Coleman 40 Watt	10

Table 4.2: Specifications of experimental test setup photovoltaic modules.

Photovoltaic Module	HESPV 10 Watt	Coleman 40 Watt
PV Type	Monocrystalline	Monocrystalline
Model	HES-10	#51840
$V_{PV,oc,ref}$ (V)	19.8	21.5
$I_{PV,sc,ref}$ (A)	0.72	2.3
$P_{PV,mp,ref}$ (W)	10	40
A_{PV} (m ²)	0.098172	0.2625

the other side of each thermoelectric module to remove the thermal energy from the HPV-TEG system, as shown in **Figure 4.1**. Each thermoelectric module is covered with a graphite layer to create an excellent contact with the aluminum and water cooling block. The high thermal conductivity of the graphite layer allows thermal energy to be uniformly absorbed and dissipated from each thermoelectric module. The entire hybrid module is insulated using rigid foam insulation to ensure that all the heat is transferred through the thermoelectric generator, as depicted in **Figure 4.2**. The thermoelectric modules are connected in series to create the HPV-TEG module's thermoelectric generator. The aluminum water cooling blocks are also connected in series.

4.2 Indoor Solar Simulation Tests

4.2.1 Indoor Experimental Solar Simulator Test Setup and Methodology

The schematic diagram of the indoor experimental test setup is shown in **Figure 4.3**. The test setup mainly consists of a solar simulator, HPV-TEG module/ PV module, electrical loads, data acquisition unit, and a cooling system. As shown in **Figure 4.4**, 8 500-watt tungsten halogen lamps arranged in a 4 x 2 matrix were used to simulate solar radiation. The solar radiation intensity was measured using an Onset silicon pyranometer positioned parallel to the photovoltaic module plane. The irradiance intensity may be varied by illuminating particular lamps and by changing the height of the solar simulator platform. Water is supplied at a known temperature and flow rate to the HPV-TEG system. The inlet and outlet temperature of the water is determined using T-type thermocouple probes TR1 and TR2. Real-time water inlet and outlet temperature measurements are recorded every 10 seconds during each experimental simulation to ensure that the water inlet temperature does not vary by more than 5%. Real-time measurements of the hot side temperature thermocouple TR3 are also recorded every 10 seconds. A variable area rotameter FL1 is used to control the volumetric flow rate of the water. A variable resistance load, also known as a rheostat, is connected to the photovoltaic modules and thermoelectric generator. Thermal profiles of the photovoltaic modules are recorded using a FLIR E4 infrared camera at an emissivity of 0.88 [113]. Steady state operation occurs when the hybrid system's photovoltaic module power at a constant electrical load resistance and TEG open-circuit voltage does not deviate by more than 0.1% after 5 minutes. Once the system reaches steady

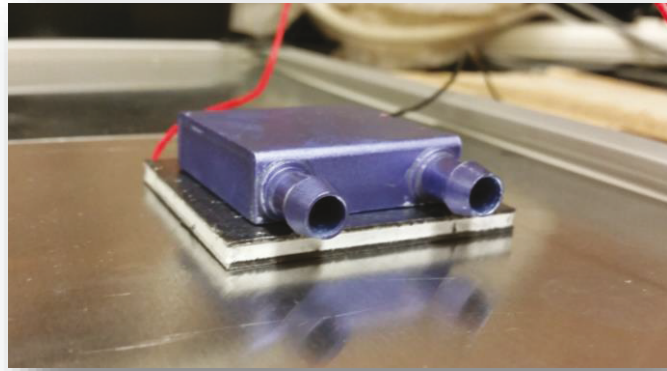


Figure 4.1: Back surface of hybrid photovoltaic module with aluminum sheet, thermoelectric generator, and aluminum cooling block.

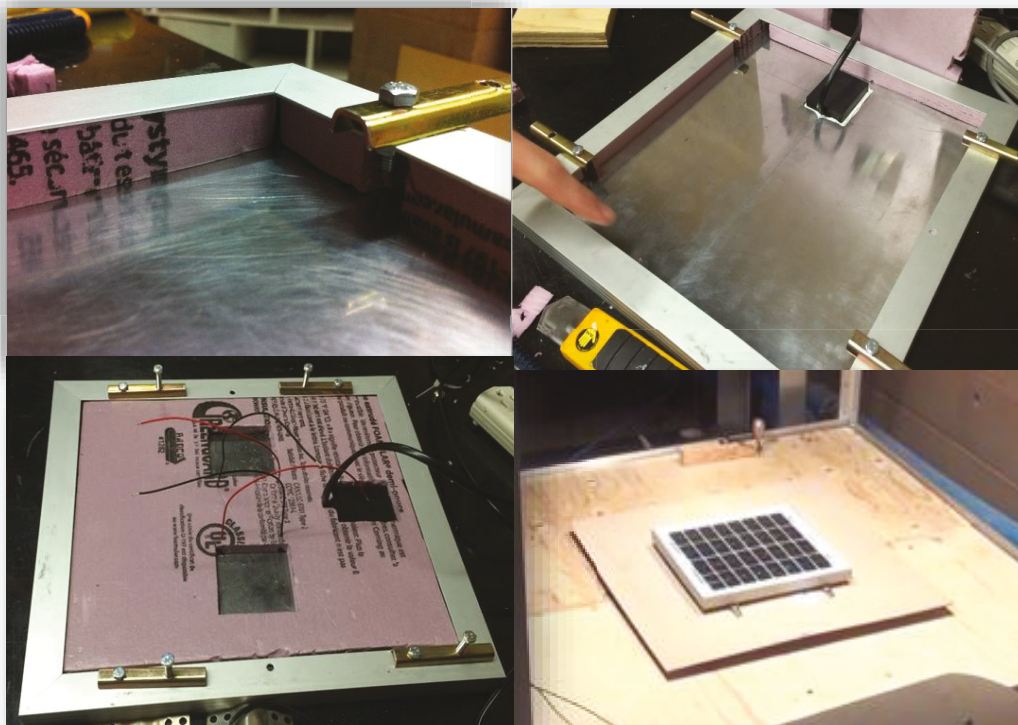


Figure 4.2: Photographs showing fabrication of 10W-HPV-2TEG module.

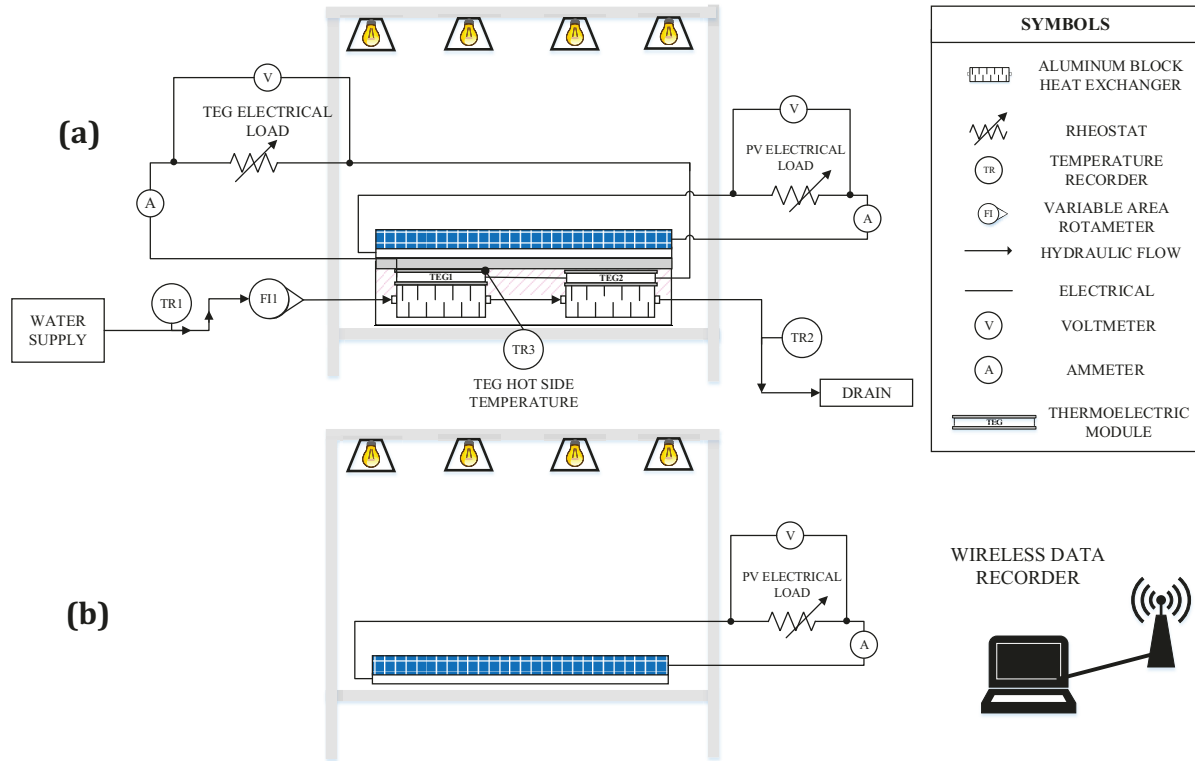


Figure 4.3: The indoor experimental test setup for (a) hybrid photovoltaic system (b) conventional photovoltaic system used in this investigation.



Figure 4.4: A photograph showing the indoor experimental simulation of 40W-HPV-10TEG module using solar simulator used in this investigation.

state, the power curves of each electrical device may be determined by incrementally increasing the load resistance connected to the PV module and TEG, and by measuring the resultant voltage and current.

4.2.2 Results and Discussion: Indoor Experimental Tests

Benchmark experimental simulations demonstrating the effect of the aluminum layer on the performance of the 10W-HPV-2TEG system were performed to determine whether the aluminum was improving or degrading the hybrid system's performance. As seen in **Figure 4.5**, both systems' back surface temperature reached a steady state operating condition in approximately 90 minutes. It was consistently observed that for each indoor test the PV/HPV-TEG system reached steady state operation in approximately 90 minutes. The HPV-TEG-2TEG system with the aluminum layer was approximately 10.7 °C cooler than the HPV-TEG-2TEG system without the aluminum layer. The thermal profiles shown in **Figure 4.6** revealed that the addition of the aluminum layer decreases the overall temperature profile of the hybrid system's PV module. The power curves of the hybrid system's PV module and thermoelectric generator are shown in **Figure 4.7** and **Figure 4.8**. Based on the experimental results, incorporating the aluminum layer into the design of the 10-HPW-2TEG system increases the maximum power output of the PV module and thermoelectric generator by approximately 6.9% and 350%. The aluminum layer in this particular design increases the heat transfer rate from the photovoltaic module to the thermoelectric generator, reducing the temperature of the photovoltaic cells, and increasing the temperature gradient across the thermoelectric modules. While the thermal resistance of the HPV-TEG system is increased with the addition of the aluminum layer, the aluminum layer acts as a heat sink when installed, increasing the heat transfer rate 2-dimensionally to the thermoelectric generator's hot side junction. One can conclude that the overall performance and thermal stability of a hybrid photovoltaic-thermoelectric generator improves significantly with the addition of the aluminum layer, thus the aluminum layer will be incorporated into the design of all the HPV-TEG modules.

Figure 4.9 shows the steady state temperature distribution of the 10W-PV, 10W-HPV-2TEG and 10W-HPV-4TEG modules under the same operating conditions. It was observed that the HPV-TEG module with more thermoelectric modules (10W-HPV-4TEG)

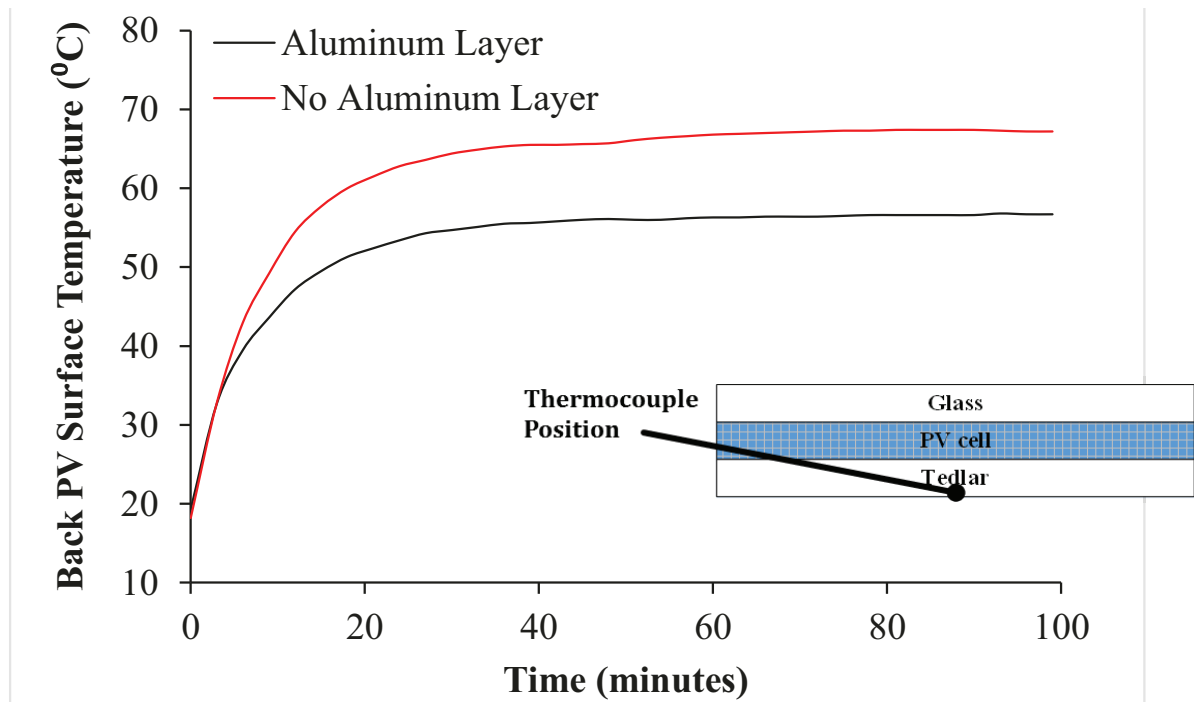


Figure 4.5: Back photovoltaic module temperature vs. time for 10W-HPV-2TEG system with and without aluminum layer, $G_T=825 \text{ W/m}^2$, $T_{w,in}=14 \text{ }^\circ\text{C}$, $\dot{V}=1 \text{ L/min}$.

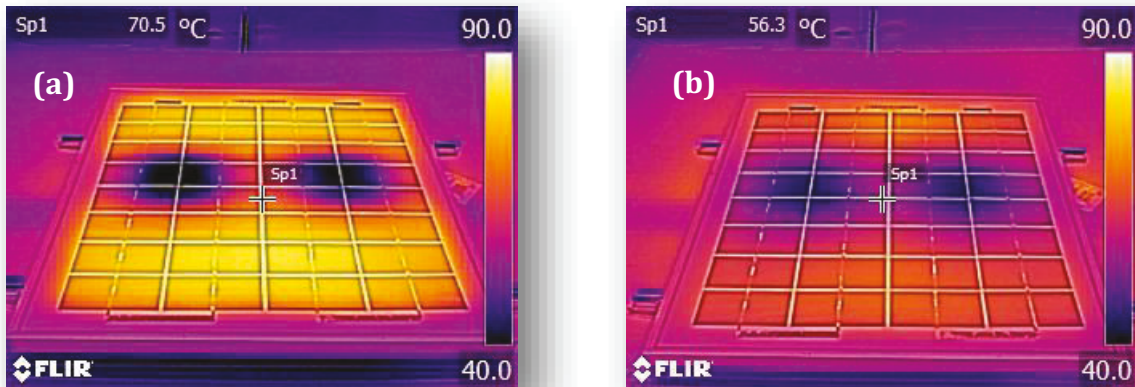


Figure 4.6: Thermal profiles of 10W-HPV-2TEG module (a) without aluminum (b) with aluminum, $G_T=825 \text{ W/m}^2$, $T_{w,in}=14 \text{ }^\circ\text{C}$, $\dot{V}=1 \text{ L/min}$.

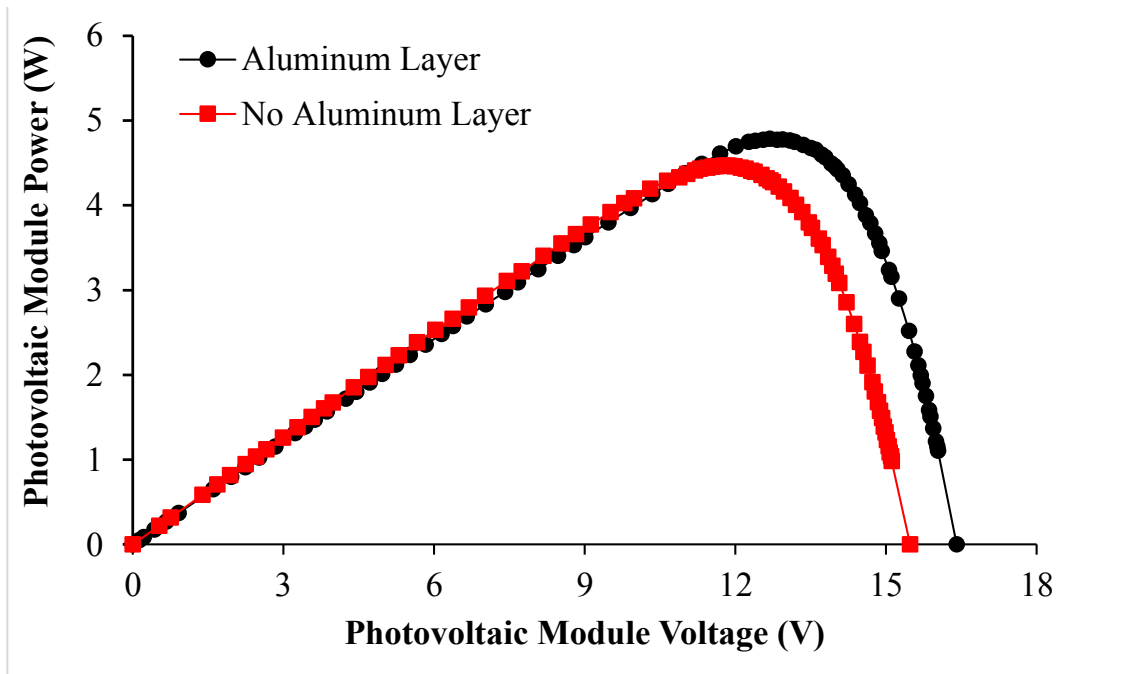


Figure 4.7: 10W-HPV(-2TEG) module power vs. voltage with and without aluminum layer, $G_T=825 \text{ W/m}^2$, $T_{w,in}=13.75 \text{ }^\circ\text{C}$, $\dot{V}=1 \text{ L/min}$.

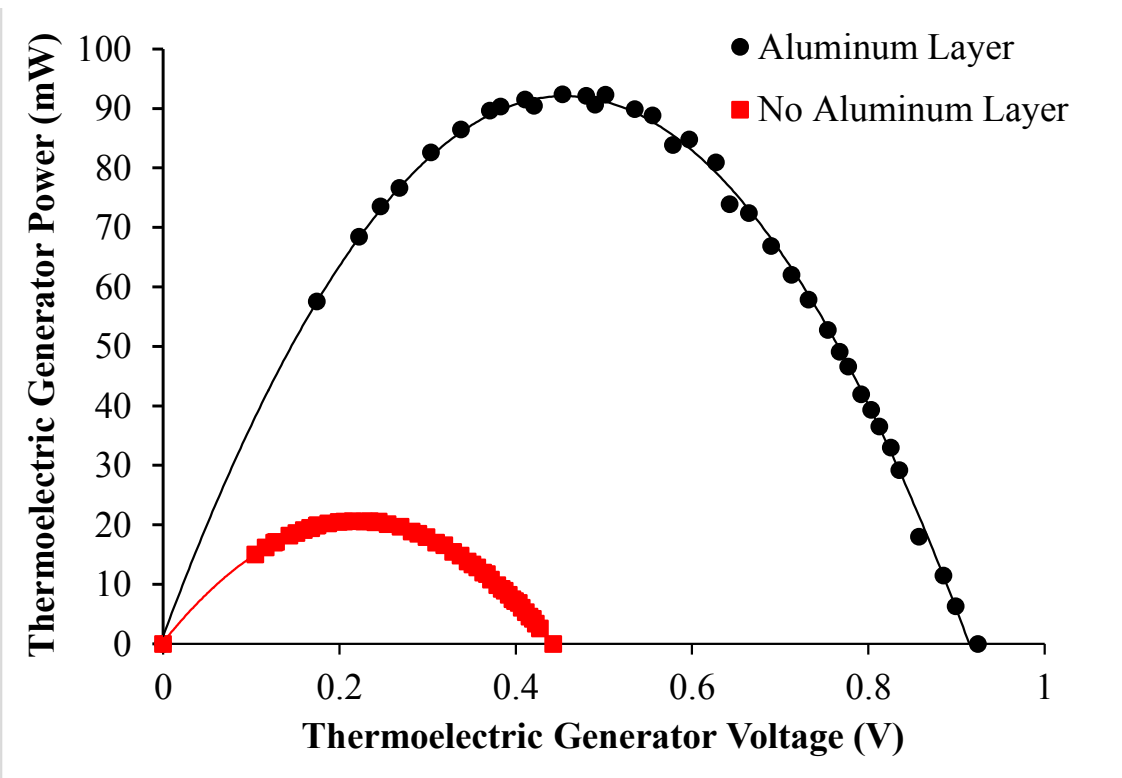


Figure 4.8: 2TEG power vs. voltage with and without aluminum layer, $G_T=825 \text{ W/m}^2$, $T_{w,in}=13.75 \text{ }^\circ\text{C}$, $\dot{V}=1 \text{ L/min}$.

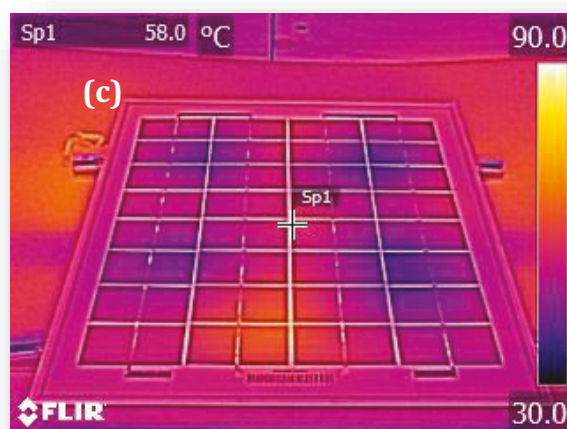
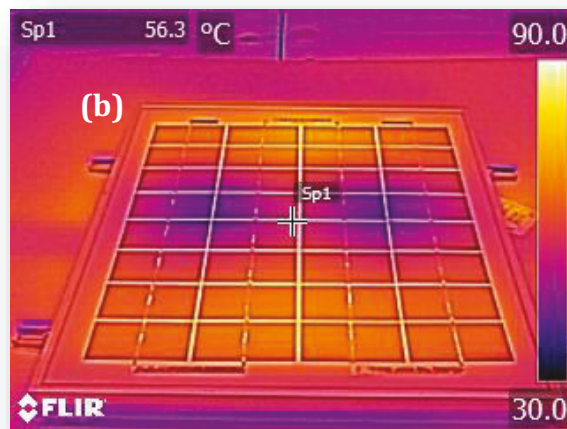
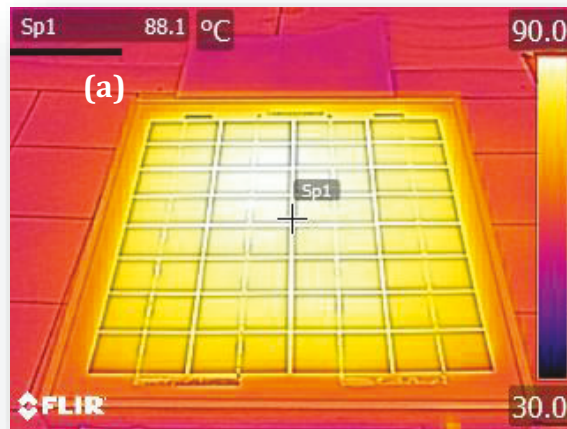


Figure 4.9: Thermal profiles of (a) 10W-PV (b) 10W-HPV-2TEG and (c) 10W-HPV-4TEG system, $G_T=825 \text{ W/m}^2$, $T_{w,in}=11 \text{ }^\circ\text{C}$, $\dot{V}=1 \text{ L/min}$.

provides a lower and more uniform thermal profile. Increasing the number of thermoelectric modules from two to four reduces the overall photovoltaic module temperature, and simultaneously increases the hybrid system's photovoltaic module from ~ 4.5 W to ~ 4.91 W, as shown in **Figure 4.10**. It may be observed in **Figure 4.11** that increasing the number of thermoelectric modules also increases the maximum power produced by the hybrid system's thermoelectric generator by approximately 23.5%. Therefore, this study has indicated that the number of thermoelectric modules in a HPV-TEG system significantly effects the system's electrical power output.

The effect of solar radiation intensity on the maximum power output of the hybrid system's photovoltaic module, hybrid system's thermoelectric generator, and the conventional photovoltaic module was investigated, as shown in **Figure 4.12** and **Figure 4.13**. In both figures, the power output of all of the electrical components appears to increase linearly with irradiance intensity. Further analysis of **Figure 4.12** shows that the hybrid system's PV module power remains approximately 0.5 W higher than the standard PV module. Increasing irradiance intensity from 500 W/m^2 to 825 W/m^2 increases the hybrid 10W-HPV(-2TEG) module power by 58.4%, the standard 10W-PV power by 63.8%, and the 2TEG power by 124.5%. Furthermore, as seen in **Figure 4.13**, increasing the irradiance intensity from 425 W/m^2 to 750 W/m^2 increases the hybrid 40W-HPV(-10TEG) module power by 76.3%, the standard 40W-PV power by 62.7%, and the 10TEG power by 115%. **Figure 4.14** shows that the standard photovoltaic module temperature profile ranged from approximately $63.3 \text{ }^\circ\text{C}$ to $86.8 \text{ }^\circ\text{C}$, whereas the hybrid photovoltaic module's temperature profile ranged from approximately $41.1 \text{ }^\circ\text{C}$ to $81.6 \text{ }^\circ\text{C}$. The hybrid system's ability to establish a lower photovoltaic module temperature allows it to generate a significantly greater amount of electricity.

The temperature gradient across the thermoelectric generator was estimated based on the hot side TEG thermocouple and the water inlet temperature. From the experimental simulations, it was observed that the difference between the water inlet and outlet temperature was negligible ($<0.1 \text{ }^\circ\text{C}$), suggesting that the water inlet temperature to each aluminum cooling block does not vary significantly. Also, one can assume that there is little difference between the water inlet temperature and the outside temperature of the aluminum water cooling blocks due to the water cooling blocks having a high thermal

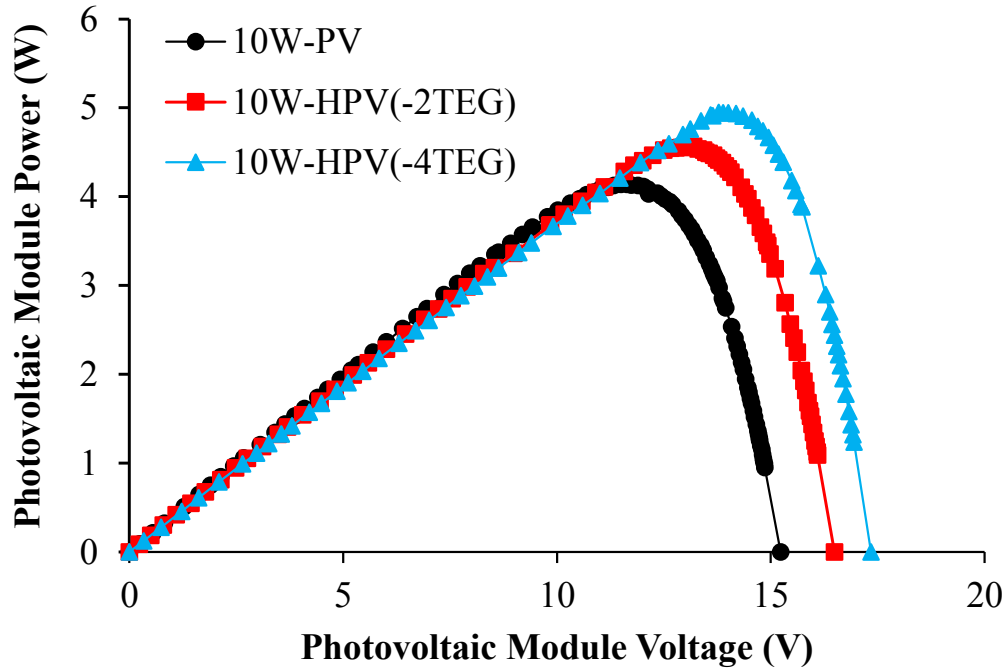


Figure 4.10: Power vs. voltage curves of conventional 10W-PV photovoltaic module, and hybrid photovoltaic module of 10W-HPV-2TEG and 10W-HPV-4TEG system, $G_T=825 \text{ W/m}^2$, $T_{w,in}=11 \text{ }^\circ\text{C}$, $\dot{V}=1 \text{ L/min}$.

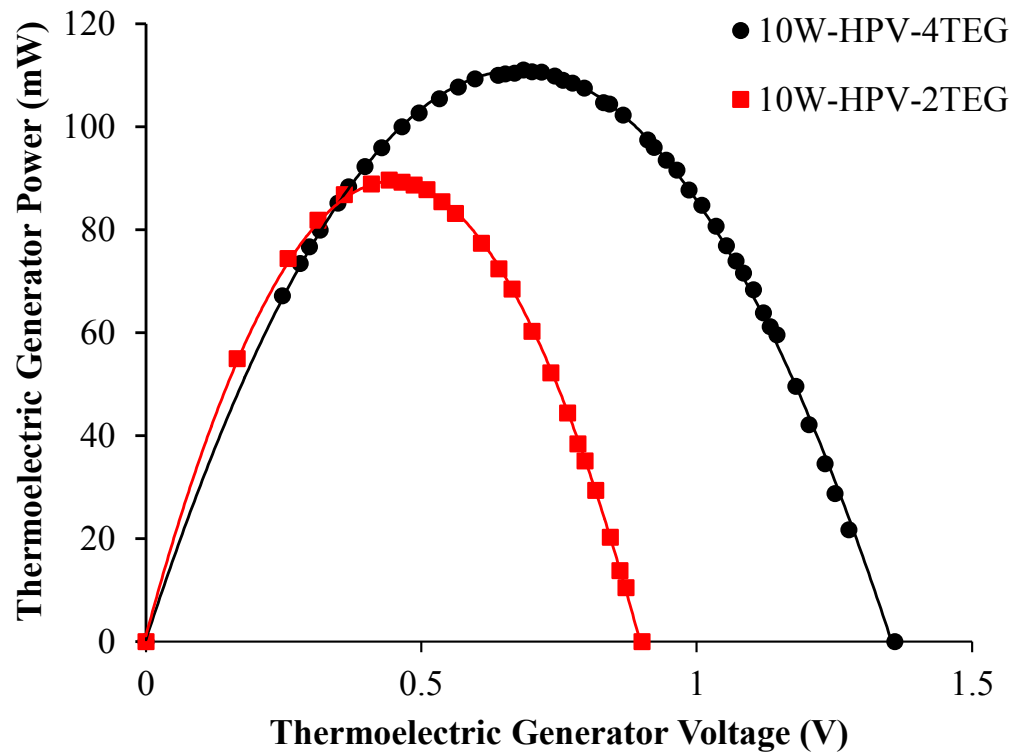


Figure 4.11: TEG power vs. voltage curves for 10W-HPV-2TEG and 10W-HPV-4TEG system, $G_T=825 \text{ W/m}^2$, $T_{w,in}=11 \text{ }^\circ\text{C}$, $\dot{V}=1 \text{ L/min}$.

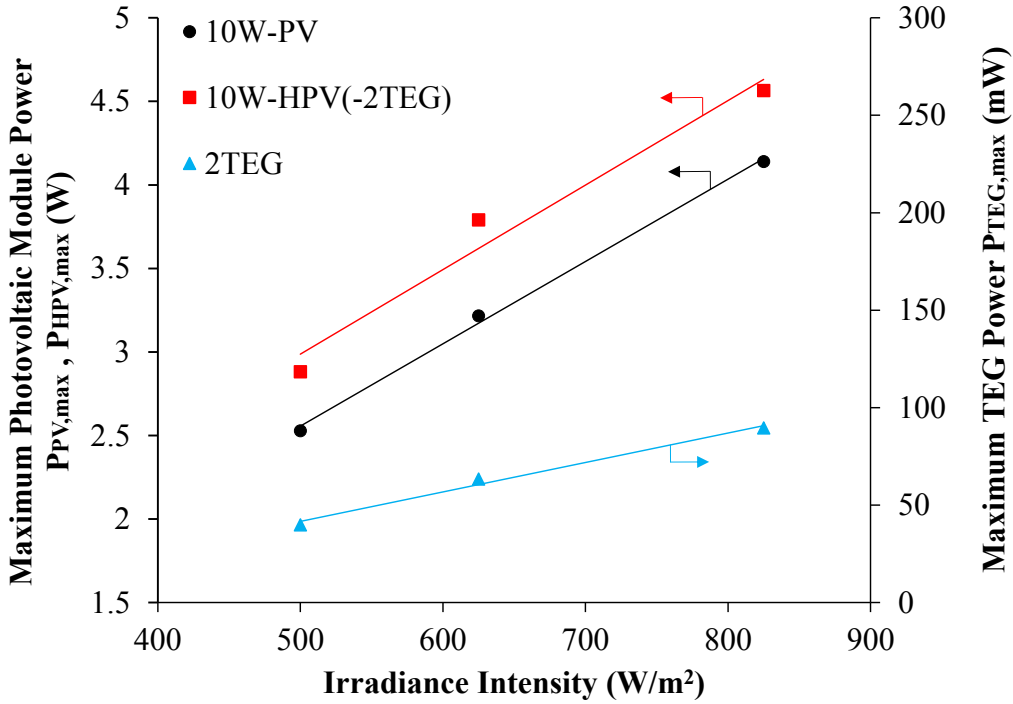


Figure 4.12: The 10W-PV, 10W-HPV(-2TEG), and 2TEG maximum power output vs. irradiance intensity, $T_{w,in}=11\text{ }^{\circ}\text{C}$, $\dot{V}=1\text{ L/min}$.

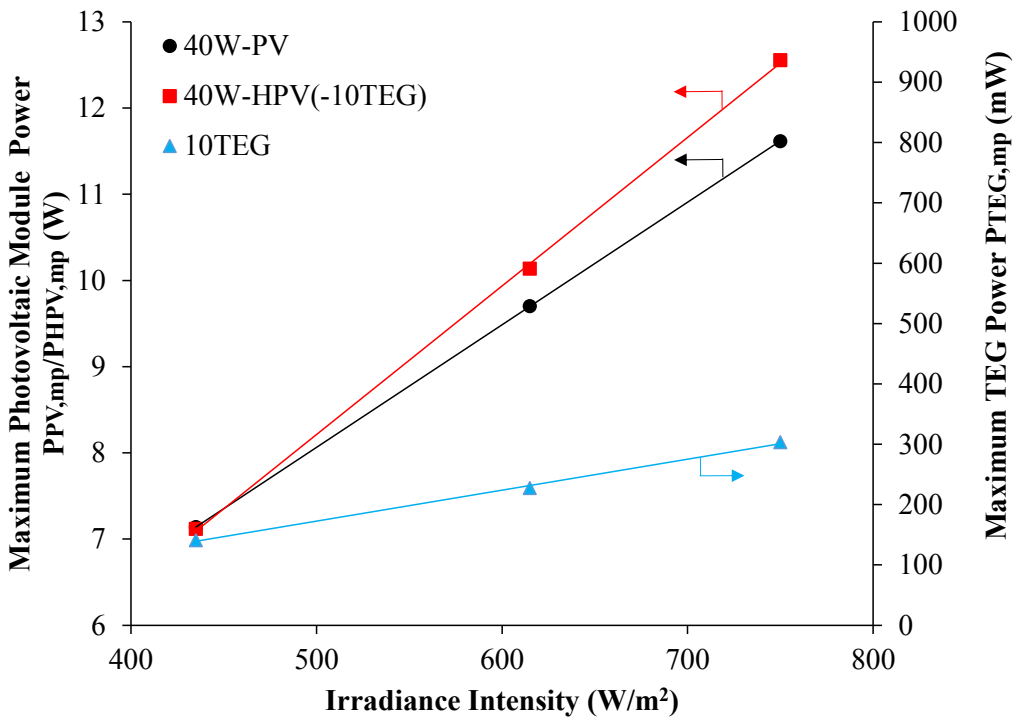


Figure 4.13: The 40W-PV, 40W-HPV(-10TEG), and 10TEG maximum power point vs. irradiance intensity, $T_{w,in}=2\text{ }^{\circ}\text{C}$, $\dot{V}=1\text{ L/min}$.

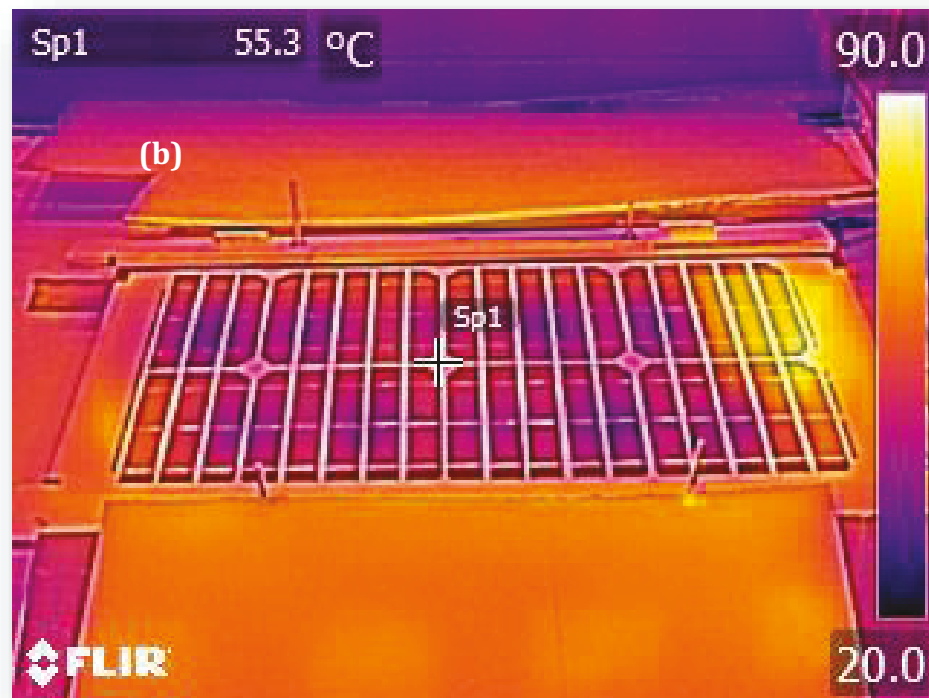
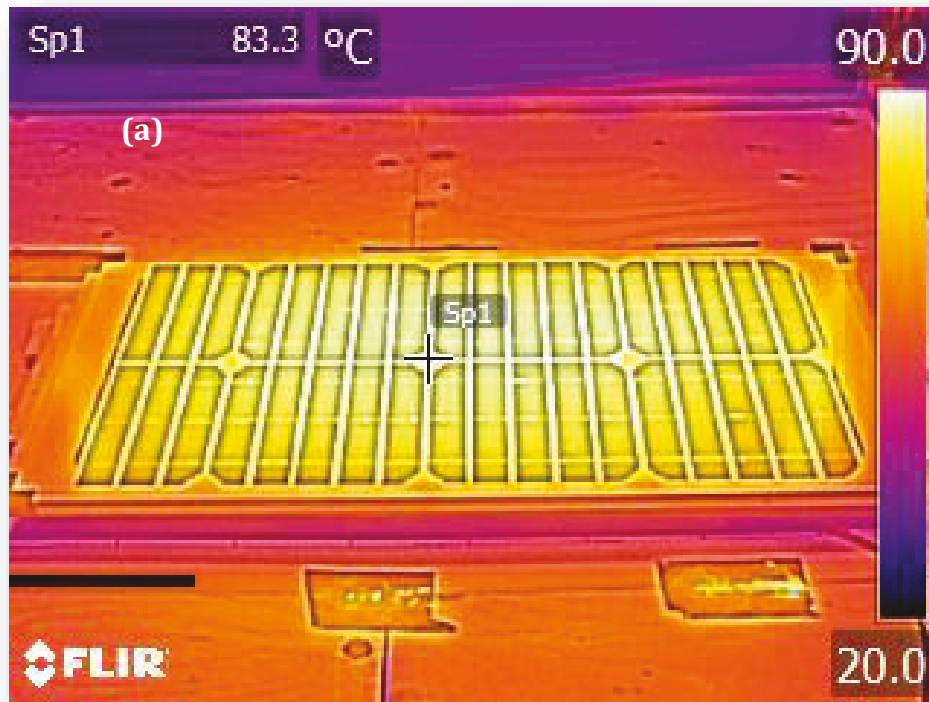


Figure 4.14: Thermal profiles of the (a) 40W-PV and (b) 40W-HPV-10TEG system, $G_T=750 \text{ W/m}^2$, $T_{w,in}=2 \text{ }^\circ\text{C}$, $\dot{V}=1 \text{ L/min}$.

conductivity and thin wall thickness (~ 0.0005 m). Therefore, based on these principles, it is accurate to estimate that the cold side temperature of the TEG is approximately equal to the water inlet temperature. The relationship between the 10W-HPV-TEG system's thermoelectric generator power output and temperature gradient as a function of irradiance intensity is shown in **Figure 4.15**. The temperature gradient appears to increase nonlinearly with irradiance intensity. The maximum temperature gradient of approximately 35.3 °C established a power output of 303.3 mW from the 40W-HPV-10TEG thermoelectric generator. **Figure 4.15** emphasizes that the power generated by the thermoelectric generator is directly proportional to the TEG's temperature gradient.

The importance of maintaining a low inlet water temperature to a HPV-TEG system was confirmed by the indoor experimental results shown in **Figure 4.16**. In this particular study, various inlet water temperatures were introduced to the 40W-HPV-10TEG system at a constant irradiance intensity of 750 W/m² and water flow rate of 1 L/min. This figure displays that increasing the water inlet temperature decreases the power output of the hybrid system's PV module and thermoelectric generator. Increasing the water inlet temperature from 2 °C to 13.5 °C decreases the hybrid system's PV module and thermoelectric generator by approximately 0.15 W and 85 mW, respectively. This decrease in the hybrid system's PV module power can be attributed to the overall increase in the photovoltaic module temperature, as seen in **Figure 4.17**. Increasing the water inlet temperature also decreases the thermal energy transferred through each thermoelectric module and the temperature gradient of the TEG. As a result, the total amount of power generated by the thermoelectric generator decreases. The water inlet temperature should be minimized to optimize the performance of the HPV-TEG system.

The final indoor experimental simulation investigated the optimization of a HPV-TEG by incorporating a v-trough concentrator to increase the total amount of electricity generated. V-troughs were implemented due to its low cost, easy manufacturability, and low solar radiation concentration. High solar radiation concentrators, such as Fresnel lenses, have a greater potential of causing permanent damage to the photovoltaic module. A photograph of the manufactured concentrated hybrid photovoltaic-thermoelectric power generation module prototype (40W-CHPV-10TEG) is shown in **Figure 4.18**. Two flat aluminum coated mirrors were tilted at an angle of 60 degrees to create a geometric

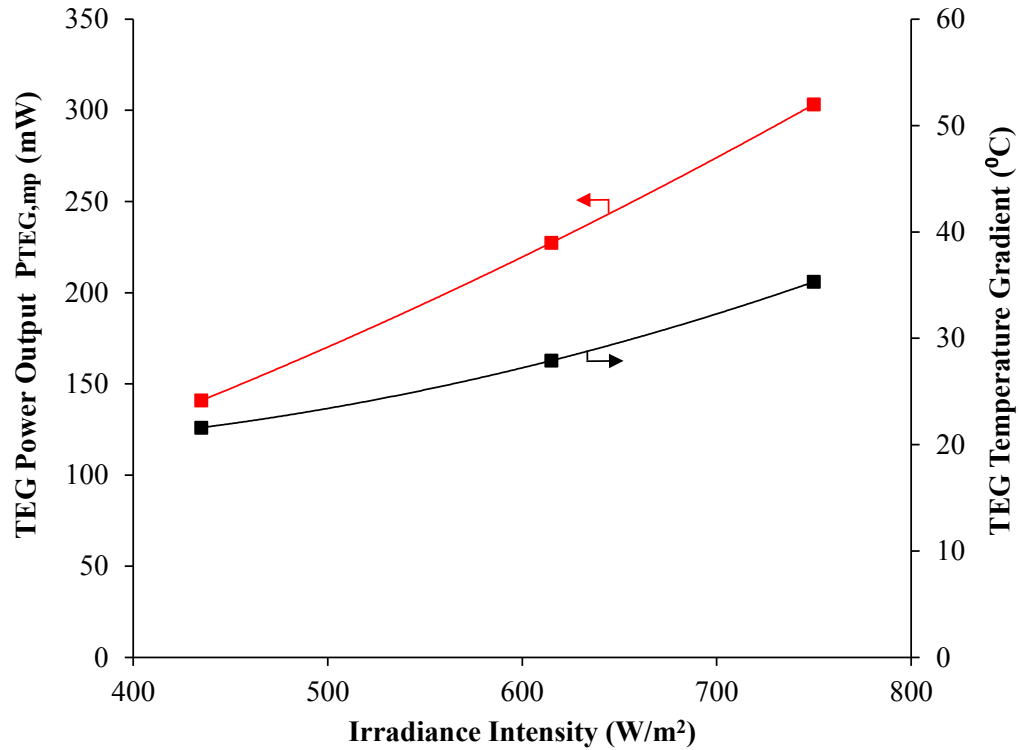


Figure 4.15: The 10TEG thermoelectric generator maximum power output and temperature difference across TEG vs. irradiance intensity, $T_{w,in}=2\text{ }^{\circ}\text{C}$, $\dot{V}=1\text{ L/min}$.

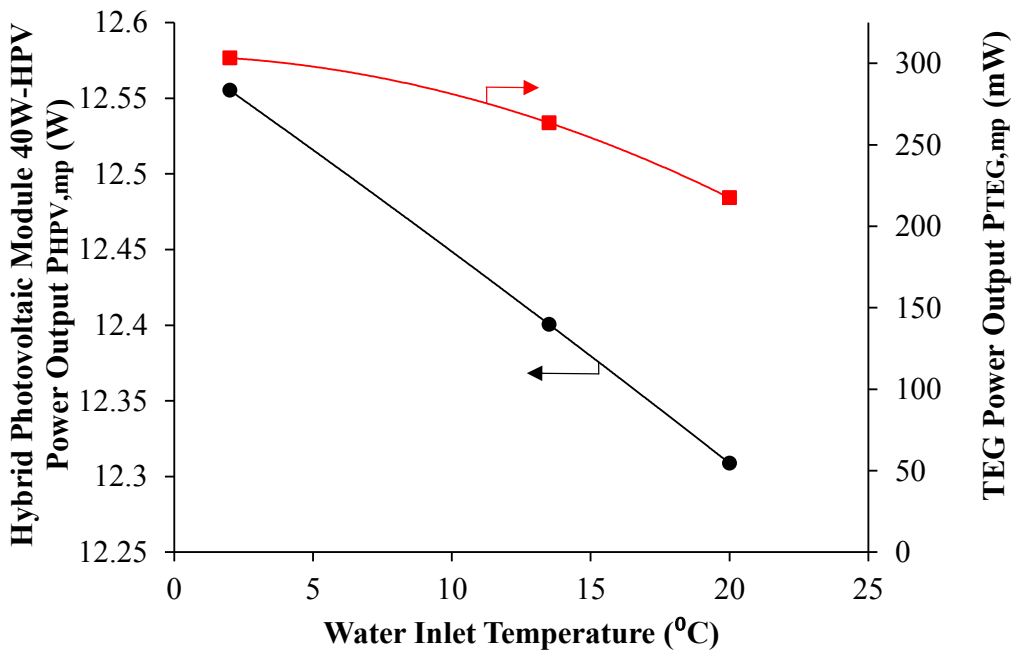


Figure 4.16: The 40W-HPV-(10TEG) module and thermoelectric generator (10TEG) power output vs. water inlet temperature, $G_T=750\text{ W/m}^2$, $\dot{V}=1\text{ L/min}$.

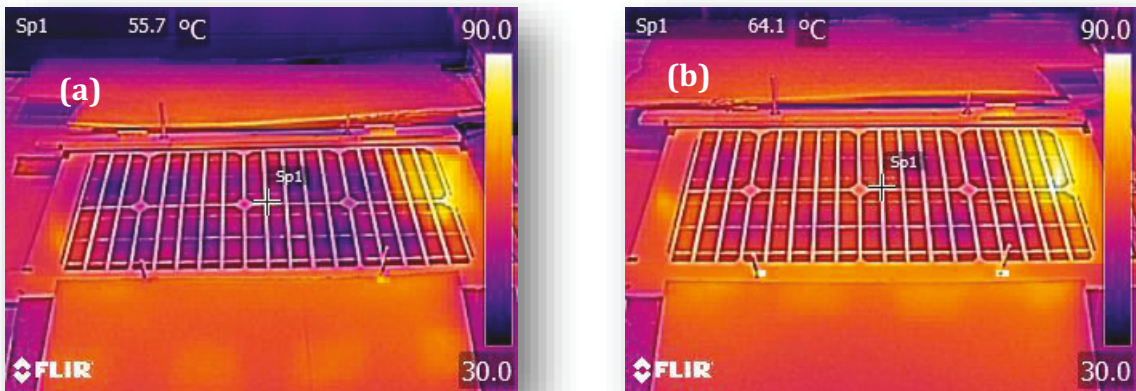


Figure 4.17: Thermal profile of the 40W-HPV-10TEG operating with a water inlet temperature of (a) 2 °C and (b) 20 °C, $G_T=750 \text{ W/m}^2$, $\dot{V}=1 \text{ L/min}$.



Figure 4.18: Photograph of the concentrated hybrid photovoltaic-thermoelectric power generation module (40W-CHPV-10TEG).

concentration ratio of ~ 2.93 . Comparison between the photovoltaic power vs. voltage curves of the 40W-PV, 40W-HPV-10TEG, and the 40W-CHPV-10TEG systems are shown in **Figure 4.19**. The maximum power generated by the concentrated hybrid PV module (40W-CHPV-10TEG) was approximately 33.2% and 23.2% greater than the power generated by the conventional (40W-PV) and hybrid PV module (40W-HPV-10TEG). The shift of the 40W-PV power curve to the 40W-HPV-10TEG power curve is due to the decrease in the operating temperature of the photovoltaic cells, whereas the shift of the 40W-HPV-10TEG power curve to the 40W-CHPV-10TEG power curve is due to an increase in the incident irradiance intensity. Recall that this power curve shift due to temperature and irradiance intensity is also illustrated in **Figure 1.8** and **Figure 1.9** on page 12. As depicted in **Figure 4.20**, the addition of the v-trough concentrator to the HPV-TEG system slightly increased the temperature profile of the PV module. However, the overall thermal profile of the 40W-CHPV-10TEG system remained lower than the standard PV module's thermal profile. Increasing the incident solar radiation using a v-trough concentrator also increases the thermal energy dissipated by the PV module and absorbed by the thermoelectric generator. As shown in **Figure 4.21** and **Figure 4.22**, additional thermal energy may be harvested by the thermoelectric generator when the incident irradiance intensity is increased using the v-trough concentrators. Increasing the incident irradiance intensity increases the current, voltage and power generated by the thermoelectric generator. The maximum power output difference between the 40W-CHPV-10TEG and 40W-HPV-10TEG thermoelectric generator was approximately 115.4 mW.

The experimental results demonstrated that the designed water cooling system has the capability to maintain a low photovoltaic module temperature when the irradiance intensity was increased through the use of a v-trough concentrator. The major disadvantage of installing v-trough concentrators to a HPV-TEG system is the additional cost of the reflectors, and the solar tracking system that is required to ensure shadows do not shade portions of the PV module. Nevertheless, as demonstrated by Sangani and Solanki's [142] research, the increase in power generated by integrating commercially available photovoltaic modules with v-trough concentrators has the potential to decrease the overall cost per watt of a PV system. The developed CHPV-TEG prototype and indoor simulation data has demonstrated that v-trough concentrators are a safe and low-cost method of increasing

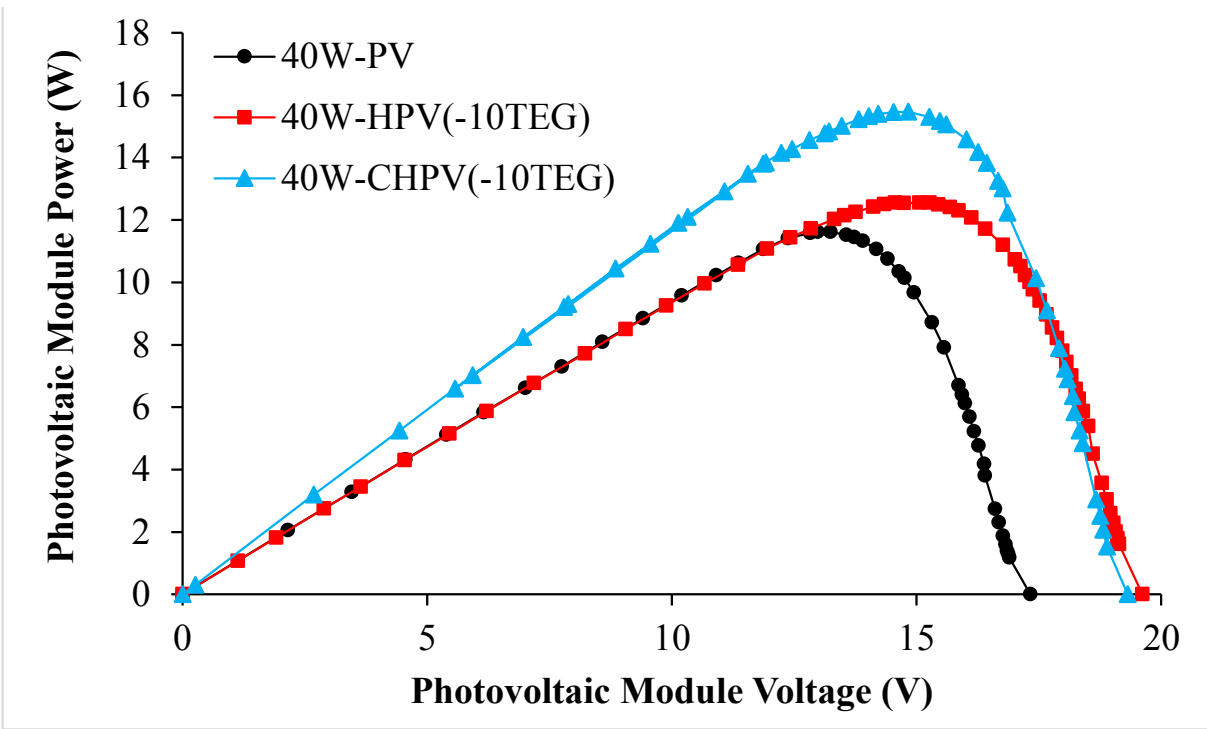


Figure 4.19: The 40W-PV, 10W-HPV(-10TEG), and 40W-CHPV(-10TEG) module power and vs. voltage curves, $G_T=750 \text{ W/m}^2$, $T_{w,in}=2 \text{ }^\circ\text{C}$, $\dot{V}=1 \text{ L/min}$.

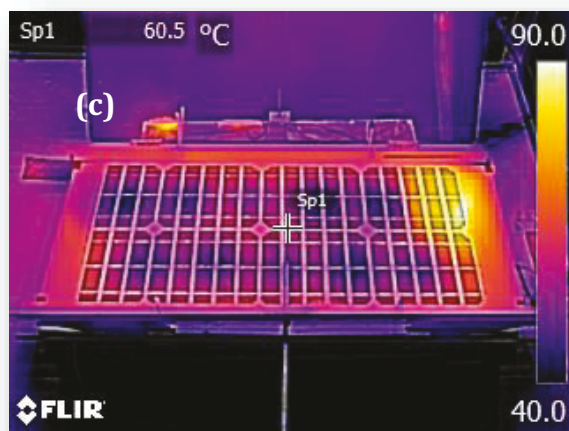
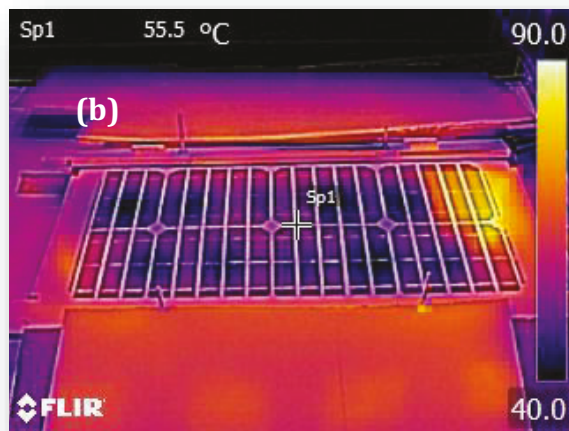
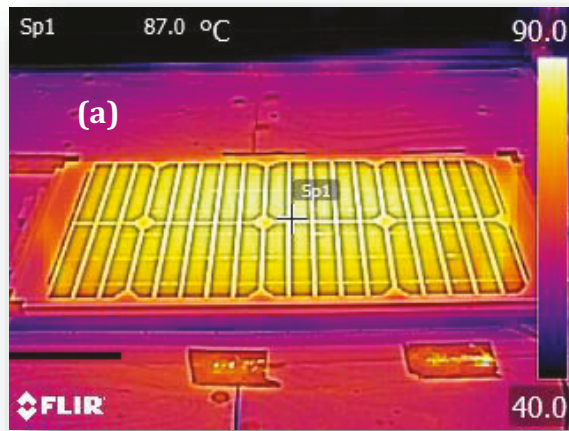


Figure 4.20: Thermal profiles of the (a) 40W-PV-10TEG (b) 40W-HPV-10TEG, and (c) CHPV-TEG module, $G_T=750 \text{ W/m}^2$, $T_{w,in}=2 \text{ }^\circ\text{C}$, $\dot{V}=1 \text{ L/min}$.

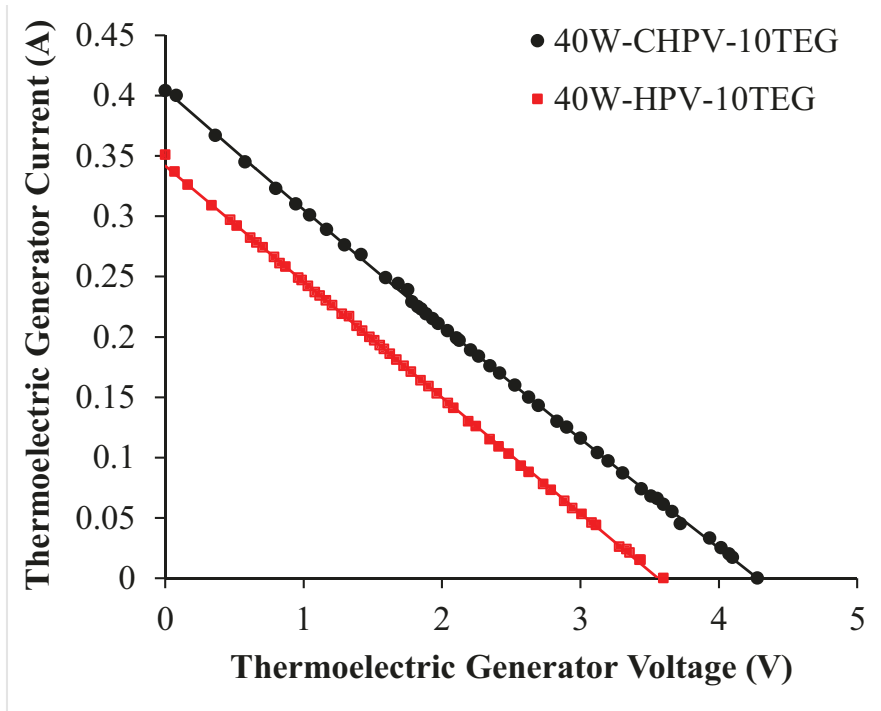


Figure 4.21: The HPV-TEG and CHPV-TEG thermoelectric generator current vs. voltage curves, $G_T=750 \text{ W/m}^2$, $T_{w,in}=2 \text{ }^\circ\text{C}$, $\dot{V}=1 \text{ L/min}$.

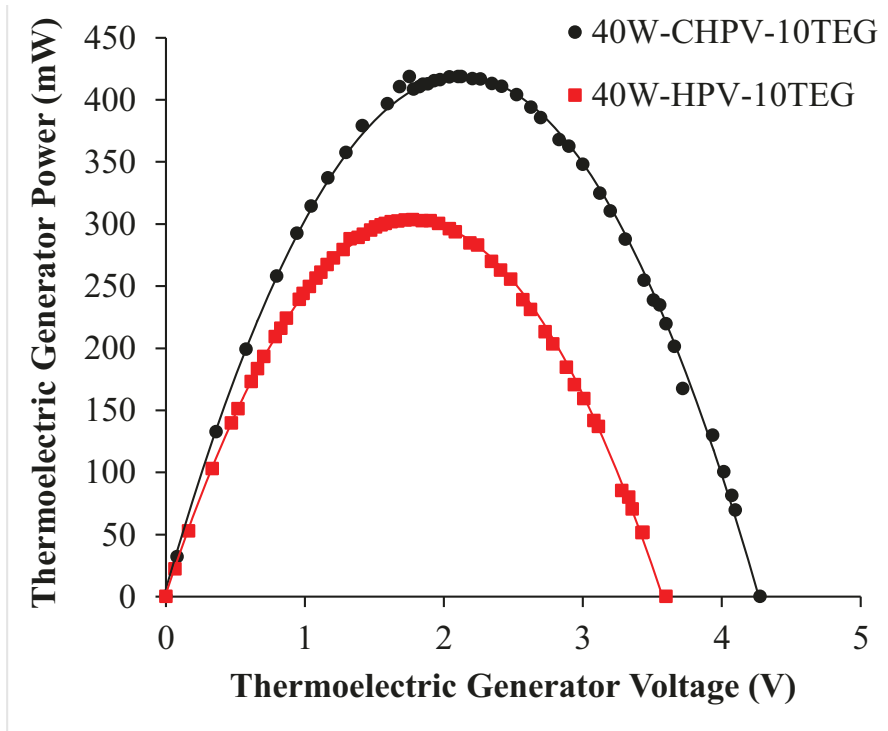


Figure 4.22: The HPV-TEG and CHPV-TEG thermoelectric generator power vs. voltage curves, $G_T=750 \text{ W/m}^2$, $T_{w,in}=2 \text{ }^\circ\text{C}$, $\dot{V}=1 \text{ L/min}$.

the electricity generated from a HPV-TEG system.

The indoor experimental simulations discussed in this section provided an incentive to investigate the performance of a HPV-TEG system in an outdoor setting. There are few factors of the indoor solar simulations that limit the accuracy of determining the viability and performance of a HPV-TEG system under real-life circumstances. The most critical shortcoming of the indoor solar simulator is that the tungsten halogen lamps do not perfectly simulate natural sunlight. Tungsten halogen lamps emit a higher spectral irradiance of infrared (long) wavelengths compared to the Sun's wavelength spectrum [143]. Photovoltaic modules directly convert these infrared wavelengths into thermal energy. Therefore, the PV and HPV-TEG system operate at higher temperatures using halogen lamps than when operating at the same irradiance intensity using natural sunlight. Additionally, the solar simulator only investigates static conditions where the ambient air temperature and irradiance intensity are constant. These constraints of the low-cost solar simulator emphasize that outdoor experimental case studies are required to further validate the proof-of-concept of a HPV-TEG system.

4.3 Outdoor Case Studies

4.3.1 Outdoor Experimental Site Location

Outdoor experimental case studies will be performed under the dynamic climate conditions of Thunder Bay (48.38 °N, 89.25 °W), Ontario, Canada. As seen in **Figure 4.23**, Thunder Bay is located in Northwestern Ontario on the shores of Lake Superior with an estimated population of 121,596 in 2011 [144]. The city experiences a large variation in weather throughout the year. For example, the minimum ambient air temperature in January 2015 was approximately -32.0 °C, while the maximum ambient air temperature in July 2014 was approximately 33.2 °C [145]. It has been estimated that Thunder Bay has an average of 2121 sunshine hours a year [146]. Although there is a substantial variation in temperature throughout the year, Thunder Bay has an adequate amount of sunshine from May to September to fully characterize the performance of various designs of HPV-TEG systems.

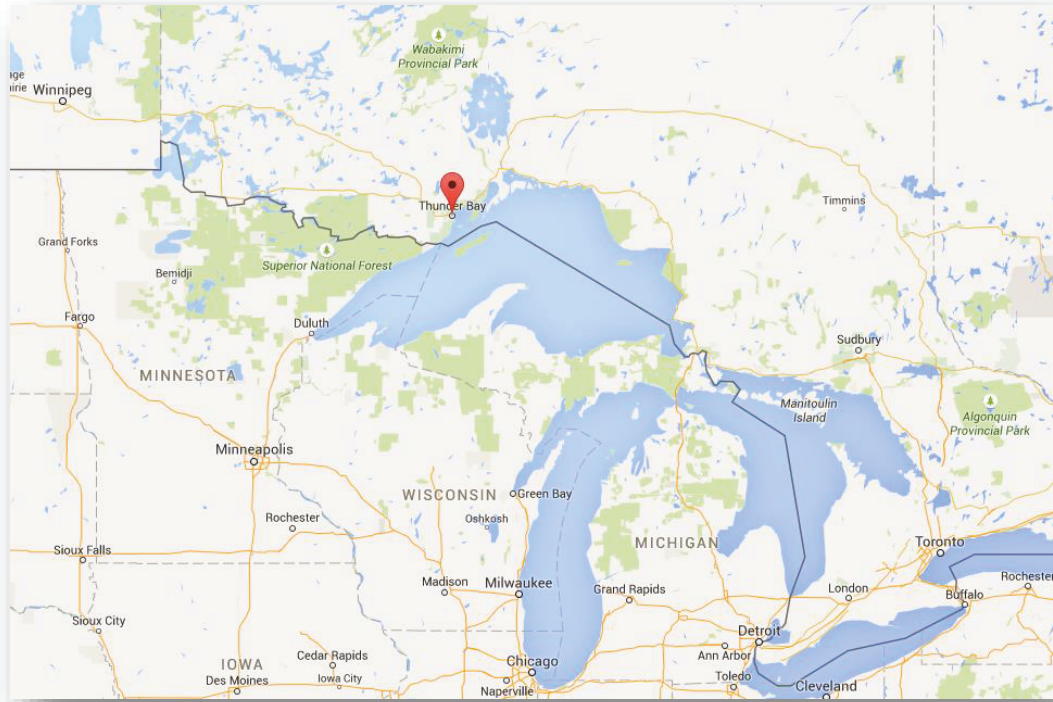


Figure 4.23: Location of Thunder Bay (48.38 °N, 89.25 °W), Ontario, Canada [147].

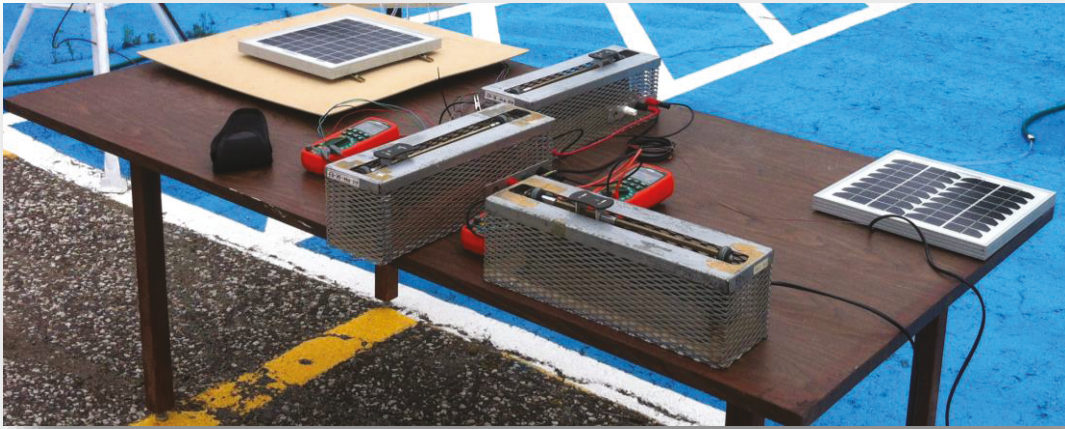
4.3.2 Outdoor Experimental Test Setup and Experimental Procedure

Experimental case studies were implemented to determine the performance of the 10W-HPV-2TEG, 10W-HPV-4TEG, and 40W-HPV-10TEG. A summary of the tests and the corresponding case study type and tilt angle is shown in **Table 4.3**. Photographs of each outdoor experimental test setup are shown in **Figure 4.24**. A schematic of a typical outdoor experimental test setup for each case study is displayed in **Figure 4.25**. The conventional PV and HPV-TEG systems are placed in an outdoor location free from shadows that may be present from trees, buildings, birds, pedestrians, etc. Each system has the exact same photovoltaic module electrical specifications. Benchmark tests were completed to ensure that the PV module used in each HPV-TEG system has the same power output as the standard PV module. A weather data logger station is used to record the wind speed, ambient air temperature, and irradiance intensity on a horizontal plane every second. For the 40W-PV and 40W-HPV-10TEG test setup, an additional pyranometer is installed to measure the incident irradiance intensity since the test setup is orientated at a tilt angle equal to the latitude of the location. An additional pyranometer is not required for tests #1-#8 since the tilt angle of the system is zero and the incident irradiance intensity may be determined by the weather data logger's pyranometer. The inlet and outlet temperature of the water is determined using T-type thermocouple probes TR1 and TR2. Experimental data is recorded from 10 AM to 2 PM EST for each test. Each photovoltaic system faces directly due south. Real-time water inlet and outlet temperature measurements are recorded every 10 seconds. Real-time measurements of the hot TEG side temperature (TR3), and the back PV module surface temperature (TR4 and TR5) are also recorded every 10 seconds. A variable area rotameter FL1 is used to set the volumetric flow rate of the water to 1 L/min. Thermal profiles of the PV and HPV-TEG systems are recorded using a FLIR E4 infrared camera every 5 minutes at an emissivity of 0.88.

In chapter three and section 4.2, it was evident that the optimal electrical load resistance for a photovoltaic module and TEG is dependent on several factors including ambient air temperature, wind velocity, incident irradiance intensity, and water inlet temperature. A conservative estimate of the optimal electrical load resistance for each electrical component for the outdoor tests is based on the optimal load resistances determined from the indoor experimental results and the electrical specifications of each

Table 4.3: Selected PV tilt angle for each test and the corresponding case study.

Test #	Case Study	Tilt Angle (degrees)
1	10W-HPV-2TEG	0
2	10W-HPV-2TEG	0
3	10W-HPV-2TEG	0
4	10W-HPV-2TEG	0
5	10W-HPV-4TEG	0
6	10W-HPV-4TEG	0
7	10W-HPV-4TEG	0
8	40W-HPV-10TEG	0
9	40W-HPV-10TEG	48.32 (latitude)
10	40W-HPV-10TEG	48.32 (latitude)
11	40W-HPV-10TEG	48.32 (latitude)
12	40W-HPV-10TEG	48.32 (latitude)



(a)



(b)

Figure 4.24: Photographs showing the outdoor experimental test setup of (a) 10W-PV/ 10W-HPV-2TEG and 10W-PV/ 10W-HPV-4TEG system (b) 40W-PV/ 40W-HPV-10TEG system.

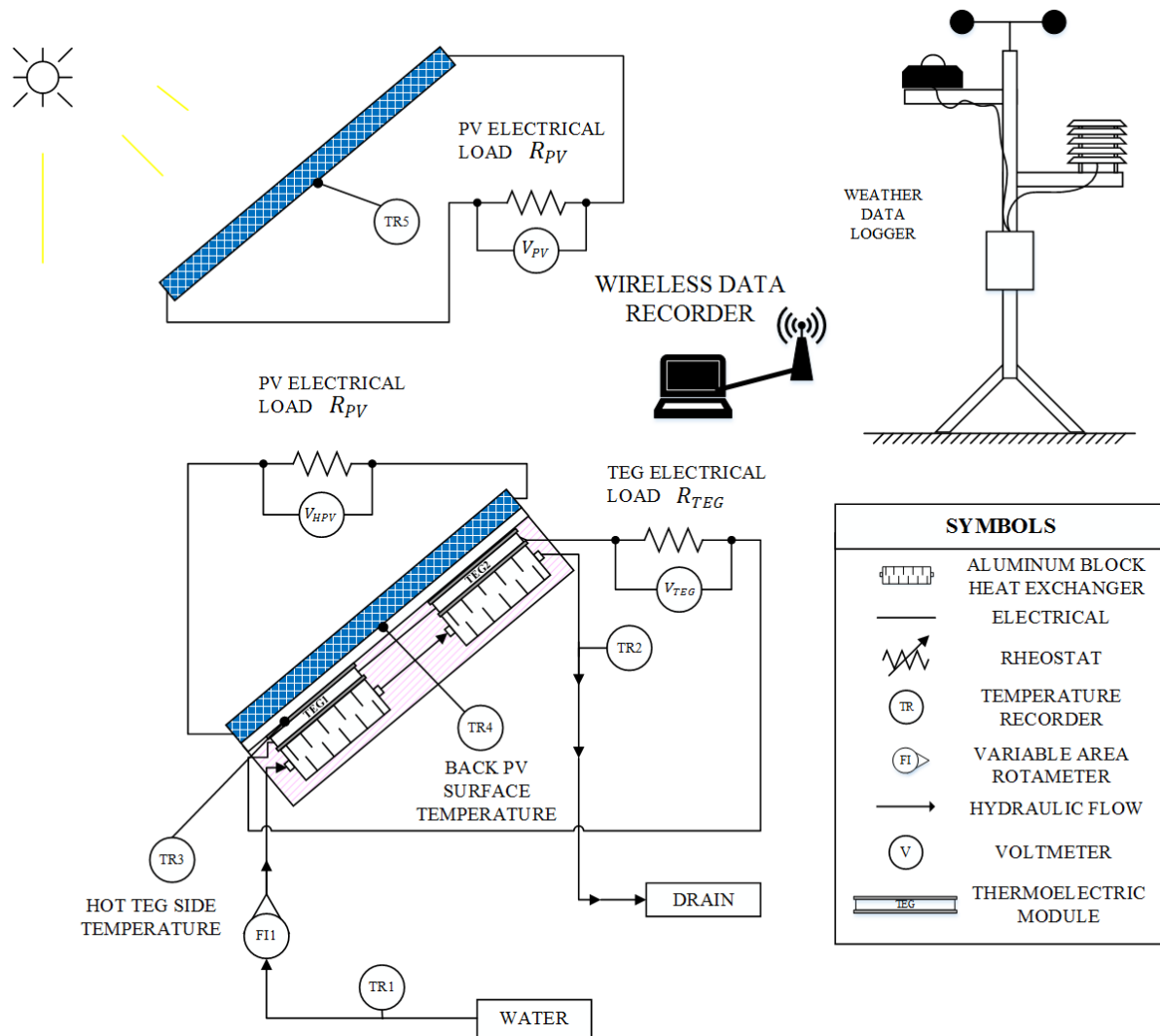


Figure 4.25: Schematic of the outdoor experimental test setup used in this research work.

device. A constant electrical load resistance of 40 ohms and 1 ohm is connected to each photovoltaic module and thermoelectric generator of the 10W-PV, 10W-HPV-2TEG, and 10W-HPV-4TEG systems. For the 40W-PV and 40W-HPV-10TEG system, an electrical load of 20 ohms and 10 ohms is connected to each photovoltaic module and thermoelectric generator. Real-time data acquisition software and a wireless data recorder is used to observe the voltage across the photovoltaic modules' loads every second. The voltage across the TEG load is measured every 5 minutes. Based on the voltage and resistance of each device, the power generated at a moment of time t by the conventional photovoltaic module, the hybrid system's photovoltaic module, and thermoelectric generator may be determined by the following equations:

$$P_{PV}(t) = \frac{V_{PV}(t)^2}{R_{PV}} \quad (4.1)$$

$$P_{HPV}(t) = \frac{V_{HPV}(t)^2}{R_{PV}} \quad (4.2)$$

$$P_{TEG}(t) = \frac{V_{TEG}(t)^2}{R_{TEG}} \quad (4.3)$$

The total electrical power generated by the entire HPV-TEG system at a time t may be determined by the formula:

$$P_{HPV-TEG}(t) = P_{HPV}(t) + P_{TEG}(t) \quad (4.4)$$

The total daily irradiance intensity received by each photovoltaic system is determined using the equation:

$$H_T = \int_{10:00 \text{ AM}}^{2:00 \text{ PM}} G_T(t) dt \quad (4.5)$$

The total daily energy generated by the conventional photovoltaic module, HPV-TEG module, and the HPV-TEG system's thermoelectric generator over the four hour outdoor test is given by the following formulas:

$$E_{PV} = \int_{10:00 \text{ AM}}^{2:00 \text{ PM}} P_{PV}(t) dt \quad (4.6)$$

$$E_{HPV} = \int_{10:00 \text{ AM}}^{2:00 \text{ PM}} P_{HPV}(t) dt \quad (4.7)$$

$$E_{TEG} = \int_{10:00 AM}^{2:00 PM} P_{TEG}(t) dt \quad (4.8)$$

The overall daily efficiency of the conventional photovoltaic system for each outdoor test may be expressed as the ratio of total power generated by the PV module to the total irradiance:

$$\eta_{PV,daily} = \frac{E_{PV}}{A_{PV}H_T} \quad (4.9)$$

The overall daily efficiency of the HPV-TEG system for each outdoor test may be expressed as the ratio of total power generated by the HPV-TEG system to the total irradiance:

$$\eta_{HPV-TEG,daily} = \frac{E_{HPV} + E_{TEG}}{A_{PV}H_T} \quad (4.10)$$

Using the experimental data, the trapezoidal rule was implemented to approximate the integrals used in equations (4.5)-(4.10).

4.3.3 Results and Discussion: Outdoor Case Studies

As shown in **Figure 4.26** and **Figure 4.27**, the average water inlet temperature varies test to test, however the water inlet temperature did not fluctuate by more than 2 °C from the daily average inlet temperature for each test. The daily average water inlet temperature ranged from 8.89 °C to 19.85 °C, in order to investigate whether an HPV-TEG system may outperform a standard photovoltaic module when the water inlet temperature is not provided at an optimal temperature.

The results of the first test are shown in **Figures 4.28-4.31**. As seen in **Figure 4.28** and **Figure 4.29**, periodic cloud cover from 10:30 AM to 11:15 AM reduced the incident irradiance intensity and directly affects the power output of the 10W-PV and 10W-HPV-2TEG systems' photovoltaic modules. The maximum power output of the 10W-PV and 10W-HPV-2TEG system during test #1 was approximately 6.25 W and 6.55 W, respectively. The 10W-PV and 10W-HPV-2TEG systems' energy conversion efficiencies when producing the maximum power output were approximately 8.74% and 9.09%, respectively. The daily average water inlet temperature of test #1 was approximately 19.85 °C, therefore, test #1 has indicated the 10W-HPV-2TEG does not require a very low water inlet temperature to cool the system's photovoltaic module and produce more electricity than the standard

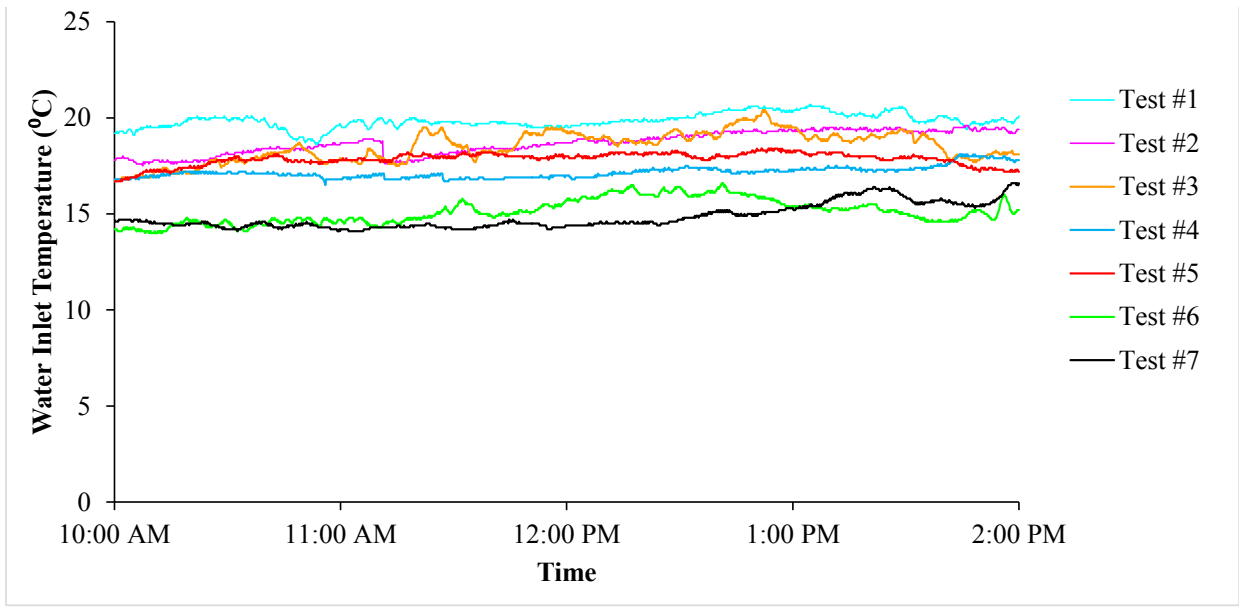


Figure 4.26: Water inlet temperature vs. time for outdoor test #1 to test #7.

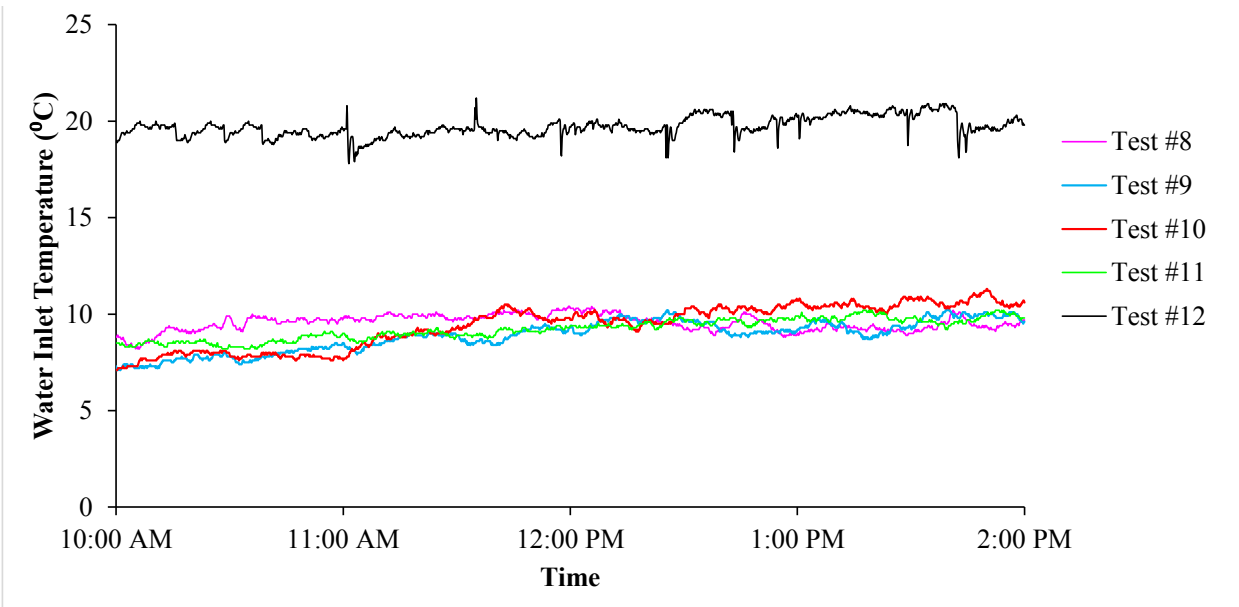


Figure 4.27: Water inlet temperature vs. time for outdoor test #8 to test #12.

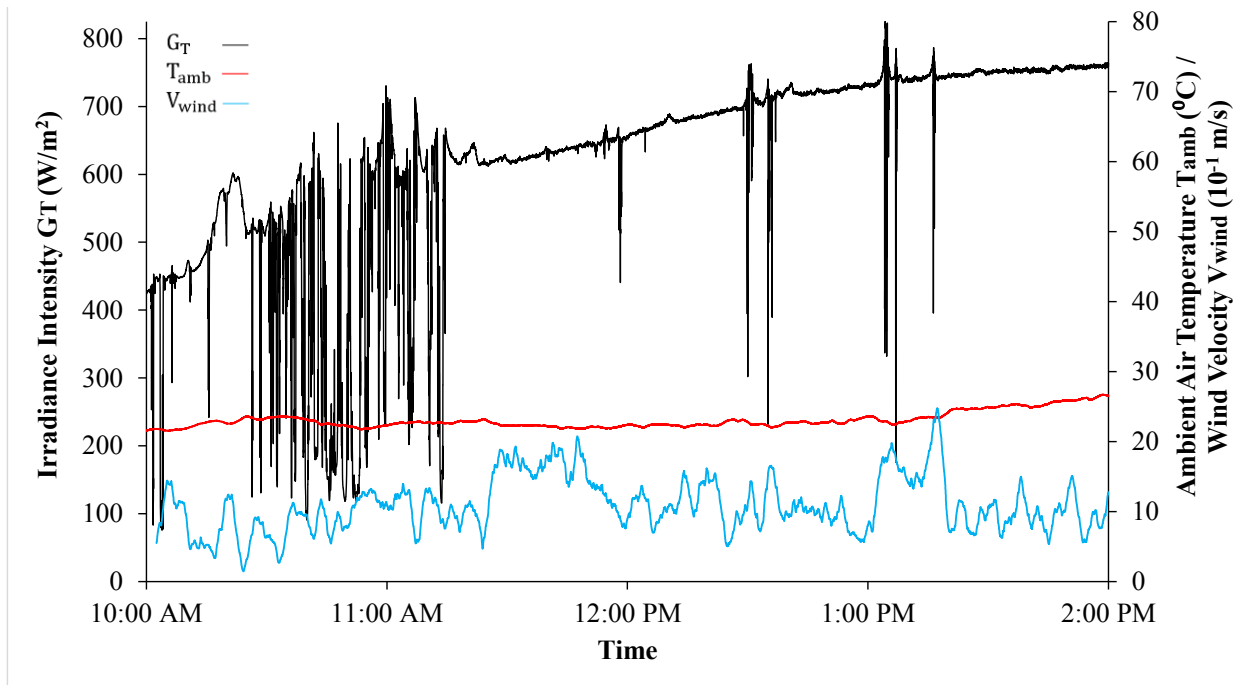


Figure 4.28: Corresponding incident irradiance intensity G_T , ambient air temperature T_{amb} , and wind speed V_{wind} vs. time (test #1).

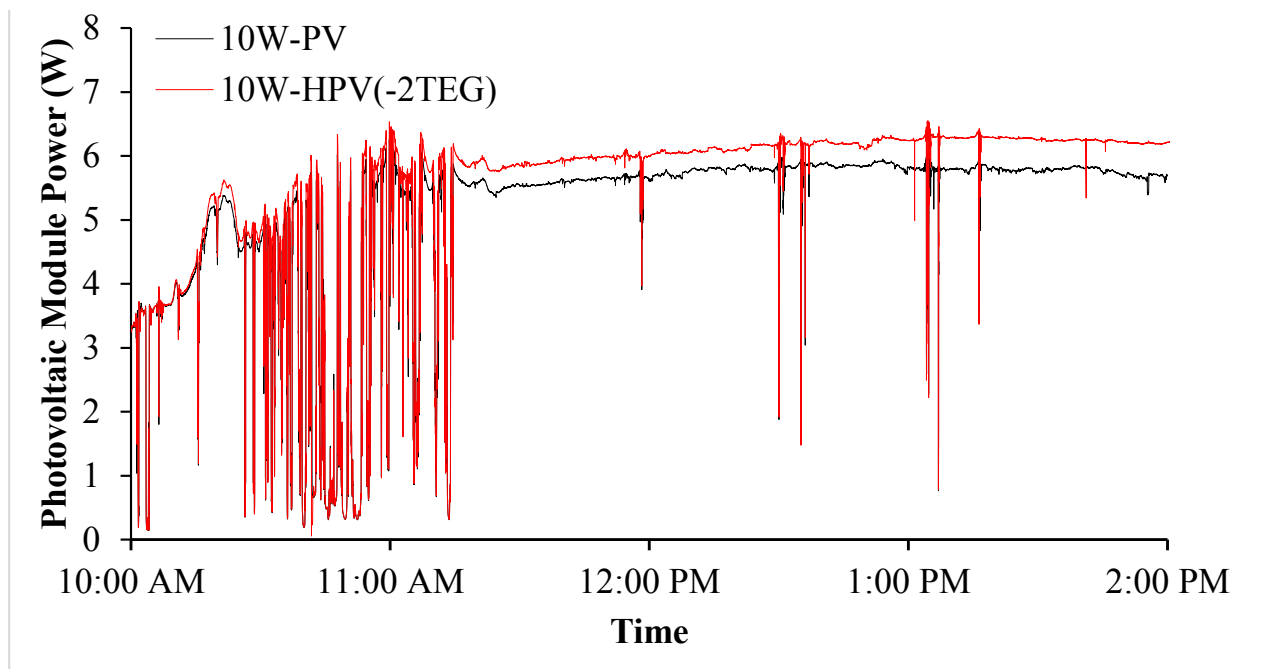


Figure 4.29: Power output of standard 10W-PV and hybrid 10W-HPV(-2TEG) photovoltaic module vs. time (test #1).

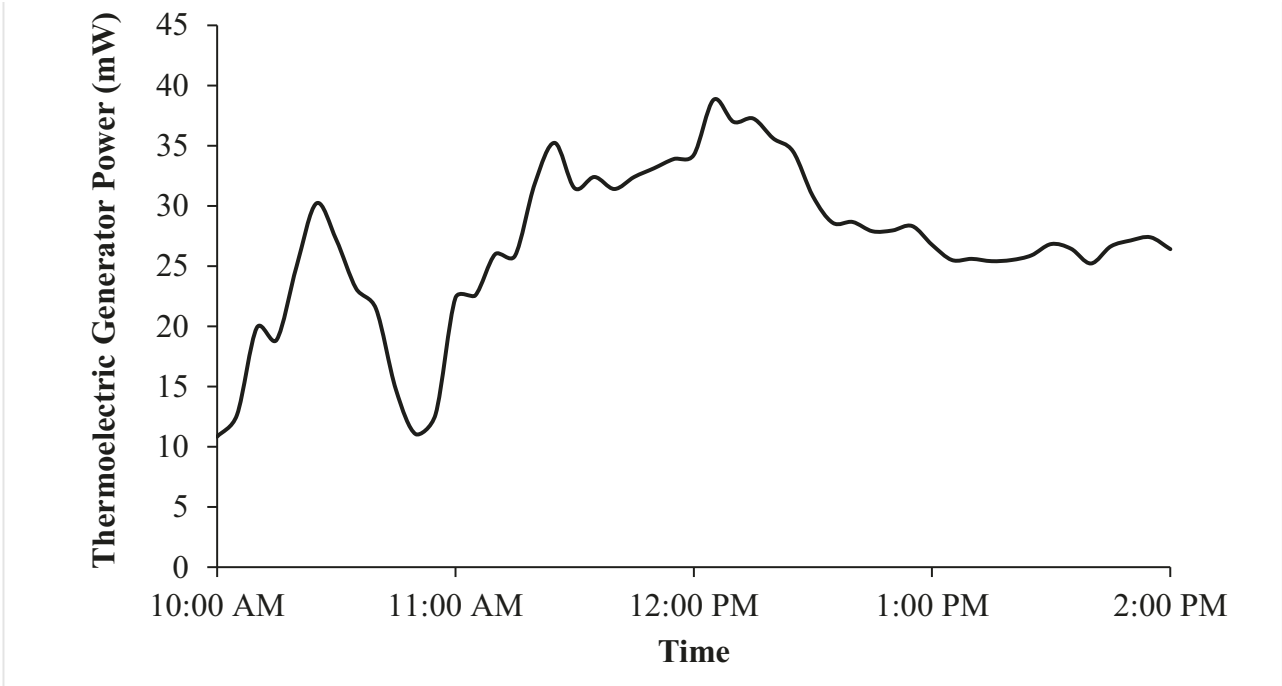


Figure 4.30: Thermoelectric generator (2TEG) power output vs. time (test #1).

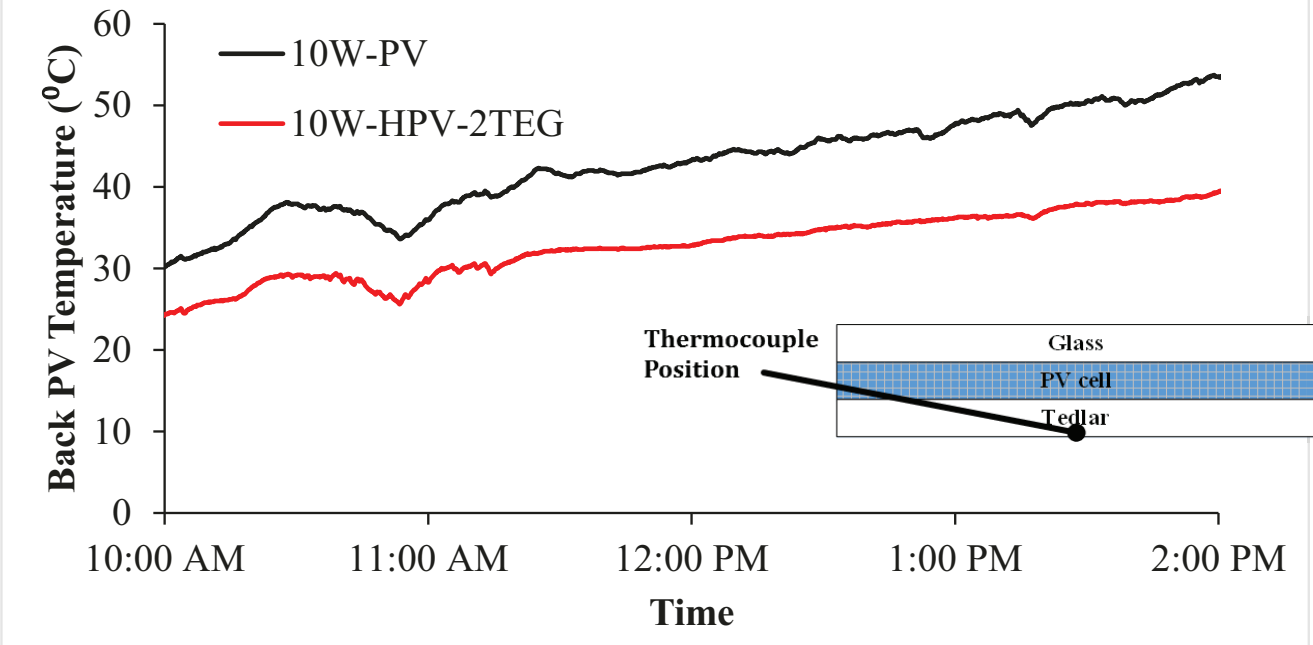


Figure 4.31: Back PV temperature vs. time (test #1).

photovoltaic module. **Figure 4.30** indicated that the cloud cover also reduced the power generated by the thermoelectric generator, establishing a minimum power output of 11.05 mW at 10:50 AM. The maximum power produced by the thermoelectric generator for test #1 was 38.8 mW. Temperature measurements of the back surface of each PV module show that the hybrid system maintained a lower operating temperature than the conventional system, as seen in **Figure 4.31**.

In comparison to test #1, test #2 also illustrated a similar relationship between photovoltaic module power and irradiance intensity. **Figure 4.32** and **Figure 4.33** show that as the irradiance intensity increases, the difference in power generated by the 10W-HPV-2TEG and 10W-PV photovoltaic modules increases. It is interesting to note, a similar trend was also examined in **Figure 3.10**, providing some confidence in the numerically obtained performance results. In **Figure 4.34**, the power generated by the TEG in test #2 appears to generally increase with time. This increasing trend in TEG electrical energy created is due to the fact that TEG power is directly proportional to irradiance intensity and the ambient air temperature, which increase with time. The minimum TEG power output of test #2 was 3.9 mW and occurred at 10:00 AM when the ambient air temperature and irradiance intensity was 15.92 °C and 413.1 W/m². The maximum TEG power generated by the TEG for test #2 was approximately 24.2 mW at 1:55 PM when the ambient air temperature and irradiance intensity was 20.82 °C and 764.4 W/m².

The performance of the 10W-HPV-2TEG system under non-ideal weather conditions was observed in test #3 and test #4. The experimental results for test #3 are shown in **Figures 4.35-4.37**. As seen in **Figure 4.35**, the irradiance intensity oscillates significantly throughout the duration of test #3, establishing a minimum and maximum irradiance intensity of 138.1 W/m² and 951.9 W/m², respectively. The responsiveness of the 10W-PV and 10W-HPV-2TEG photovoltaic modules' power output to the dynamic weather conditions is shown in **Figure 4.36**. The 10W-PV and 10W-HPV-2TEG daily total photovoltaic module energy produced from 10 AM to 2 PM for test #3 was approximately 15.29 Wh and 16.21 Wh, based on equations (4.6) and (4.7) respectively. Test #3 has a daily overall PV and HPV-TEG system energy conversion efficiency that was approximately 0.71% lower compared to test #2. Research completed by Durisch et al. [148] has shown that the energy conversion efficiency of a photovoltaic module generally increases with irradiance intensity. Therefore,

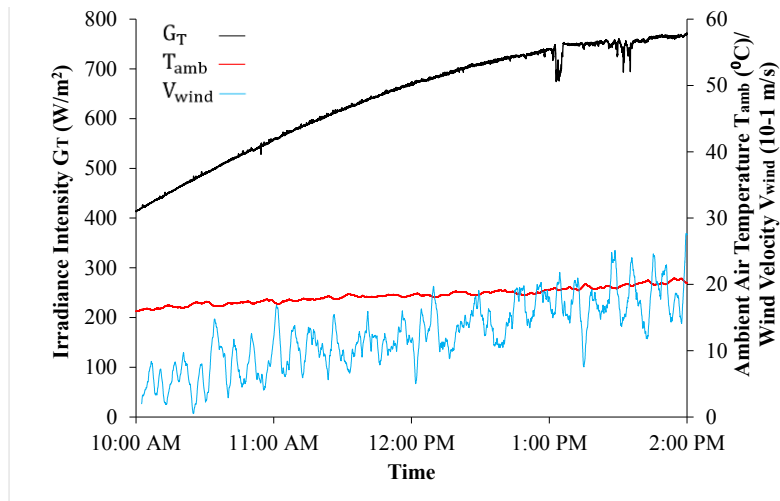


Figure 4.32: Corresponding incident irradiance intensity G_T , ambient air temperature T_{amb} , and wind speed V_{wind} vs. time (test #2).

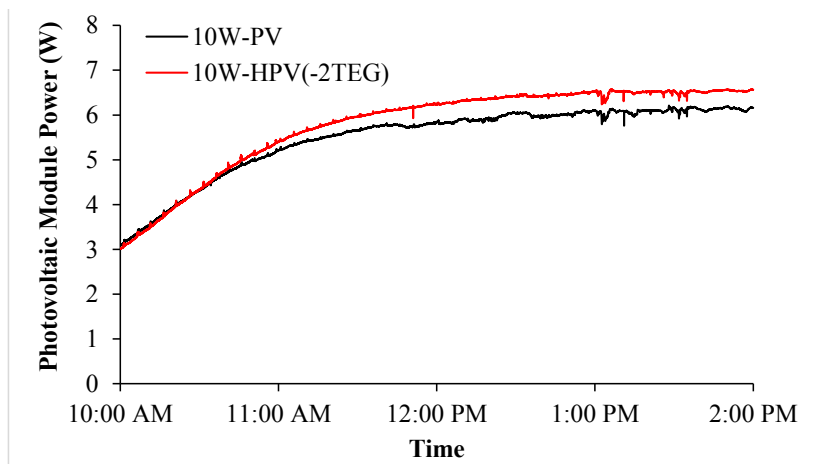


Figure 4.33: Power output of standard (10W-PV) and hybrid 10W-HPV(-2TEG) photovoltaic module vs. time (test #2).

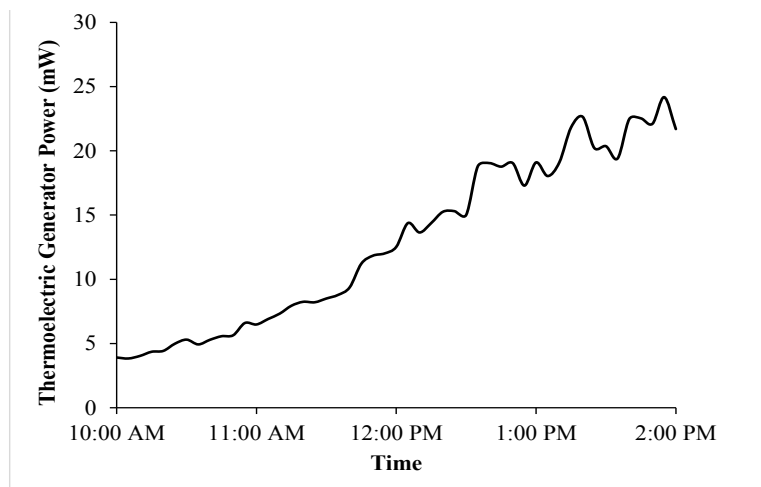


Figure 4.34: Thermoelectric generator (2TEG) power output vs. time (test #2).

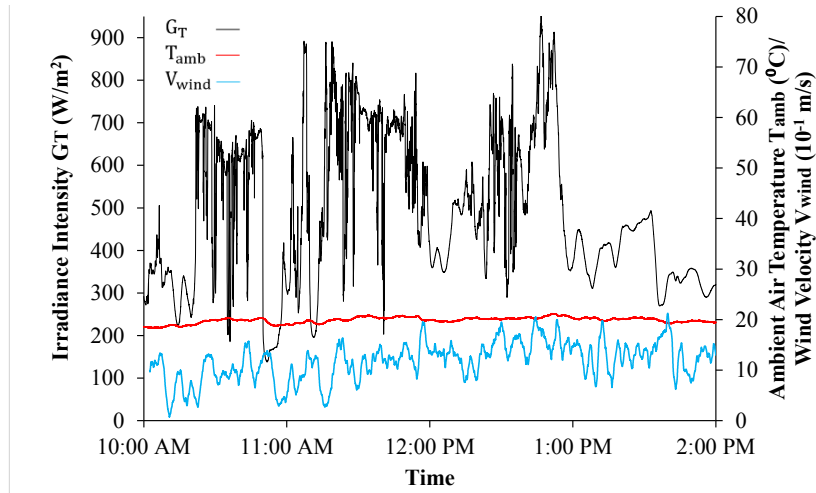


Figure 4.35: Corresponding incident irradiance intensity G_T , ambient air temperature T_{amb} , and wind speed V_{wind} vs. time (test #3).

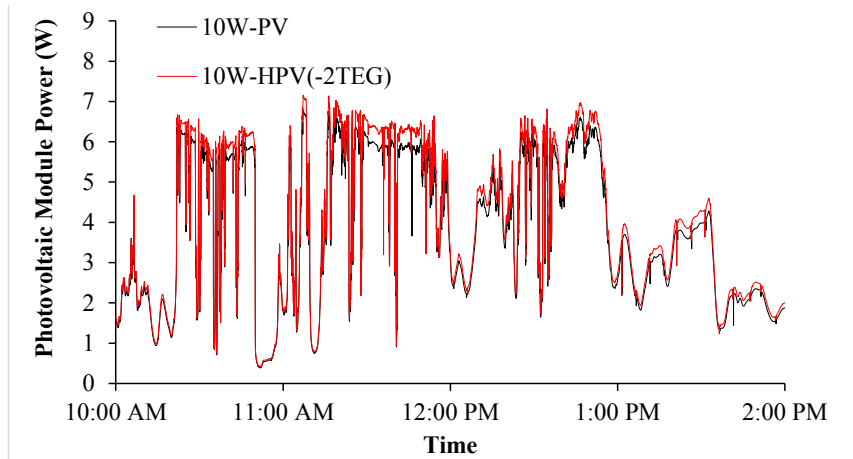


Figure 4.36: Power output of standard (10W-PV) and hybrid 10W-HPV(-2TEG) photovoltaic module vs. time (test #3).

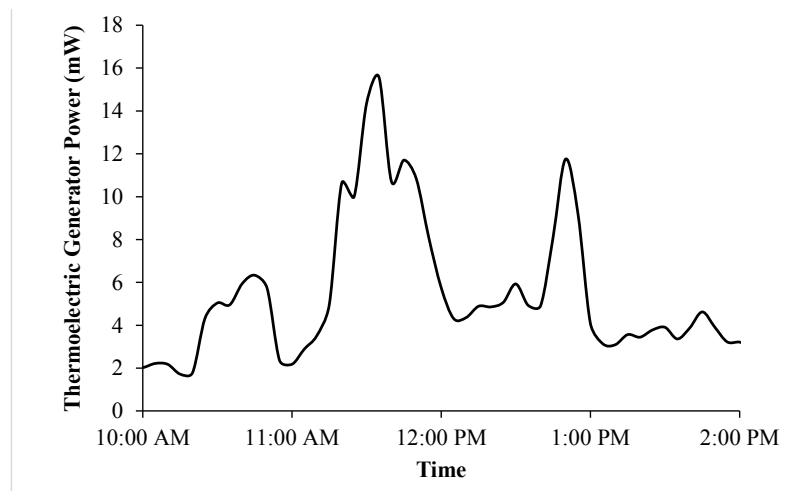


Figure 4.37: Thermoelectric generator (2TEG) power output vs. time (test #3).

since test #2 has a higher total daily incident irradiance intensity than test #3, test #2 will also have a higher daily overall PV and HPV-TEG system efficiency than test #3. It is evident that there is a direct relationship between irradiance intensity and TEG power output when comparing **Figure 4.35** and **Figure 4.37**. Periods of high irradiance intensity gradually increase the power generated by the thermoelectric generator. For example, the irradiance intensity from 11:30 AM to 11:35 AM remains greater than 650 W/m^2 , establishing the maximum TEG power output of 15.6 mW at 11:35 AM. Apparently, periodic cloud cover after 11:35 AM decreases the power output of the TEG, reaching 4.4 mW at 12:05 PM.

The performance of the 10-HPV-2TEG was also investigated under very low irradiance intensities in test #4, as shown in **Figures 4.38-4.40**. The irradiance intensity for test #4 remains less than 400 W/m^2 for the entire duration of the experiment. **Figure 4.39** shows that despite the low irradiance intensity, the 10W-HPV-2TEG photovoltaic module consistently produces more electrical energy than the standard PV module. The overall daily efficiency of the 10W-PV and 10W-HPV-2TEG in test #4 was approximately 3.68% and 3.81%, confirming the results from other research works [115, 141, 148] that a photovoltaic system's energy conversion efficiency is significantly reduced while operating under low irradiance intensities. The effect of the low irradiance intensity on the amount of electricity generated by the TEG is apparent in **Figure 4.40**. The thermoelectric generator in test #4 produces a very low amount of electrical energy, producing only 5.32 mWh over the course of the four hour test. Test #3 and test #4 have very similar ambient air and water inlet temperatures, however test #4 had a total daily incident irradiance intensity which was approximately 67% less than test #3. This lower daily incident irradiance intensity results in the HPV-TEG system's photovoltaic module and TEG in test #4 to generate 13.81 Wh and 17.08 mWh less electricity than the HPV-TEG system's photovoltaic module and TEG in test #3.

The number of thermoelectric modules integrated into the 10-watt photovoltaic module was increased from two (10W-HPV-2TEG) to four (10W-HPV-4TEG). Similar to test #2, test #5 shows the performance of a 10W-HPV-4TEG under clear sky and sunny conditions, as shown in **Figure 4.41**. It can be observed in **Figure 4.42** that the difference between the PV module electrical energy generated by the 10W-PV and 10W-HPV-4TEG increases with irradiance intensity. In test #5, the power output of the 10W-HPV-4TEG

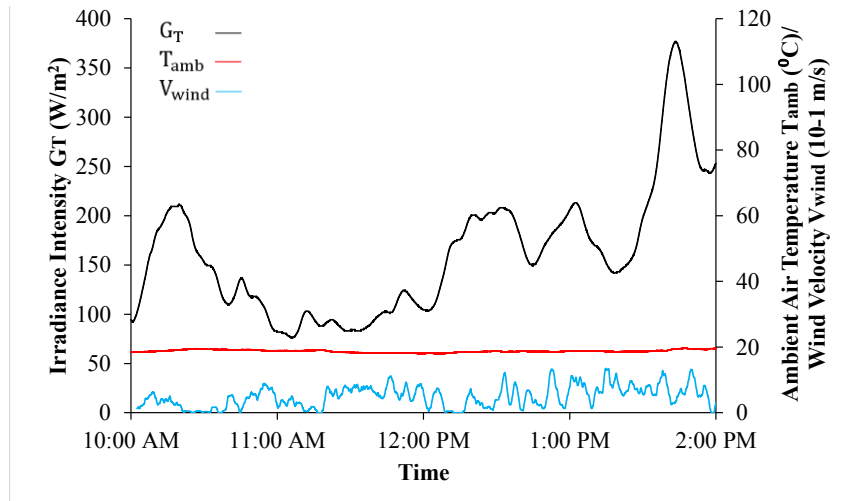


Figure 4.38: Corresponding incident irradiance intensity G_T , ambient air temperature T_{amb} , and wind speed V_{wind} vs. time (test #4).

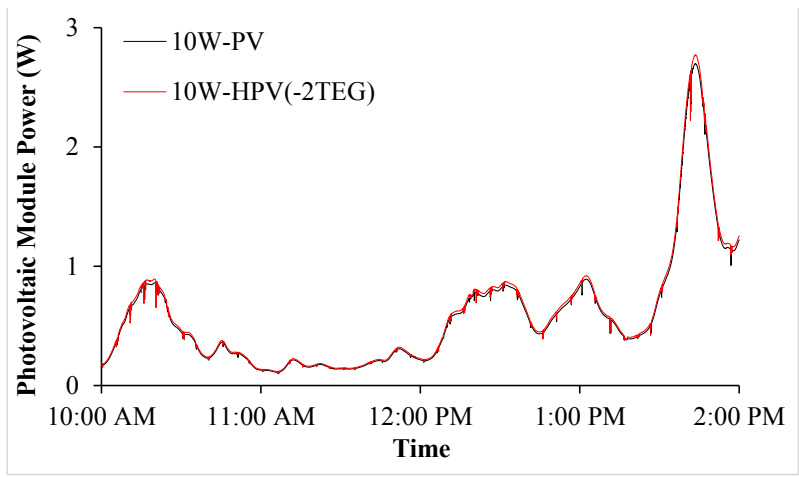


Figure 4.39: Power output of standard (10W-PV) and hybrid 10W-HPV(-2TEG) photovoltaic module vs. time (test #4).

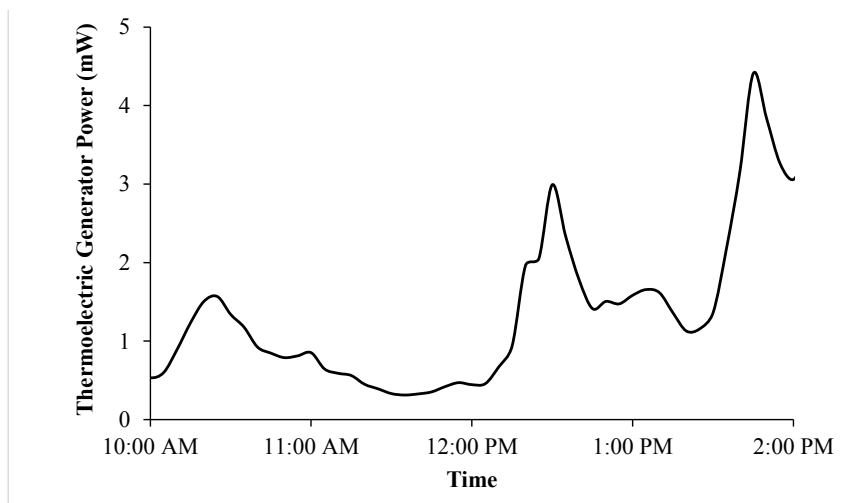


Figure 4.40: Thermoelectric generator (2TEG) power output vs. time (test #4).

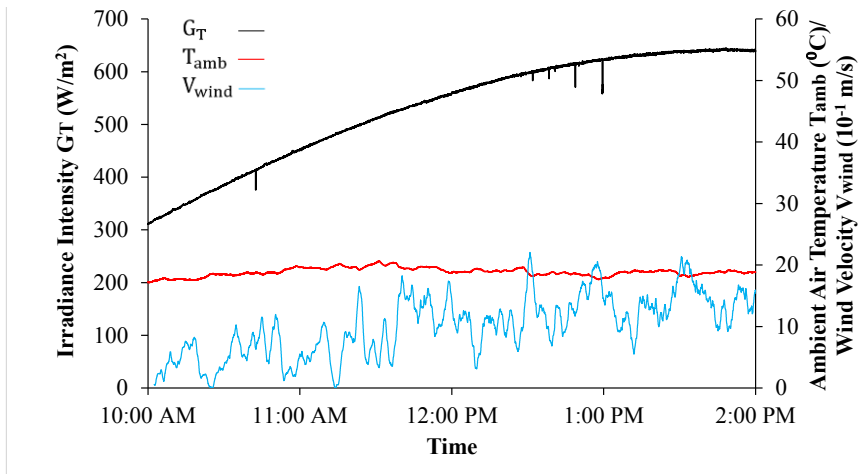


Figure 4.41: Corresponding incident irradiance intensity G_T , ambient air temperature T_{amb} , and wind speed V_{wind} vs. time (test #5).

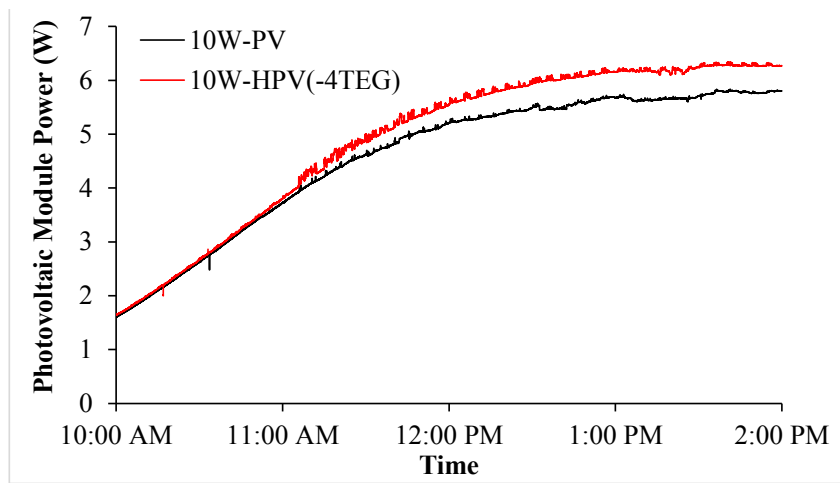


Figure 4.42: Power output of standard 10W-PV and hybrid 10W-HPV(-4TEG) photovoltaic module vs. time (test #5).

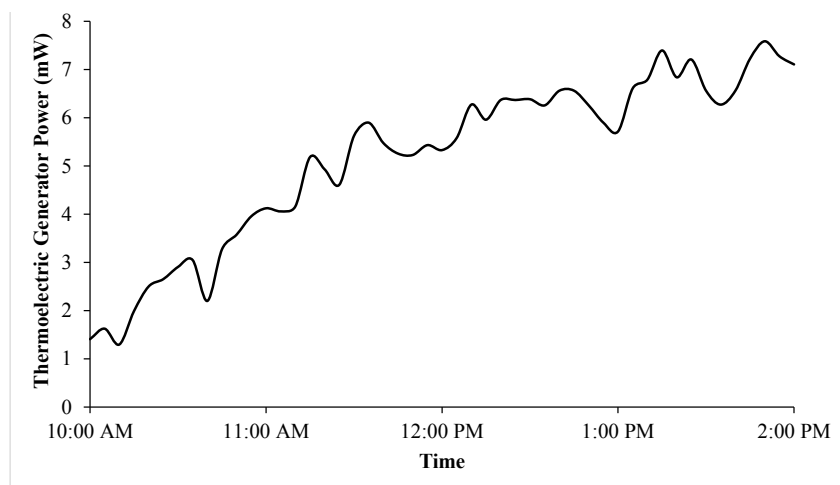


Figure 4.43: Thermoelectric generator (4TEG) power output vs. time (test #5).

system's photovoltaic module was approximately 1.65 W when the irradiance intensity was 313.1 W/m², and approximately 6.24 W when the irradiance intensity was increased to 636.9 W/m². The daily energy conversion efficiency of the 10W-HPV-4TEG system was 0.63% greater than the 10W-PV system. Power characteristics of test #5 highlights that as the irradiance intensity increases, the difference between the HPV-TEG and PV system power output increases, proposing that the HPV-TEG system is more feasible in geographical location with high irradiance intensities. Using experimental TEG data shown in **Figure 4.43**, it was determined that the overall daily efficiency of the 10W-HPV-4TEG system was increased by only 0.11% due to the electrical energy produced by the thermoelectric generator, suggesting that the main beneficial characteristic of the 10W-HPV-4TEG system's design is its ability to cool and increase the power output from the PV module.

It can be seen by comparing **Figure 4.32** and **Figure 4.41** that test #2 and test #5 have similar irradiance profiles, however the weather conditions of test #5 establish lower irradiance intensities than test #2. The daily average irradiance intensity for test #2 and test #5 was approximately 640.75 W/m² and 530.99 W/m². **Figure 4.43** demonstrates that the TEG in test #5 generates less electrical energy than the TEG in test #2 due to the lower irradiance intensity. The thermal profiles of the experimental study also concluded that the 10W-HPV-4TEG system's operating temperature was efficiently reduced using the water-cooling/TEG system, as shown in **Figure 4.44**. At 10:30 AM, the 10W-HPV-4TEG and 10W-PV operate at an irradiance intensity of 385.6 W/m² and an ambient air temperature equal to 18.51 °C. During this time, the temperature of the 10W-HPV-4TEG photovoltaic cells was 4 °C to 10 °C less than the temperature of the 10W-PV photovoltaic cells. The incident irradiance intensity and ambient air temperature for test #5 at 2:00 PM was about 639.4 W/m² and 18.82 °C. The minimum and maximum temperatures of the 10W-PV module at 2:00 PM are approximately 28.8 °C and 33.7 °C, while the minimum and maximum temperatures of the 10W-HPV-4TEG module are approximately 19.7 °C and 27.4 °C. It is evident from the thermal performance graphs that the decrease of the photovoltaic cell temperature increases the power output of the hybrid system's photovoltaic module, allowing it to generate an extra 1.3 Wh during test #5.

The performance of the 10W-HPV-4TEG was investigated under low irradiance intensities and with a daily average water inlet temperature greater than the daily average

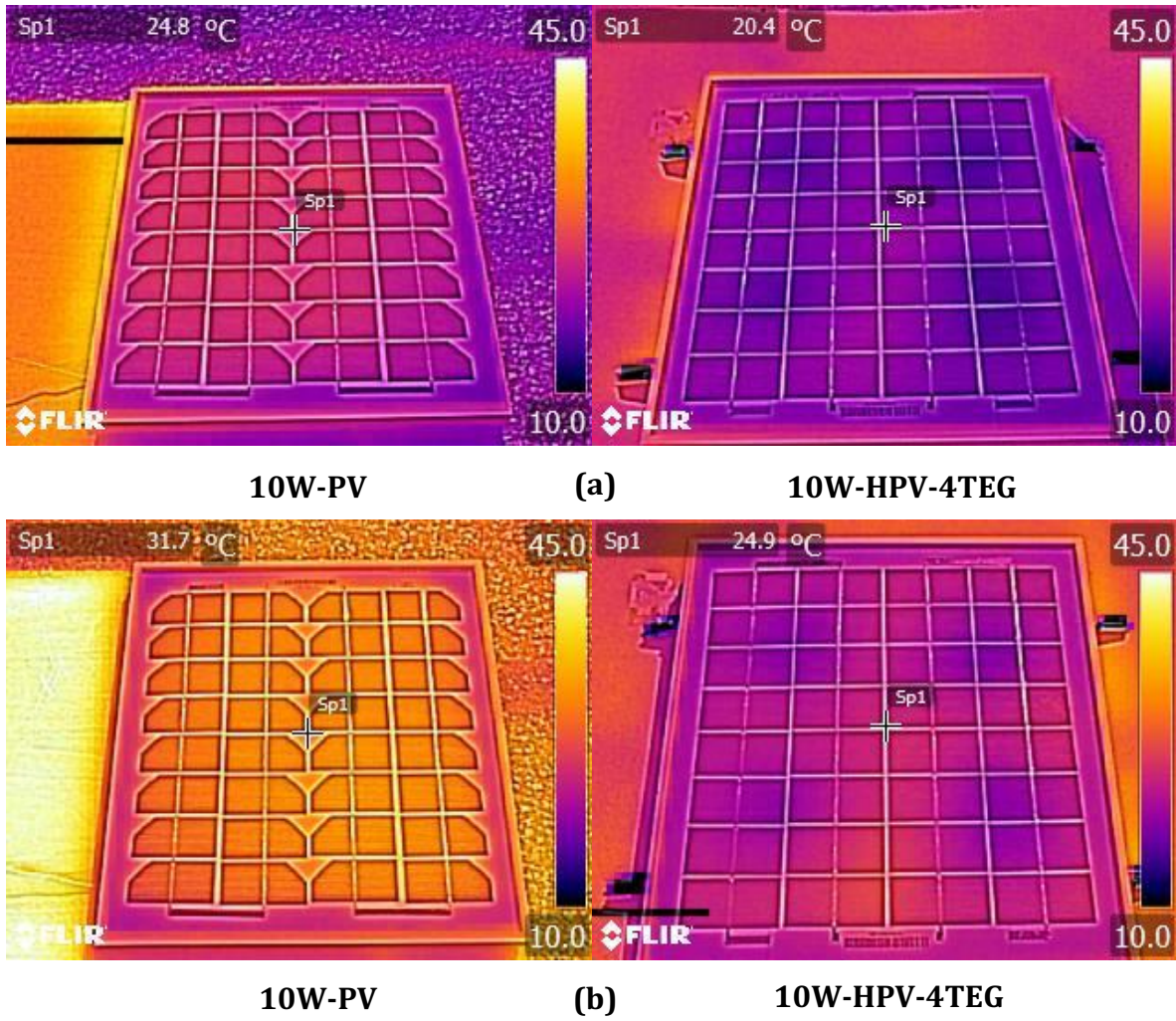


Figure 4.44: Thermal profile of 10W-PV and 10W-HPV-4TEG (a) 10:30 AM and (b) 2:00PM (test #5).

ambient air temperature in test #6 and test #7. The weather conditions of test #6 are illustrated in **Figure 4.45**. The PV and HPV-TEG system in test #6 experience frequent periods of cloudiness and sunshine. According to the results shown in **Figure 4.46**, the total energy generated by the 10W-HPV-4TEG and 10W-PV photovoltaic module was approximately 11.90 Wh and 12.58 Wh for test #6. The power generated by the HPV-TEG system's module ranges from 0.12 W and 7.63 W due to the irradiance intensity varying between 96.9 W/m² to 944.4 W/m² throughout the day. **Figure 4.47** presents the thermoelectric generator power output of test #6 versus time. For this test, the minimum and maximum TEG power produced was approximately 0.01 mW and 18.7 mW. The minimum TEG power output of approximately 0.01 mW occurs at 1:15 PM and 2:00 PM at a low incident irradiance intensity of 210.6 W/m² and 221.9 W/m² respectively.

The weather conditions and performance of the 10W-HPV-4TEG system in test #7 may be examined in **Figures 4.48-4.50**. Test #6 and test #7 have very comparable daily average ambient air temperatures, establishing daily average ambient air temperatures of approximately 12.70 °C and 12.68 °C, respectively. Test #6 and test #7 also have very comparable daily average daily average water inlet temperatures, establishing daily average water inlet temperatures of approximately 15.05 °C and 14.83 °C, respectively. However, there is a noticeable difference between the amount of solar radiation that occurred for each test when analyzing **Figure 4.45** and **Figure 4.48**. **Figure 4.48** shows that for test #7, the irradiance intensity remains less than 300 W/m² until approximately 1:15 PM, then irregular short durations of sunlight occur for the remainder of the experiment. The power output of the 10W-PV and 10W-HPV-4TEG photovoltaic module is shown in **Figure 4.49**. The 10W-HPV-4TEG photovoltaic module has a larger power output than the standard 10 watt photovoltaic module for the entire duration of test #7. For example, at 11:15 PM (test #7), the 10W-HPV-4TEG photovoltaic module produces 1.53 W, while the 10W-PV photovoltaic module produces 1.62 W. **Figure 4.50** shows that the thermoelectric generator produces low amounts of electrical energy due to the small amount of thermal energy transferred to each thermoelectric module. The thermoelectric generator requires long intervals of high irradiance intensity or a large difference between the water inlet temperature and ambient air temperature to establish a sufficient temperature gradient and power output. Therefore, due to the conditions of test #7, the TEG only produces 1.60 mWh of electrical energy. The

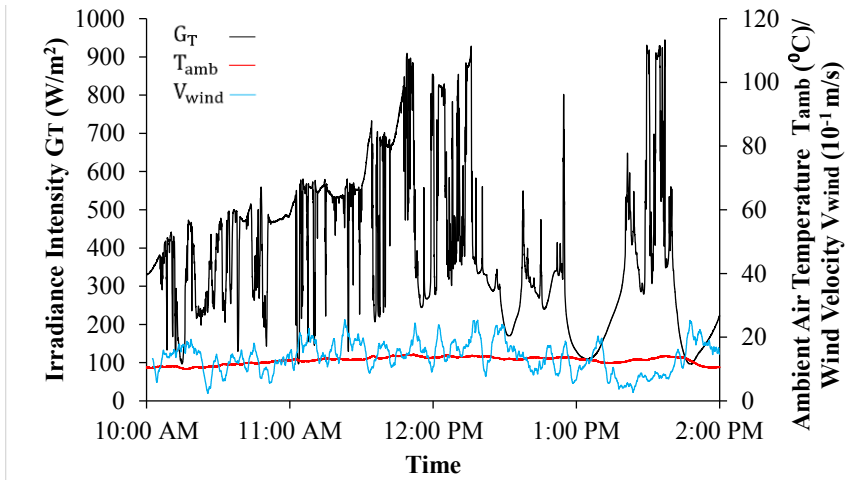


Figure 4.45: Corresponding incident irradiance intensity G_T , ambient air temperature T_{amb} , and wind speed V_{wind} vs. time (test #6).

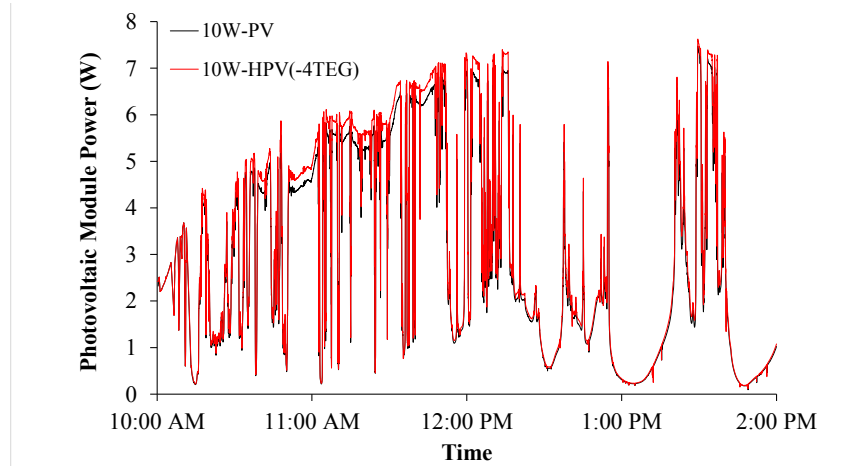


Figure 4.46: Power output of standard 10W-PV and hybrid 10W-HPV(-4TEG) photovoltaic module vs. time (test #6).

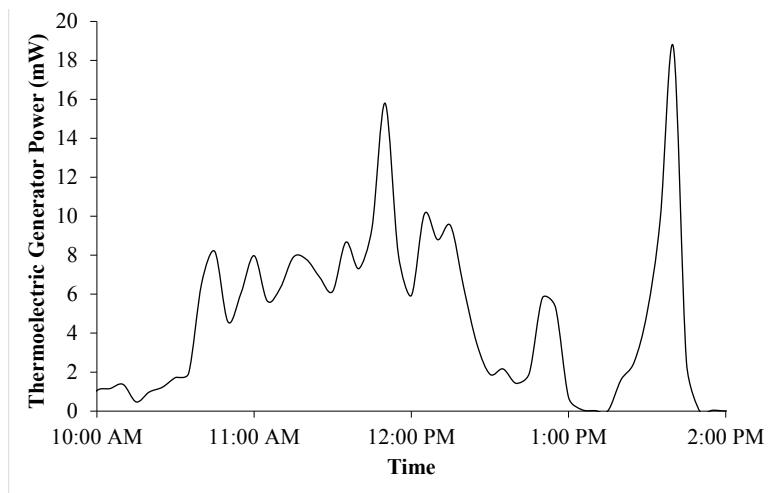


Figure 4.47: Thermoelectric generator (4TEG) power output vs. time (test #6).

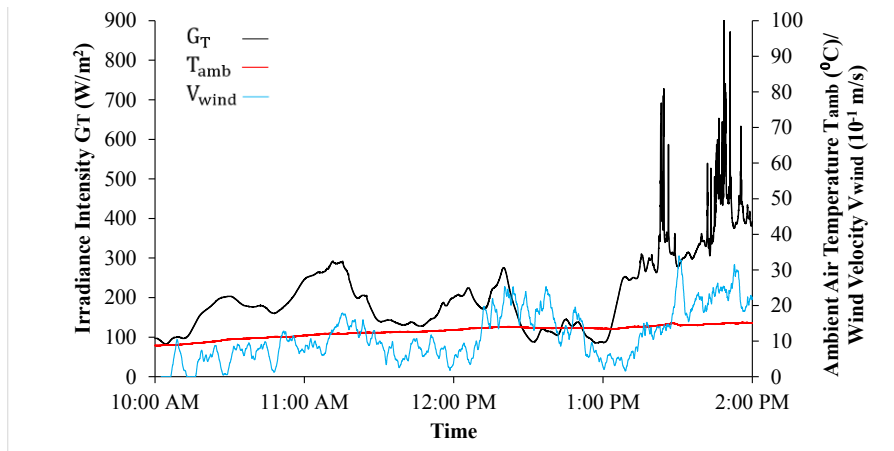


Figure 4.48: Corresponding incident irradiance intensity G_T , ambient air temperature T_{amb} , and wind speed V_{wind} vs. time (test #7).

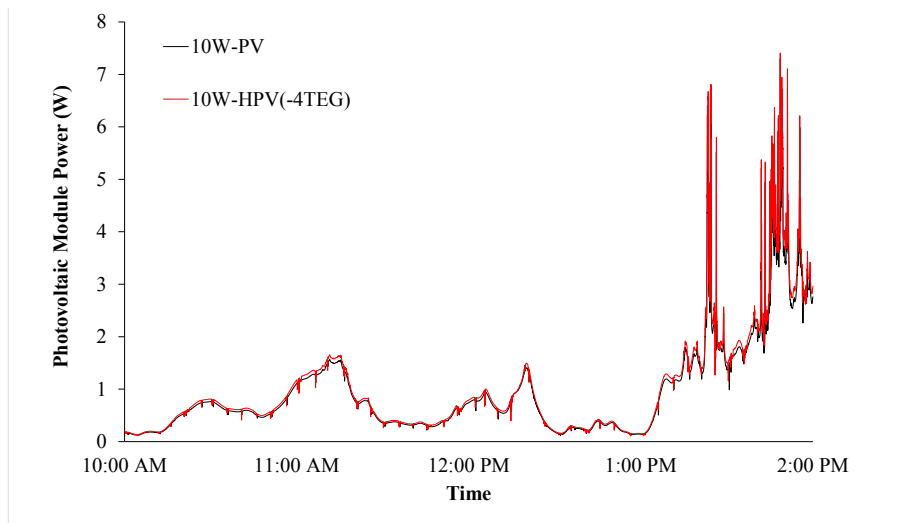


Figure 4.49: Thermoelectric generator (4TEG) power output vs. time (test #7).

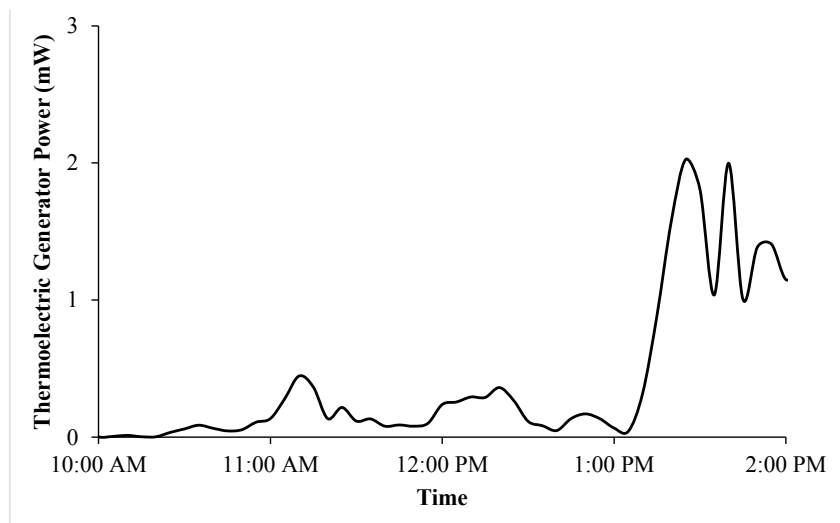


Figure 4.50: Thermoelectric generator (4TEG) power output vs. time (test #7).

experimental results of test #6 and test #7 have provided conclusive evidence that the 10W-HPV-4TEG system has the capability to produce more electrical energy than the standard 10W-PV system even though the water inlet temperature is not supplied at a low temperature.

The larger HPV-TEG system comprised of a 40-watt photovoltaic module and 10 thermoelectric modules (40W-HPV-10TEG) was orientated horizontally and investigated in test #8. The results of test #8 are presented in **Figures 4.51-4.53**. The weather during test #8 was a mix of sunny and cloudy periods, as shown in **Figure 4.51**. The total daily incident irradiance intensity for test #8 was calculated to be 2231.54 Wh/m². The daily average ambient air temperature of test #8 was approximately 19.28 °C. When analyzing the experimental data shown in **Figure 4.52**, it was calculated that the 40W-HPV-10TEG photovoltaic module generated approximately 0.45 Wh more electrical energy than the 40W-PV photovoltaic module. Although the 40W-HPV-10TEG has a larger photovoltaic module than the tests previously discussed, the designed cooling system was able to efficiently remove the waste-heat at a rate that noticeably increases the power output of the 40W-HPV-10TEG system's photovoltaic module. In **Figure 4.53**, it is apparent that the cloudy periods in the afternoon significantly decrease the power produced by the thermoelectric generator. These cloud periods occur from approximately from 12:20 PM to 12:38 PM, from 12:46 PM to 1:06 PM, and from 1:10 PM to 1:37 PM. The low irradiance intensity caused by the cloudy periods establishes a TEG power output of 19.92 mW, 15.74 mW, and 12.89 mW at 12:30 PM, 1:00 PM, and 1:20 PM respectively during test #8. In test #8, the thermoelectric generator has a maximum and minimum power output of approximately 54.54 mW and 12.88 mW, respectively.

The performance of the 40W-HPV-10TEG system at a tilt angle of approximately 48° (latitude) was studied in tests #9-#12. The experimental results of the first test (test #9) completed with the tilted 40W-HPV-10TEG system are given in **Figures 4.54-4.56**. The increase of the incident solar radiation by tilting the photovoltaic system is clearly represented in **Figure 4.54** by the difference between the incident solar radiation (G_T) and solar radiation on a horizontal plane (G). The daily total irradiance on a horizontal plane and the incident irradiance from 10 AM to 2 PM was determined to be approximately 2902.53

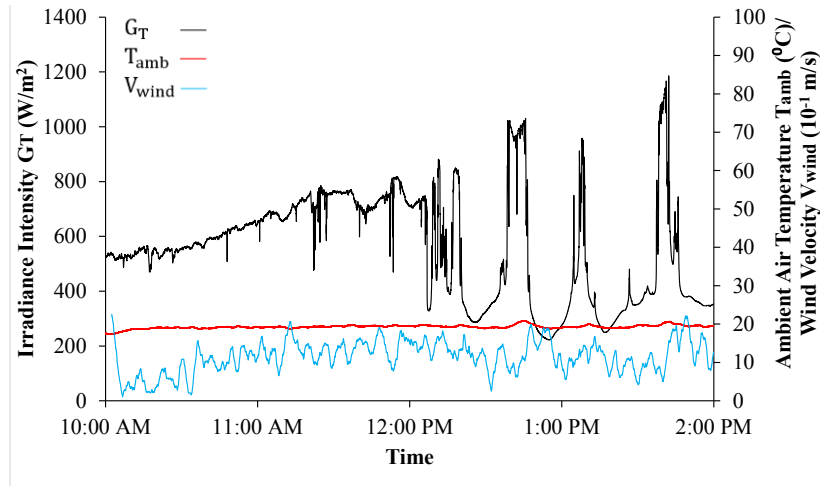


Figure 4.51: Corresponding incident irradiance intensity G_T , ambient air temperature T_{amb} , and wind speed V_{wind} vs. time (test #8).

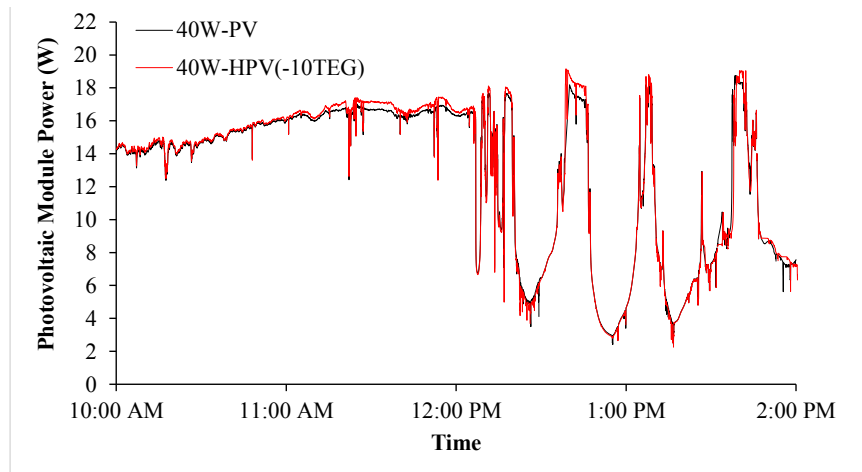


Figure 4.52: Power output of standard 10W-PV and hybrid 10W-HPV(-4TEG) photovoltaic module vs. time (test #8).

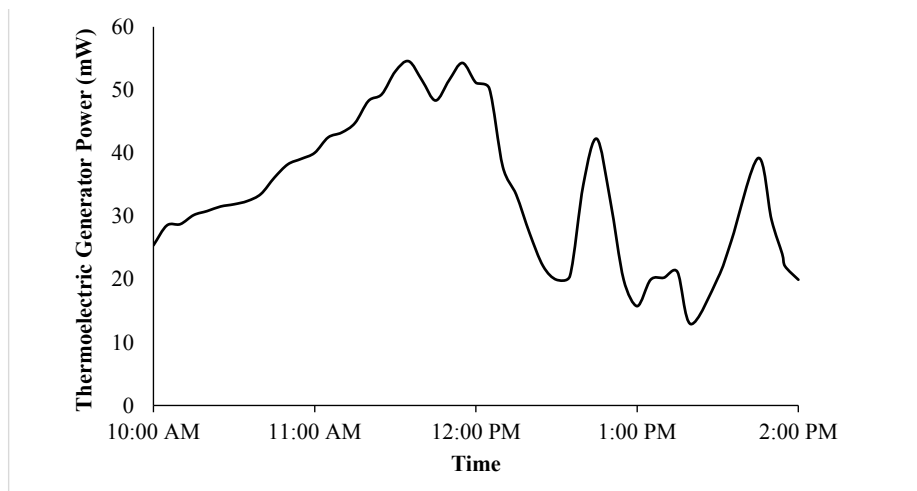


Figure 4.53: Thermoelectric generator (4TEG) power output vs. time (test #8).

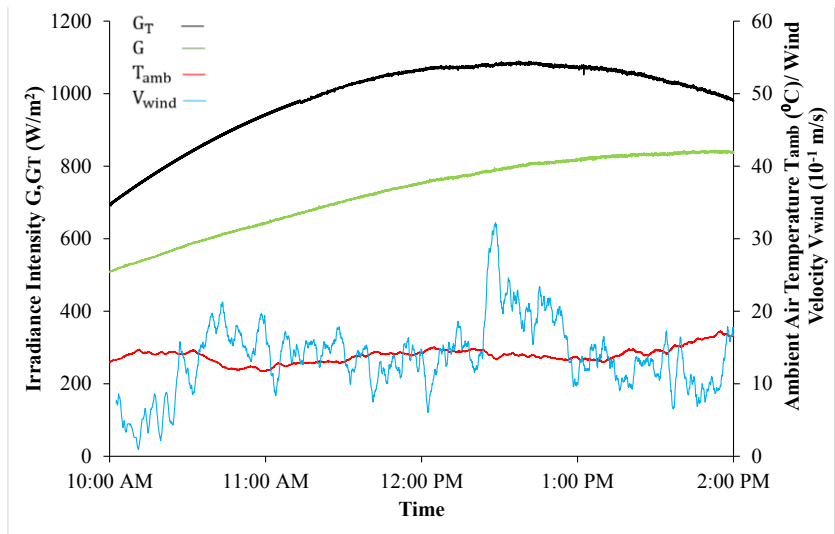


Figure 4.54: Incident irradiance intensity G_T , irradiance intensity on horizontal plane G , ambient air temperature T_{amb} , and wind speed V_{wind} vs. time (test #9).

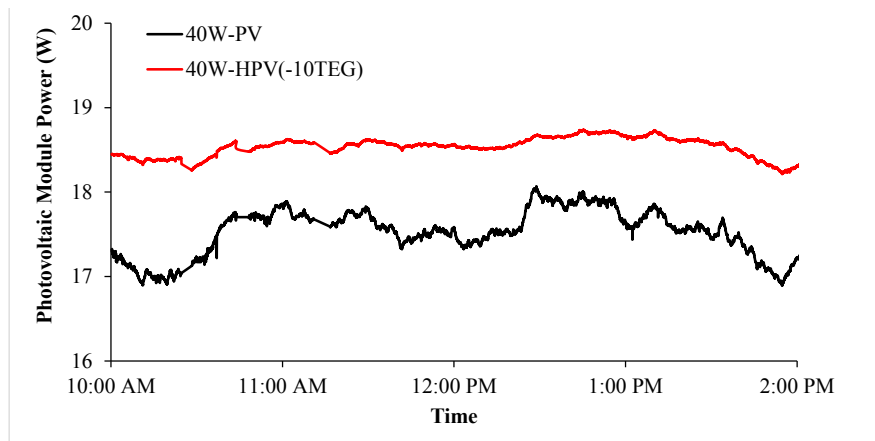


Figure 4.55: Power output of standard 10W-PV and hybrid 10W-HPV(-10TEG) photovoltaic module vs. time (test #9).

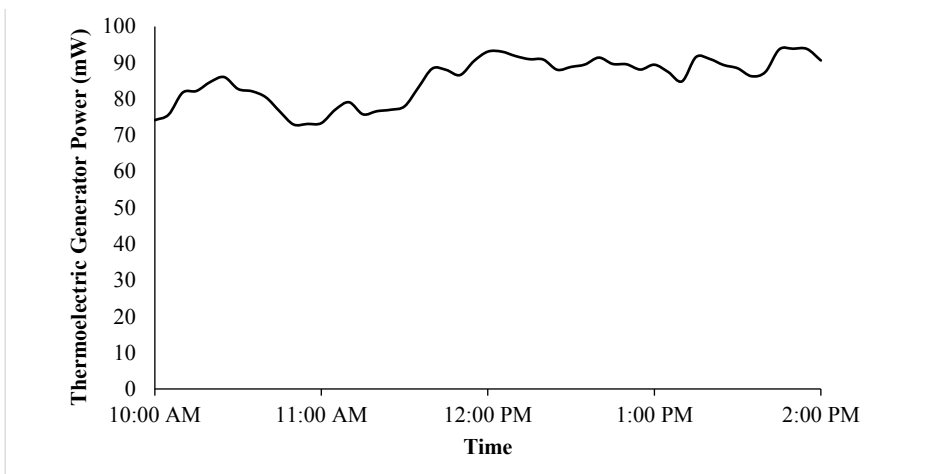


Figure 4.56: Thermoelectric generator (10TEG) power output vs. time (test #9).

Wh/m² and 3957.78 Wh/m². **Figure 4.55** shows that for test #9, the 40W-HPV-10TEG photovoltaic module constantly produces more electrical energy than the standard 40W-PV photovoltaic module. The difference in power generated between the 40W-PV and 40W-HPV-10TEG photovoltaic module ranges between approximately 0.6 W and 1.5 W throughout the duration of test #9. The power output of the photovoltaic modules does not fluctuate significantly during test #9, suggesting that the constant electrical load condition implemented in this test setup does not significantly vary the electrical energy generated by the photovoltaic modules when the irradiance intensity was greater than 700 W/m². The total daily electrical energy generated by the 40W-PV and 40W-HPV-10TEG photovoltaic modules was determined to be 70.11 Wh and 74.14 Wh. The thermoelectric generator output for test #9 establishes a minimum and maximum power output of 72.88 mW and 107.54 mW, as shown in **Figure 4.56**. In test #9, the thermoelectric generator's electrical output was also fairly stable and does not deviate by more than 15% from the TEG power output average. The HPV-TEG system's thermoelectric generator can produce a reliable power output while operating under the weather conditions given in **Figure 4.54**. It is also apparent that the 40W-HPV-10TEG system produces a significantly larger amount of power from its thermoelectric generator than the 10W-HPV-2TEG and 10W-HPV-4TEG case studies investigated in test #1 to test #7. This larger power output from the 40W-HPV-10TEG system's TEG is due to the system having a greater quantity of thermoelectric modules and a higher temperature gradient, as shown in **Figure 4.57**. The 10W-HPV-4TEG system's thermoelectric generator in test #5 experiences temperature gradients ranging from 1.4 °C to 6.1 °C, whereas the 40W-HPV-10TEG system's thermoelectric generator in test #9 experiences temperature gradients ranging from 15.1 °C to 18.2 °C. The 40W-HPV-10TEG system's ability to maintain a lower temperature profile than the 40W-PV system is depicted in **Figure 4.58**. The temperature of the 40W-PV system's photovoltaic cells at 12:00 PM (test #9) ranged from 26.7 °C to 39.3 °C. As expected, the temperature of the 40W-HPV-10TEG system's photovoltaic cells at 12:00 PM (test #9) was lower, ranging between 20.8 °C to 39.2 °C. The 40W-HPV-10TEG system's cooling uniformly reduces the temperature of the photovoltaic cells. Test #9 has confirmed that it is possible to increase the power output and reduce the overall temperature of a large 40-watt photovoltaic module using the designed TEG/cooling system under clear sky and sunny conditions.

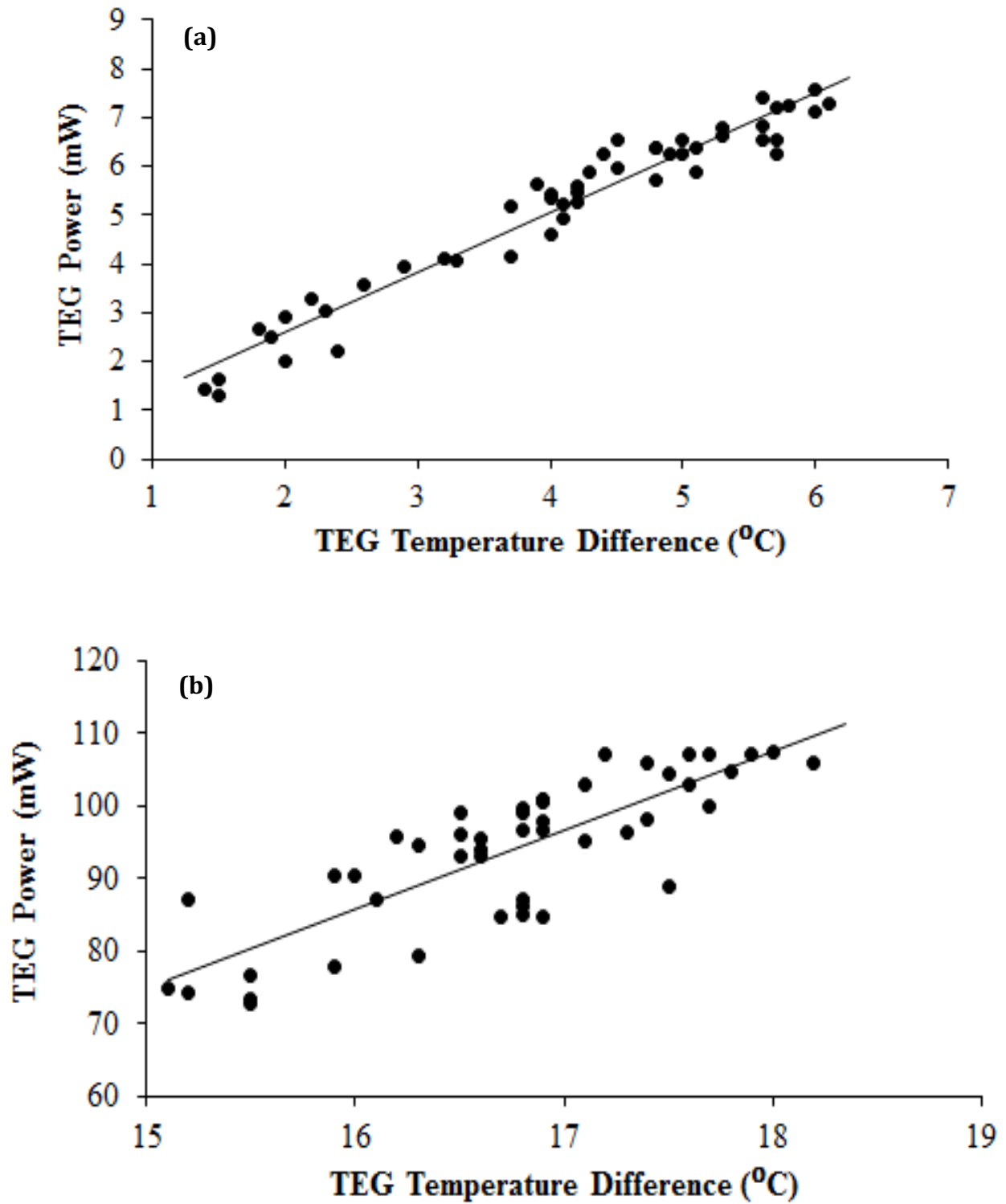


Figure 4.57: Thermoelectric generator power vs. TEG temperature difference for (a) 4TEG (test #5) and (b) 10TEG (test #9).

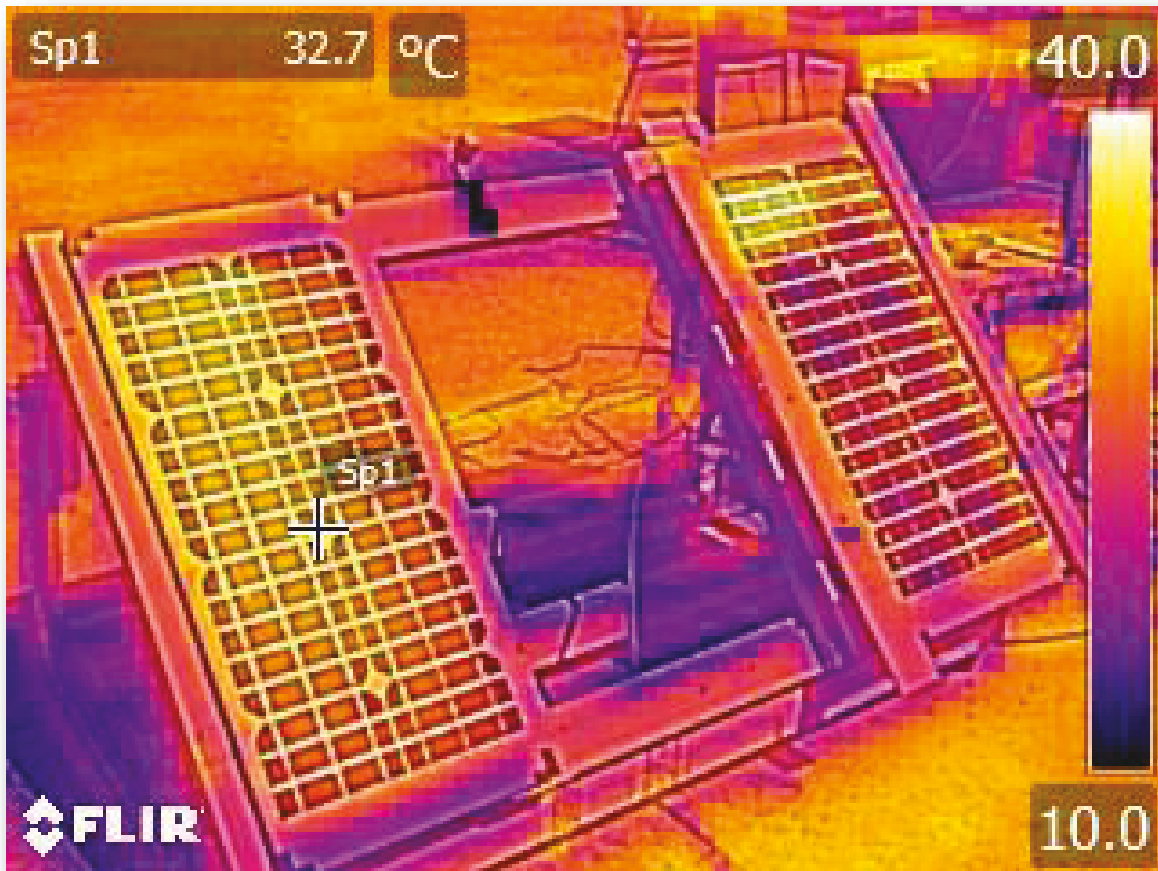


Figure 4.58: Thermal profile of 40W-PV (left side) and 40W-HPV-10TEG (right side) at 12:00 PM (test #9).

The 40W-HPV-10TEG system was further investigated in test #10 and test #11. Test #10 and test #11 obtained very similar results to test #9 with a daily average water inlet temperature of 9.41 °C and 9.23 °C, respectively. The results of test #10 are shown from **Figures 4.59-4.62**. From the recorded weather conditions of test #10 shown in **Figure 4.59**, it was found that the total daily incident irradiance intensity and ambient air temperature was 4212.18 W/m² and 16.84 °C, respectively. **Figure 4.60** provides further evidence that the 40W-HPV-10TEG system's photovoltaic module is able to continuously outperform the 40W-PV photovoltaic module. The 40W-HPV-10TEG photovoltaic module produces 2.51% more electrical energy than the 40W-PV photovoltaic module over the four hour test #10. **Figure 4.61** presents the thermoelectric power output as a function of time. Continuous solar radiation and the warm atmospheric conditions of test #10 produce a TEG power output greater than 73 mW throughout the experiment. The total daily TEG electrical energy generated equal to 341.10 mWh was achieved during test #10 due to the high irradiance intensity, high ambient air temperature, and low water inlet temperature. The daily efficiency of the 40W-PV and 40W-HPV-10TEG system was calculated to be 6.54% and 6.70%, respectively. Detailed thermal profiles of the 40W-PV and 40W-HPV-10TEG systems at 1:45 PM during test #10 are shown in **Figure 4.62**. It was observed that ~80% of the 40W-HPV-10TEG system operated at a temperature less than 28 °C, whereas the majority of the 40W-PV system operated at temperatures ranging from 28 °C to 35 °C.

The weather conditions of test #11 are shown in **Figure 4.63**. Test #11 has a similar irradiance intensity profile to test #9 and test #10, however test #11 experienced very high wind speeds, recording a daily average wind speed of 3.05 m/s. Based on the experimental results shown in **Figure 4.64**, the HPV-TEG photovoltaic module generated approximately 2.33 Wh of additional electricity compared to the 40W-PV photovoltaic module in test #11. The thermoelectric generator's minimum and maximum power output for test #11, shown in **Figure 4.65**, was about 57.42 mW and 88.72 mW. The total energy generated by the TEG during test #11 was calculated to be 309.26 mWh. It was observed that the high wind speeds during test #11 did not have a major impact on the electrical power characteristics of the PV and HPV-TEG system.

Tests #9 to #11 show that the 40W-HPV-10TEG system can consistently reduce the operating temperature of the photovoltaic module, generate more electricity than the

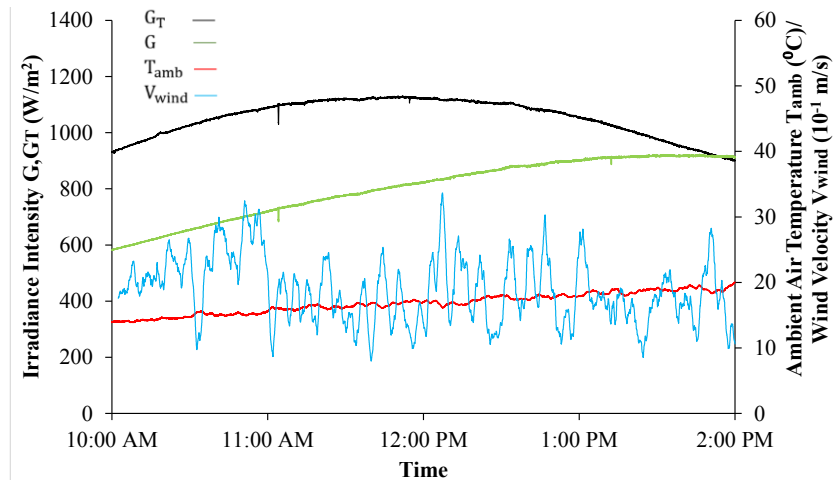


Figure 4.59: Incident irradiance intensity G_T , irradiance intensity on horizontal plane G , ambient air temperature T_{amb} , and wind speed V_{wind} vs. time (test #10).

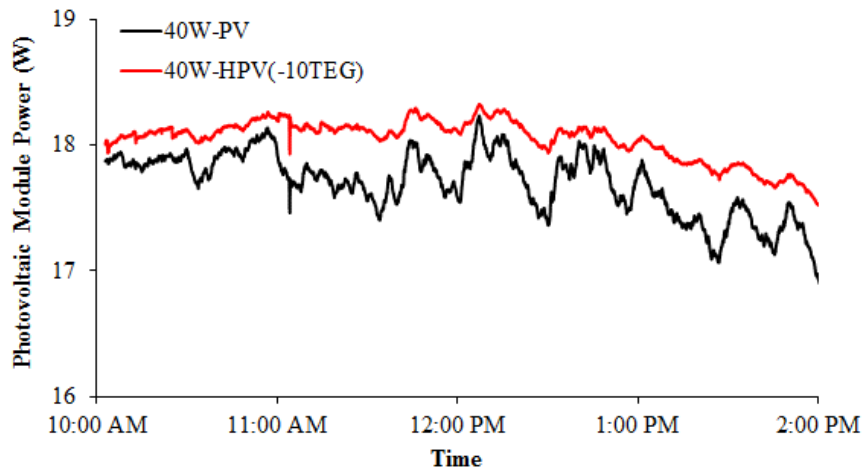


Figure 4.60: Power output of standard 10W-PV and hybrid 10W-HPV(-10TEG) photovoltaic module vs. time (test #10).

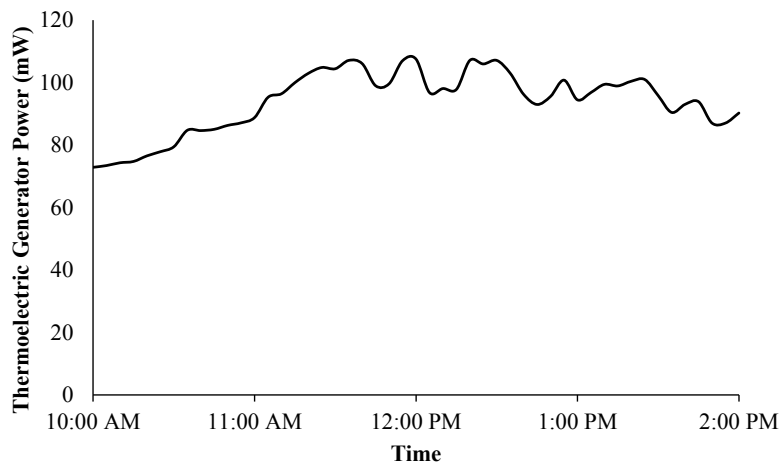
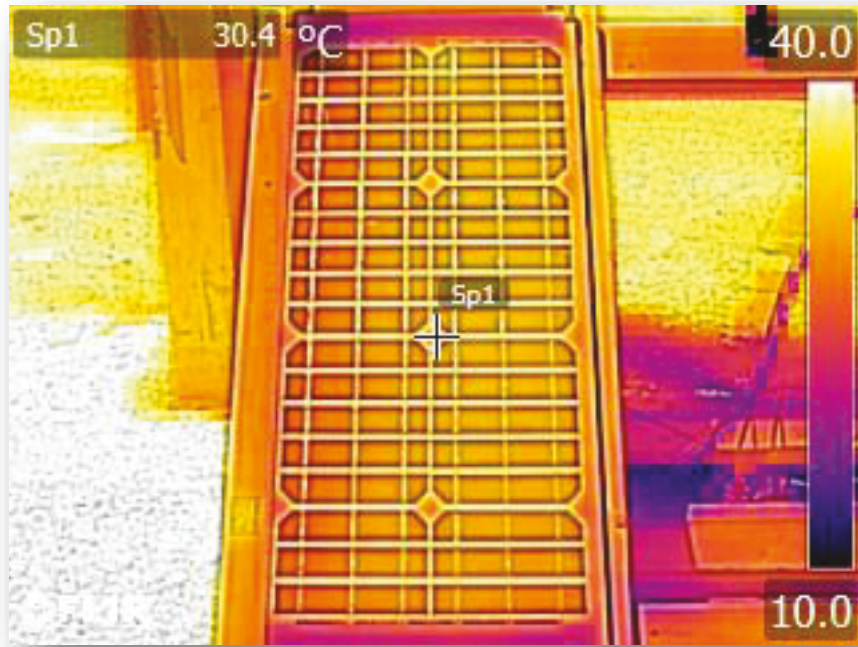
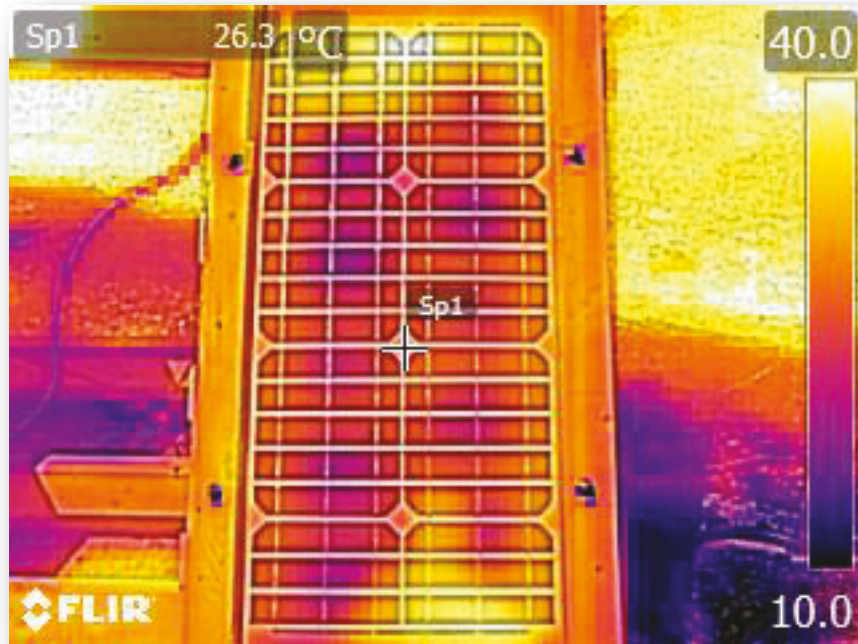


Figure 4.61: Thermoelectric generator (10TEG) power output vs. time (test #10).



(a)



(b)

Figure 4.62: Thermal profile of (a) 40W-PV and (b) 40W-HPV-10TEG at 1:45 PM (test #10).

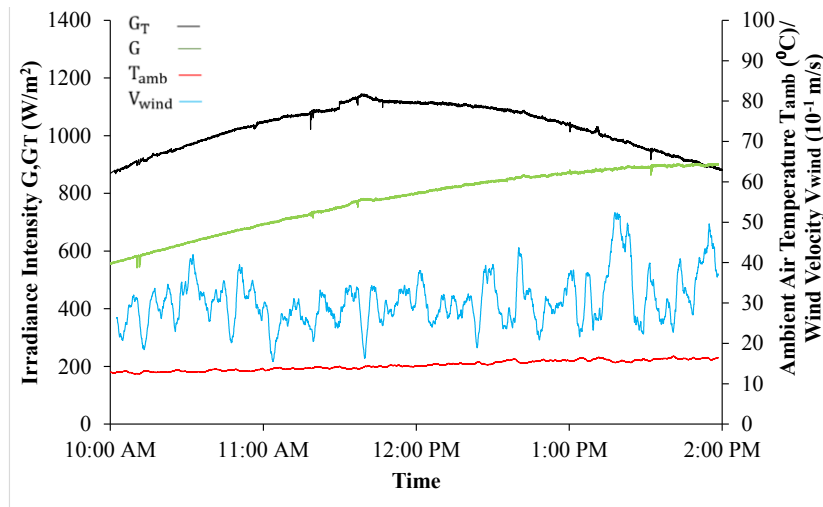


Figure 4.63: Incident irradiance intensity G_T , irradiance intensity on horizontal plane G , ambient air temperature T_{amb} , and wind speed V_{wind} vs. time (test #11).

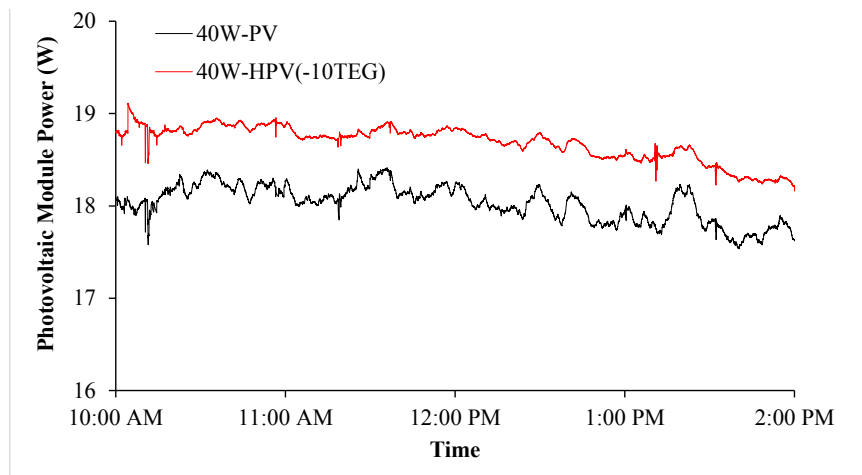


Figure 4.64: Power output of standard 10W-PV and hybrid 10W-HPV(-10TEG) photovoltaic module vs. time (test #11).

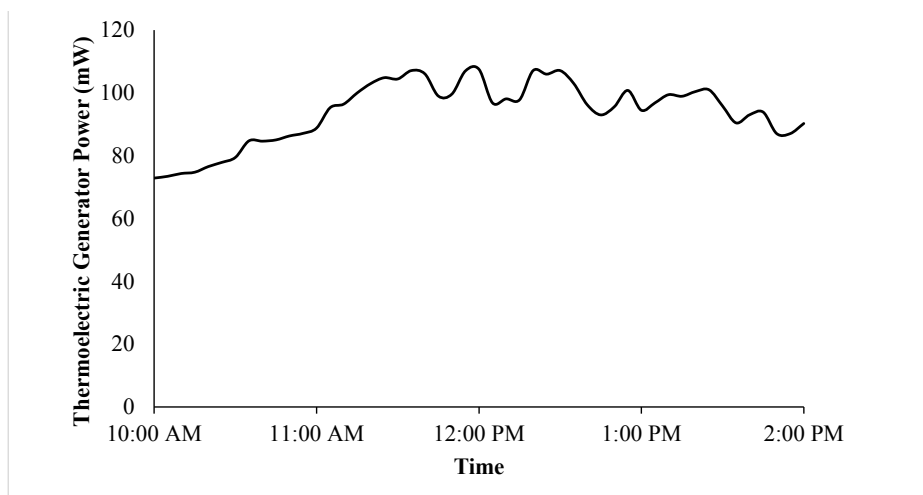


Figure 4.65: Thermoelectric generator (10TEG) power output vs. time (test #11).

conventional photovoltaic module, and produce electrical energy from the thermoelectric generator that consistently exceeds 60 mW. The 40W-HPV-10TEG system's higher photovoltaic module and thermoelectric generator power output may be attributed to the higher incident irradiance intensity established by tilting the HPV-TEG system to 48.38 degrees.

The final outdoor experimental test #12 investigated the performance of the 40W-HPV-10TEG system with a relatively high water inlet temperature. The results of the final test are shown in **Figures 4.66-4.68**. The daily average water inlet temperature for test #12 was approximately 19.71 °C. It is evident from **Figure 4.27** that the previous completed tests #8-#11 using the 40W-HPV-10TEG system have a significantly lower water inlet temperature. The weather conditions of test #11 are given in **Figure 4.66**. Test #12 obtained the highest daily average ambient air temperature of all outdoor tests, at 26.17 °C. Nevertheless, the 40W-HPV-10TEG was still able to outperform the conventional 40-watt photovoltaic module with a relatively high water inlet temperature. The power output of the conventional and hybrid photovoltaic modules with respect to time is presented in **Figure 4.67**. The 40W-HPV-10TEG photovoltaic module generates a total of 1.14 Wh more electrical energy than the 40W-PV photovoltaic module during test #12. Examining **Figure 4.66** and **Figure 4.67** shows that short periods of cloud cover from 1:30 PM to 2:00 PM significantly reduces the electrical power output of both photovoltaic modules. During test #12, the power output of the hybrid system's photovoltaic module ranges from 1.54 W to 17.50 W. In **Figure 4.68**, it is clear that the short periods of cloud cover also decrease the overall power output of the thermoelectric generator. For example, prior to the cloud cover at 1:20 PM for test #12, the TEG produces 62.4 mW at an incident irradiance intensity of 989.4 W/m². During the duration of the first cloud cover, the irradiance intensity and TEG power output at 1:30 PM decreases to 165.6 W/m² and 33.3 mW, respectively.

Summary of the weather conditions and performance characteristics of the various case studies and corresponding tests are given in **Table 4.4** and **Table 4.5**. For each test, the total daily energy generated by the HPV-TEG system's photovoltaic module (equation 4.7) is greater than the total daily power generated by the standard photovoltaic module (equation 4.6). The minimum total daily TEG electrical energy output of 1.60 mWh was obtained in test #7. In comparing test #6 and test #7, it is evident that even though both tests have similar

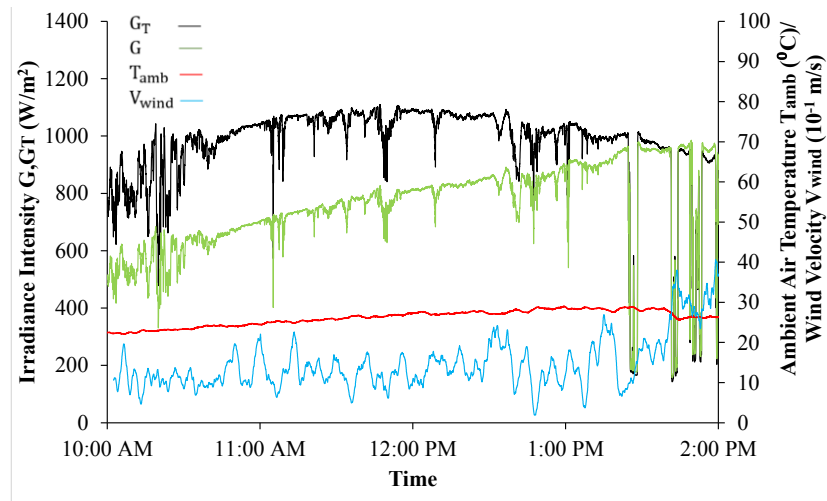


Figure 4.66: Incident irradiance intensity G_T , irradiance intensity on horizontal plane G , ambient air temperature T_{amb} , and wind speed V_{wind} vs. time (test #12).

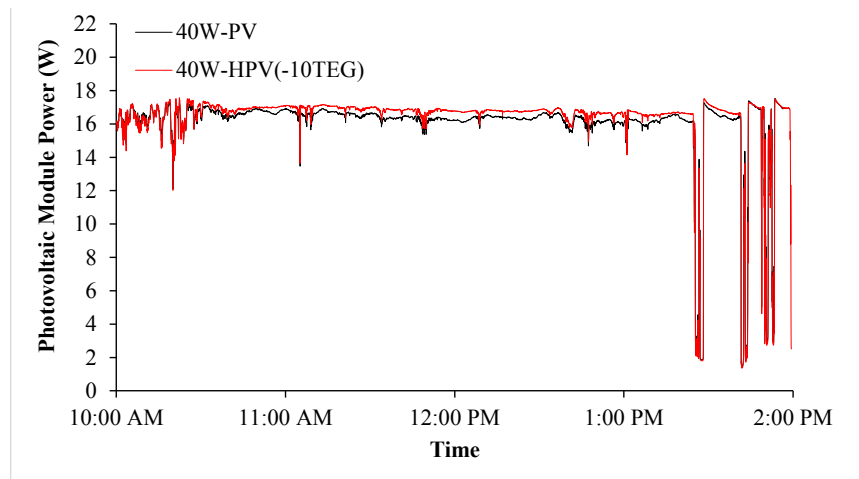


Figure 4.67: Power output of standard 10W-PV and hybrid 10W-HPV(-10TEG) photovoltaic module vs. time (test #12).

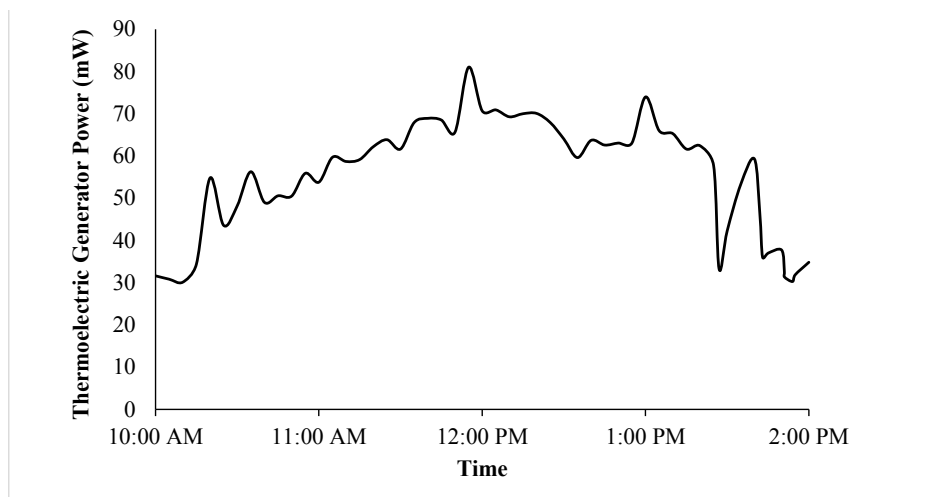


Figure 4.68: Thermoelectric generator (10TEG) power output vs. time (test #12).

Table 4.4: Summary of weather conditions for each outdoor experimental test.

Test #	Case Study	Total Daily Incident Irradiance Intensity (Wh/m ²)	Daily Average Ambient Air Temperature (°C)	Daily Average Water Inlet Temperature (°C)	Daily Average Wind Velocity (m/s)
1	10W-HPV-2TEG	2485.34	23.04	19.85	1.09
2	10W-HPV-2TEG	2563.05	18.33	19.21	1.25
3	10W-HPV-2TEG	1945.10	19.88	18.5	1.18
4	10W-HPV-2TEG	642.59	19.74	17.39	0.49
5	10W-HPV-4TEG	2123.99	18.87	17.86	1.00
6	10W-HPV-4TEG	1546.65	12.70	15.05	1.38
7	10W-HPV-4TEG	832.14	12.68	14.83	1.15
8	40W-HPV-10TEG	2231.54	19.28	9.55	1.16
9	40W-HPV-10TEG	3957.78	13.92	8.89	1.37
10	40W-HPV-10TEG	4212.18	16.84	9.41	1.88
11	40W-HPV-10TEG	4108.1	14.57	9.23	3.055
12	40W-HPV-10TEG	3867.27	26.17	19.71	1.48

Table 4.5: Summary of performance characteristics of standard photovoltaic module (PV), hybrid system's photovoltaic module (HPV), and thermoelectric generator (TEG) for each outdoor test.

Test #	Case Study	Total PV Power (Wh) E_{PV}	Total Daily HPV Power (Wh) E_{HPV}	Total Daily TEG Power (mWh) E_{TEG}
1	10W-HPV-2TEG	20.45	21.66	108.16
2	10W-HPV-2TEG	21.94	23.13	51.66
3	10W-HPV-2TEG	15.29	16.21	22.4
4	10W-HPV-2TEG	2.32	2.40	5.32
5	10W-HPV-4TEG	18.39	19.69	20.76
6	10W-HPV-4TEG	11.90	12.58	19.71
7	10W-HPV-4TEG	3.8	4.04	1.60
8	40W-HPV-10TEG	51.02	51.47	136.08
9	40W-HPV-10TEG	70.11	74.14	341.31
10	40W-HPV-10TEG	70.52	71.91	377.1
11	40W-HPV-10TEG	72.11	74.74	309.26
12	40W-HPV-10TEG	64.00	65.14	227.77

daily average ambient air and water inlet temperatures, test #7 operates under a significantly lower total daily incident irradiance intensity which impedes the performance of the thermoelectric generator. In test #10, the power produced by the thermoelectric generator (10TEG) accounts for approximately 0.52% of the total electrical energy generated by the 40W-HPV-10TEG system. In comparison, the power generated by the thermoelectric generator (4TEG) in test #7 accounts for approximately 0.04% of the total power generated by the 10W-HPV-4TEG system. As expected, the overall daily efficiency of the standard photovoltaic system (equation 4.9) was less than the overall daily efficiency of the HPV-TEG system (equation 4.10) for all outdoor tests, as shown in **Figure 4.69**. The minimum overall daily efficiency of 3.68% occurred in test #4, while the HPV-TEG system in test #5 established the maximum overall daily efficiency of 9.45%. The minimum difference of 1.15% between the overall daily efficiency of the HPV-TEG system and the PV system occurred in test #4. Furthermore, the maximum difference of 7.18% between the overall daily efficiency of the HPV-TEG system and PV system occurred in test #5. When analyzing all of the outdoor tests, the HPV-TEG system establishes an average daily efficiency approximately 4.79% greater than the conventional PV system.

Based on the experimental data provided by the outdoor tests, a sizing correlation was determined to estimate the power density of a HPV-TEG system's thermoelectric generator. The power density of the thermoelectric generator may be given as the ratio of TEG power output to the area of the photovoltaic module (P_{TEG}/A_{PV}). Previously discussed experimental case studies found that the irradiance intensity, water inlet temperature, and ambient air temperature were significant operating conditions that influence the performance of the HPV-TEG system. Therefore, TEG power density as a function of the variable $G_T T_{amb}/T_{w,in}$ was investigated, as shown in **Figure 4.70**. The power density of the thermoelectric generator increases nonlinearly with respect to the operating condition variable. Analysis of **Figure 4.70** suggests that the thermoelectric generator power density increases as the irradiance intensity increases, as the ambient air temperature increases, and as the water inlet temperature decreases. The line of best fit shown in **Figure 4.70** represents the sizing correlation developed based on the outdoor experimental data using the method of least squares [149]. The following sizing correlation may be used to estimate the power density of a HPV-TEG system's thermoelectric generator as a function of

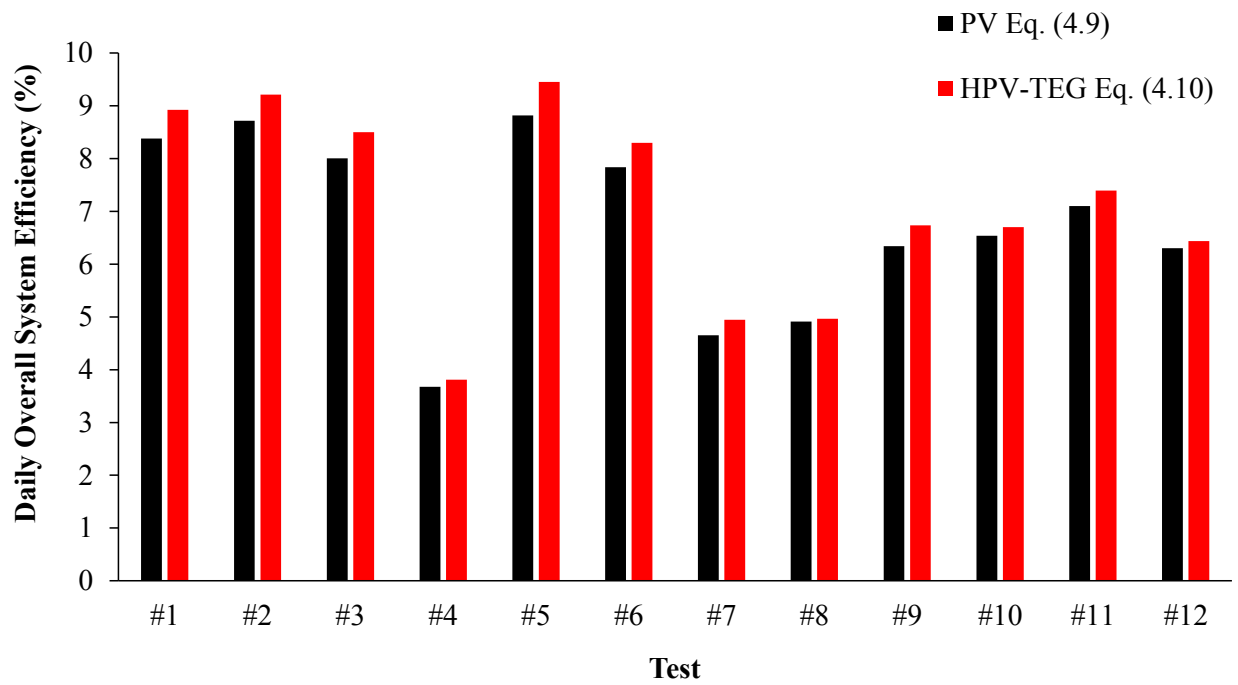


Figure 4.69: Daily overall system efficiency of conventional PV and HPV-TEG systems for each outdoor experimental test.

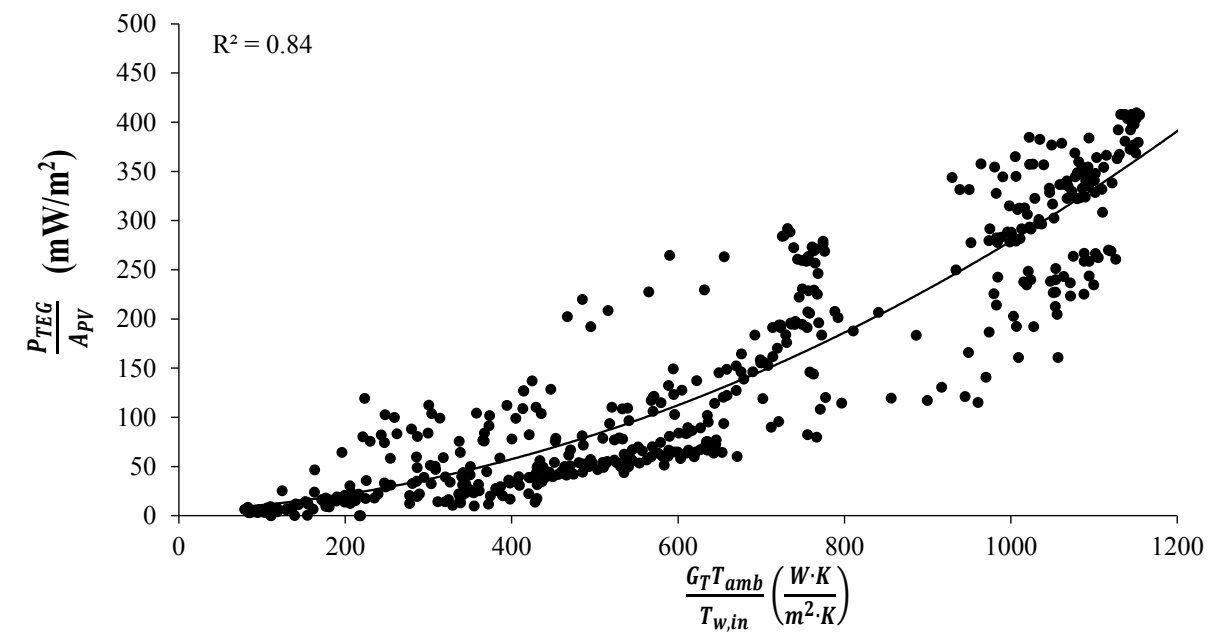


Figure 4.70: Thermolectric generator power density (P_{TEG}/A_{PV}) vs. ($G_T T_{amb}/T_{w,in}$).

irradiance intensity (W/m^2), ambient air temperature (K), and water inlet temperature (K):

$$\frac{P_{TEG}}{A_{PV}} = 2.38E - 4 \left(\frac{G_T T_{amb}}{T_{w,in}} \right)^2 + 3.66E - 2 \left(\frac{G_T T_{amb}}{T_{w,in}} \right) + 4.86 \quad (4.11)$$

where,

$$80 < \frac{G_T T_{amb}}{T_{w,in}} < 1200 \left(\frac{\text{W} \cdot \text{K}}{\text{m}^2 \cdot \text{K}} \right) \quad (4.12)$$

$$0.06 < C_{HPV-TEG} < 0.13 \quad (4.13)$$

where, $C_{HPV-TEG}$ is the thermoelectric generator concentration ratio. The thermoelectric generator concentration ratio is defined as the photovoltaic module surface area covered by the thermoelectric generator:

$$C_{HPV-TEG} = \frac{A_{TEG}}{A_{PV}} \quad (4.14)$$

This correlation assumes that the HPV-TEG system is fabricated similarly to the HPV-TEG modules in this research work. Variations between the experimental data and the sizing correlation are expected, since the experimental data was recorded during dynamic weather conditions. The sizing correlation is in good agreement with the experimentally obtained data, establishing a coefficient of determination R^2 equal to approximately 0.84 [149]. Therefore, the sizing correlation could be used to approximate the total power generated by a large-scale HPV-TEG system's thermoelectric generator. For example, consider the case where a HPV-TEG system experiences a constant irradiance intensity of $1000 \text{ W}/\text{m}^2$, ambient air temperature of $20 \text{ }^\circ\text{C}$, and water inlet temperature of $10 \text{ }^\circ\text{C}$. Assuming the HPV-TEG system is composed of 10 HPV-TEG modules each with an area (A_{PV}) of 0.25 m^2 and a TEG concentration ratio (C_{TEG}) equal to 0.12, the total power generated from the HPV-TEG system's thermoelectric generator is estimated to be 7.45 W. Further analysis of the relationship between the TEG power density and temperature gradient across the thermoelectric generator is shown in **Figure 4.71**. The TEG power density trend increases nonlinearly as the TEG temperature gradient increases. The temperature gradient across the TEG for the outdoor tests ranges from $0.1 \text{ }^\circ\text{C}$ to $18.5 \text{ }^\circ\text{C}$. Furthermore, the following correlation between the TEG power density and the temperature gradient across the thermoelectric generator was found based on the outdoor tests:

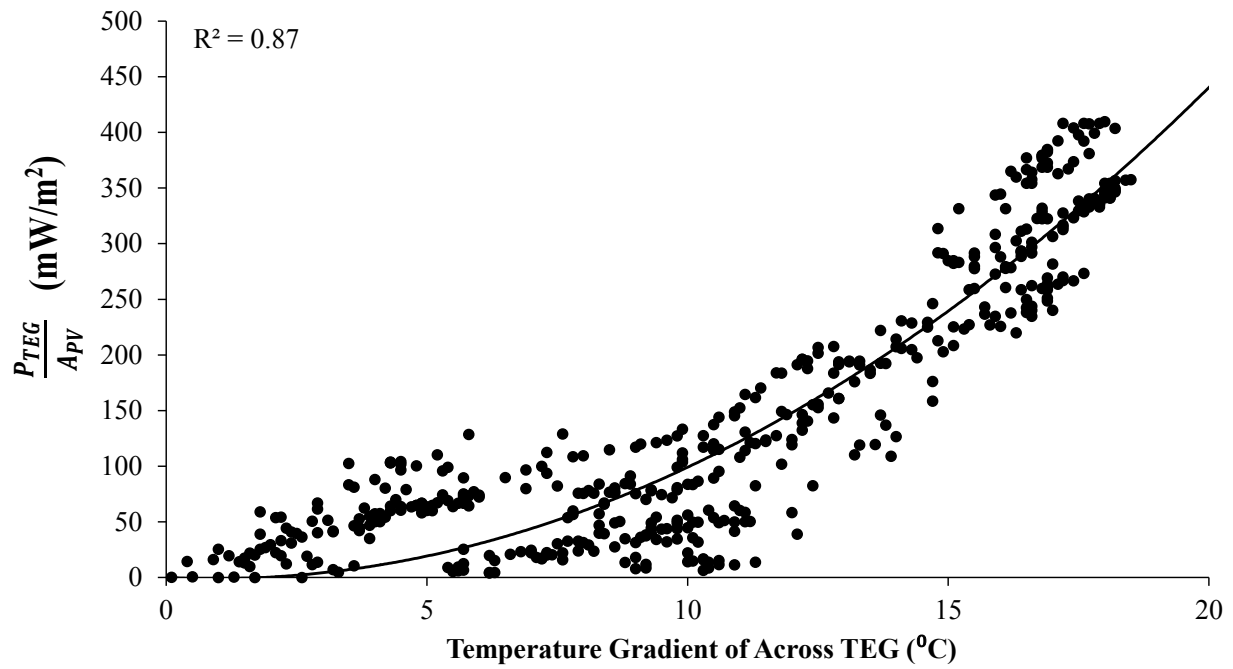


Figure 4.71: Thermoelectric generator power density P_{TEG}/A_{PV} vs. temperature gradient across TEG.

$$\frac{P_{TEG}}{A_{PV}} = 1.21(T_{h,TEG} - T_{c,TEG})^2 - 2.19(T_{h,TEG} - T_{c,TEG}) \quad (4.15)$$

where,

$$0 < (T_{h,TEG} - T_{c,TEG}) < 20 \text{ (}^{\circ}\text{C)} \quad (4.16)$$

$$0.06 < C_{HPV-TEG} < 0.13 \quad (4.17)$$

The outdoor results presented in **Figure 4.71** emphasize that the driving force for thermoelectric power generation is indeed the temperature gradient.

4.4 Proposed Scheme for Large-scale Application of HPV-TEG System

This research has provided valuable experimental performance characteristics and correlations of a HPV-TEG system. Large-scale application of HPV-TEG systems would increase the economic feasibility of the system due to the fact that increasing the capacity of a photovoltaic system decreases the overall cost (\$/W). For example, the total cost of a photovoltaic project through the California Solar Initiative program in 2011 with a capacity less than 10 kW was 6.37 \$/W, while the total cost of a PV system with a capacity greater than 100 kW was approximately 5.05 \$/W [150]. A proposed large-scale HPV-TEG system using a thermal regulated water tank is shown in **Figure 4.72**. The HPV-TEG system's modules are composed of a photovoltaic module, thermoelectric modules, aluminum layer, cooling channel, and insulation. A pump circulates water to each HPV-TEG module to maintain a low photovoltaic module temperature and temperature gradient across each thermoelectric module. Water exits each HPV-TEG module and is cooled through the use of a heat exchanger that is installed in the water storage tank. Circulating water can be added at any time to the storage tank to ensure the water inlet temperature remains cool in comparison to the photovoltaic module temperature. Circulating water may also be removed at any time to supply hot water to a water distribution system for heating or bathing purposes. Relief valves are installed for removing excess hot water when the water inlet or outlet from the HPV-TEG system establishes elevated temperatures. A controller connected to the pump is used to optimize the water flow rate to the HPV-TEG system. Electrical energy generated by the photovoltaic modules and thermoelectric generator is supplied to an inverter, where the electrical energy is converted from direct current (DC) to alternative current (AC). The AC electricity is delivered to an AC breaker where the electrical energy

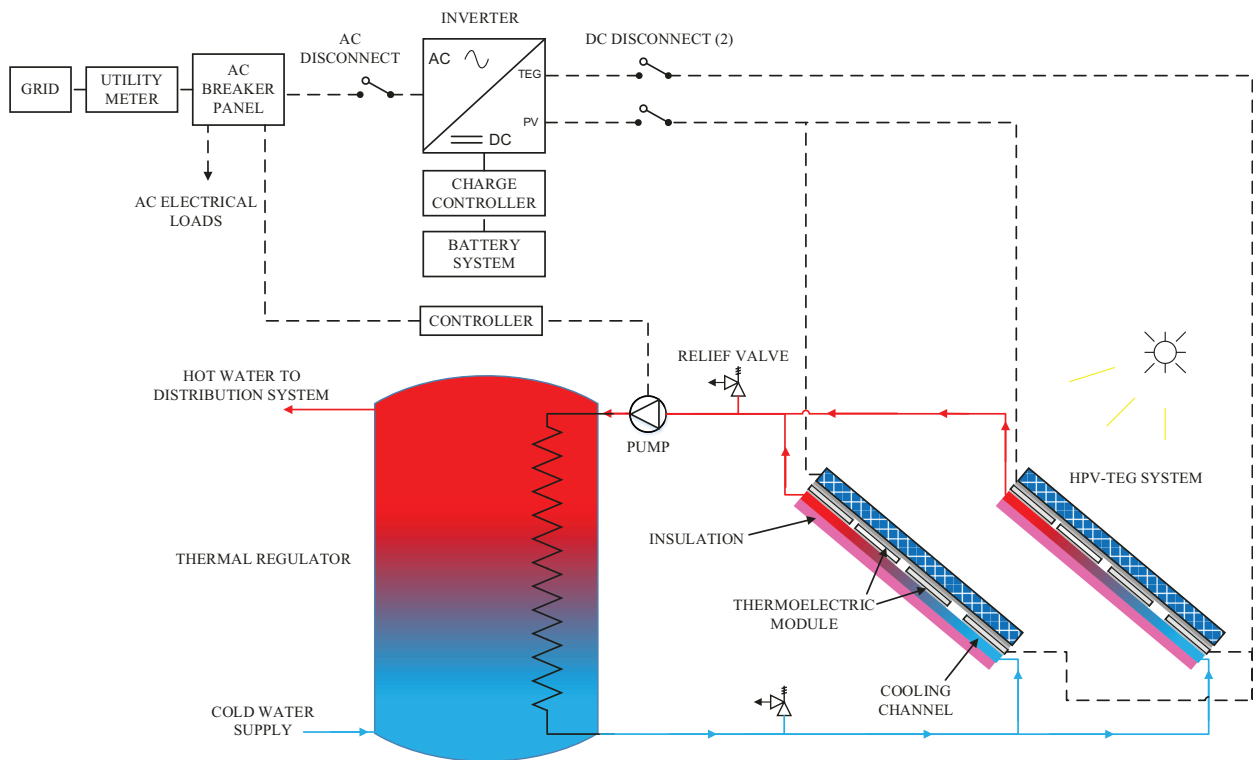


Figure 4.72: Proposed HPV-TEG system for large-scale application using thermal regulation water tank.

may be distributed to various electrical loads. Excess electrical energy may be directed to a charge controller which regulates the power supplied to the battery system. Electrical energy may be supplied from the batteries to the inverter if the power from the HPV-TEG system cannot meet the electrical loads' demand. If the battery is completely charged, the excess electricity may be supplied to the electrical grid at a price (typically ¢/kWh or \$/MWh) determined by the local power authority. The system would be more feasible in geographical location where the irradiance intensity and ambient air temperature remains high.

4.5 Uncertainty Analysis of Experimental Results

The uncertainty in the experimentally measured and calculated results is given in **Table 4.6**. An EXTECH wireless multimeter was used to measure the voltage and current output of the photovoltaic modules and thermoelectric generators, as well as the resistance of the electrical loads. T-type thermocouples with an operating range of -250 °C to 350 °C are used to measure the bottom surface of the photovoltaic modules and the hot side temperature of the thermoelectric generator. The accuracy of the T-type thermocouples is 1 °C or 0.75% of the measured temperature (whichever is maximum). The rotameter used to measure the water flow to the HPV-TEG system has an accuracy of 2% of the measured flow rate. The solar radiation intensity is measured using a silicon pyranometer sensor. The pyranometer has an operating range of 0 W/m² to 1280 W/m² with a spectral range of 300 to 1100 nm. A FLIR E4 camera is used to record the thermal profiles of the PV and HPV-TEG systems. The FLIR infrared camera has a least count of 0.1 °C and an accuracy of approximately 2%. For all FLIR camera measurements, the emissivity was set to 0.88. Uncertainty analysis of experimentally calculated parameters, such as power output of the photovoltaic module and TEG, was completed based on the methodology presented by Kline and McClintock [149]. Consider a variable y which is a function of multiple independent variables x_1, x_2, \dots, x_n :

$$y = f(x_1, x_2, \dots, x_n) \quad (4.18)$$

The uncertainty of the function y may be given by [149]:

$$w_y = \left[\left(\frac{\partial y}{\partial x_1} w_{x_1} \right)^2 + \left(\frac{\partial y}{\partial x_2} w_{x_2} \right)^2 + \dots + \left(\frac{\partial y}{\partial x_n} w_{x_n} \right)^2 \right]^{\frac{1}{2}} \quad (4.19)$$

where, $w_{x_1}, w_{x_2}, \dots, w_{x_n}$ are the uncertainties of the independent variables [149]. Based on the methodologies shown in equation (4.19), the uncertainty of the power output of the electrical devices in the indoor and outdoor simulations is approximately 1.0% and 0.32%, respectively.

Table 4.6: Uncertainty of experimentally measured and calculated parameters of indoor and outdoor simulations.

Parameter	Instrumentation	Uncertainty
DC voltage (V)	EXTECH wireless multimeter	0.06% [151]
DC current (A)	EXTECH wireless multimeter	1.0% [151]
Resistance (Ω)	EXTECH wireless multimeter	0.3% [151]
Water Temperature ($^{\circ}\text{C}$)	T-type thermocouple probe	$\max(1.0^{\circ}\text{C}, 0.75\%)$ [152]
Water flow (ml/min)	Rotameter	2% [152]
Irradiance intensity (W/m^2)	Onset pyranometer sensor	$\max(10 \text{ W}/\text{m}^2, 5\%)$ [153]
Ambient air temperature ($^{\circ}\text{C}$)	Onset temperature sensor	0.2 $^{\circ}\text{C}$ [153]
Wind Speed (m/s)	Onset wind speed sensor	$\max(1.1 \text{ m}/\text{s}, 4\%)$ [153]
Back PV surface Temperature ($^{\circ}\text{C}$)	T-type thermocouple	$\max(1.0^{\circ}\text{C}, 0.75\%)$ [152]
Hot TEG side temperature ($^{\circ}\text{C}$)	T-type thermocouple	$\max(1.0^{\circ}\text{C}, 0.75\%)$ [152]
Temperature profile ($^{\circ}\text{C}$)	FLIR E4 infrared camera	2% [154]
PV and TEG power for indoor simulations (W)	EXTECH wireless multimeter	1.0%
PV and TEG power for outdoor simulations (W)	EXTECH wireless multimeter	0.32%

Chapter 5: Conclusion and Future Recommendations

5.1 Conclusion

HPV-TEG systems have the potential to decrease the PV module temperature, increase PV module power, and generate additional electrical energy from the waste-heat using the TEG. The objective of this research work was to investigate the performance characteristics of a HPV-TEG system through numerical modeling, and extensive experimental case studies. The waste-heat from a solar-photovoltaic (PV) system may be efficiently removed by installing a thermoelectric generator and cooling system to the back surface of a photovoltaic module. This system is known as a hybrid photovoltaic-thermoelectric power generation system (HPV-TEG). The cooling system increases the rate of heat transferred from the photovoltaic module, and consequently reduces temperature and increases the energy conversion efficiency of the PV module. Additional electrical energy from the HPV-TEG system's thermoelectric generator is produced due to the temperature difference between the photovoltaic module and cooling system.

Prior to completing experimental simulations, the numerical model presented in chapter three was used to investigate the detrimental operating parameters that impede the performance of a HPV-TEG system. Due to the low temperature gradient across the TEG, the Thomson effect was initially determined to have a negligible effect on the photovoltaic module temperature, and power output of the PV module and thermoelectric generator. Parametric analysis of the irradiance intensity, ambient air temperature, and convective heat transfer coefficient concluded that the HPV-TEG system has the ability to outperform the conventional photovoltaic module while operating at high irradiance intensities and ambient air temperatures. The numerical model results also showed that the thermoelectric generator efficiency increases with respect to irradiance intensity and ambient air temperature. Energy and exergy analysis showed that the HPV-TEG system has the potential to establish higher energy and exergy efficiencies than the standard PV system under particular circumstances. The rate of exergy destruction of a HPV-TEG is significantly

influenced by the irradiance intensity, with the majority of the exergy destruction caused by optical losses from the top surface of the photovoltaic module.

The experimental work concentrated on evaluating the performance of three fully-instrumented hybrid photovoltaic-thermoelectric power generation systems. Two HPV-TEG systems were constructed using a 10-watt monocrystalline photovoltaic module, with one HPV-TEG system's thermoelectric generator consisting of two thermoelectric modules (10W-HPV-2TEG), and the other consisting of four thermoelectric modules (10W-HPV-4TEG). The third HPV-TEG system was comprised of a 40-watt monocrystalline photovoltaic module with a thermoelectric generator containing 10 thermoelectric modules (40W-HPV-10TEG).

The performance characteristics of these HPV-TEG systems was first completed using an indoor tungsten halogen solar simulator. The indoor simulator is a low-cost testing method that was developed to optimize the performance of the HPV-TEG systems. Preliminary indoor experiments determined that the addition of an aluminum layer significantly reduces the operating temperature of the HPV-TEG system, and increases the power output of the HPV-TEG system's photovoltaic module and thermoelectric generator. Power curves and thermal profiles using an infrared camera provided conclusive evidence that increasing the number of thermoelectric modules improves the overall performance and temperature distribution of a HPV-TEG system. The indoor tests showed that increasing the irradiance intensity by 315 W/m^2 increases the maximum power output and temperature gradient of the 10TEG by approximately 158.3 mW and $13.7 \text{ }^\circ\text{C}$. Elevated water inlet temperatures were shown to have a negative effect on the power output of the HPV-TEG system's photovoltaic module and thermoelectric generator. Lastly, the indoor simulation and performance of a HPV-TEG with a v-trough concentrator safely increased the power output of the photovoltaic module and thermoelectric generator, while maintaining a low operating temperature.

Experimental results of 12 outdoor tests compared the performance of the three different HPV-TEG systems under various operating conditions. The test results indicated that the HPV-TEG system is able to consistently produce more electrical energy than the conventional photovoltaic system for each four hour test. In test #10, the thermoelectric generator was able to produce approximately 0.52% of the total electrical energy generated

by the HPV-TEG system. The results of the outdoor tests also confirmed that the HPV-TEG system consistently has a higher daily overall system efficiency than the standard PV system. A sizing correlation based on the results of the outdoor tests was determined to estimate the thermoelectric generator power density based on the operating conditions of a HPV-TEG system for a specific thermoelectric generator concentration ratio.

5.2 Future Works and Recommendations

Numerical modeling and extensive experimental characterization of various designs of HPV-TEG systems has been implemented in this research work. The indoor solar simulator presented in section 4.2 provided a low cost method for testing and optimizing of the HPV-TEG system. However, the solar radiation simulated from the tungsten halogen lamps does not perfectly imitate the solar radiation from the Sun, establishing a higher intensity of infrared (longer) wavelengths. Future work may improve the simulated solar spectrum by using optical filters, such as dichroic filters, to reduce the intensity of infrared wavelengths emitted from the tungsten halogen lamps.

The designed HPV-TEG module prototypes successfully utilized the waste-heat from the photovoltaic module to produce electrical energy using a thermoelectric generator. It is recommended that future HPV-TEG system prototypes incorporate an all-in-one thermoelectric generator/cooling system that may be easily attached to a photovoltaic module. This optimized module design would make HPV-TEG systems a more attractive technology. Future research projects may also study the effect of the composition of the thermoelectric generator, investigating how different thermoelectric module types and sizes affect the power output and temperature distribution of the HPV-TEG system.

The outdoor experimental case study tests thoroughly examined the performance of multiple HPV-TEG systems with the system's corresponding unaltered photovoltaic module. Future outdoor experimental simulations may incorporate a solar tracker to maximize the irradiance intensity projected onto the HPV-TEG and PV systems. It should be noted that using a solar tracker may significantly increase the total cost of the system the type of technology used. The addition of a solar tracker would also permit a low concentration concentrator to be integrated into the HPV-TEG system. Low concentration concentrators, such as Fresnel lenses or v-trough concentrators, require a solar tracking system to

optimally focus and uniformly distribute the Sun's solar radiation onto the photovoltaic module. Based on the indoor solar simulator results, such a system would significantly increase the power output of the HPV-TEG system's photovoltaic module and thermoelectric generator. In the outdoor test setup, the HPV-TEG system's cooling liquid is supplied from a water distribution system. A practical HPV-TEG experimental test setup, including a thermal regulator water tank and pump similar to **Figure 4.72**, may be manufactured to determine the performance and constraints limiting the application of a stand-alone HPV-TEG system.

References

- [1] U. N. F. C. o. C. Change, "Definitions," United Nations, [Online]. Available: http://unfccc.int/essential_background/convention/background/items/2536.php. [Accessed 14 January 2015].
- [2] S. VijayaVenkataRaman, S. Iniyar and R. Goic, "A review of climate change, mitigation and adaptation," *Renewable and Sustainable Energy Reviews*, vol. 16, pp. 878-897, 2012.
- [3] T. Boden, G. Marland and R. Andrew, "Global, Regional, and national Fossil-Fuel CO₂ Emissions," Carbon Dioxide Information Analysis Center, Oak Ridge National Laboratory, U.S. Department of Energy, Oak Ridge, Tenn., U.S.A., [Online]. Available: http://cdiac.ornl.gov/trends/emis/tre_glob_2010.html. [Accessed January 2015].
- [4] T. Stocker, G. Qin, G. -K. Plattner, L. V. Alexander, S. K. Allen, N. L. Bindoff, F. -M. Bréon, J. Church, U. Cubasch, S. Emori, F. Piers, P. Friedlingstein, N. Gillett, J. M. Gregory, D. L. Hartmann, E. Jansen, B. Kirtman, R. Knutti, K. K. Kanikicharla, P. Lemki, J. Marotzke, V. Masson-Delmotte, G. A. Meehl, I. I. Mokhov, S. Piao, V. Ramaswamy, D. Randall, M. Rhein, M. Rojas, C. Sabine, D. Shindell, L. D. Talley, D. G. Vaughan and S. - P. Xie, "2013: Technical Summary," in *Climate Change 2013: Physical Science Basis, Contribution of working Group I to the Fifth Assessment Report of the Intergovernmental Panel on Climate Change*, T. F. Stocker, D. Qin, G. -. Plattner, M. Tignor, S. K. Allen, J. Boschung, A. Nauels, Y. Xia, V. Bex and P. M. Midgley, Eds., Cambridge, pp. 53-59.
- [5] 2. REN21, "Renewables 2014 Global Status Report," REN21 Secretariat, Paris, 2014.
- [6] N. S. Observations, "GISS Surface Temperature Analysis (GISTEMP)," 1 January 2015. [Online]. Available: <http://data.giss.nasa.gov/gistemp/>. [Accessed 2015 7 January].
- [7] IEA (2013), "Key World Energy Statistics 2013," OECD Publishing, Paris, 2013.
- [8] IEA (2014), "Renewable Energy Medium-Term Market Report," OECD Publishing, Paris, 2014.
- [9] J. A. Duffie and W. A. Beckman, *Solar Engineering of Thermal Processes*, Hoboken, New Jersey: John Wiley & Sons, Inc., 2013.
- [10] A. Goetzberger and V. U. Hoffmann, *Photovoltaic Solar Energy Generation*, Springer Berlin Heidelberg, 2005.

- [11] Z. Sen, *Solar Energy Fundamentals and Modeling Techniques*, Springer-Verlag London, 2008.
- [12] B. Hodge, "Alternative Energy Systems and Applications," John Wiley & Sons Inc., Danver, MA, 2010.
- [13] M. E. Meral and F. Dincer, "A review of the factors affecting operation and efficiency of photovoltaic based electricity generation systems," *Renewable and Sustainable Energy Reviews*, vol. 15, pp. 2176-2184, 2011.
- [14] S. R. Wehnam, M. A. Green, M. E. Watt, R. Corkish and A. Sproul, *Applied Photovoltaics*, Third, Ed., New York, NY: Earthscan, 2011.
- [15] M. K. Siddiki, J. Li, D. Galipeau and Q. Qiao, "A review of polymer multijunction solar cells," *Energy & Environmental Science*, vol. 3, pp. 867-883, 2010.
- [16] A. Shah, *Thin-film Silicon Solar Cells*, Boca Raton, FL: CRC Press, 2010.
- [17] K. Yamamoto, A. Nakajima, M. Yoshimi, T. Sawada, S. Fukuda, T. Suezaki, M. Ichikawa, Y. Koi, M. Goto, T. Meguro, T. Matsuda, M. Kondo, T. Sasaki and Y. Tawada, "A high efficiency thin film silicon solar cell and module," *Solar Energy*, vol. 77, pp. 939-949, 2004.
- [18] D. L. King and J. A. Krotochvil, "Temperature Coefficients for PV Modules and Arrays: Measurement Methods, Difficulties, and Results," Sandia National Laboratories, Albuquerque, NM, 1997.
- [19] L. Castaner and S. Silvestre, *Modeling Photovoltaic Systems Using PSpice*, Hoboken, NJ: John Wiley & Sons Inc., 2002.
- [20] E. Skoplaki and J. Palyvos, "On the temperature dependence of photovoltaic electrical performance: A review of efficiency/power correlations," *Solar Energy*, Vols. 614-624, p. 83, 2009.
- [21] Q. Mei, M. Shan, L. Liu and J. M. Guerrero, "A Novel Improved Variable Step-Size Incremental-Resistance MPPT Method for PV Systems," *IEEE Transactions on Industrial Electronics*, vol. 58, no. 6, pp. 2427-2434, June 2011.
- [22] A. H. Alqahtani, "A Simplified and Accurate Photovoltaic Module Parameters Extraction Approach using Matlab," *IEEE International Symposium on Industrial Electronics*, pp. 1748-1753, 2012.
- [23] D. H. Li, G. H. Cheung and J. C. Lam, "Analysis of the operational performance and efficiency characteristic for photovoltaic system in Hong Kong," *Energy Conversion and Management*, vol. 46, pp. 1107-1118, 2005.

- [24] F. Sarhaddi, S. Farahat, H. Ajam and A. Behzadmehr, "Exergetic performance assessment of a solar photovoltaic thermal (PV/T) air collector," *Energy and Buildings*, vol. 42, pp. 2184-2199, 2010.
- [25] S. Dubey, S. Solanki and A. Tiwari, "Energy and exergy analysis of PV/T air collectors connected in series," *Energy and Buildings*, vol. 41, pp. 863-870, 2009.
- [26] S. Nayak and G. Tiwari, "Energy and exergy analysis of photovoltaic/thermal integrated with a solar greenhouse," *Energy and Buildings*, vol. 40, pp. 2015-2021, 2008.
- [27] T. Chow, "A review on photovoltaic/thermal hybrid solar technology," *Applied Energy*, vol. 87, pp. 365-379, 2010.
- [28] D. Evans, "Simplified method for predictiong photovoltaic array output," *Solar Energy*, vol. 27, pp. 555-560, 1981.
- [29] "Research Cell Efficiency Records," National Center for Photovoltaics (NREL), 2014. [Online]. Available: <http://www.nrel.gov/ncpv/>. [Accessed January 2015].
- [30] H. Zondag, "Flat-plate PV-thermal collectors and systems: A review," *Renewable and Sustainable Energy Reviews*, vol. 12, pp. 891-959, 2008.
- [31] F. Sarhaddi, S. Farahat, H. Ajam and A. Behzadmehr, "Exergetic Optimization of a Solar Photovoltaic Array," *Journal of Thermodynamics*, pp. 1-11, 2009.
- [32] F. Sarhaddi, S. Farahat, H. Ajam and A. Behzadmehr, "Exergy efficiency of a solar photovoltaic array based on exergy destructions," *Proceedings of the Institution of Mechanical Engineers Part A: Journal of Power and Energy*, pp. 813-825, 2010.
- [33] A. S. Joshi, I. Dincer and B. V. Reddy, "Thermodynamic assessment of photovoltaic systems," *Solar Energy*, vol. 83, pp. 1139-1149, 2009.
- [34] A. Joshi, A. Tiwari, G. Tiwari, I. Dincer and R. B.V., "Performance evaluation of a hybrid photovoltaic thermal (PV/T) (glass-to-glass) system," *International Journal of Thermal Sciences*, vol. 48, pp. 154-164, 2009.
- [35] W. Zhou, H. Yang and Z. Fang, "A novel model for photovoltaic array performance prediction," *Applied Energy*, vol. 84, pp. 1187-1198, 2007.
- [36] H. Mousazadeh, A. Keyhani, A. Javadi, H. Mobli, K. Abrinia and A. Sharifi, "A review of principle and sun-tracking methods for maximizing solar systems output," *Renewable and Sustainable Energy Reviews*, vol. 13, pp. 1800-1818, 2009.

- [37] A. Rhif, "A Position Control Review for a Photovoltaic System: Dual Axis Sun Tracker," *IETE Technical Review*, vol. 28, no. 6, pp. 479-485, 2011.
- [38] T. Khatib, "A Review of Designing, Installing and Evaluating Standalone Photovoltaic Power Systems," *Journal of Applied Sciences*, vol. 10, no. 13, pp. 1212-1228, 2010.
- [39] W. T. Xie, Y. Dai, R. Wang and K. Sumathy, "Concentrated solar energy applications using Fresnel lenses: A review," *Renewable and Sustainable Energy Reviews*, vol. 15, pp. 2588-2606, 2011.
- [40] E. L. Meyer and E. E. van Dyk, "Assessing the Reliability and Degradation of Photovoltaic Module Performance Parameters," *IEEE Transactions on Reliability*, vol. 53, no. 1, pp. 83-91, 2004.
- [41] A. Luque and V. Andreev, Springer Series in Optical Sciences 130: Concentrator Photovoltaics, Springer, 2007.
- [42] N. Aste, C. del Pero and F. Leonforte, "Water flat plate PV-thermal collectors: A review," *Solar Energy*, vol. 102, pp. 98-115, 2014.
- [43] Y. Tripanagnostopoulos, T. Nousia, M. Souliotis and P. Yianoulis, "Hybrid Photovoltaic/thermal Solar Systems," *Solar Energy*, vol. 72, no. 3, pp. 217-234, 2002.
- [44] R. R. Avezov, J. S. Akhatov and N. R. Avezova, "A Review on Photovoltaic-Thermal (PV-T) Air and Water Collectors," *Applied Solar Energy*, vol. 47, no. 3, pp. 169-183, 2011.
- [45] J.-H. Kim and J.-T. Kim, "The Experimental Performance of an Unglazed PVT Collector with Two Different Absorbed Types," *International Journal of Photoenergy*, vol. 2015, pp. 1-6, 2012.
- [46] B. I. Ismail and H. W. Ahmed, "Thermoelectric Power Generation Using Waste-Heat Energy as an Alternative Green Technology," *Recent Patents on Electrical Engineering*, vol. 2, pp. 27-39, 2009.
- [47] K. Uchida, S. Takahashi, K. Harii, W. Koshibae, K. Ando, S. Maekawa and E. Saitoh, "Observation of the spin Seebeck effect," *Nature*, vol. 455, pp. 778-781, 2008.
- [48] Riffat, S. Riffat and X. Ma, "Thermoelectrics: a review of present and potential applications," *Applied Thermal Engineering*, vol. 23, pp. 913-935, 2003.
- [49] C. Goupil, W. Seifert, W. Zabrocki, E. Muller and G. J. Snyder, "Thermodynamics of Thermoelectric Phenomena and Applications," *Entropy*, vol. 13, pp. 1481-1517, 2011.

- [50] D. Rowe, *Thermoelectric handbook: macro to nano*, Boca Raton, FL: Taylor & Francis Group, 2006.
- [51] Y. A. Skripnik and A. I. Khimicheva, "Methods and Devices for Measuring the Peltier Coefficient of an Inhomogeneous Electric Circuit," *Measurement Techniques*, vol. 40, no. 7, pp. 673-677, 1997.
- [52] E. J. Sandoz-Rosado, S. J. Weinstein and R. J. Stevens, "On the Thomson effect in thermoelectric power devices," *International Journal of Thermal Sciences*, vol. 66, pp. 1-7, 2013.
- [53] B. I. Ismail, "Automotive Exhaust Gas Waste-heat Recovery for Green Electrical Power Generation Using Thermoelectric Technology," *Recent Patents on Electrical & Electronics Engineering*, vol. 5, pp. 185-197, 2012.
- [54] D. Rowe and G. Min, "Evaluation of thermoelectric modules for power generation," *Journal of Power Sources*, vol. 73, pp. 193-198, 1998.
- [55] "TE Technology," 2015. [Online]. Available: <https://tetech.com/>. [Accessed January 2015].
- [56] "TEGTEC MFR,," [Online]. Available: <http://tecteg.com/>. [Accessed January 2015].
- [57] "Custom Thermoelectric," Custom Thermoelectric, 2014. [Online]. Available: <http://www.customthermoelectric.com/>. [Accessed 20 April 2015].
- [58] "Ferro Tec," [Online]. Available: <https://www.ferrotec.com/>. [Accessed January 2015].
- [59] S. B. Riffat and X. Ma, "Improving the coefficient of performance of thermoelectric cooling systems: a review," *International Journal of Energy Research*, vol. 28, pp. 753-768, 2004.
- [60] K. W. Lindler, "Use of Multi-stage Cascades to Improve Performance of Thermoelectric Heat Pumps," *Energy Conversion Management*, vol. 39, no. 10, pp. 1009-1014, 1998.
- [61] "Marlow," [Online]. Available: <http://www.marlow.com/>. [Accessed February 2015].
- [62] "amsTECHNOLOGIES," 2015. [Online]. Available: <http://www.amstechnologies.com/products/thermal-management/thermoelectric-technologies/thermoelectric-modules/thermoelectric-cooler-modules-peltier-modules/view/multistage-thermoelectric-coolers/>. [Accessed February 2015].

- [63] "Thermoelectric Power Generator Module Selection," TEC, 2014. [Online]. Available: <http://thermoelectric-generator.com/thermoelectric-power-generator-module-selection/>. [Accessed 20 April 2015].
- [64] L. Francioso, C. De Pascali, I. Farella, C. Martucci, P. Creti, P. Siciliano and A. Perrone, "Flexible thermoelectric generator for ambient assisted living wearable biometric sensors," *Journal of Power Sources*, vol. 196, pp. 3239-3243, 2011.
- [65] G. Min and R. D.M., "Ring-structured thermoelectric module," *Semiconductor Science and Technology*, vol. 22, pp. 880-883, 2007.
- [66] A. Yadav, K. Pipe and M. Shtein, "Fiber-based flexible thermoelectric power generator," *Journal of Power Sources*, vol. 175, pp. 909-913, 2008.
- [67] Z. Wang, V. Leonov, P. Fiorini and C. Van Hoof, "Realization of a wearable miniaturized thermoelectric generator for human body applications," *Sensors and Actuators A*, vol. 156, pp. 95-102, 2009.
- [68] D. M. Rowe, "Review: Thermoelectric Waste Heat Recovery as a Renewable Energy Source," *International Journal of Innovations in Energy Systems and Power*, vol. 1, no. 1, pp. 13-23, 2006.
- [69] H. Xi, L. Luo and G. Fraisse, "Development and applications of solar-based thermoelectric technologies," *Renewable and Sustainable Energy Reviews*, vol. 11, pp. 923-936, 2007.
- [70] P. Li, L. Cai, P. Zhai, X. Tang, Q. Zhang and M. Niino, "Design of a Concentration Solar Thermoelectric Generator," *Journal of Electronic Materials*, vol. 39, no. 9, pp. 1522-1529, 2010.
- [71] X. W. Wang, H. Lee, Y. C. Lan, G. H. Zhu, G. Joshi, D. Z. Wang, J. Yang, A. J. Muto, M. Y. Tang, J. Klatsky, S. Song, M. S. Dresselhaus, G. Chen and Z. F. Ren, "Enhanced thermoelectric figure of merit in nanostructured n-type silicon germanium bulk alloy," *Applied Physics Letters*, vol. 93, pp. 1-3, 2008.
- [72] X. Shi, H. Kong, C. -P. Li, C. Uher, J. Yang, J. R. Salvador, H. Wang, L. Chen and W. Zhang, "Low thermal conductivity and high thermoelectric figure of merit in n-type $\text{Ba}_x\text{Yb}_y\text{Co}_4\text{Sb}_{12}$ double-filled skutterudites," *Applied Physics Letters*, vol. 92, pp. 1-4, 2008.
- [73] Z. Dughaish, "Lead telluride as a thermoelectric material for thermoelectric power generation," *Physica B*, vol. 322, pp. 205-223, 2002.

- [74] J. T. Jarman, E. E. Khalil and E. Khalaf, "Energy Analyses of Thermoelectric Renewable Energy Sources," *Open Journal of Energy Efficiency*, vol. 2, pp. 143-153, 2013.
- [75] V. Semenyuk, "A Comparison of Performance Characteristics of Multistage Thermoelectric Coolers Based on Different Ceramic Substrates," *Journal of Electronic Materials*, vol. 43, no. 6, pp. 1539-1547, 2014.
- [76] "96% Alumina Material Properties," Accuratus Ceramic Corporation, [Online]. Available: <http://accuratus.com/pdf/96aluminaprops.pdf>. [Accessed February 2015].
- [77] "Fine Ceramics (Advanced Ceramics) - Thermal Conductivity," Kyocera, [Online]. Available: <http://global.kyocera.com/prdct/fc/list/tokusei/denndou/index.html>. [Accessed February 2015].
- [78] "Beryllium Oxide Ceramic," Aavid Thermalloy, [Online]. Available: <http://www.aavid.com/product-group/interface/insulators/beryllium>. [Accessed January 2015].
- [79] D. Rowe and G. Min, "Design theory of thermoelectric modules for electrical power generation," *IEE Proceedings - Science, Measurement and Technology*, vol. 143, no. 6, pp. 351-356, 1996.
- [80] O. Yamashita, H. Odahara and S. Tomiyoshi, "Effect of metal electrode on thermoelectroc power in bismuth telluride compounds," *Journal of Materials Science*, vol. 39, pp. 5653-5658, 2004.
- [81] A. Kane, V. Verma and B. Singh, "Temperature Dependent Analysis of Thermoelectric Module using Matlab/Simulink," *IEEE Conference on Power and Energy*, pp. 632-637, 2012.
- [82] X. Gou and H. Xiao, "Modeling, experimental study and optimization on low-temperature waste heat thermoelectric generator system," *Applied Energy*, vol. 87, pp. 3131-3136, 2010.
- [83] Y. Y. Hsiao, W. C. Chang and S. L. Chen, "A mathematical model of thermoelectric module with applications on waste heat recovery from automobile engine," *Energy*, vol. 35, pp. 1447-1454, 2010.
- [84] C. Borgnakke and R. E. Sonntag, *Fundamentals of Thermodynamics*, Seventh ed., Danvers, MA: John Wiley & Sons Inc., 2009.

- [85] F. J. Lesage and N. Pagé-Potvin, "Experimental analysis of peak power output of a thermoelectric liquid-to-liquid generator under an increasing electrical load resistance," *Energy Conversion and Management*, vol. 66, pp. 98-105, 2013.
- [86] H. Wang, R. Mccarty, J. R. Salvador, Y. Atsushi and J. Konig, "Determination of Thermoelectric Module Efficiency: A Survey," *Journal of Electronic Materials*, vol. 43, no. 6, pp. 2274-2285, 2014.
- [87] G. Min, D. Rowe and K. Kontostavlakis, "Thermoelectric figure-of-merit under large temperature differences," *Journal of Physics D: Applied Physics*, vol. 37, pp. 1301-1304, 2004.
- [88] H. Zhang, "A general approach in evaluating and optimizing thermoelectric coolers," *International Journal of Refrigeration*, vol. 33, pp. 1187-1196, 2010.
- [89] O. Yamashita, "Effect of temperature dependence of electrical resistivity on the cooling performance of a single thermoelectric element," *Applied Energy*, vol. 85, pp. 1002-1014, 2008.
- [90] O. Yamashita and S. Sugihara, "High-performance bismuth-telluride compounds with highly stable thermoelectric figure of merit," *Journal of Materials Science*, vol. 40, pp. 6439-6444, 2005.
- [91] K. T. Kim, K. J. Kim and G. H. Ha, "Thermoelectric Properties of P-type Bismuth Telluride Powders Synthesized by a Mechano-Chemical Process," *Electronic Materials Letters*, vol. 6, no. 4, pp. 177-180, 2010.
- [92] M. Yasukawa, T. Kono, K. Ueda, H. Yanagi, S. W. Kim and H. Hosono, "Thermoelectric properties and figure of merit of perovskite-type $Ba_{1-x}La_xSnO_3$ with $x=0.002-0.008$," *Solid State Communications*, vol. 2013, pp. 49-53, 2013.
- [93] W. Kim, J. Zide, A. Gossard, D. Klenov, S. Stemmer, A. Shakouri and A. Majumdar, "Thermal Conductivity Reduction and Thermoelectric Figure of Merit Increase by Embedding Nanoparticles in Crystalline Semiconductors," *Physical Review Letters*, vol. 96, pp. 1-4, 2006.
- [94] R. Venkatasubramanian, E. Siivola, T. Colpitts and B. O'Quinn, "Thin-film thermoelectric devices with high room-temperature figures of merit," *Nature*, vol. 413, pp. 597-602, 2001.
- [95] Y. Z. Pei, J. Yang, L. D. Chen, W. Zhang, J. R. Salvador and J. Yang, "Improving thermoelectric performance of caged compounds through light-element filling," *Applied Physics Letters*, vol. 95, pp. 1-3, 2009.

- [96] J. P. Heremans, V. Jovovic, E. S. Toberer, A. Saramat, K. Kurosaki, A. Charoenphakdee, S. Yamanaka and G. J. Snyder, "Enhancement of Thermoelectric Efficiency in PbTe by Distortion of the Electronic Density of States," *Science*, vol. 321, pp. 554-557, 2008.
- [97] H. Alam and S. Ramakrishna, "A review on the enhancement of figure of merit from bulk to nano-thermoelectric materials," *Nano energy*, pp. 1-23, 2013.
- [98] B. Fortunato, M. Torresi and A. Deramo, "Modeling, performance analysis and economic feasibility of mirror-augmented photovoltaic system," *Energy Conversion and Management*, vol. 80, pp. 276-286, 2014.
- [99] U. E. I. Administration, "Levelized Cost and Levelized Avoided Cost of New Generation Resources in the Annual," April 2014. [Online]. Available: http://www.eia.gov/forecasts/aeo/pdf/electricity_generation.pdf. [Accessed February 2015].
- [100] S. Agrawal, G. Tiwari and H. Pandey, "Indoor experimental analysis of glazed hybrid photovoltaic thermal tiles air collector connected in series," *Energy and Buildings*, vol. 53, pp. 145-151, 2012.
- [101] S. Solanki, S. Dubey and A. Tiwari, "Indoor simulation and testing of photovoltaic thermal (PV/T) air collectors," *Applied Energy*, vol. 86, pp. 2421-2428, 2009.
- [102] S. Karabetoglu, A. Sisman, Z. F. Ozturk and T. Sahin, "Characterization of a thermoelectric generator at low temperatures," *Energy Conversion and Management*, vol. 62, pp. 47-50, 2012.
- [103] C.-T. Hsu, G.-Y. Huang, H.-S. Chu, B. Yu and D.-J. Yao, "An effective Seebeck coefficient obtained by experimental results of a thermoelectric generator module," *Applied Energy*, vol. 88, pp. 5173-5179, 2011.
- [104] P. Yodovard, J. Khedari and J. Hirunlabh, "The Potential of Waste Heat Thermoelectric Power Generation From Diesel Cycle and Gas Turbine Cogeneration Plants," *Energy Sources*, vol. 23, pp. 213-224, 2001.
- [105] A. Date, A. Date, C. Dixon and A. Akbarzadeh, "Progress of thermoelectric power generation systems: Prospect for small to medium scale power generation," *Renewable and Sustainable Energy Reviews*, vol. 33, pp. 371-381, 2014.
- [106] D. Dai, Y. Zhou and J. Liu, "Liquid metal based thermoelectric generation system for waste heat recovery," *Renewable Energy*, vol. 36, pp. 3530-3536, 2011.

- [107] M. H. Nia, A. A. Nejad, A. M. Goudarzi, M. Valizadeh and P. Samadian, "Cogeneration solar system using thermoelectric module and fresnel lens," *Energy Conversion and Management*, vol. 84, pp. 305-310, 2014.
- [108] W.-H. Chen, C.-C. Wang, C.-I. Hung, C.-C. Yang and R.-C. Juang, "Modeling and simulation for the design of thermal-concentrated solar thermoelectric generator," *Energy*, vol. 64, pp. 287-297, 2014.
- [109] D. Kraemer, B. Poudel, H. Feng, J. C. Caylor, B. Yu, X. Yan, Y. Ma, X. Wang, D. Wang, A. Muto, K. McEnaney, M. Chiesa, Z. Ren and G. Chen, "High-performance flat-panel solar thermoelectric generators with high thermal concentration," *nature materials*, vol. 10, pp. 532-538, 2011.
- [110] E. Chávez-Urbiola, Y. V. Vorobiev and L. Bulat, "Solar hybrid systems with thermoelectric generators," *Solar Energy*, vol. 86, pp. 369-378, 2012.
- [111] M. Daud, N. B. Mohd Nor and T. Ibrahim, "Novel Hybrid Photovoltaic and Thermoelectric Panel," *IEEE International Power Engineering and Optimization Conference*, pp. 269-274, June 2012.
- [112] H. Najafi and K. A. Woodbury, "Optimization of a cooling system based on Peltier effect for photovoltaic cells," *Solar Energy*, vol. 2013, pp. 152-160, 2013.
- [113] H. Najafi and K. A. Woodbury, "Modeling and Analysis of a Combined Photovoltaic-Thermoelectric Power Generation System," *Journal of Solar Energy Engineering*, vol. 135, pp. 1-8, August 2013.
- [114] T. Liao, B. Lin and Z. Yang, "Performance characteristics of a low concentrated photovoltaic-thermoelectric hybrid power generation device," *Internternational Journal of Thermal Sciences*, vol. 77, pp. 158-164, 2014.
- [115] W. van Sark, "Feasibility of photovoltaic - Thermoelectric hybrid modules," *Applied Energy*, vol. 88, pp. 2785-2790, 2011.
- [116] Y. A. Cengel, *Heat Transfer: A Practical Approach*, Second ed., New York, NY: McGraw-Hill Science/Engineering/Math, 2002.
- [117] F. P. Incropera, D. P. Dewitt, T. L. Bergman and A. S. Lavine, *Introduction to Heat Transfer*, Fifth ed., Hoboken, New Jersey: John Wiley & Sons, 2007.
- [118] HES PV, "HES-10 and HES-20 Spec Sheet," [Online]. Available: <http://hespv.ca/>. [Accessed 14 March 2015].
- [119] Z. Lu and Q. Yao, "Energy analysis of silicon cell modules based on an optical model for arbitrary layers," *Solar Energy*, vol. 81, pp. 636-647, 2007.

- [120] "Thermal," FINE CERAMICS WORLD, [Online]. Available: <http://global.kyocera.com/fcworld/charact/heat/thermalcond.html>. [Accessed 20 March 2015].
- [121] R. Ahiska and K. Ahiska, "New method for investigation of parameters of real thermoelectric modules," *Energy Conversion and Management*, vol. 51, pp. 338-345, 2010.
- [122] C. Wu, "Analysis of Waste-heat Thermoelectric Power Generators," *Applied Thermal Engineering*, vol. 16, no. 1, pp. 63-69, 1996.
- [123] W. He, J. Zhou, J. Hou, C. Chen and J. Ji, "Theoretical and experimental investigation on a thermoelectric cooling and heating system driven by solar," *Applied Energy*, vol. 107, pp. 89-97, 2013.
- [124] L. Chen, F. Meng and F. Sun, "Effect of heat transfer on the performance of thermoelectric generator-driven thermoelectric refrigerator system," *Cryogenics*, vol. 52, pp. 58-65, 2012.
- [125] A. Kane and V. Verma, "Performance Enhancement of Building Integrated Photovoltaic Module using Thermoelectric Cooling," *International Journal of Renewable Energy Research*, vol. 3, no. 2, pp. 320-324, 2013.
- [126] J. Chen and Z. Yan, "The influence of Thomson effect on the maximum power output and maximum efficiency of a thermoelectric generator," *Journal of Applied Physics*, vol. 79, no. 11, pp. 8823-8828, 1996.
- [127] J. Chen and C. Wu, "Analysis on the Performance of a Thermoelectric Generator," *Journal of Energy Resources Technology*, vol. 122, no. 61-63, 2000.
- [128] A. Montecucco, J. Buckle and A. Knox, "Solution to the 1-D unsteady heat conduction equation with internal Joule heat generation for thermoelectric devices," *Applied Thermal Engineering*, vol. 35, pp. 177-184, 2012.
- [129] S. A. Kalogirou, "Solar Energy Engineerings: Processes and Systems," Academic Press, 2009.
- [130] E. Saloux, A. Teyssedou and M. Sorin, "Explicit model of photovoltaic panels to determine voltages and currents at the maximum power point," *Solar Energy*, vol. 85, pp. 713-722, 2011.
- [131] W. De Soto, S. Klein and W. Beckman, "Improvement and validation of a model for photovoltaic array performance," *Solar Energy*, vol. 80, pp. 78-88, 2006.

- [132] A. Virtuani, D. Pavanello and G. Friesen, "Overview of Temperature Coefficients of Different Thin Film Photovoltaic Technologies," *Proceedings of 25th European Photovoltaic Solar Energy Conference*, pp. 4248-4252, 6-10 September 2010.
- [133] R. A. Messenger and J. Ventre, *Photovoltaic Systems Engineering*, Second ed., Boca Raton, FL: CRC Press, 2004.
- [134] "Choosing a Solver," MathWorks, 2015. [Online]. Available: <http://www.mathworks.com/help/optim/ug/choosing-a-solver.html>. [Accessed 20 April 2015].
- [135] "Equation Solving Algorithms," Mathworks, 2015. [Online]. Available: <http://www.mathworks.com/help/optim/ug/equation-solving-algorithms.html>. [Accessed 20 April 2015].
- [136] Y. A. Cengel and M. A. Boles, *Thermodynamics: An Engineering Approach*, New York, NY: McGraw-Hill, 2008.
- [137] A. Bejan, *Advanced Engineering Thermodynamics*, Hoboken, New Jersey: John Wiley & Sons, Inc., 2006.
- [138] I. Dincer and M. A. Rosen, *Exergy: Energy, Environment and Sustainable Development*, Oxford, UK: Elsevier Ltd., 2007.
- [139] C.-C. Wang and C.-I. Hung, "Effect of Irreversibilities on the Performance of Thermoelectric Generator Investigated Using Exergy Analysis," *Journal of Thermal Science and Technology*, vol. 8, no. 1, pp. 1-14, 2013.
- [140] J. Szargut, *Exergy Method: Technical and Ecological Applications*, Ashurst, Southampton, UK: WIT Press, 2005.
- [141] E. Akyuz, C. Coskun, Z. Oktay and I. Dincer, "A novel approach for estimation of photovoltaic exergy efficiency," *Energy*, vol. 44, pp. 1059-1066, 2012.
- [142] C. S. Sangani and C. S. Solanki, "Experimental evaluation of V-trough (2 suns) PV concentrator system using commercial PV modules," *Solar Energy Materials & Solar Cells*, vol. 91, pp. 453-459, 2007.
- [143] R. J. Matson, K. A. Emergy and R. E. Bird, "Terrestrial Solar Spectra, Solar Simulation and Solar Cell Short-circuit Current Calibration: A Review," *Solar Cells*, vol. 11, pp. 105-145, 1984.

- [144] Statistics Canada, "Census metropolitan area of Thunder Bay, Ontario," 8 January 2015. [Online]. Available: <https://www12.statcan.gc.ca/census-recensement/2011/as-sa/fogs-spg/Facts-cma-eng.cfm?LANG=Eng&GK=CMA&GC=595>. [Accessed April 2015].
- [145] Government of Canada, "Monthly Climate Summaries," 11 February 2015. [Online]. Available: http://climate.weather.gc.ca/prods_servs/cdn_climate_summary_e.html. [Accessed May 2015].
- [146] Current Results, "Sunshine in Ontario: Average Hours and Days a Year," 2015. [Online]. Available: <http://www.currentresults.com/Weather/Canada/Ontario/sunshine-annual-average.php>. [Accessed May 2015].
- [147] Google Maps, "Thunder Bay, ON," 2015. [Online]. Available: <https://www.google.ca/maps/place/Thunder+Bay,+ON/@48.8019462,-82.4996501,5z/data=!4m2!3m1!1s0x4d5921774c16e98d:0x3d0557348f1d8b74>. [Accessed May 2015].
- [148] W. Durisch , B. Bitnar, J.-C. Mayor, H. Kiess, K.-h. Lam and J. Close, "Efficiency model for photovoltaic modules and demonstration of its application to energy yield estimation," *Solar Energy Materials & Solar Cells*, vol. 91, pp. 79-84, 2007.
- [149] J. P. Holman, *Experimental Methods for Engineers*, McGraw-Hill, Inc. , 1989.
- [150] D. Feldman, G. Barbose, R. Margolis, R. Wiser, N. Darghouth and A. Goodrich, "Photovoltaic (PV) Pricing Trends: Historical, Recent, and Near-Term Projections," National Renewable Energy Laboratory, 2011.
- [151] EXTECH INSTRUMENTS. [Online]. Available: <http://www.extech.com/instruments/>. [Accessed May 2015].
- [152] OMEGA. [Online]. Available: <http://www.omega.ca/>. [Accessed 2015 May].
- [153] onset HOBOData Loggers. [Online]. Available: <http://www.onsetcomp.com/>. [Accessed May 2015].
- [154] FLIR INSTRUMENTS. [Online]. Available: <http://www.flir.ca/home/>. [Accessed May 2015].

Appendix-A



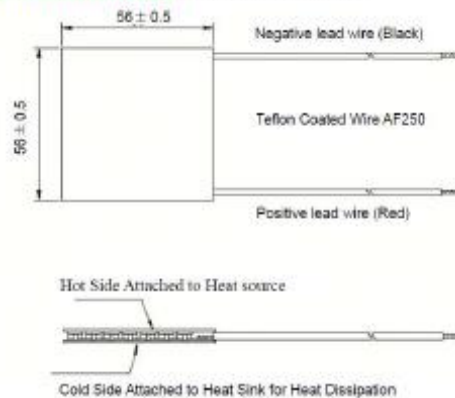
Specifications TEG Module TEG1-12611-6.0



SNAPSHOT SPECIFICATION OF TEG1-12611-6.0

Hot Side Temperature (°C)	300
Cold Side Temperature (°C)	30
Open Circuit Voltage (V)	8.4
Matched Load Resistance (ohms)	1.2
Matched load output voltage (V)	4.2
Matched load output current (A)	3.4
Matched load output power (W)	14.6
Heat flow across the module(W)	≈ 365
Heat flow density(W/cm ²)	≈ 11.6
AC Resistance(ohms) Measured under 27 °C at 1000Hz	0.5-0.7

Geometric Characteristics Dimensions in millimeter

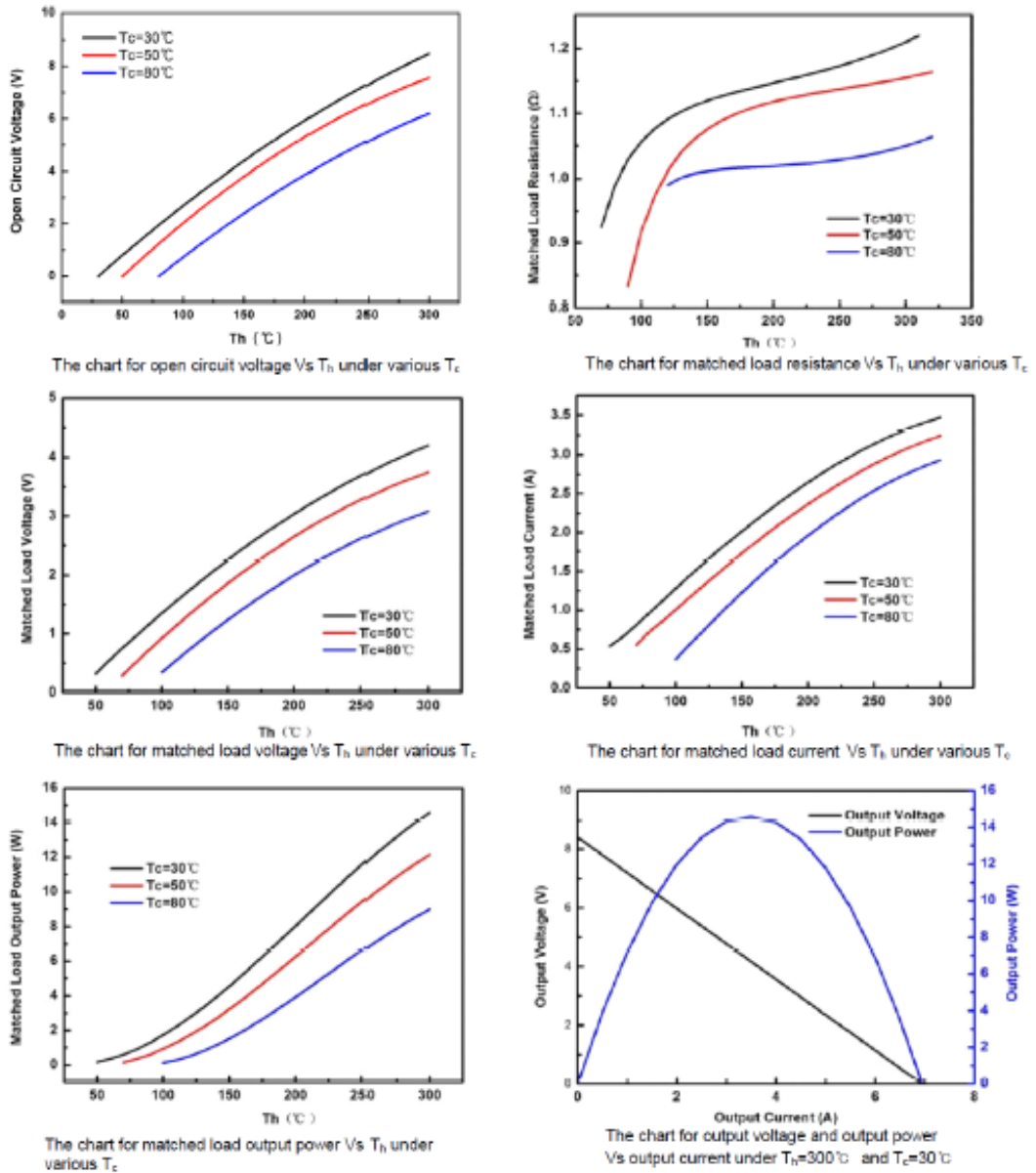


TECTEG@ROGERS.COM N.A 1-800-769-2395 World 1-905-751-1362 website: www.TEGPOWERGENERATOR.COM

Figure A.1: Specifications of TEG1-12611-6.0 thermoelectric module used in HPV-TEG system.



SNAPSHOT SPECIFICATION OF TEG1-12611-6.0



TECTEG@ROGERS.COM N.A 1-800-769-2395 World 1-905-751-1362 website: www.TEGPOWERGENERATOR.COM

Figure A.2: Electrical specifications of TEG1-12611-6.0 thermoelectric module used in HPV-TEG system.



www.hespv.ca

HES-10 // HES-20 // 10/20 Watt Max Power Solar Module

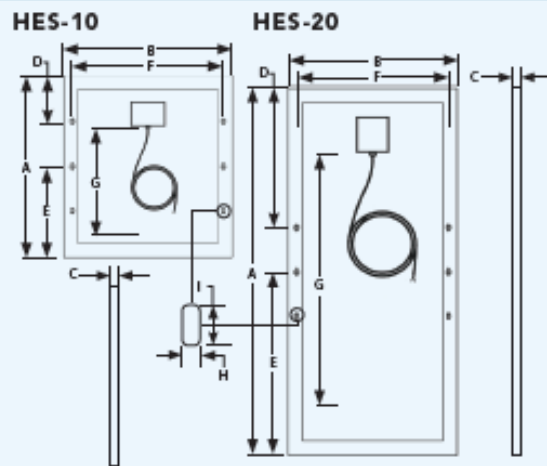
ELECTRICAL CHARACTERISTICS		
Model	HES-10	HES-20
Max Power (Pmax)	10 W	20 W
Tolerance of (Pmax)	0~+ 3W	
Type of Cell	Mono-Crystalline	
Cell Configuration	36 in series	
Open Circuit Voltage (Voc)	19.8 V	22.1 V
Maximum Power Voltage (Vpm)	15.7 V	17.2 V
Short Circuit Current (Isc)	0.72 A	1.32 A
Maximum Power Current (Ipm)	0.64 A	1.17 A
Series Fuse Rating	10 A	10 A

STC - Standard Test Conditions: Irradiation 1000 W/m² - Air mass AM 1.5 - Cell temperature 25 °C

* Calculated using maximum power

MECHANICAL CHARACTERISTICS		
Model	HES-10	HES-20
Dimensions (A x B x C)	12.8" x 11.9" x 1.0" 324 x 303 x 25 mm	25.9" x 11.8" x 1.0" 659 x 300 x 25 mm
Cable Length	120" 3048 mm	
Weight	1.1 kg / 2.42 lbs	2.8 Kg / 6.12 lbs
Operating Temperature	-40 to 85° C -40 to 185°F	

DIMENSIONS

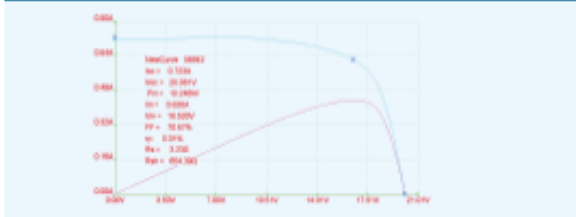


HES-10				
A	B	C	D	E
12.8"/324mm	11.9"/303 mm	1.0"/25mm	3.3"/83mm	6.4"/162mm
F	G	H	I	
10.6"/270mm	120"/3048mm	.15"/3.8 mm	.28"/7.1mm	

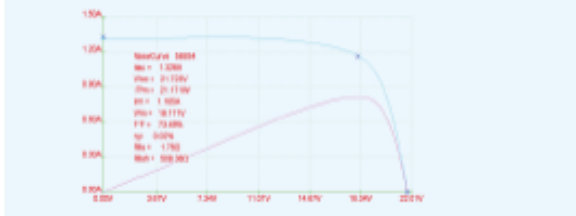
HES-20				
A	B	C	D	E
25.9"/659mm	11.8"/300 mm	1.0"/25mm	9.8"/250mm	13.0"/329mm
F	G	H	I	
10.6"/270mm	120"/3048mm	.15"/3.8 mm	.28"/7.1mm	

WARRANTY
10 Year limited warranty on material and workmanship
25 Year Power Guarantee
Years 0 - 10 > 90%
Years 10 - 25 > 80%

HES-10 IV CURVES



HES-20 IV CURVES



CERTIFICATIONS

CE Standard 



t. 866.258.0110 w. hespv.ca
f. 866.437.5531 e. sales@hespv.ca

Design and specifications are subject to change without notice. HES PV is a registered trademark™ of Home Energy Solutions Ltd. All other trademarks are property of their respective owners. Contact Home Energy Solutions to obtain the latest product manuals before using any HES PV Products.

Figure A.3: Dimensions and electrical specifications of HES-10 photovoltaic module.